The Development of Lightweight Cellular Structures for Metal Additive Manufacturing

Submitted by **Ahmed Yussuf Hussein** to the **University of Exeter**

as a thesis for the degree of

Doctor of Philosophy in Engineering

In November 2013

I certify that all material in this thesis which is not my own work has been identified and that no material has previously been submitted and approved for the award of a degree by this or any other University.

Signature: ……………………………………………………………..

Abstract

Metal Additive Manufacturing (AM) technologies in particular powder bed fusion processes such as Selective Laser Melting (SLM) and Direct Metal Laser Sintering (DMLS) are capable of producing a fully-dense metal components directly from computer-aided design (CAD) model without the need of tooling. This unique capability offered by metal AM has allowed the manufacture of inter-connected lattice structures from metallic materials for different applications including, medical implants and aerospace lightweight components. Despite the many promising design freedoms, metal AM still faces some major technical and design barriers in building complex structures with overhang geometries. Any overhang geometry which exceeds the minimum allowable build angle must be supported. The function of support structure is to prevent the newly melted layer from curling due to thermal stresses by anchoring it in place. External support structures are usually removed from the part after the build; however, internal support structures are difficult or impossible to remove.

These limitations are in contrast to what is perceived by designers as metal AM being able to generate all conceivable geometries. Because support structures consume expensive raw materials, use a considerable amount of laser consolidation energy, there is considerable interest in design optimisation of support structure to minimize the build time, energy, and material consumption. Similarly there is growing demand of developing more advanced and lightweight cellular structures which are self-supporting and manufacturable in wider range of cell sizes and volume fractions using metal AM.

The main focuses of this research is to tackle the process limitation in metal AM and promote design freedom through advanced self-supporting and low-density Triply Periodic Minimal Surface (TPMS) cellular structures. Low density uniform, and graded, cellular structures have been developed for metal AM processes. This work presents comprehensive experimental test conducted in SLM and DMLS processes using different TPMS cell topologies and materials. This research has contributed to new knowledge in understanding the manufacturability and mechanical behaviour of TPMS cellular structures with varying cell sizes, orientations and volume fractions. The new support structure method will address the saving of material (via low volume cellular structures and easy removal of powder) and saving of energy (via reduced build-time).

List of Contents

List of Figures

List of Tables

Acknowledgement

All praise and thanks to Allah the exalted, the Lord of the universe, the One who, by His blessing and favour, good works are accomplished.

I would like to express my sincere gratitude to my supervisor Dr. Liang Hao for the continuous support of my PhD study, for his patience, motivation, and enthusiasm. His guidance helped me in all aspects of this research.

I would like to thank my second supervisor Prof. Richard Everson for his valuable advice and support during this project. His contribution in my modelling work was crucial to my understanding of the metal AM process.

I would like to express my special thanks to Dr. Chunze Yan for his support in my experimental work. This PhD work would not have been possible without his guidance, encouragement, and experience.

For the provision of research facilities, I would like to thank Exeter Advanced Technologies (X-AT) and Centre for Additive Layer Manufacturing (CALM).

For the materials analysis, I would like to thank Dr. Lesley Wears and Dr. Hong Chang. I would like to thank all my colleagues in the college of engineering and mathematics who supported me directly or indirectly.

I would like to thank the SAVING project partners (3T RPD Ltd, Simpleware Ltd., DELCAM, Crucible Industrial Design Ltd, EOS GmbH, and Plunkett Associates Ltd) for their collaboration in the project. Special thanks to 3T RPD Ltd., for allowing me to conduct experimental works in their machines and in particular Dr. Simon Bubb for his technical support. Special thanks also go to Simpleware for providing me their software and in particular Dr. David Raymont for his continuous support.

I would like to thank the Technology Strategy Board (TSB) for providing the financial support for this project.

I would like to express very special thanks to my lovely wife for her patience, prayers, sacrifice, and ideas throughout my study period. Many thanks to my beloved son and daughter for bringing joy and happiness to my life.

I acknowledge my sincere indebtedness and gratitude to my dearest parents and sibling for their continuous love throughout my life.

List of Publications

Journal Papers:

Hussein A, Hao L, Yan C, Everson R, Raymont D, Young P. (2014) Developing Functionally Graded Cellular Support Structures for Metal Additive Manufacturing, International journal of solids and structures . **(Submitted)**

Yan, C., Hao, L., Hussein, A., Young, P., & Raymont, D. (2014). Advanced lightweight 316L stainless steel cellular lattice structures fabricated via selective laser melting. Materials & Design, volume 55, pages 533-541. **(Accepted)**

Hussein A, Hao L, Yan C, Everson R. (2013) Finite element simulation of the temperature and stress fields in single layers built without-support in selective laser melting, Materials and Design, volume 52, pages 638-647. **(Accepted)**

Hussein A, Hao L, Yan C, Everson R, Young P. (2013) Advanced lattice support structures for metal additive manufacturing, Journal of Materials Processing Technology, volume 213, pages 1019-1026. **(Accepted)**

Yan, C., Hao, L., Hussein, A., Bubb, S. L., Young, P., & Raymont, D. (2013). Evaluation of light-weight AlSi10Mg periodic cellular lattice structures fabricated via direct metal laser sintering. Journal of Materials Processing Technology, volume 214, pages 856-864. **(Accepted)**

Yan C, Hao L, Hussein A, Raymont D. (2012) Evaluations of cellular lattice structures manufactured using selective laser melting, International Journal of Machine Tools and Manufacture, volume 62, pages 32-38. **(Accepted)**

Conference Papers:

Hussein, A., Yan; C., Everson, R; Hao, L. (2012). Preliminary investigation on cellular support structures using SLM process. Innovative developments in virtual and physical prototyping-Bartolo et al. (eds). 609-612, Taylor & Francis Group, London. **(Accepted)**

Hao, L.; Raymont, D.; Yan, C.; Hussein, A.; Young, P. (2012). Design and additive manufacturing of cellular lattice structures. Innovative developments in virtual and physical prototyping-Bartolo et al. (eds). 249-254, Taylor & Francis Group, London. **(Accepted)**

Part One: Introduction and Literature Review

CHAPTER 1 Introduction

1.1 Background

Additive Manufacturing (AM) describes a family of technologies that, in an automatic process, produce three dimensional objects directly from a digital model by the successive addition of material(s), without the use of a specialized tooling. It is also known as 3D printing, Solid Freeform Fabrication (SFF) and Additive Layer Manufacturing (ALM). AM is considered as one of the most important emerging material processing technologies that will drive the future manufacturing industry. Many of the traditional Design for Manufacture (DFM) principles are no longer applicable to AM as it can produce parts with complex internal and re-entrant features (Hopkinson et al., 2005).

AM has been increasingly used to produce topologically optimized parts to save materials and costs. It also makes high value products without using tooling, jigs and fixtures. This particularly helps to save a considerable amount of additional material and process cost for the production of one-off or small volume parts or products. In addition, the non-processed raw materials can be recycled and re-used by AM to reduce material waste drastically. AM is therefore considered as a sustainable manufacturing approach for new products, in particular lightweight and sustainable products which are now highly demanded by many industries due to the tighter environmental regulations.

AM is potential to enable Manufacturing for Design (MfD) to produce complex, lightweight and high value products. Additive manufacturing is now being recognized as a serious method of manufacturing. Many events conducted by industry, academia, and government have presented examples of how the technology is being applied to the production of parts for products. The examples shown in Fig. 1.1 fully demonstrate the metal AM capabilities which allows the redesign of the existing products or design of new products that cannot made by conventional methods. Worldwide research also investigates the use of AM for the production of low-volume aerospace components in particular considering the opportunities to reduce their weights and make them be more sustainable in its life-time operation. Medical industry represents the most diversified market place for AM parts. AM is used to produce medical models, surgical tools, dental implants, acetabular cups and maxillofacial implants, hearing-aid etc. These products have huge markets due to global ageing population and help to improve the quality life. The application of AM in engineering sector also spreads widely from new niche areas (e.g. low-carbon vehicle, sport, art, creative industry) to traditional areas (e.g. defence, marine, oil and energy sector).

(a) Aeroplane seat belt buckle made from Titanium using metal AM, with potential weight saving of 87g per buckle - Case study from SAVING Project [Courtesy: 3T RPD Ltd.]

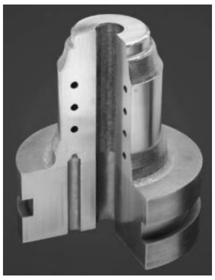

(b) Injection moulding with conformal cooling channels [Courtesy: http://www.ilt.fraunhofer.de]

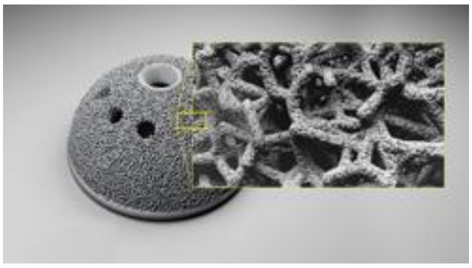

(c) Acetabular cup for a hip implant with external cellular structures made from Titanium [Courtesy: EOS Gmbh]

(d) Dental restoration parts [Courtesy: EOS Gmbh]

e) Lightweight heat exchanger with intricate internal channels [Courtesy: 3T RPD Ltd.]

Figure 1.1 Capabilities of AM technology

1.2 Metal Based Powder Bed Fusion Processes

Metal based powder bed fusion (PBF) describes AM processes in which electron beams or laser beams construct engineered parts from metal powders in a powder bed. The thermal energy melts the powder material, which then changes to a solid phase as it cools. Terms that are also used in the AM industry for powder bed fusion processes and systems include selective laser melting (SLM), direct metal laser sintering (DMLS), LaserCusing, and electron beam melting (EBM). Metal based PBF processes are one of the most versatile and used AM processes to fabricate complex 3D functional components from various metal powders including stainless steel, cobalt-chrome, Inconel, titanium and aluminium alloys.

At present parts produced with metal PBF systems have reached a status which makes them competitive to conventionally produced parts concerning material properties as density and strength. Geometrical accuracy and surface quality have reached a level which requires only very little post treatment. For example, SLM and DMLS has become an essential method of producing highly complex small scale components in the aerospace industry. By using these technologies, the time to produce replacement parts is reduced significantly compared to previous fabrication techniques.

1.3 Materials and process bottlenecks

Metal AM processes are expensive due to high machines and material costs. According to The Economist, UK "Industrial 3D printing systems start at about £100,000 for polymer systems and go up to nearly £1 million for metal AM systems". In addition, the cost of raw material materials is very high (e.g. £ 70-80/kg of 316 L stainless steel, 250-£450/kg of titanium powders). Furthermore, metal AM processes including SLM and DMLS have to solidify extra materials into sacrificial support structures to manufacture overhang geometries (See Fig. 1.2). Meantime, SLM/DMLS use relatively high energy tools such as laser to consolidate metal powders. They could require large energy consumption if more layers of support structure are needed to be consolidated for a large size product. To minimize the electrical energy consumption, build time must be minimized as this is the most influential parameter of AM processes (Mognol et al. 2006). There are other difficulties also associated with recovering raw powder trapped inside the support structure after the build. Hence, the functional metal parts produced in SLM/DMLS can be disproportionately expensive when compared to cast or even machined parts, simply due to the cost of raw materials, slower build-time and the use of sacrificial support structures. These downstream issues result some restrictions to metal AM even in high value aerospace, medical and engineering sectors.

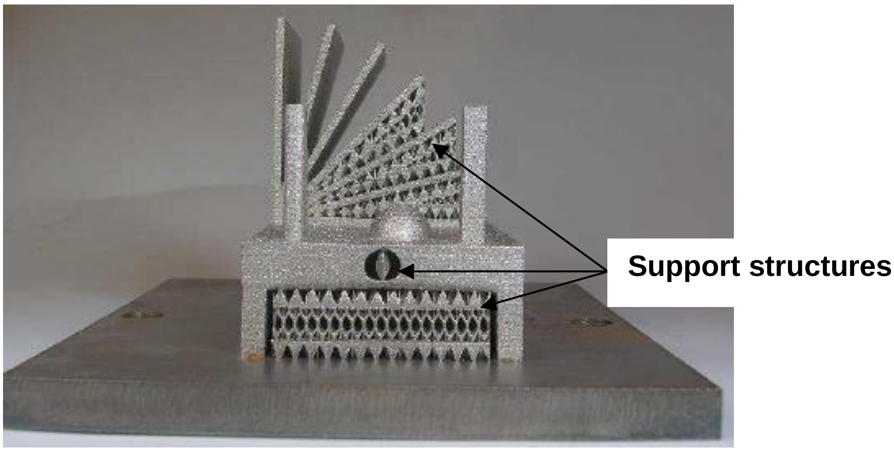

Figure 1.2 SLM Part with support structures (Castillo, L. 2005)

One of the potential area in which the largest gain in SLM/DMLS can be attained is through the use of lightweight cellular lattice structure which require less material and energy during processing while offering enhanced functional performance required in metal products. Development of SLM/DMLS for the manufacture of these lattice structures from high performance light alloys would pace their application. A key advantage offered by internal structures is high strength accompanied by a relatively low mass (Chu et al. 2008). These structures can provide good energy absorption characteristics and good thermal and acoustic insulation properties as well (Gibson and Ashby, 1997). The emerging applications for metal cellular lattice structures range from ultra-light weight multifunctional structures to automobile, medical and aerospace components.

In recent years, various types of lattice structures have been designed and produced in AM processes, however, a very little effort has been made to study the constraints and challenges for the manufacturability of these structures in metal AM processes. Internal geometries with very fine structures below 1 mm still are a technical challenge in SLM/DMLS processes. The manufacturability is an important factor for the selection of the cell type, size, build orientation, and density of cellular structure for specific applications.

1.4 Definition of the Research

This pioneering research investigates the manufacturability and mechanical behavior of advanced lightweight cellular structures in metal AM processes. The cellular structures are based on Triply Periodic Minimal Surface (TPMS) cell topologies. The study includes the novel application of low-density cellular structures as supports for overhanging geometries of metal AM parts. The aim of the cellular support is to tackle the process limitation in building complex geometreis with internal voids having a solid shell that will otherwise require non-removable support structures by replacing them with multifunctional permanant cellular support structure. The concept of lightweight cellular structure is motivated by the desire to put material only where it is needed for a specific application. The build time and cost of making parts can be significantly decreased by using internal low-volume structures that can replace bulk materials.

These multi-functional celular structures are expected to fullfil the following design and performance requirements,

1. To promote design freedom and enhance the manufacturabiltiy of, complex geometries with internal cavities that result an internal overhang, by using self-supporting permanent cellular support structures that are suitable for metal AM processes.
2. To meet the functional design requirements such as stiffness and strength while providing lightweight solution for metal AM parts.
3. To reduce the material, build-time and energy consumption of external support for geometries with external overhang, by using low-density, uniform and graded cellular support structures that can be easily removed.

This work presents a comprehensive experimental tests conducted at different cell topologies using commerically available 316L stainless steel, Titanium alloy (Ti-6Al-4V), and Aluminium alloy (AlSi10Mg) metal powders. The fabrication of cellular structures has been investigated in SLM MCP Realizer and DMLS EOSINT M270/M280, two of the most commonly used metal AM systems. The research has contributed to new knowledge on the manufacturability and mechanical properties of low-density TPMS cellular structures with varying cell size, orientation and volume fractions from various metallic powders. The evaluation on the mechanical properties of these cellular structures aims to illustrate the compressive behaviour of various cell types, sizes, orientation, and volume fractions. The mechanical properties will aid the designer on the selection and use of the right cell type, size, and volume fraction to suit the functional demands of particular application.

The study also contributes to the design and manufacturing of support structures through the novel applications of low-density uniform and graded cellular support structures for metal AM process. The new uniform and graded support structure method will address the saving of energy (via reduced built-time and material) which could waste very expensive raw metal materials and time in building complex parts that require large support. Knowledge gained from thermal modelling aids in our understanding on the temperature and stress fields during SLM processing. Proper knowledge on temperature and stress gradients is essential for the design of more efficient support structure for overhang geometries in metal AM parts.

1.5 Research Objectives

1. To predict the temperature and stress fields of overhang single layers built on powder bed without-support in SLM.
2. To evaluate the manufacturability of cellular structure with various cell types, sizes, orientations, and volume fractions using different metallic powders in SLM and DMLS processes.
3. To determine the effect of cell type, size, orientation, and volume fraction on the mechanical behaviour of cellular structure under compressive loading.
4. To develop low-density uniform cellular support structures, to reduce material and energy consumption of metal AM parts.
5. To develop low-density functionally graded cellular support structure to be used as temporary/removable external support and permanent internal support structures of sustainable light-weight parts.

1.6 Outline of this Thesis

Fig. 1.3 presents a schematic flowchart of this dissertation. The research investigation and findings has been presented through three major parts, Part 1: Introduction and Literature review (chapters 1 and 2). Part 2: Materials and methods, Preliminary experiments, and finite element simulation on temperature and stress fields in SLM (chapters 3, 4 and 5). Part 3: Design, Manufacturability and Mechanical properties of cellular structures (chapters 6, 7 and 8). Part 4: Development of cellular support structures (chapters 9 and 10). The closing chapter of this dissertation is the conclusions and future recommendations (chapter 11).

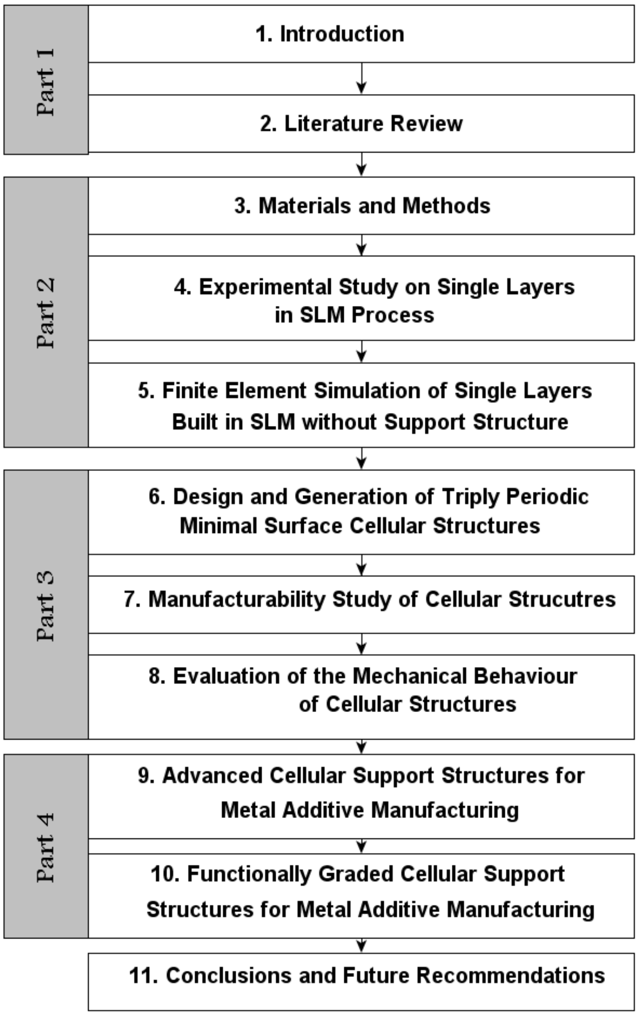

Figure 1.3 Flowchart of the dissertation

Chapter 1 Provides a background on additive manufacturing technology; current issues in metal based AM processes; and the research definition and objectives to tackle design and process limitations in SLM and DMLS.

Chapter 2 Discusses the current state-of-the-art in AM technologies and available materials, and provides the necessary background for this dissertation. The opportunities and limitations of metal AM technologies are discussed, in particular their applications in manufacturing complex cellular structures. Literature pertaining to structural design and use of sacrificial support structure and thermal gradients in SLM are included. Furthermore, an overview is given to the cellular structure for lightweight applications to provide understanding on their geometrical and mechanical characteristics as well as the structure-property relations between them.

Chapter 3 Describes the powder materials, manufacturing machines and experimental set-up, and measurement instruments used during the experimental work. It also illustrates the post-processing steps used for the cellular structures such as stress-relieving heat treatment cycles, wire-EDM cutting, and Air/bead blasting operations.

Chapter 4 Presents experimental work on single 316L stainless steel layers built on the powder without-support in SLM. It investigates the effect of scanning speed on melted depth in the powder bed.

Chapter 5 Uses three-dimensional finite element simulation to investigate the temperature and stress fields in single 316L stainless steel layers built on the powder bed without support in SLM. A non-linear transient model based on sequentially coupled thermo-mechanical field analysis code was developed in ANSYS parametric design language (APDL).

Chapter 6 Presents the design procedure and the software tools used for generating cellular structures. It presents different cell types used in the experimental tests and the characteristics of these cellular structures.

Chapter 7 Evaluates the manufacturability of cellular structures using SLM-MCP Realizer and DMLS-M270 and M280 machines using different metal powders such as 316L Stainless steel, Ti-6Al-4V, and AlSi10Mg. The effect of cell type, size, volume fraction, and cell orientation on the manufacturability was investigated.

Chapter 8 Evaluates the compressive behaviour of cellular structures manufactured in SLM and DMLS processes. Rigorous mechanical testing was performed to provide the understanding of the behaviour of periodic cellular structures under monotonic compression loading. The effect of cell size, volume fraction, and cell orientation on compressive elastic modulus and yield strength was examined for both gyroid and diamond type cellular structure. Experimental results were compared with analytical model of Gibson and Ashby to determine the accuracy of the model and to provide a prediction approach.

Chapter 9 Develops a novel application of cellular lattices as support structure for metallic AM parts. It presents a comprehensive experimental study to prove this new concept and illustrate the effects of type, volume fraction and size of cellular lattice structures on the support performance in terms of manufacturability, building time, weight of support, and preventing the thermal deformations.

Chapter 10 Proposes a functionally graded cellular structure with variant porosity and cell size for temporary and permanent support structure applications in metal additive manufacturing. Different cell sizes and volume fractions were tested to establish a relationship between cellular topology and manufacturability. Dimensional accuracy and residual stresses were studied for various methods of graded cellular support structure.

Chapter 11 provides general conclusions as well as future recommendation perspectives for the continuation of this work.

CHAPTER 2 Literature Review

2.1 Introduction

The aim of this chapter is to provide the necessary background and state-of-the-art regarding the AM processes, support structure, and cellular lattice structures.

To provide some background on AM technology, section 2.2 gives an overview of AM techniques, materials, and applications. In section 2.3, the opportunities and limitations of metal AM techniques are addressed. Emphasis is given to the limitations that are related to the process as well as manufacturing of complex designs in metal AM processes. Section 2.4 discusses the design and manufacturing of support structures that are used in some AM processes to anchor/hold overhang and fragile geometries during the build. The design and manufacturing of cellular structure is presented and discussed in detail in section 2.5. The limitations of traditional manufacturing techniques for metal foam and 2D periodic honey-comb solid structures are also discussed in section 2.5, as well as the potential for the additive manufacturing of promising new designs of triply periodic minimal surfaces paradigm that will be pursued in the remainder of this work. Finally, the conclusion of this literature review is presented in section 2.6, which puts the most important findings into perspective, formulating concrete goals and guidelines regarding the work in this dissertation.

2.2 Additive Manufacturing Technologies – State Of The Art

The ASTM International Committee F42 on AM Technologies defines additive manufacturing as the process of joining materials to make objects from 3D model data, usually layer upon layer, as opposed to subtractive manufacturing methods (ASTM-F42 Committee). The term 3D printing is defined by the ASTM F42 committee as the fabrication of objects through the deposition of a material using a print head, nozzle, or other printer technology. However, the term is often used synonymously with AM In particular; it is associated with machines that are lower in relative price and/or overall functional capability. AM is the official industry standard term according to

ASTM and ISO, but 3D printing has become the de facto standard term, and has become more popular than AM (Wohlers, 2013).

Design and manufacturing companies has increasingly adopted AM to make products used in the consumer, industrial, medical products. In an effort to reduce time to market, improve product quality, and reduce cost, companies of all sizes have come to rely on AM as a mainstream tool for rapid product development. AM processes help companies reduce the likelihood of delivering flawed products, or the wrong products, to the marketplace. The chart in Fig. 2.1 shows the results of a survey conducted by Wohlers Associates on AM market distribution (Wohlers, 2013). Consumer products/electronics is the leading industrial sector, followed by motor vehicles. Medical/dental has established itself as a strong sector for AM and has been the third largest over the past 12 years.

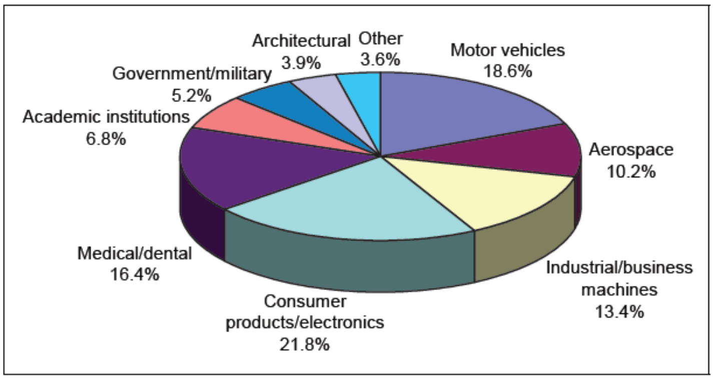

Source: Wohlers Associates, Inc.

Figure 2.1 Market distribution of AM industry (Wohlers, 2013)

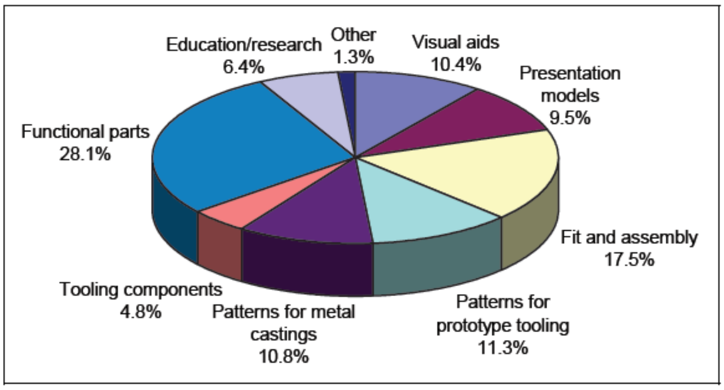

Source: Wohlers Associates, Inc.

Figure 2.2 Application areas of AM industry (Wohlers, 2013)

The survey results in Fig. 2.2 show that companies use AM technology to produce functional parts more than anything else. The second most popular application for AM parts is as prototypes for fit and assembly.

2.2.1 Additive Manufacturing Processes

The ASTM-F42 Committee whose primary work is the development of standards for additive manufacturing technologies has classified additive manufacturing into the following categories:

- **Material extrusion processes (e.g. FDM)**

This is an AM process in which material is selectively dispensed through a nozzle or orifice. The base material often is a paste or a plastic. In the case of the paste a syringe type extruder can be used to deposit the paste. For plastics usually a plastic filament is fed through a heated nozzle that melts the plastic so it can be deposited. Fused Deposition Modeling (FDM) shown in Fig. 2.3 (a) is a process that uses a reel of plastic filament. Once deposited the filament will stick to underlying layers and neighboring filaments and will almost directly solidify. Due to the nature of the FDM process overhanging features should be held by support material.

- **Material jetting (e.g. Objet, Solidscape)**

This is an AM process in which droplets of build material are selectively deposited (see Fig. 2.3(b)). Two types of material are predominantly used in this group of processes; wax and photopolymers. Some processes are able to directly jet metals. The advantage of this group of processes is that the nature of the process allows changing the product material during a build. In this way multi-functional or graded material properties are possible.

- **Binder jetting (e.g. Z-corp, Voxeljet)**

This is an additive-manufacturing process in which a liquid bonding agent is selectively deposited to join powder materials (see Fig. 2.3(c)). In the binder jetting process group the product material is in a powdered form and the inkjet head is used to locally disperse glue, thus binding the powders locally. Typically two bins are used, a bin in where the product is formed and an extra bin with fresh powder. After the powder in a layer has been solidified using the glue, the build container is lowered and the powder bin is raised. A roller or a doctor blade is used to move the powder from the storage bin to the build bin. A big advantage of this method is that all kinds of powders can be used, albeit only one powder type per build. Also it is very easy to add colour to the printed final products. If no other post processing steps are used (for example oven sintering) the final products is normally not very strong.

- **Sheet lamination (e.g. LOM)**

This is an additive-manufacturing process in which sheets of material are bonded to form an object. Sheet Lamination is a group of processes that create a layer by cutting the contours of the layer. Laminated Object Manufacturing (LOM) (see Fig. 2.3(d)) does so by stacking plastic sheet material on top on the sheets below and for uses a computer controlled cutting device (laser, knife) to cut the lines that form the edges of the desired shape. When the product has been printed the excess material is removed. Paper Lamination Technology (PLT) uses especially develop paper sheets instead of plastic; successive layers are glued to each other by thermally activated glue.

- **Vat photo-polymerization (e.g. SLA)**

This is an additive-manufacturing process in which liquid photopolymer in a vat is selectively cured by light-activated polymerization. Like in some material jetting processes vat photo polymerization also use a light curable resin. Where the material jetting systems selectively deposits the material, the vat photo polymerization systems always supply a layer of non-cured material and use a light source to selectively cure parts of the layer. Stereo lithography (SLA) (see Fig. 2.3(e)) uses a laser and a set of mirrors to solidify the layer while the digital light processing (DLP) technology uses a light source also found in beamers.

- **Directed energy deposition (DED) (e.g. LENS, Laser Cladding)**

This is an additive-manufacturing process in which focused thermal energy is used to fuse materials by melting as the material is being deposited. Direct Energy Deposition is a group of processes process where the material is directly deposited on the final location in the product. It does so by jetting the build material into the heated zone, created by a laser, electron beam or an ionized gas. As with the other methods that jet the product material, DED can change the product material easily, thus allowing for the graded functional materials. Laser-engineered net shaping (LENS) from Optomec (see Fig. 2.3(f)) is a DED process that injects a metal powder into a pool of molten metal created by a focused laser beam.

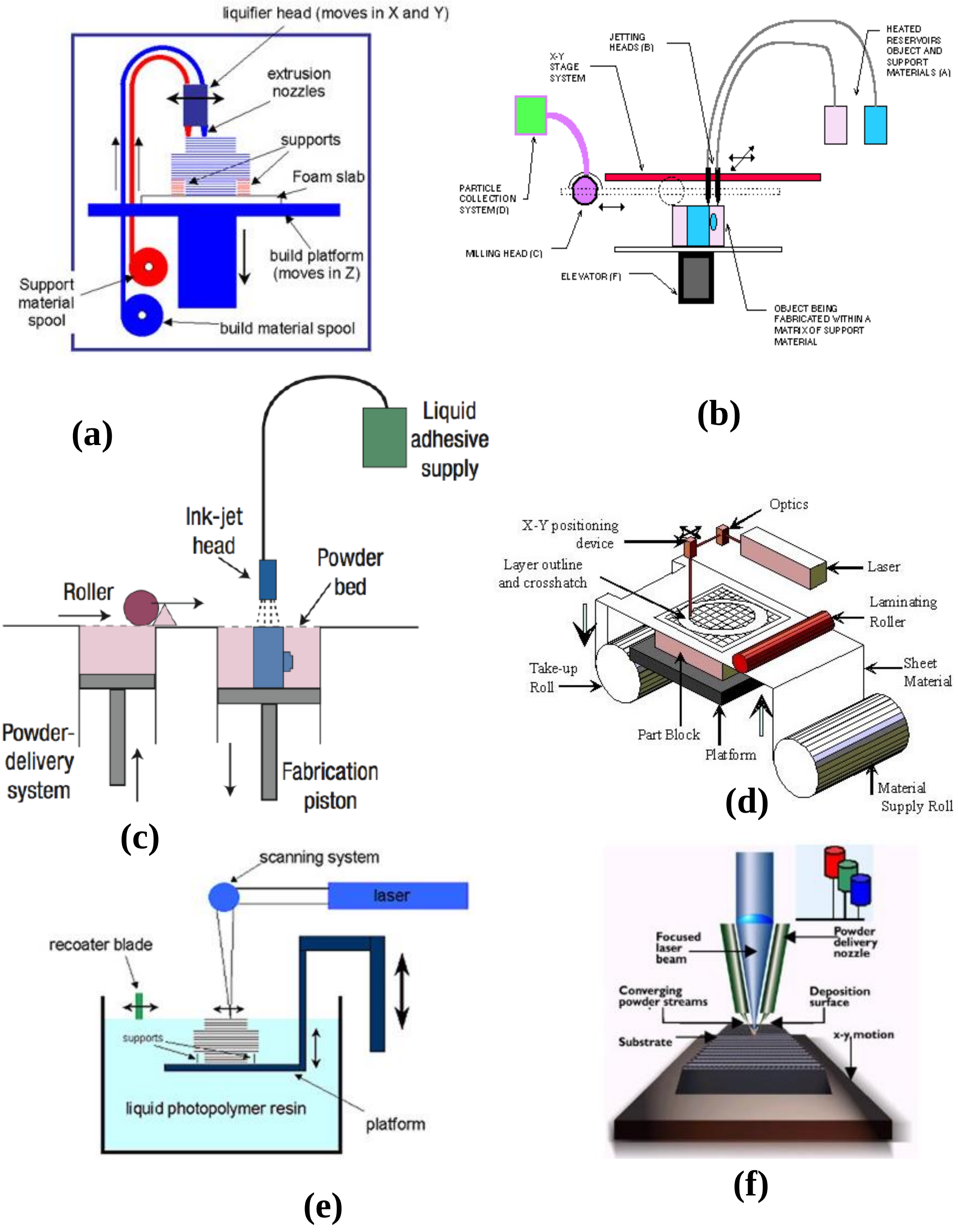

Figure 2.3 Schematic illustrations of AM processes (a) FDM process [courtesy: xpress3d.com] (b) Solidscape’s ink-jet technology [courtesy: additive3d.com] (c) 3D printing [courtesy: additive3d.com (d) LOM Process [courtesy: jharper.demon.co.uk] (e) SLA Process [courtesy: xpress3d.com] (f) LENS process [courtesy: rpmandassociates.co

- **Powder bed fusion (e.g. SLM,DMLS,SLS,EBM, LaserCUSING)**

As described in chapter 1 (section 1.2) this is an AM process by which thermal energy fuses selective regions of a powder bed (see Fig. 2.4). The source of the thermal energy is a laser or an electron beam. This is a direct production method in which the desired components are produced directly from 3D data. Based on the data at hand (standard format STL), even highly complex parts can be produced from metallic materials in layer-by-layer fashion. To accomplish this, the metal is applied in thin layers of very fine powder and, using a laser beam, melted onto those areas where the workpiece will be developed. In SLM, DMLS, and LaserCusing, a powerful fibre laser selectively melts the designated areas. Sharp focusing mirrors direct the beams with a very high power density to melt powder bed in a precise manner. The thermal energy melts the powder material, which then changes to a solid phase as it cools. Depending on the surface quality and production speed requirements, the powder is automatically applied with layer thicknesses of 20 to 100 µm.

Terms that are also used in the AM industry for powder bed fusion processes and systems also include selective laser sintering (SLS), a polymer based processes. For polymers used in SLS, the un-fused powder surrounding a part serves as an anchoring system, so no additional supports are usually needed. For metal parts, anchors are typically required to attach part(s) to a base plate and support down-facing surfaces. This is necessary because of the higher melting point of metal powders. Thermal gradients in the build chamber are high, which can lead to thermal stresses and warping if anchors are not used. Because powder bed fusion is a thermal process, warping, stresses, and heat-induced distortion are potential problems for all materials and in particular for metals.

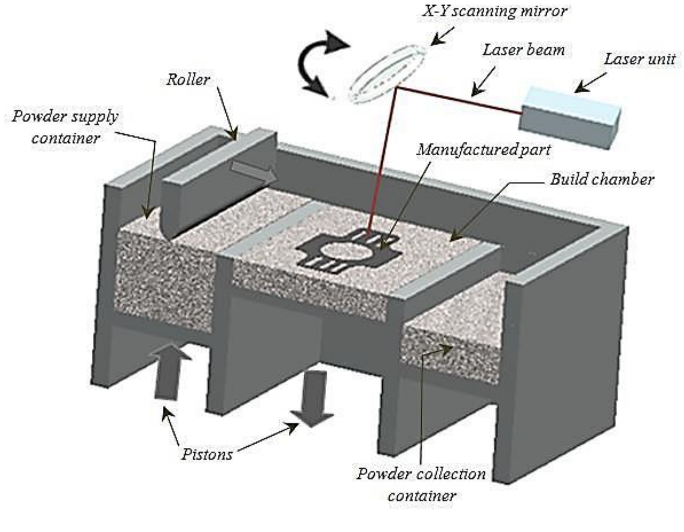

Figure 2.4 Schematic of Powder bed fusion process (courtesy: HiETA technologies Ltd.)

2.2.2 Product Development Process in AM Process

The design and manufacturing steps involved in AM are illustrated in Fig. 2.5. The CAD model which represents the part to be manufactured is converted into STL format. Nearly every AM technology uses the STL file format. The term STL was derived from STereoLithograhy, which was the first commercial AM technology from 3D Systems in the 1990s. Considered a de facto standard, STL is a simple way of describing a CAD model in terms of its geometry alone. It works by removing any construction data, modelling history, etc., and approximating the surfaces of the model with a series of triangular facets (Gibson et al. 2010). The minimum size of these triangles can be set within most CAD software and the objective is to ensure the models created do not show any obvious triangles on the surface. The basic rule of thumb is to ensure that the minimum triangle offset is smaller than the resolution of the AM machine.

This STL file is then transferred into the AM machine software which slices the model into 2D slices with specified thicknesses. Different AM machines use different slicing formats such as SLI (System layer interface) by 3D systems, CLI (Common Layer Interface) by EOS, F&S (Fochele and Schwarze) by MTT now Renishaw, SLC (Stratasys Layer Interface) by Stratasys. This is followed by setting-up the processing parameters and preparing the materials. In metal AM systems, an argon or nitrogen gas is pumped into the build chamber prior to the build to evacuate the oxygen content and prevent the melt-pool contamination. After the build is complete, the part is removed from the build chamber and cleaned. Further post-processing may be required for parts containing support structure. For metal parts, post stress-relieving heat treatment cycle is required to relax the residual stresses accumulated in the part during the build.

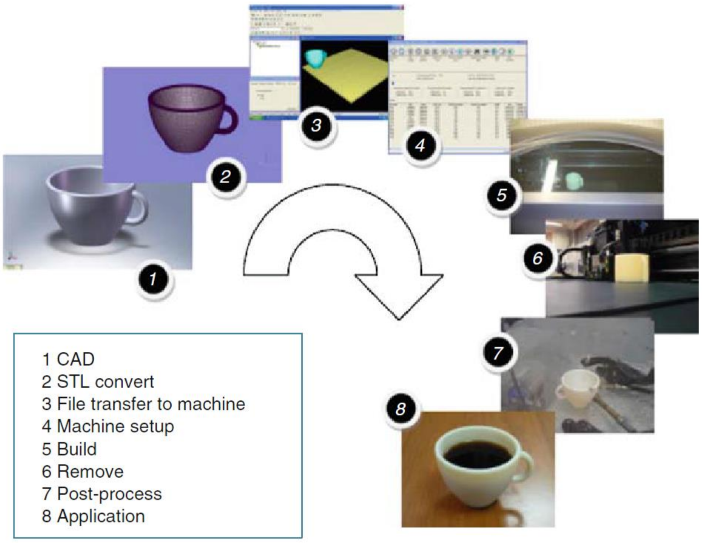

Fig. 2.5 Generic process of CAD to part, showing all 8 stages (Gibson et al., 2010)

2.3 Opportunities and Limitations of Metal AM Processes

From a designer's perspective, metal PBF process such as SLM and DMLS presents both opportunities and challenges. On the positive side, it offers greater design freedom through the ability to produce shapes that would be otherwise impossible or prohibitively expensive. These opportunities will be discussed first in the following section, followed by process limitations.

2.3.1 Opportunities

2.3.1.1 Tool-less manufacturing of complex geometries

One key benefit is the direct part fabrication, which reduces tooling, manufacturing, inventory, assembly, labour, maintenance, and inspection costs. When tooling is removed from the equation, it becomes feasible to introduce new products in low quantities to determine if a market demand exists for them. Many of the restrictions of design for manufacture and assembly (DFMA) that are essential in a conventional manufacturing environment are imposed by the need for tooling (Hague et al. 2003).

Metal AM machines also allow for much greater geometric complexity, and hence, provide increased design freedom for creating new types of products (Springs et al., 2011). As the ratio of size to complexity improves, AM becomes more economically viable. In other words, if a part is small and complicated, AM is more likely to be a good option for part production. A designer can create a small number of complex parts rather than a large number of simple parts, as is typical for many conventional manufacturing processes (Gibson et al.2010). A result of this reduction in part count also offers the possibility to reduce or eliminate links in the traditional supply chain, thereby reducing lead times and simplifying supply chain logistics.

2.3.1.2 Complex tooling with conformal cooling channels

The production of tools containing complex cooling channels (Conformal Cooling) is already state of the art and allows the reduction of cycle time and the improvement of the part quality in plastic injection moulding (Mansour and Hague, 2003; Rännar et al., 2007). Example of this was shown in chapter 1 (Fig. 1.1)

2.3.1.3 Lightweight structures and performance improvements

Another area where AM can contribute to greater customer satisfaction is through lightweight structures and improved product performance. The key is to create a geometric shape that is closer to an “optimum” design rather than settling for a compromise due to manufacturability constraints (Rosen et al. 2007). AM is capable of producing parts of unparalleled design complexity, and when coupled to product functionality, the production of lightweight and more efficient parts is possible. In AM, Lightweight structures are motivated by the desire of putting material only where it is needed in the product. This also requires tailoring the mechanical properties of lightweight structures to product functional requirements. The build time and cost of making parts can be significantly decreased by using internal low-volume structures that can replace bulk materials.

Many of the highly structured organic forms in trees, bones, corals, and sponges would be impossible to create using conventional manufacturing but could be possible with AM. Such structures are can be used to reduce material and weight or deliver more efficient heat transfer. These structures also offer good aesthetic appearance.

2.3.1.4 Available Materials

The number of metal materials available for metal AM process is growing. A lot of research has been conducted in AM processes on various metallic materials such as stainless steels and tool steels (Childs et al. 2005, Kruth et al.

2004, Rombouts et al. 2006); Titanium alloys (Abe et al. 2003); Aluminum alloys (Brandl et al. 2012); Nickel-based alloys (Amato et al. 2012); Cobalt–chromium alloys (Wu et al., 2007; Jevremović et al. 2011); Copper-based alloys (Li et al. 2007); Gold (Hollander et al. 2003). Metal powders can vary widely in shape (from spherical to irregular), size, and size distribution. For this reason, processing characteristics in AM metal systems can vary widely as well. System manufacturers work closely with powder suppliers to ensure consistency and repeatability of metal powders to guarantee consistency and repeatability of their AM processes. However, there are also a number of challenging limitations on both process and design aspects that hinder a wider use of metal AM for the production of functional parts, especially for sectors with high material requirements like aerospace, automotive or medical. These limitations will be highlighted in the following sections.

2.3.2 Limitations

2.3.2.1 Vapor*i*zation

One of undesirable phenomenon in metal AM is the vaporization that occurs when the bed of powder is irradiated with high energy intensity. During the laser melting process, the temperature of the powder particles exposed to the laser beam exceeds the melting temperature of the material. A further increase in temperature (about twice the material melting temperature) causes the evaporation of the powder, so, there are fast-moving expansions of evaporated particles, which generate an overpressure on the melted zone and the material is ejected from its bed (Morgan et al., 2001).

2.3.2.2 Balling phenomenon

The other problem that may occur during the metal AM process is the "balling" phenomenon, i.e. the formation of isolated spheres with a diameter equal to the laser beam focus, which inhibits deposition and decreases the density of produced part. It occurs when the molten material is unable to fully wet the substrate because of surface tension. The phenomenon is caused by an excessive amount of energy, which gives to the melted powder a too low value in viscosity (Gu and Shen, 2009; Simchi 2006).

2.3.2.3 Anisotropic part properties

Most powder bed based metal AM systems that build metal parts melt the materials and produce parts that approach 100% density. Metal parts produced by metal AM have properties that can be quite different from conventional wrought or cast metals. This has proven to be one of the biggest barriers to widespread adoption of the technology. The properties of additive manufactured metal materials are already widely analysed by many researchers: density (Spierings & Levy 2009a), microstructure (Kruth et al. 2004, Simchi 2006) and the static mechanical performance (Spierings et al. 2011, Yasa et al. 2010) are well studied, pointing out that the static mechanical properties are typically in the range of wrought conventional materials, although a specific anisotropy exist which depend on build direction of the part. However, besides the description of the material microstructure and some mechanical properties, the today's knowledge about the correlation between the microstructure of SLM materials and corresponding properties are still poorly analysed.

2.3.2.4 Thermal stresses and deformation

In order to reach a high density in metal AM processes, the metallic powder particles are fully molten, laser melting process is accompanied by the development of residual stresses that derive from high thermal gradients in the material. These stresses can cause distortion of the part, cracks or delamination (Pohl et al., 2001; Matsumoto., 2002). As a result, sacrificial support structures are needed for successful manufacturing of overhang and undercut sections in complex metallic parts. These supports are essential for AM metallic parts made by AM processes in order to prevent curling. After high power laser irradiation, the metal which is cooled from high temperatures to room temperature have a tendency to deform during the process due to thermal stresses gradients generated which result a curling effects (Mercelis and Kruth, 2006). Support structure function is therefore to dissipate heat from the newly melted layer and restrain part deflection caused by thermal stresses during layer solidification. This ensures proper build condition and evenly distributed layer for subsequent builds.

2.3.2.5 Material and energy consumption of support structures

The use of the support structures in AM are reported as being the main restriction on part geometries, and the support placement is equally as important as the part design (Pullin & Offen, 2008). Support structure influence the amount of material used, build-time, surface finish, energy-consumption, cost and post-processing requirements of the metal AM parts. Supports waste materials and energy and add no direct value to the part and therefore, once the manufacturing of the part is completed, it is necessary to remove them from the part manually or in some cases by machining. AM machines consume significant amounts of electrical energy per unit mass of material processed (Mognol et al. 2006).

2.3.2.6 Lack of knowledge of design rules in AM

On the other hand, AM also poses some distinctive challenges for designers. There is a need to learn and understand the specific constraints that AM brings to manufacturing. Examples include minimum wall thickness, achievable tolerances, support requirement, preferred build orientation, and manufacturable cellular structures. These constraints are analogous to the design-for-manufacture rules associated with conventional processes but are a great deal less restrictive. Some AM design guidelines have been written to help designers with this task. For example, a set of design rules for SLM was developed by Thomas (2010). Some AM system manufacturers are also providing guidelines for designers.

2.4 Sacrificial Support Structures

2.4.1 Support structure for SLA and FDM processes

Literatures involving the design and manufacturing of support structures in AM are mainly related to polymer based processes such as Stereolithography (SLA) and Fused Deposition Modelling (FDM) and have reported three main aspects of work.

2.4.1.1 Minimize support volume by optimizing orientation

Many attempts have been made to minimize the support volume by changing orientation of the parts of SLA (Allen and Dutta, 1994; Asberg, et al. 1997; Hur and Lee, 1998; Majhi, et al. 1999; Yang, et al., 2001). Asberg, et al. (1997)

developed an algorithm for deciding if a part can be made by SLA without using supports. Majhi et al. (1999) found that the quantity of supports used affects both the build time and the cost. So they gave algorithms for computing a build direction which minimizes the volume of support structures in their two papers. Their attempt is to minimize three parameters, i.e. stair-step error, volume of supports and contact area of supports, considered independently (i.e., in isolation from one another).

Hur and Lee (1998) reported that support structures are used in SLA for four different situations. First, support structures prevent the overhang surfaces from warping, sagging, toppling and parachuting. Second, support structures enable a floating and ceiling components to be built without dropping. The third situation is that support structures can make the part stable during the solidification. Last, support structures are used to raise the part off the platform. They believed that it is important to minimize the number of support structures, and the number of support structures is wholly dependent on the build-up orientation. Therefore, they developed an algorithm to optimize the part orientation choosing support structures as a criterion.

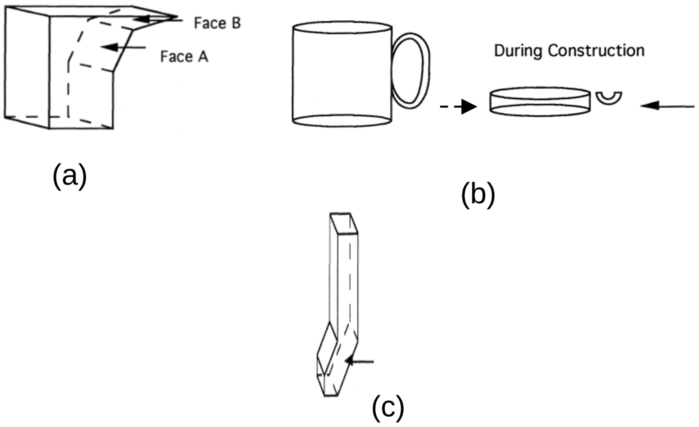

(a)

(b)

(c)

Figure 2.6 (a) The overhang in Face B needs support structure but Face A does not (b) Support structure for to floating geometry (c) Support structure tall and thin geometry (Allen and Dutta, 1994)

Allen and Dutta (1994) found that support structure would be needed in three different situations. The most common need for support structure occurs when material on one layer overhangs the previous layer by more than a specified amount. As shown in Fig. 2.6(a), Face B needs support structure, but Face A does not need any support structure. The second situation where support structures are needed is when a floating component is introduced during the construction. See, for example, Fig. 2.6(b). The third case where external supports might be required is when the object becomes unstable during the construction, as shown in Fig. 2.6(c).

Support structures are built, layer by layer, simultaneously with the object. After the object is constructed, the support structure must be removed, often manually. For a complicated object this removal may be difficult, and also reduce the quality of the surface finish. Therefore, Allen and Dutta (1994) found the best direction for formation of an object with a minimal support structure. In the orientation determined by the best direction of formation, the object needs a minimal support structure, and has a lower centre of mass.

2.4.1.2. Generating support structures

In general, two methods are adopted to generate supports in practice. In the past, supports were made by the design engineer working with the CAD system. They were developed by trial and error, and were often too much or too little for the parts being supported. Therefore, many researchers provided some algorithms to automatically generate supports. Before designing an algorithm to generate supports, researchers have to obtain some guidelines for support structure design through practical experiments.

There also exist algorithms developed to automatically generate the support structure for SLA and FDM processes (Kirschman et al., 1991; Oud-Heverlee and Herenthout 2010; Huang et al., 2009; Kumar et al., 1995). Kirschman et al. (1991) describes that support structures design consists of thin webbing, usually the width of the laser beam. As illustrated in Fig. 2.7, the manufacturer recommends that these webs should be 0.025mm thick, 6.35 to 12.7 mm tall and 6.35 to 12.7mm apart in SLA (3D Systems, Inc., 1989). In addition, they also recommend that the supports continue into the part for a distance of 1.0 to 1.5mm for proper adhesion. This adhesion is important for holding the part in position. Some other guidelines for SLA support structures include: the base support should be hatched at intervals of 17.8mm in an x-y pattern. All surfaces within 20 degree of the horizontal and any perimeters must be supported. All projections longer than 1.78 mm need gusset supports. Kirschman et al. (1991) gives an automated support structure algorithm to relieve the user of the trial and error approach to support design. This saves both time and money.

Supports that had taken over an hour to generate in CAD were successfully by the program in less than one minute.

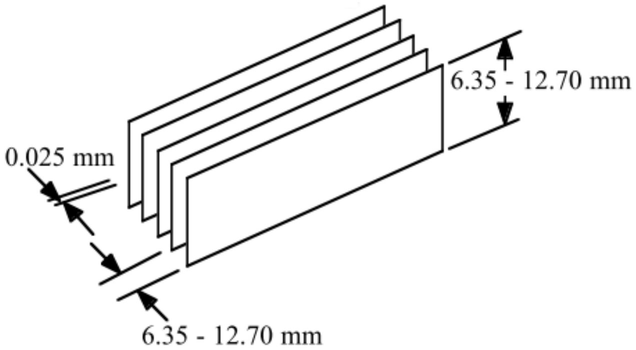

Figure 2.7 Recommended support structure for SLA (3D Systems, Inc., 1989).

Oud-Heverlee and Herenthout (2010) invented a new method to automatically generate support structures for SLA or other RP technologies. In their method, the region that requires support in each layer is first determined, and a number of support points are defined in this region. In the next step, a support mesh is generated connected to the object using these support points. Finally, a support is generated from this support mesh. Their invention may facilitate the generation of supports data by employing more automation and less user analysis. Earl et al. (1999) provided an algorithm for automatically generating support data from three-dimensional object data in their invention patent. Huang et al. (2009) designed three different types of supports with sloping walls. Compared to the generally adopted straight wall structure, these sloping structures significantly reduce the volume of supports. They also provided a robust algorithm to generate the sloping structures for FDM.

Three-Dimensional Printing (3DP) sometimes requires a larger support structure to be used, and in some cases the downward facing surfaces of the parts are completely encased in support material that can be removed by breaking away or using a high-pressure water jet. FDM can also produce supports in a soluble material that can be dissolved in a water-based solution after the parts are produced.

2.4.1.3. Structural design of support structure

To remedy the disadvantages of the supporting structure made of solid standing walls, some airier supporting structures are designed by Putte et al.

(1997). The author described the lattice as airier structures (i.e. more dispersed and less dense) that can minimize the consumption of materials, time and energy for making the RP components. Some airy supporting structures are shown in Fig.2.8.

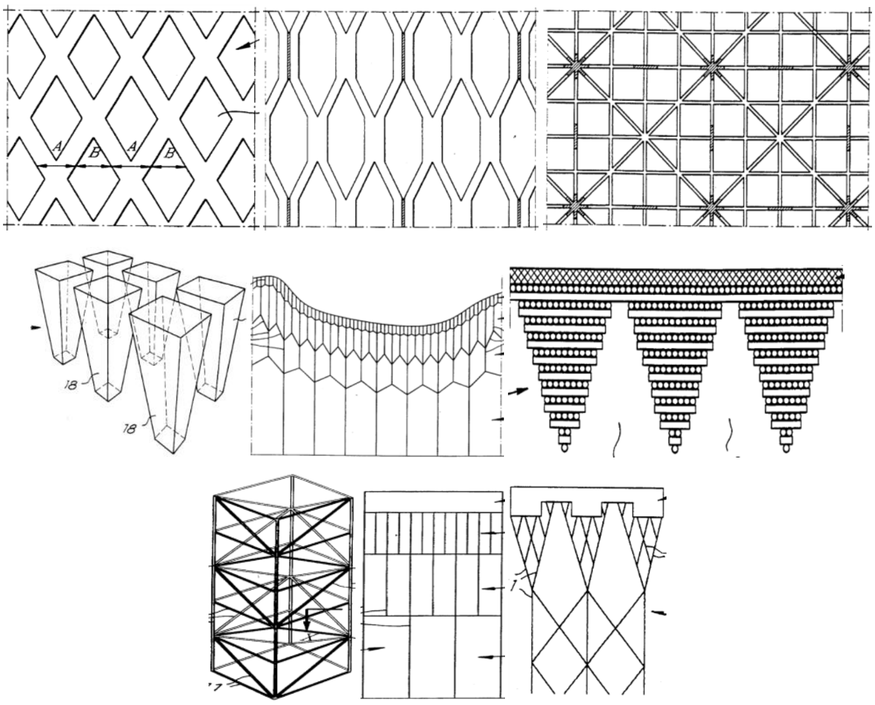

Figure 2.8 Some support structures designed by Putte et al. (1997)

2.4.2 Support structures for metal PBF processes

One of the major concerns in metal PBF processes such as SLM and DMLS is the high residual stresses and distortion. Due to localised heating of laser irradiation, complex thermal and phase transformation stresses are generated. In addition, frequent thermal expansion and contraction of the previously solidified layers during the process generate considerable thermal stresses and stress gradients that can exceed the yield strength of the material. Residual stresses can lead to part distortion, initiate fracture, and unwanted decrease in strength of the part (Mercelis et al. 2006). In forming parts with overhanging parts, it is important to make the first layer without distortion on the powder bed, because the underlying powders do not restrict the distortion M. Matsumoto et al. (2002).

Out of all the AM, metal based powder bed fusion processes have the most difficult support requirements and most difficult to remove the supports as they are dense metal, the traditional support methods and designs which are developed for SLA and FDM are still used to support metallic functional components built in PBF processes. The design of a part determines the amount of support structures that is needed to prevent such distortion. Fig. 2.9 shows geometries that will require support structure in metal PBF process. Support structures are needed to anchor the parts to a substrate, to prevent movement during the process and to prevent overhang and floating surfaces from curling up away from the correct geometry.

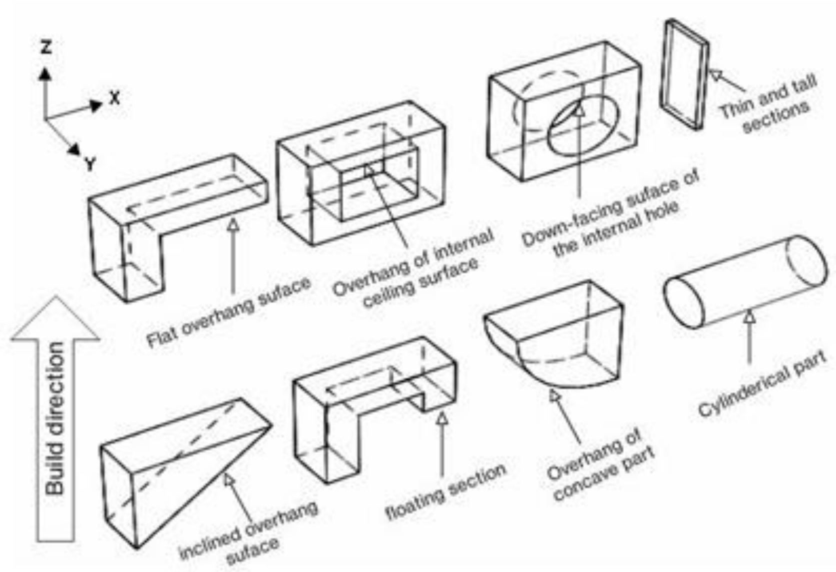

Figure 2.9 Geometric features that require support structures in SLM

There has been increasing demand and research of developing efficient methods of making support structures for metallic AM process. Jhabvala et al. (2012) propose a pulsed radiation for building the support structure. The pulsed radiation utilizes different laser power for the part and the support, much lower power used to consolidate the support structure which provides just enough energy to bond the powder materials together. Mumtaz et al. (2011) developed a method to eliminate the need for support by preventing parts from completely solidifying during processing in certain low melting eutectic alloys such as bismuth and zinc, but this method is currently restricted to only eutectic materials. While much of these researches on metallic support are focused on the process improvement, more effort is needed to enhance the structural design of the support structure.

2.4.3 Commercial Software Tools for Generating Support Structure

Magics software (from Materialise, Belgium)) and AutoFab (from Marcam, Germany- Now acquired by Materialise, Belgium) have functions to generate support structures manually or automatic. For the manual, the user selects the type of support needed to support the geometry while for the automatic generation the system selects the optimum design for the specific geometry. The most commonly used support structures are thin, scaffold-like structures with small pointed teeth for minimising the amount of part contact so that they can be broken away from the part easily using hand tools. Examples of different scaffold support structure designs that are available for selection in Magics software are shown in Fig. 2.10. In most cases, the user verifies the generated support structure in order to make sure that it is not excessive or deficient to cause build failures.

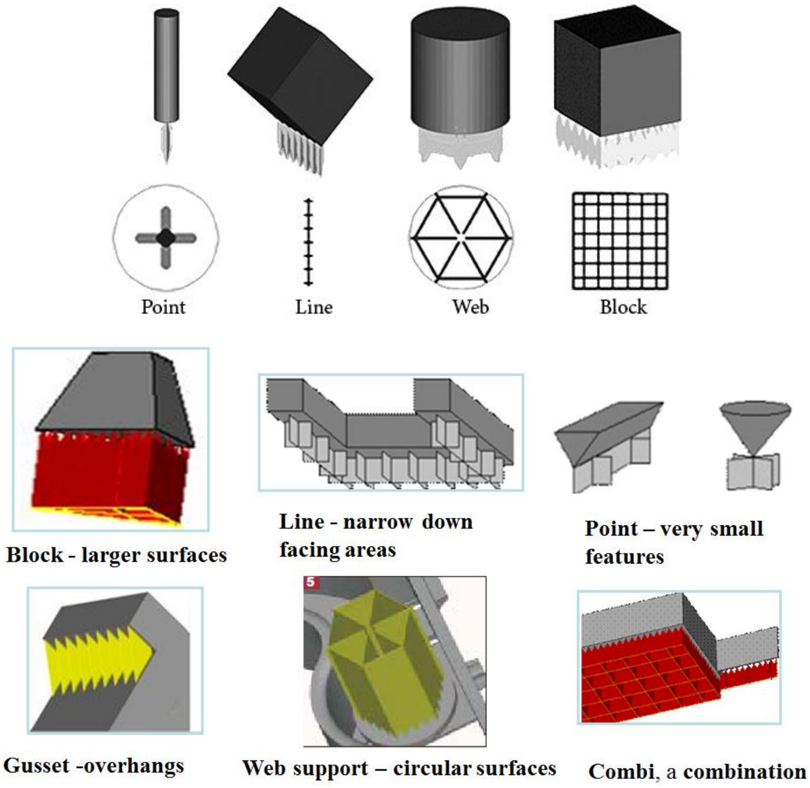

Figure 2.10 some of the support structure designs available in Magics software (Courtesy: Magics, Materialise.com)

2.5 Cellular lattice structures

2.5.1 Cellular solids

In bulk metallic structural materials, porosity is invariably avoided since it results in unacceptable losses of mechanical performance. However, observations of natural materials (e.g., bone, and wood) have long indicated that weight efficient load bearing members have a cellular structure consisting of either reticulated ligaments (i.e., open cell) or encapsulated membranes (i.e., closed cell). Examples from the work of Gibson and Ashby (1997) are shown in Fig. 2.11. Cellular solids are those made up of interconnected network of solid strut or beam which form the edges and faces of cells. A significant body of research into the structure and properties of these natural materials has now been accumulated and organized (Gibson and Ashby, 1997). Metallic foams may be considered the first attempt at creating engineered cellular solids. Fig. 2.12 shows examples of the topology of several metal foam products now commercially available. A recently published design guide by Ashby M.F (2000) reviews ways of making metal foams, their fundamental properties and some of their current applications.

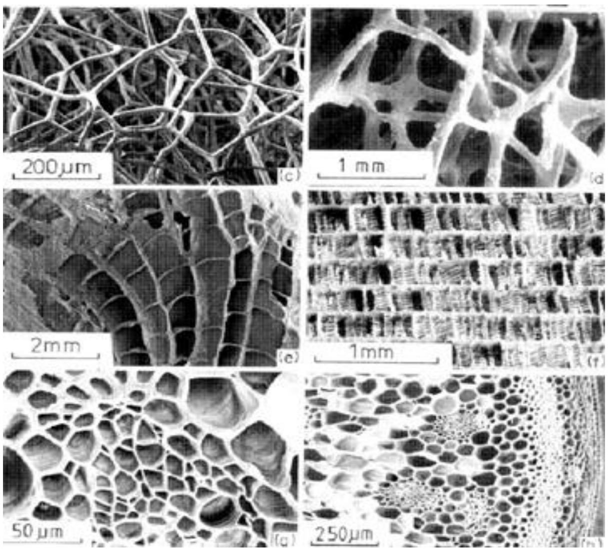

Figure 2.11 Examples of cellular solids found in biological systems. These materials generally consist of reticulated (open cell) materials such as sponge and bone, and membrane (closed cell) materials such as the various wood based materials (courtesy Gibson and Ashby, Cellular Solids, 1997).

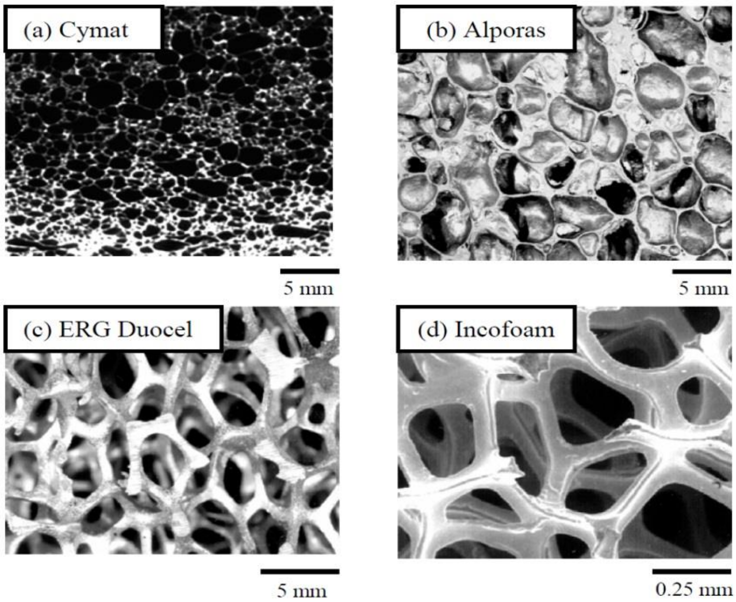

Figure 2.12 Examples of several metal foams. The Cymat, Alporas and ERG Duocel foams are made from aluminum alloys by particle decomposition (Cymat), gas melt injection (Alporas), and pressure casting (ERG Duocel). The nickel based Incofoam is made by an electroless deposition process (Courtesy: Ashby, 2000).

2.5.2 Classification of cellular solids

Two common types of metal cellular structures include stochastic cellular solids and non-stochastic periodic cellular solids (Chu et al., 2008). Example of stochastic cellular structure is the metal foams shown in Fig. 2.12 which has a random distribution of open or closed voids. Non-stochastic periodic structures are those which have a characteristic 2-D or 3-D periodicity (i.e. repeating and ordered unit cells). Honeycomb structure is good example of a prismatic cellular solid. Fig. 2.13 shows a schematic profile representation of some common and less common prismatic cellular solids. It should be noted that honeycomb is a highly efficient 2-D load supporting topology, but nearly optimal for only a few loading conditions, as is the case for all prismatic. There is another class of cellular solids that is based upon 3-dimensional lattices of trusses (Gibson and Ashby, 1997). 3-dimensional periodic lattice solids have uniform structures that are based on repeating unit cells in three co-ordinates. They have been shown to have superior mechanical properties including energy absorption, strength and stiffness, as well as easier control of structure properties, better load sustaining capabilities and higher surface area densities than stochastic and prismatic cellular solids.

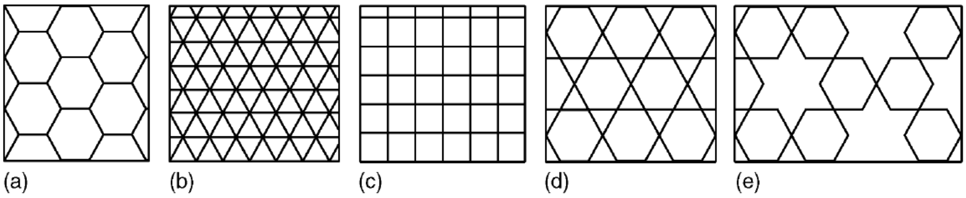

Figure 2.13 Five samples of prismatic cellular topologies (a) hexagonal honeycomb used as core material for sandwich panel constructions. (b) triangulated, (c) square, (d) Kagomé, (e) Star-hex (Kim et al. 2000).

2.5.3 3D periodic lattice structures

Recent efforts continue to improve the weight to stiffness and/or strength ratios of multifunctional cellular solids have begun to investigate lattice truss structures (Evans, 1999). The lattice truss topologies (Fig. 2.14) of interest include the Octet-truss (Deshpande, 2001), its derivative mono-layer tetrahedral structure (Deshpande and Fleck 2001; Chiras et al. 2002; Wicks and Hitchinson 2001), and the 3-D Kagomé structure (Wang et al., 2003; Hyun et al., 2003), a variant of the tetrahedral topology.

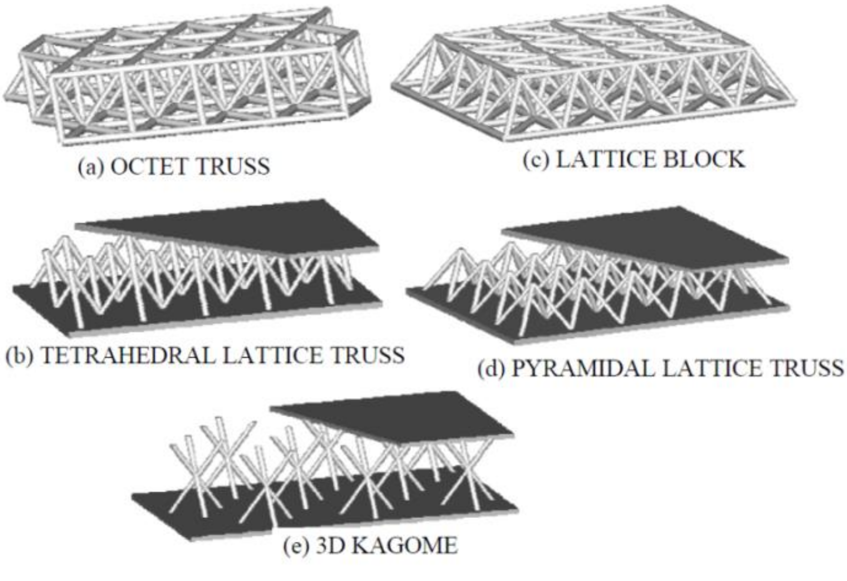

Figure 2.14 Lattice truss topologies recently investigated. All have been made by investment casting. The tetrahedral (b) and pyramidal (d) trusses have also been fabricated by the folding of perforated sheet. In (b),(d) and (e) the lattice truss structure is bounded by solid face sheets.

Lattice truss structures utilized for the cores of sandwich panels has been suggested as a means to achieve efficient load support and other functionality such as cross flow heat exchange or high intensity dynamic load mitigation. The emerging applications for metal periodic lattice structures range from ultra-light weight multifunctional structures to automobile, medical and aerospace components.

Development of suitable methods for the manufacture of these lattice truss structures from high performance light alloys has paced their application. Initial efforts utilized investment casting of high fluidity non-ferrous casting alloys such as copper/beryllium (Cu-2Be wt.%) aluminium/silicon (Al-7Si-0.3Mg wt.%), and silicon brass (Cu-4Si-14Zn wt.%). In fact, current metal periodic lattice structures made by conventional methods such as investment casting, deformation forming, metal wire approaches, brazing etc. possess relatively simple geometries and limited design freedoms, and consequently lack advanced functionality to meet the requirements of many applications. These methods are either difficult to employ or are unsuccessful in producing porous structures with the tight constraints of porosity, optimum pore size, and mechanical strength that are required (Yang, 2000). These manufacturing difficulties have hindered the design possibilities for more advanced and complex 3-dimensional periodic cellular structures that mimic natural structures with controlled density and strength.

To overcome the drawbacks of the conventional techniques, AM technology are attracting the interest of the practicing engineers and designs. The AM techniques allow the fabrication of very complex 3d structure in a layer-wise fashion in a reproducible way (Heinel et al. 2008). AM has the advantages of being able to build structures with customized shapes and better control over localized pore morphologies, porosities and material composition to suit the requirements of multiple cell types arranged in hierarchical structures.

2.5.4 Additive Manufacturing of Periodic Cellular Structures

Recent advances in AM or 3D printing techniques have allowed for the manufacture of a more complex open periodic cellular structure with controlled porosity using range of metallic powders. Some researchers investigated the manufacturability and mechanical properties of stainless steel cellular lattice structures with various unit cell geometries and cell sizes through the metal AM technologies (Brooks et al. 2005; Santorinaios et al. 2006; McKown 2008). McKown et al. (2006) have manufactured a range of 316L stainless steel lattice structures based on two kinds of unit cells that possess octahedral and pillaroctahedral topologies respectively by the SLM process and studied the compression and blast loading behavior of the lattice structures. A few studies attempted to fabricate pure titanium and titanium alloy periodic cellular lattice structures with interconnected pores by metal AM technologies, most of which were aimed at medical applications such as bone implants because the mechanical properties of periodic lattice structures can be tailored to match those of natural bones. Example of this is the work by Heinl et al. (2008) who manufactured periodic cellular Ti-6Al-4V structures with interconnected porosity suitable for bone ingrowth using EBM.

The compressive strength and elastic modulus are similar to those of human bone, which might minimize stress-shielding effects; Mullen et al. (2009) have manufactured cellular titanium structures based on an octahedral unit cell through SLM for the purpose of bone in-growth applications, and the produced structures possessed the porosity of 10-95% and compression strength of 0.5-350MPa comparable to the typical naturally occurring range of natural bones; Bertol et al. (2010) reported the DMLS process and its constraints for the production of customized implants in titanium alloy with complex geometry and internal periodic lattice structures. More recently, Ramirez et al. (2011) fabricated Cu open periodic mesh structures by EBM, which exhibit considerable potential for complex multi-functional electrical and thermal management systems, especially heat exchange devices due to the superior thermal and electrical conductivity of Cu.

These 3D periodic lattice structures reported in literature mainly consist of strait prismatic strut making up the unit cell with specific cell size and thickness. The Magics software has recently introduced some of these structures including Hexagon, Sphere, Octagon, Cube, Tower, Rhombic, Diamond, Diagonal cross, X-cross, Circular-pipe, and Triangular etc. as shown in Fig. 2.15.

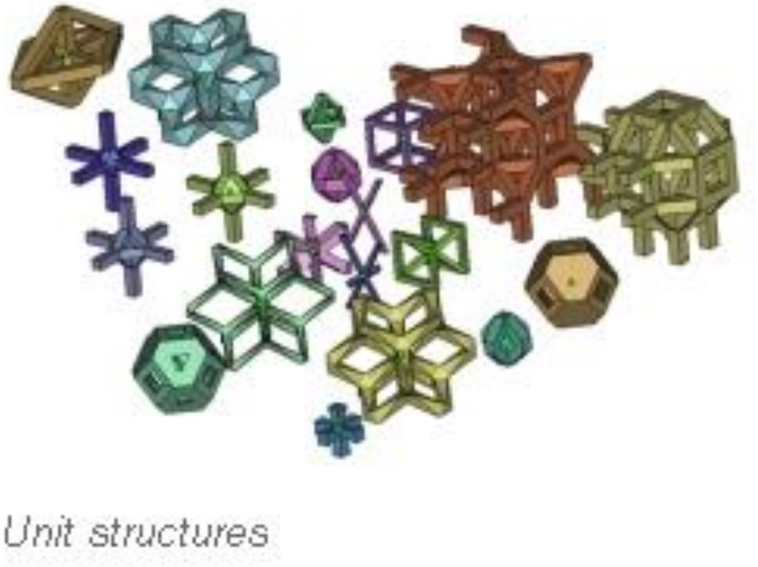

Figure 2.15 Unit cell types in Magics software [courtesy: materialise.com]

2.5.4.1 Triply Periodic Minimal Surfaces (TPMS) Cellular Structures

The majority of existing approaches generate lattice structure by producing CAD based scaffolds with straight edges and sharp turns or those derived from Boolean intersections of geometric primitives such as spheres and cylinders. These periodic lattice structures reported in literature and shown in Fig. 2.15 which possess straight beam-like struts and a polyhedral core would not exhibit good manufacturability in the metal AM machines in large unit cell sizes and low volume fractions. Because it will result a long overhang in strut structure that would lead to the occurrence of thermal deformation due to thermal stresses. There is a cross-sectional shift of the new layer from the previously deposited layer and that causes an overhang exceeding the maximum allowable angle, requiring support structure. The most suitable cell structure for metal AM is the one with curved strut/beams having little variation in subsequent layers during the build. The continuous curve in the strut allows it to be self-supporting during the build.

The biomorphic geometry that best mimics this structural configuration would be surfaces that are continuous through space and divided into two (pore and non-pore) not-necessarily-equal sub-spaces by a nonintersecting two-sided surface. Minimal surfaces are ideal to describe such a space. The triply periodic minimal surfaces (TPMS) are minimal surfaces periodic in three independent directions, extending infinitely and, in the absence of self-intersections, partitioning the space into two labyrinths. Fig.2.16 shows the TPMS Primitive (P) surface, the Diamond (D) surface discovered by Schwartz (1890) and the Gyroid (G) surface discovered by Schoen (1970). Surfaces whose mean curvature H is everywhere zero are minimal surfaces – any sufficiently small patch cut from a minimal surface has the least area of all surface patches with the same boundary. The TPMS are particularly fascinating because they are without self-intersections and partition in the space into two labyrinths.

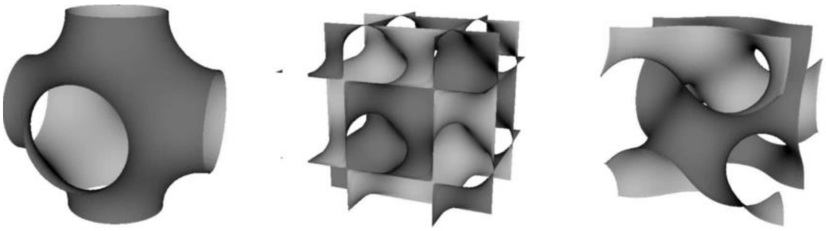

Fig. 2.16 Dimensional tessellations of Schwarz's Primitive (left), and Diamond (centre) and Schoen's Gyroid (right) Triply Periodic Minimal Surfaces [courtesy: susqu.edu]

2.6 Conclusion

Metal AM in particular powder bed fusion processes such as SLM and EBM are capable of producing nearly fully-dense inter-connected metal components directly from computer-aided design (CAD) models using a range of metallic powders. Recently, metal AM technologies have been employed to build more advanced metallic cellular lattice structures using several metal materials including stainless steel, pure titanium, titanium alloy and copper. Despite the many promising design freedoms, metal AM faces a major technical and design barriers in building complex geometries. One of the main challenges is that overhanging geometries require support structures during the build. The function of support structure is to prevent part curling or distortion resulting from thermal stresses by anchoring the newly melted layer in position. Because support structures consume expensive raw materials, use a considerable amount of laser consolidation energy and add to production time and cost there is considerable interest of design optimisations to reduce support structures materials.

The periodic lattice structures reported in literature studies with unit cells possessing straight beam-like struts and a polyhedral core would not exhibit good manufacturability in large unit cell sizes and low volume fractions. Because the long overhanging struts in big unit cells would lead to the occurrence of serious deformation during the metal AM processes. The most suitable cell type for metal AM is the one with continuously curved beams having little variation in subsequent layers during the build. The cellular structure which best fits to this criterion is triply periodic minimal surface (TPMS) with an infinitely connected triply periodic non-self-intersecting minimal surface with triple junctions and which contains no straight lines on the surface. The triply periodic minimal surface cellular structures which are self-supporting can be considered to be a suitable candidate for metal AM processes.

To tackle the process limitation in metal AM and promote design freedom and quality parts, the focus of this research will be the investigation of these self-supporting TPMS cellular structures in the first time using various metallic powders and metal AM machines. The aim is to improve the manufacturability of complex light-weight cellular structure without the need of support structure in wider range of cell sizes and densities. The properties of these structures will be evaluated so that designers will have confidence to use and tailor their properties to specific applications. The TPMS cellular structures will also be test to be used as support structure in reducing support material and built time.

Part Two:

Materials and Methods, Preliminary experiments, and Finite Element Simulation

CHAPTER 3 Materials and Methods

3.1 Introduction

This chapter explains the powder materials, manufacturing machines, and measurement equipment used during the experimental work in this research. Section 3.2 presents the various metal powders and their characteristics used during the experimental work. Section 3.3 describes the manufacturing machine set-up of SLM and DMLS systems, the two machines used throughout the experimental studies. This includes description on the processing parameters used in these experiments. Section 3.4 discusses the post-processing techniques used after the built is completed. This includes bead blasting, heat treatments, and support structure removal process. The measurement techniques used for sample analysis and characterisation is detailed in section 3.5.

3.2 Powder Materials

3.2.1 316L Stainless steel

316L Stainless Steel is a pre-alloyed austenitic stainless steel in fine powder form. This powder meets the chemical requirements of AISI 316L, DIN 17006 X2CrNiMo17-12-2, and W.Nr1.4404. This kind of steel is characterised by having higher corrosion resistance and mechanical properties than the more common 304 alloy, and can be used over a wide temperature range down to cryogenic temperatures. This type of steel is widely used in a variety of food processing, medical, aerospace, oil and gas, and other engineering applications requiring high strength and corrosion resistance.

The 316L stainless steel powder which was gas atomized and produced by Sandvik Osprey Ltd. UK. Table 3.1 shows the specified chemical composition of the powder. As shown in Fig. 3.1, the powder has an average particle size distribution of approximately 45 µm and is nearly spherical in shape, which leads to a good flowability. The powder particles have a rough surface with some smaller and irregular particles of approximately 3 to 8 µm sticking on the surface.

Table 3.1 - Chemical compositions of 316L stainless steel powder, wt.-% (Sandvik Osprey, UK)

C	Si	Mn	Mo	Ni	Cr	P	S	Fe
≤ 0.03	0.7	1.4	2 - 3	12 - 14	16 -18	≤ 0.04	≤ 0.035	Bal.

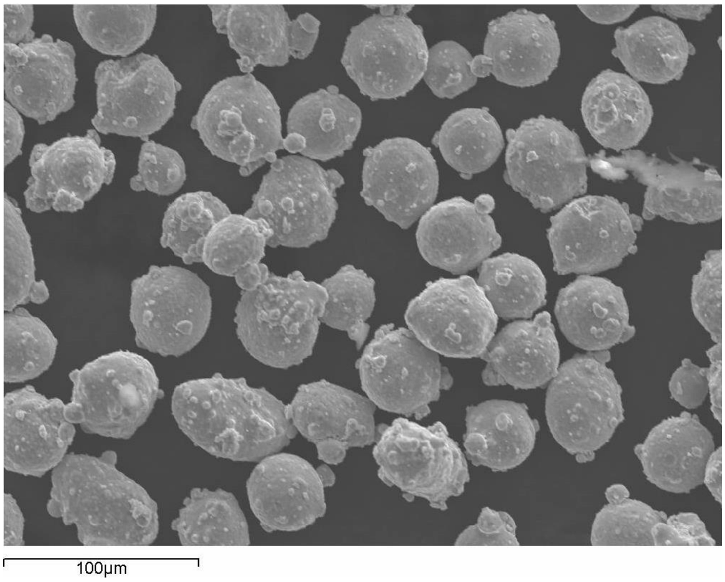

Figure 3.1 Typical SEM micrograph of 316L stainless steel powder

3.2.2 Ti-6Al-4V

Ti-6Al-4V is known as the "workhorse" of the titanium industry because it is by far the most common Titanium alloy, accounting for more than 50% of total titanium usage. This well-known light alloy is characterised by having excellent mechanical properties and corrosion resistance combined with low specific weight and biocompatibility. This material is ideal for many high-performance engineering applications, for example in aerospace and motor racing, and also for the production of biomedical implants. Parts built in Titanium Ti-6Al-4V fulfil the requirements of ASTM F1472 regarding maximum concentration of impurities. The pre-alloyed Ti-6Al-4V is prepared in fine powder form for SLM/DMLS process and was supplied by LPW Technology Ltd. UK. Table 3.2 shows the specified chemical composition of the Ti-6Al-4V powder. Fig 3.2 shows the Ti-6Al-4V powder particles that have a spherical shape and containing a mixture of very small and big sizes particle distribution with average particle size of 30 µm.

Table 3.2- Chemical compositions of Ti-6Al-4V powder, wt. % (LPW Technology, UK)

Al	N	H_2	O	V	C	Fe	Ti
5.5-6.5	0.3 Max.	0.0125 Max.	0.2 Max.	3.5-4.5	0.08 Max.	0.25 Max.	Bal.

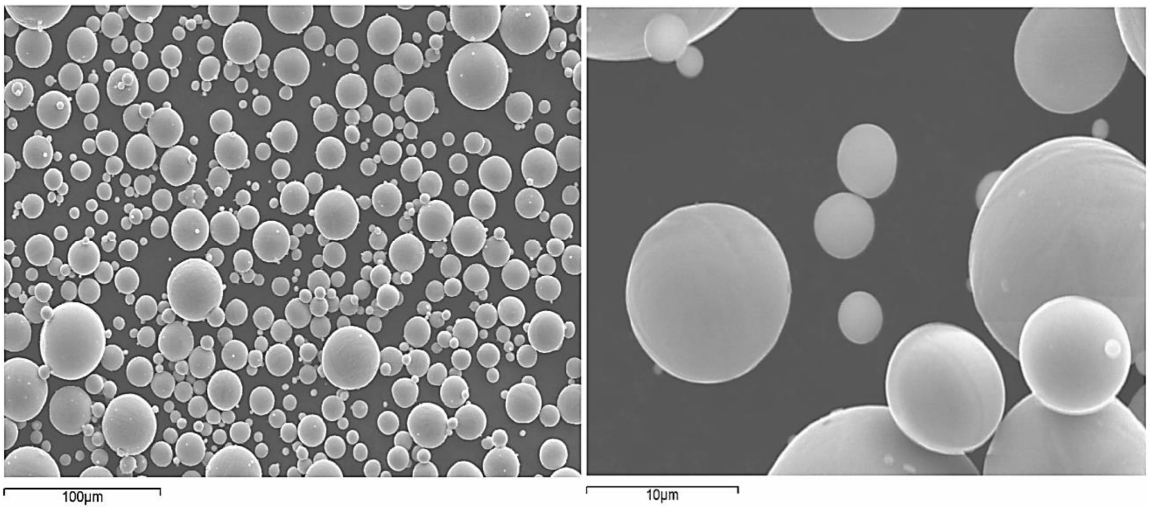

Figure 3.2 SEM micrograph of Titanium alloy (Ti-6Al-4V) powder with different magnification

3.2.3 AlSi10Mg

Aluminium AlSi10Mg is a typical casting alloy used for parts with thin walls and complex geometry. AlSi10Mg are ideal for applications which require a combination of good thermal properties and low weight. Table 3.3 shows the chemical composition of the AlSi10Mg powder. The AlSi10Mg powder which is prepared for DMLS machines was supplied by EOS GmbH, Germany. Fig 3.3 depicts the SEM images of the as-received AlSi10Mg alloy powder. The powder has a nearly spherical shape and smooth surfaces with an average particle size of 40 µm.

Table 3.3- Chemical compositions of AlSi10Mg powder, wt. % (LPW Technology, UK)

Si	Cu	Mn	Mg	Zn	Fe	Al
9-11	<0.1.	0.05	0.45-0.6	0.05	<0.55	Bal.

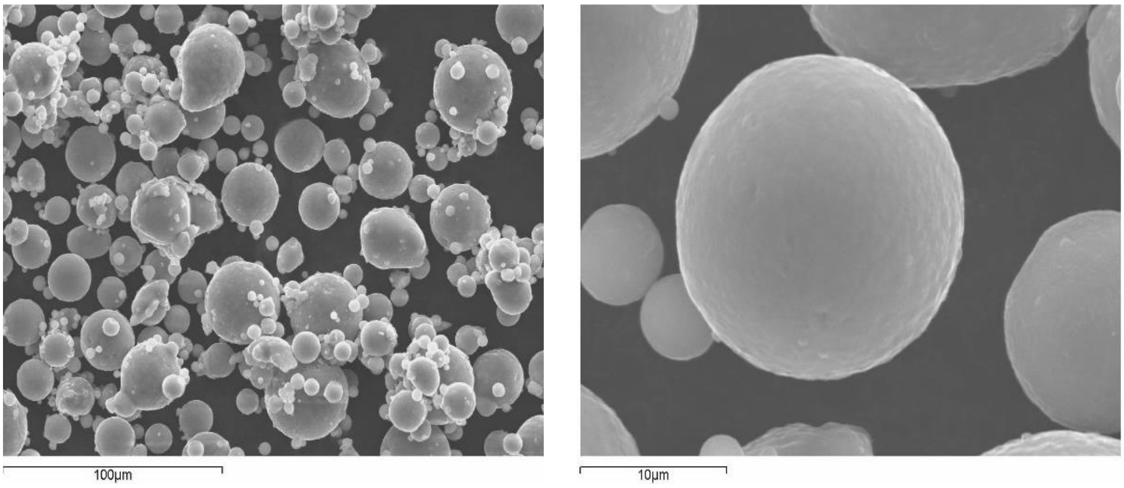

Figure 3.3 SEM images with different magnifications of the AlSi10Mg alloy powder

3.3 Manufacturing Machine set-up

3.3.1 SLM MCP-Realizer 250

All experiments on 316L stainless steel were carried out by SLM machine (MCP Realizer 250, MTT Technologies Group, see Fig. 3.4). This machine has a build volume of 250mmx250mmx300mm and is equipped with Ytterbium Fibre laser and continuous wave length of 1064nm.

Table 3.4 shows the processing parameters used in processing the 316L stainless steel powder.

Table 3.4 – Processing parameters of SLM MCP-Realizer machine

Processing parameters	Value
Laser power	100 W
Scanning speed	500 mm/s
Laser spot diameter	100 µm
Hatch spacing	75 µm
Layer thickness	75 µm
Oxygen content	<1%
Inert gas used	Argon
Chamber pressure	0.6 bar ± 0.2 bar
Processed material	316L stainless steel

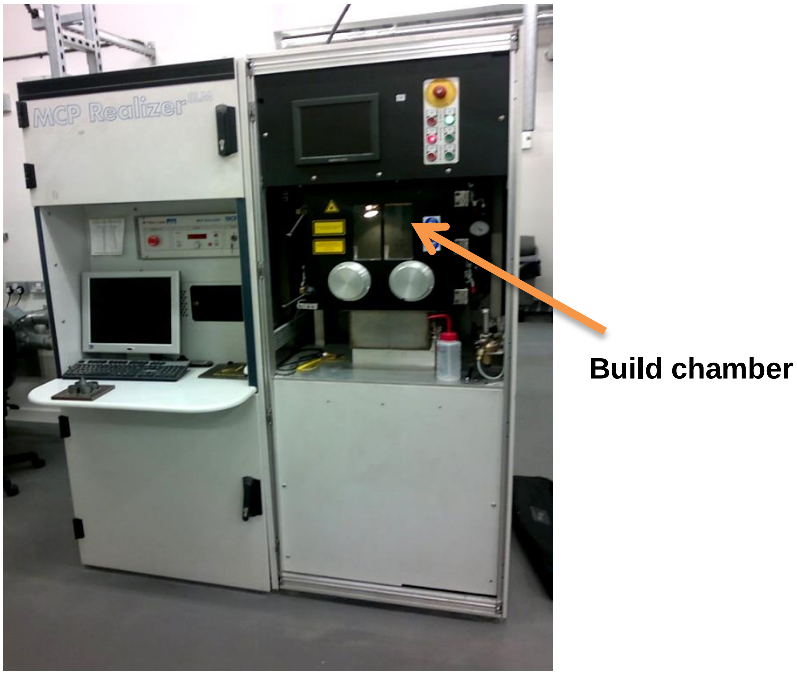

Figure 3.4 SLM MCP- Realizer 250 Machine *(*Courtesy: *University of Exeter)*

To ensure that quality test parts are produced, the process parameters were set according with guidance from SLM suppliers and initial parameter optimization tests conducted in the machine. The parameters in Table 3.4 were then selected to give the best result for 316L Stainless steel powder. The scanning speed is controlled by two parameters, the point distance (μm) and exposure time (μs) as,

$$Scanning\ speed\ (m/s) = \frac{Point\ distance\ (\mu m)}{Exposure\ time\ (\mu s)} \tag{3.1}$$

Fig. 3.5 shows the scanning strategy used in SLM machine. Both strategies, uni-directional and bi-directional are common strategies that can be used in the process. The laser first scans the outer boundary contour of the layer and then hatches the inner core using uni-directional or bidirectional strategy. The subsequent layer is either scanned in similar fashion or the scan line is rotated at 90 degree and perpendicular to the previous layer (i.e, alternating x and y scan line for subsequent layers).

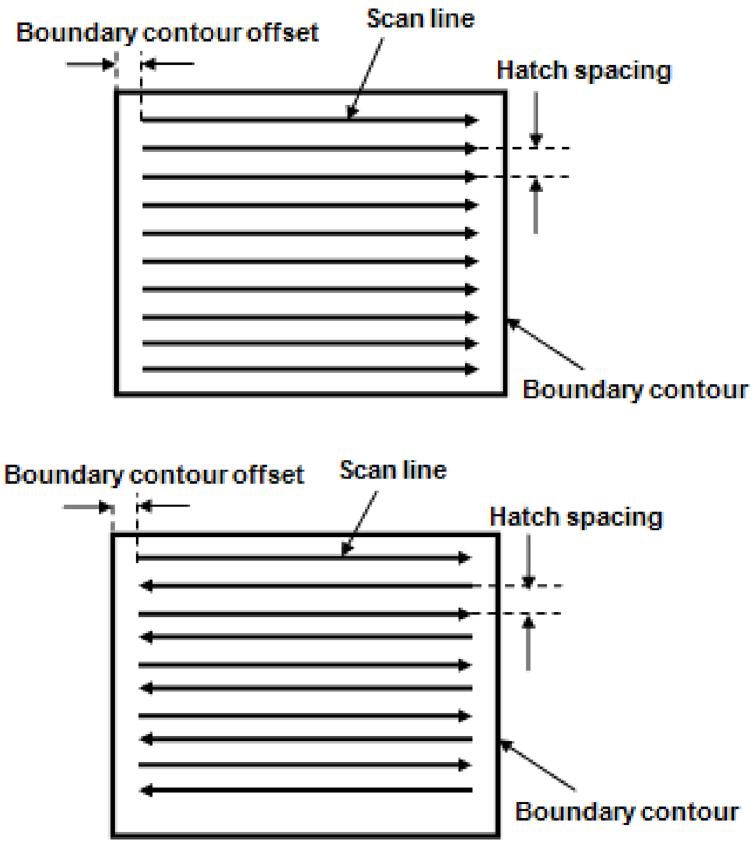

Figure 3.5 Scanning strategy used in SLM (a) Uni-directional (b) Bi-directional

The powder deposition is controlled by the build platform movement in z-axis and equivalent to the layer thickness and the back-and-forth movement of recoater, which spreads a thin powder layer on the build plate. All parts were built on a thick steel plate pinned on to the platform. To minimize disruptions during the build, a sufficient amount of powder was stored in a tank located at the back side of the machine. To reduce oxygen content in the chamber and avoid oxidation during the build process, an Argon gas is pumped into the build chamber with controlled pressure level and allowed to flash out oxygen until oxygen level reads below 1%.

After the machine set-up and powder preparation is completed the part files are loaded into the machine software (usually Magics software is used to slice the geometry according to the layer thickness and choose the location of the part in the platform). The machine controller software translates the 2D slice data into key processing instructions consisting of co-ordinates, point distances, exposure/dwell time of the laser beam etc.

3.3.2 DMLS EOSINT M280 & M270

All experiments on *Ti-6Al-4V* and *AlSi10Mg* alloys were conducted through a collaborative research project partner at 3T RPD Ltd. UK using "DMLS EOSINT M270 and EOSINT M280" machines supplied by EOS GmbH, Munich, Germany. The EOSINT M 280 has slightly a bigger build chamber which is 250mm x 250mm x 325mm compared to 250mm x 250mm x 215mm of EOSINT M270. They are both equipped with a solid state fibre laser with M280 having higher laser power of up to 400 W. Table 3.5 shows the processing parameters used in these machines. The EOS machine software provides two types of scanning strategy which are Skin and Core (this is similar to contour and hatch scan of the SLM machine). Skin refers to the outer shell of part while Core refers to the inner part. As the part can be divided into two portions, the set-up software allows a user to define different parameters such as layer thickness and scan speed according to the area. This will speed up the processing time by optimizing the machine's parameters for each region. Fig. 3.6 shows the EOSINT M270 machine.

Table 3.5- Processing parameters used in DMLS EOSINT M280 & M270 machines

EOSINT M280		EOSINT M270	
Parameters	Value	Parameters	Value
Laser power	280 W	Laser power	170 W
Scanning speed	2000 mm/s	Scanning speed	1250 mm/s
Spot size	100 µm	Spot size	100 µm
Layer thickness	30 µm	Layer thickness	30 µm
Oxygen content	<0.1%	Oxygen content	<0.1%
Processed material	AlSi10Mg	Processed material	Ti-6Al-4V

Figure 3.6 EOS GmbH M270 Machine*, source; (*Courtesy: *www.eos.info*)

3.4 Post-processing

3.4.1 Heat treatment

In normal SLM and DMLS manufacturing practice, all parts go through stress-relieving heat treatment process prior to support structure removal, whereby all residual stresses are released from the part. Residual stresses if not properly released through heat treatment processes could cause the part to deflect after it is removed from base plat/platform and the supporting structure due to stress relaxation. The Ti-6Al-4V and AlSi10Mg parts were annealed in an electric oven with controllable temperature using the following stress-relieving heat treatment cycles:

Heat Treatment Cycle:

- Ramp to 720°C – 60mins
- Hold at 720°C – 35mins
- Ramp to 680°C – 25mins
- Hold at 680°C – 180mins
- Cool in argon to below 400˚C
- Cool in air / argon to room temperature

3.4.2 Wire-Electric Discharge Machine (Wire- EDM)

Wire-Electric Discharge Machine (Agie Challenge V2 Wire EDM) was used to remove the parts from the base plate and support structure. The schematic of the wire-EDM process is as shown in Fig. 3.7. In this process a thin singlestrand metal wire, usually brass, is fed through the work piece which is either submerged in a tank of dielectric fluid or dielectric is supplied through nozzle. The wire is constantly fed from a spool and is held between upper and lower diamond guides. Due to the inherent properties of the process, wire-EDM can easily machine complex parts and precision components out of hard conductive materials. The phenomenon of erosion is same in wire-EDM process however; the tool electrode takes the form of a wire of generally 100 to 300 μm in diameter.

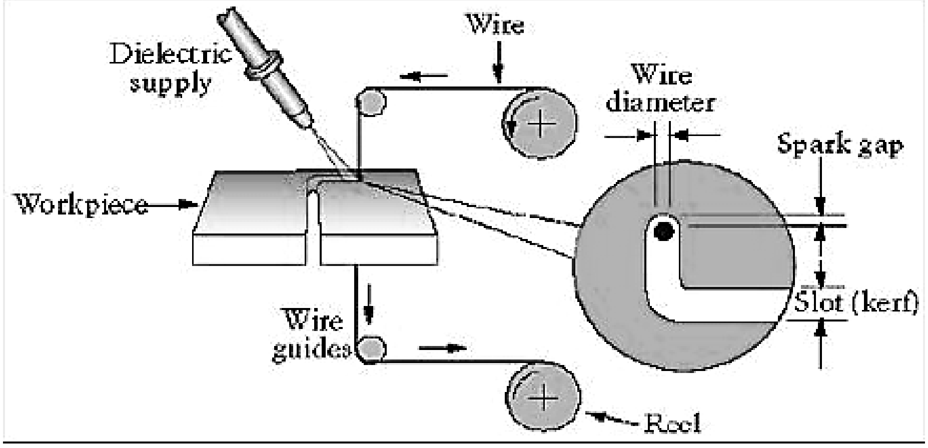

Figure 3.7 Schematic of Wire-EDM process
[Courtesy: ncpre.com)

3.4.3 Bead blasting - finishing

After the parts were annealed and then wire-cut from build platform/base or support structure, they were bead blasted. When a part is subjected to bead blast finishing, residual material is removed. This gives the product a uniform look that works well for aesthetic purposes. Dry oxide blasting was done using fine aluminium oxide. This produces a smooth matt grey finish, which is even throughout.

3.5 Measurements and Characterisations

3.5.1 Micro-CT Analysis

A micro-CT scanner (Bench top CT 160Xi, X-Tek) was used to scan the manufactured parts. Slices from the scanned object can be stacked to produce a 3D reconstruction model. VGstudio MAX2.1 software was used to reconstruct the 3D models of the fabricated parts using the 2D slice images data obtained from micro-CT scans. By analyzing the reconstruction 3D models, the features of the manufactured part such as internal defects and geometric irregularities can be identified. Fig. 3.8 (a) shows the micro-CT scanner used to analyse the experimental samples.

X-Tek Bench top CT 160 Xi:

- 5 µm Focal Spot X-Ray Source, 25 to 160 kV, 0 to 1000 µA (non continuous) 60 Watt.
- The 60W source operates at up to 160kV, giving good penetrating power of heavier samples.
- 3 micron resolution, max diameter 90mm, 5kg max load.
- 5 axis manually controlled manipulator. Full system control and image processing software.

3.5.2 Scanning Electron Microscopy (SEM)

The manufactured parts underwent a micro-morphological characterization using HITACHI S-3200N Scanning Electron Microscope (SEM) (see Fig. 3.8 (b)). SEM was also used for studying the morphology of the processed powder. The SEM is an instrument that produces a largely magnified image by using electrons instead of light to form an image. Because the SEM utilizes vacuum conditions and uses electrons to form an image, special preparations must be done to the sample. All metals are conductive and require no preparation before being used except proper cleaning process of the loose powder.

HITACHI S-3200N SEM:

- 27 µm resolution
- 120 KV voltages and
- 182 µA current

Figure 3.8 (a) X-Tek Bench top CT 160 Xi (b) Scanning Electron Microscope (SEM) – Hitachi S3200N (Courtesy: University of Exeter)

3.5.3 Optical Microscopy

The optical microscopy (Dino-lite AM413ZT-A) shown in Fig. 3.9 was used to measure the dimensional accuracy of the experimental parts. This allows the comparison of the optical measurements with the original CAD dimensions. Table 3.6 shows the specification of the optical microscope.

Table 3.6 – Optical microscopy

Specifications:	
Diameter	3.2 cm
Dimensions	3.2 Dia. X 10.5 cm
Frame rate	30 fps
Illuminated	Yes
Interface type	USB 2.0
Length	10.5 cm
Magnifier power	1→ 50, 200
Resolution	1300000 pixel
Weight	105 g

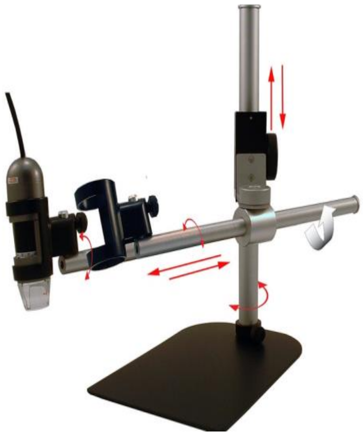

Figure 3.9 Dino-Lite optical Microscope (Courtesy: University of Exeter)

3.5.4 Uni-axial compression test

Uni-axial compression tests were carried out to assess the compression properties of the manufactured parts using EZ20 and LR300K Universal Material Testing Machine, Lloyd Instruments Ltd., UK equipped with a 20 kN load cell (see Fig.3.10 (a)). The EZ20 machine was used for the compression testing of 316L stainless steel while LR300K was used for the Ti-6Al-4V and AlSi10Mg cellular structures (see Fig.3.10 (b)). Two smooth steel plates which are polished and hardened were used to reduce friction in compression test. The speed of loading was set a constant of 0.4 mm/min for all of the tests. The stress-strain curves, yield strengths and Young's modulus data were obtained from machine installed software.

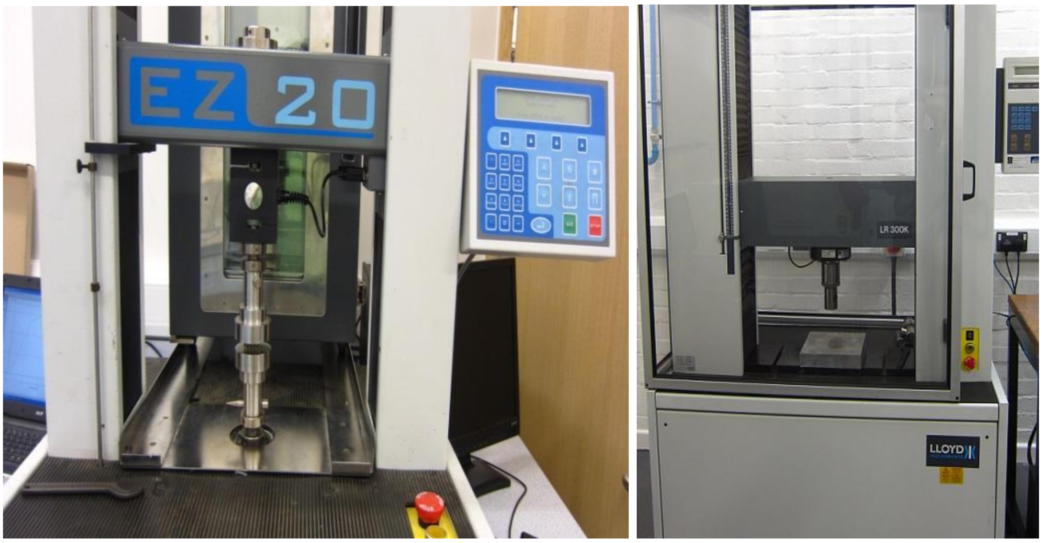

(a) (b)

Figure 3.10 (a) EZ20 Universal Material Testing Machine c) LR300K Universal Material Testing Machine (Courtesy: University of Exeter)

3.5.5 Deformation measurements

The resulting deflection in support structure geometries was measured using Roland MDX-20 (see Fig. 3.11). This is a 3D scanner for scanning 3D objects and creating 3D cloud data by using a moving needle probe to touch the surface of the object and record data points. Dr. PICZA scanning software which is installed in the machine is used for dynamic graphic display, curve smoothing, and adjusting the height of the scanned surface. The scanned data was exported as a point cloud data (ASCII) and processed in MATLAB software for visualization.

Figure 3.11 3D scanner - Rolland MDX-20 (Courtesy: University of Exeter)

CHAPTER 4

Preliminary Experiment on Single Layers Built on Powder Bed Without-Support in SLM Process

4.1 Introduction

As has been discussed in literature (chapter 2), SLM process is associated with large temperature and stress gradients during melting and solidification of the material. The process is generally accompanied with the formation of various defects such as deformation and cracks. In particular, overhanging and floating layers which are built in SLM and DMLS processes are usually associated with highest temperature gradients and thermal stresses.

This chapter presents the results of preliminary experiment of single overhanging layers using 316L stainless steel powder. The objective is to determine the effect of processing parameters on melt depth of single layers built on powder bed without support structure. In fact, only one layer can be built this way, otherwise, the powder recoater would wipe out if not supported properly. The first layer in the build is always crucial, as it stands the foundation for subsequent layer of the part. It is important that this base layer is built successfully without deformation. Any irregularities in the base layer will be transferred into the upper layers and could affect the whole build. Measurements were taken on layer thickness of the processed single layers. SEM micrographs were taken from sample surface to observe signs of defects and porosities. This work aids in our understanding of the relationship between process parameters and laser melting penetration depth and surface characteristics of overhang layers introduced during the build.

This chapter is divided into the following sections: section 4.2 describes the experimental procedures used during sample manufacturing. Section 4.3 presents results and discussions. Section 4.4 concludes the chapter highlighting the most important findings in this chapter.

4.2 Experimental Procedure

Single layers have been produced on the loose powder bed from a commercially available 316L stainless steel powder which was gas atomized and produced by Sandvik Osprey Metals Ltd., UK. The experiments were carried out on the SLM MCP-Realizer. To avoid oxidation during laser processing, the oxygen level in the building chamber was kept below 1 % by continuously pumping argon gas. The powder were spread and levelled in a flat build plate of 150 x 150 mm with a powder depth of 1 mm. Single layers were scanned by the laser with different scanning speeds on the surface of the powder bed. The energy supplied by the laser beam on the powder surface was varied by using different scanning speed *(V)* ranging from 100 - 300 mm/s. The laser power (*P)* and hatch spacing (*H)* was held constant at approximately 100 W and 75 µm respectively.

A typical uni-directional scanning strategy was used to form the scan tracks which form the layer by overlapping of linear single scans. Due to overlap between the successive adjacent scans, the hatch spacing is always less than the laser beam radius and some points on the powder bed are exposed to multiple scanning. The geometrical dimensions of the single layers were 10 x 10 mm. After processing, layers were removed from build platform and cleaned from loose powder while observing signs of deformation and crack. A digital Vernier calliper having a rated accuracy of 0.02 mm and a resolution of 0.01 mm was used to measure the thicknesses of the processed parts. Each processing condition was repeated at least twice and the result of the thickness measurement was expressed using the mean value. The surface as-processed layers were observed in Scanning Electron Microscope (Hitachi S-3200N) for defect and porosity.

4.3 Results and discussions

4.3.1 Effect of scanning speed on layer thickness

Fig. 4.1 shows the effect of scanning speed on layer thickness of single layer parts. The results reveal that the layer thickness depends on scanning speed when other parameters are fixed. In general, as the energy input increases (higher laser power, *P*, or lower scan rate, *v*) higher penetration depth of the laser is obtained and a thicker layer is formed on the powder bed. In an un-supported part built on loose power bed, most of the laser heat energy is transported into the powder material through conduction and convection mechanisms. It is known that when interaction of laser radiation with metal powders occurs, the energy deposition is performed by both bulk-coupling and powder-coupling mechanisms (Simchi 2006). This energy rapidly heats up the particles above the melting point and cause particle bonding to occur. The density change during irradiation and formation of metal agglomerates also affect the coupling efficiency and thus influence the absorbed energy.

On the other hand, the effective thermal conductivity of the bed is lower than that of single particle and it highly depends on the amount of porosity, the arrangement of the particles and the contacts between them. The exposure period of the laser irradiation (*d/v*) ranges between 0.2 and 8ms. In such time scale, the heat flow distance during the interaction time is considerably less than the particle diameter, leading to very fast heating up the skin of the particles. The absorbed energy is then transferred to the surroundings by thermal diffusion. The temperature of the exposed powder particles can easily exceed the melting temperature, leading to full melting of the particles. As a result, thick layers are formed when layer are built on powder. Since the laser power was fixed during the experiment, the low scanning speeds are accompanied with high energy density due to the longer interaction time with the powder leading to higher penetration depth and layer thickness. As the speed is increased from 100 mm/s to 200 and 300 mm/s, the measured layer thickness is dropped. The layer thickness is formed by fully melted core solid upper section and partially melted bonded particles at the bottom and boundary of the layer.

When layers are built on solid material being a previous layer; base plate; or even supporting structures, the layer thickness is fixed and ranges from 20 µm to 100 µm. In these cases, much of the laser heat is dissipated through the supporting solid material. As the conductivity of solid is higher compared to porous powder, the heat is dissipated more quickly in the process and the layer solidification time is shortened. On the other hand, large unstable melt pool is formed in single layers built on powder as there is no sufficient time for the previous tracks to cool and solidify.

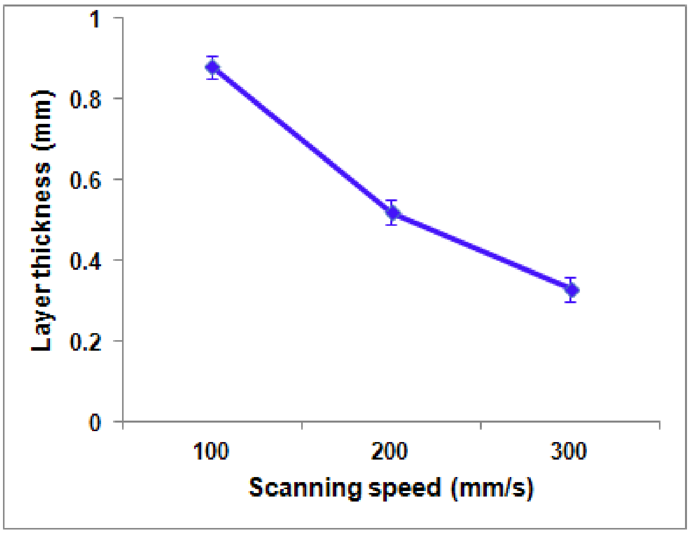

Figure 4.1 Measured layer thickness for various scanning speeds

4.3.2 Surface morphology of the processed single layers

Initial results obtained from a preliminary visual inspection of the processed layers show that the surface morphology changes as the scanning speed increases. The SEM micrographs taken from the surface of single layer specimens are shown in Fig. 4.2 (a-c). At high laser energy inputs (lower scanning speeds) delamination of melted layers and formation of large pores are feasible as depicted in Fig. 4.2(a). The surface tension effect and solidification shrinkage contribute to the formation of large inter-agglomerates pores and cracks. The high thermal gradients present in the materials are accompanied by thermal stresses, which in fact may also cause cracks in the processed layers.

There is a definitive tendency that as the speed increases the scan width decreases and becomes more unstable up to a point where a balling effect becomes noticeable. The balling effect is the sphereodisation of the liquid melt pool. The higher scanning speeds leads to the balling phenomena and track segregation due to the surface tensions on the powder bed. The bonding between the tracks forming the layer also becomes more apparent at higher scanning speeds (see Fig. 4.2 (c)). The balling phenomenon and lack of overlap between tracks causes unevenness and deficiency in powder particles for the next track and may lead to high porosity and large pore formations. The layer starts to fragment due to weak bonding between the tracks. Since the layers were built on the top of loose powder bed, partially melted particles could be attached to the bottom surface which result very rough surface. Hence, the shape and the size of powder particles significantly influence the surface roughness and densification of SLM parts.

Melt-pool stability is not the only result to consider in SLM. The optimum result will be a scan track of constant, uniform width and adequate penetration. Vector stability without penetration into the substrate or support structure is also undesirable. Inadequate penetration into the substrate will cause an insufficient bond between the substrate and the first layer of the processed part that will in its turn cause the part to separate from the substrate and cause the SLM machine to stop prematurely and the job will be a failure.

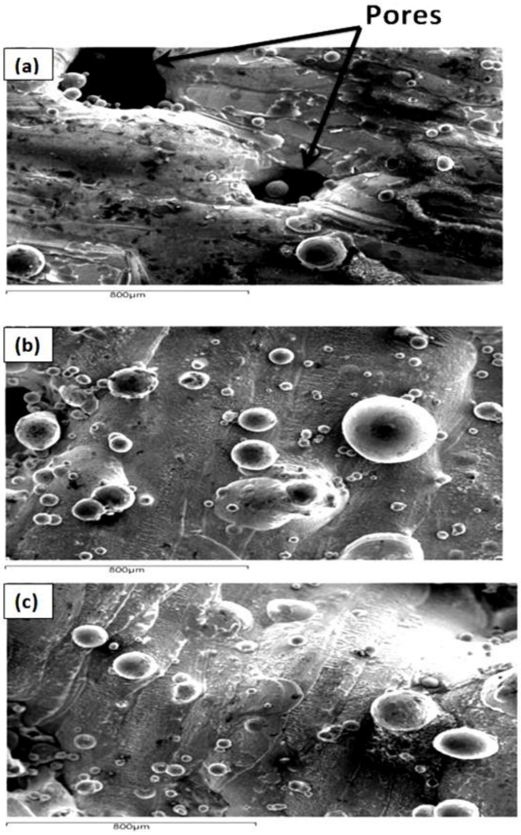

Fig.4.2 SEM micrograph of top surface of the single layer parts (a) 100 mm/s (b) 200 mm/s (c) 300 mm/s

4.4 Conclusion

The results of these experiments demonstrate the relation between layer thickness, scanning speed and surface characteristics of processed single layers built on powder bed in SLM process. The layer thickness increases at lower scanning speed due to higher penetration depth resulting from longer interaction time of the laser. Although the development of thermal stresses highly depends on the scanning strategy. It is noteworthy that even at very intensive laser energy full densification cannot be obtained in single layers built on powder bed because of delamination of the layers due to thermal stresses, formation of gas pores during solidification and porosity formation due to material shrinkage and the balling effect. This work was important for our understanding on the mechanisms of laser and material interactions in SLM process. To understand these mechanisms better, the next chapter will address the temperature and stress field in single layers processed in SLM process by means of numerical simulation.

CHAPTER 5

Finite Element Simulation of the Temperature and Stress Fields in Single Layers Built in SLM Process

5.1 Introduction

This Chapter presents a numerical approach using a three-dimensional finite element simulation to investigate the temperature and stress fields in single 316L stainless steel floating layers built on the powder bed without support in SLM. Experimental work alone, as was described in chapter 4 is not sufficient to explain the thermal mechanism involved during laser and material interactions. The simulation is expected to widen our knowledge on the mechanisms of overhang layer consolidation and melt-pool characteristics in SLM process. The magnitude of temperature and stresses could inform us the high stress gradient regions in the layer so that proper support structure becomes necessary.

Section 5.2 gives an overview of the modelling techniques used to study the temperature and stresses in metal AM process. Section 5.3 describes the finite element approach taken in this study. Section 5.4 presents the results and discussion of the numerical model. Section 5.5 is a conclusion of the chapter highlighting the main findings of the study.

5.2 Modeling the Temperature and Stress Fields in Metal AM Processes

One of the major limitations of metal AM processes including SLM and DMLS is the thermal distortion of the part during forming, which may lead to undesired shrinkage and cracks. The elevated temperature gradients developed during the SLM process yield a non-homogeneous permanent strains and residual stresses distributed within consolidated layers (Kruth et al. 2004). These could considerably affect the layer consolidation and deformation behaviours during the SLM process and consequently the dimensional accuracy, geometric shape, and mechanical properties of the fabricated parts. The processing parameters such as laser power, scanning speed, laser spot size, and scanning strategy all play a crucial role on the development of temperature gradients and residual stresses in the consolidated layers and resulting three dimensional parts (Mercelis et al. 2006). These parameters are usually optimized through experimental means for specific machines and materials. However, detailed investigation of all different parameters and materials for SLM through experiments can be time consuming and costly. Therefore, numerical methods could be used as an effective tool to study the role of these parameters on temperature distribution, residual stress and other thermal mechanisms.

The finite element analysis (FEA) method is the most commonly used numerical method for predicting temperature and stress fields in SLM. An investigation was also carried out to illustrate the effect of layer thickness on part deformation in SLM parts (Zaeh and Branner 2010), revealing that a thinner layer thickness resulted in a higher deformation due to the effect of higher temperature variation concentrated within thin layers. The work did not investigate the temperature and stresses in tracks forming the layer. Matsumoto et al., (2002) developed a FEA method to simulate the temperature and stress field for single layer parts on the loose powder in SLM. A 2D non-linear heat transfer with volumetric internal heat source problem is numerically solved based on the coupling of Matlab and ANSYS FEM models (Patil and Yadava 2007). The work did not consider the melted depth of the layer which is important in SLM process. The surface temperature distribution during SLM of 90W–7Ni–3F materials was predicted by (Zhang et al. 2010). The effect of laser scanning strategy on residual thermal stresses and distortion was investigated using FEA (Dai and Shaw 2002). This is one of the first such works conducted in understanding the effect of scanning strategy on temperature distribution and stresses. A FEA model was developed by Nickel et al. (2001) to simulate the laser deposition process and found that the deposition pattern has a significant effect on the part stresses and deflections. Researchers (Yin et al. 2012; Ameer et al. 2003; Shuai et al. 2012) reported their research results of temperature fields in single metallic layer SLM processes by using element birth and death technique. A more comprehensive understanding of the SLM thermal field has been achieved by creating a 3D model and considering the interval time for new powder recoating (Roberts et al. 2009).

A 3D FEA model with fixed temperature heat source for calculating the evolution of temperature and thermal stresses within a single metallic layer formed on the powder bed using two different scanning patterns in SLM was proposed Ma et al. (2007). It was found that the distortion and transient stresses of a layer processed by a moving laser beam decreased with fractal scanning pattern. From this review, it is evident that using 2D analysis with generalized plane strain conditions seems to be convenient with less computer processing requirements, but 3D analysis remains absolutely necessary to fully understand the thermal induced problems in SLM process.

An in-depth understanding of the materials and laser interaction in overhanging regions and its associated thermal and stress mechanisms has not been properly investigated in literature. This is an essential step for understanding the requirements of support structure design and development. This study was undertaken to highlight these issues with regard to support structure and to understand the magnitude of temperature and thermal stresses that are developed in single layers built on the powder bed. The study also takes into account the effect of the processing parameters such as the scanning speed on temperature gradients and melt-pool dimensions (length, width, and depth of melting).

The numerical approach taken is a 3D non-linear (i.e., material properties are temperature dependant) transient finite element model based on sequentially coupled thermo-mechanical field analysis was developed in ANSYS programme to predict the temperature distribution, thermal stresses and melt pool dimensions of laser scanned single layers built on the powder bed. Simulation of the moving heat source and changing boundary conditions is conducted through a user written subroutine implemented in ANSYS parametric design language (APDL). Since the heat energy is transported well below the surface of the powder bed in SLM, the laser energy density was applied as a volumetric heat source rather than a surface heat flux which has been the route taken in most literature works. Temperature dependent physical properties of 316L stainless steel powder material are taken into account and latent heat of fusion is considered.

5.3 Three-Dimensional Finite Element Modelling

ANSYS is a general purpose finite element modelling package for numerically solving a wide variety of mechanical and thermal problems. ANSYS software is developed by ANSYS, Inc. (Pittsburgh, United States). ANSYS provides the capability of performing indirect sequentially coupled thermo-mechanical analysis for both heat and stress analysis. In this study, a multiple physics environment was used in a single database as this allows a quick switching between physics environments for subsequent stress analysis. A non-linear transient thermal analysis was performed first to obtain the global temperature history generated during the laser melting. A transient stress analysis is then developed with an automatic exchange of the element type from thermal-to-structural, and applying the temperatures obtained from previous transient thermal analysis, as a thermal loading for the mechanical analysis.

The 3D thermal and structural/mechanical element used was SOLID70 and SOLID185 respectively. This element selection allows single meshing to be performed with an automatic exchange of the element type from thermal-to-structural during processing. SOLID70 has a 3-D thermal conduction capability. It has eight nodes with a single degree of freedom, temperature, at each node and is applicable to a three-dimensional, steady-state or transient thermal analysis. SOLID185 is used for the 3-D modelling of solid structures and is defined by eight nodes having three degrees of freedom at each node: translations in the nodal x, y, and z directions. The element has plasticity, stress stiffening, large deflection, and large strain capabilities. The 3D FEA model representing the single layers built on the powder bed can be seen in Fig. 5.1(a). The model illustrates a single layer of 10mm long scanned by the laser beam on the powder bed using a uni-directional scanning strategy. In order to reduce computational time, only five adjacent tracks were scanned and the elements which interact with the laser beam are finely meshed with hexahedral element sizes equal to 75 µm and coarser mesh is used for the surrounding loose powder. The FEA model assumes a powder thickness of 1mm; this was deliberately selected to allow sufficient laser penetration into the powder bed during scanning and so that un-melted material will still remain at the bottom of the bed. Table 5.1 summarizes the parameters used in the finite element simulation.

For the thermal analysis, the laser beam with calculated energy density as in Fig. 5.1(b) strikes a number of elements equal to the laser spot size of 150 µm and moves with the specific scanning speed in the X-direction on the powder bed. When the laser moves to next load step, the previous load step is deleted to account for the cooling cycle. The analysis is divided into several steps in order to move the heat source from laser over few elements at the time in the laser path. The time period for which the laser beam is retained on each step, is given as,

$$T_{step} = \frac{dx}{V} \tag{5.1}$$

Where *dx* is the length of elements under the laser spot in mm and *V is* the scanning speed of the laser beam in mm/s.

Table 5.1- Finite element simulation parameters

Parameter	Value
Laser power, *P*	*100 Watt*
Scanning speed, *V*	*100, 200, 300 mm/s*
Track length, *L*	*10 mm*
Number of tracks scanned, *N*	*5 tracks*
Power bed thickness, *T*	*1 mm*
Hatch spacing, H_s	*75 µm*
Laser spot size, *D*	*150 µm*
Thermal element type, 3D	*SOLID70*
Structural element type, 3D	*SOLID185*

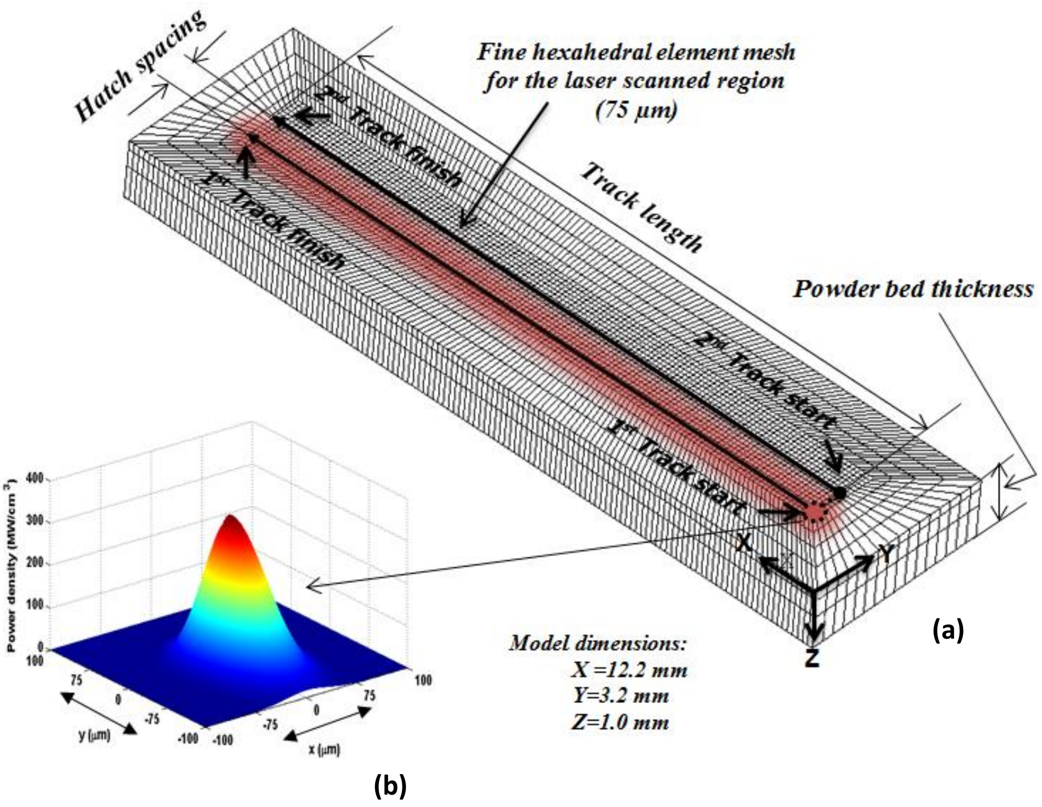

Figure 5.1 (a) 3D finite element model (b) Gaussian laser energy densit

5.3.1 Thermal modelling

The thermal equilibrium equation satisfies the following classical 3D heat conduction equation given by Carslaw and Jaeger (1959),

$$\rho c \frac{\delta T}{\delta t} = \frac{\delta}{\delta x}\left(k \frac{\delta T}{\delta x}\right) + \frac{\delta}{\delta y}\left(k \frac{\delta T}{\delta y}\right) + \frac{\delta}{\delta z}\left(k \frac{\delta T}{\delta z}\right) + Q \tag{5.2}$$

Where ρ is the material density (Kg/m^3); c is the specific heat capacity (J/KgK); T is the temperature; t is the interaction time; k is thermal conductivity (W/mK); and $Q = (x, y, z, t)$ is the volumetric heat generation (W/m^3).

The effective thermal conductivity is a function of porosity of the powder (Dong et al. 2009). The porosity of the powder ϕ can be calculated as,

$$\phi = \frac{\rho_{bulk} - \rho_{powder}}{\rho_{bulk}} \tag{5.3}$$

Where ϕ is the porosity of the powder; ρ_{bulk} and ρ_{powder} are the densities of the bulk and powder materials. The porosity is assumed to vary from ϕ = 0.4 for powder state to ϕ = 0 at solid state after solidification. However, in reality its difficult to achieve full density.

The thermal conductivity of the powder can be expressed as (Thummler 1993),

$$k_{powder} = k_{bulk}(\,1 - \phi) \tag{5.4}$$

Where k_{powder} and k_{bulk} are thermal conductivities of powder and bulk materials.

The latent heat of fusion is simulated by an artificial increase in the liquid specific heat and the relationship between the enthalpy, *H,* density, *p*, and specific heat, *c* can be written as,

$$H = \int \rho c(T) dT \tag{5.5}$$

Fig. 5.2 shows the calculated temperature dependant thermal conductivity and enthalpy of the material up to the melting temperature. The sudden change of the thermal conductivity from low value calculated from eqn. (5.4) to higher value in the curve is due to transition of material from powder state to liquid state, in which case the corresponding bulk material properties is used (Mills and Kenneth 2002),

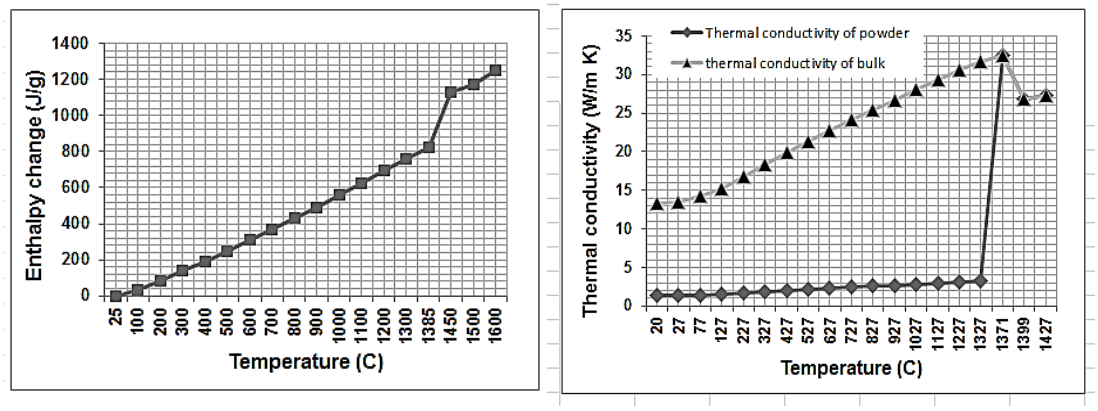

(a) (b)

Figure 5.2 (a) Enthalpy of 316L stainless steel as a function of temperature (b) Thermal conductivity of 316L stainless steel as a function of temperature

Boundary conditions:

The initial condition of uniform temperature distribution throughout the powder bed prior to laser melting at time *t* = 0 can be applied as,

$$T(x,y,z,0) = T_0(x,y,z) \tag{5.6}$$

T_o is the ambient temperature taken as 298 K (25^{0}C)

Laser axis direction at z = 0,

$$-k\left[\frac{\partial T}{\partial z}\right]_{z=0} = Q - h(T_0 - T_{surf}) \tag{5.7}$$

Where *h* is the heat transfer coefficient at the powder surface which is taken as ($10\ W/mK$); and T_{surf} is the temperature of the powder bed surface.

Since the layers are built on powder bed with large thickness (i.e., very thick single layers) exceeding the heat affected zone, the heat transfer at the bottom of loose powder can be assumed negligible.

$$\left[\frac{\partial T}{\partial z}\right]_{z=z_m} = 0 \ \ and \ \ T_{zm} = T_0 \tag{5.8}$$

5.3.2 Heat source modelling

The SLM process uses a fibre laser beam with circular spot profile. There are several beam profile approximations that exist in literature including square and triangular spot shapes. However, the most common laser beam profile that can resembles the actual spot profile in SLM is the Gaussian profile of energy distribution that was shown in Fig. 5.1 (b) and given by,

$$I = I_0 exp\left(-\frac{2r^2}{\omega^2}\right) \tag{5.9}$$

Where r is the radial distance from the beam centre; I_o is the intensity of the beam at $r = 0$; and ω is the radius of the beam at which $I = I_0 e^{-2}$.

This can be written as,

$$I(r) = \frac{2AP}{\pi\omega^2} \exp\left(-\frac{2r^2}{\omega^2}\right) \tag{5.10}$$

Where A is the absorptivity of the powder material which can be calculated if the reflectivity of the material λ is known. $A = 1 - \lambda$ (A reflectivity of iron = 0.7 was considered for 316L stainless steel).

5.3.3 Mechanical modelling

The same FE mesh used in thermal analysis is employed here, except for the element type and the boundary conditions. To calculate the distribution of stress, the elastic FEA simulation is used. Stress is related to strain by (Boresi 1993),

$$\{\sigma\} = [D]\{\varepsilon^e\} \tag{5.11}$$

Where $\{\sigma\}$ is the stress vector, [D] is the stiffness matrix and

$$\{\varepsilon^e\} = \{\varepsilon\} \times \{\varepsilon^{th}\} \tag{5.12}$$

Where $\{\varepsilon\}$ the total is strain vector and $\{\varepsilon^{th}\}$ is the thermal strain vector.

Equation (4.11) may be written as

$$\{\varepsilon\} = [D]^{\times 1}\{\sigma\} \times \{\varepsilon^{th}\} \tag{5.13}$$

For isotropic material, the above stress-strain relationship can be written in Cartesian co-ordinates as follows (Boresi 1993; Yilbas 2001),

$$\varepsilon_{xx} = \frac{1}{E}\left[\sigma_{xx} \times \nu\left(\sigma_{yy} + \sigma_{zz}\right)\right] + \alpha_e \Delta T$$

$$\varepsilon_{yy} = \frac{1}{E}\left[\sigma_{yy} \times \nu(\sigma_{xx} + \sigma_{zz})\right] + \alpha_e \Delta T$$

$$\varepsilon_{zz} = \frac{1}{E}\left[\sigma_{zz} \times \nu\left(\sigma_{xx} + \sigma_{yy}\right)\right] + \alpha_e \Delta T$$

$$\varepsilon_{xy} = \frac{1+\nu}{E}\sigma_{xy} \;\;,\;\; \varepsilon_{xz} = \frac{1+\nu}{E}\varepsilon_{xz} \;\;,\;\; \varepsilon_{yz} = \frac{1+\nu}{E}\varepsilon_{yz} \tag{5.14}$$

Where E, ν and α_e are the modulus of elasticity, Poison's ratio and coefficient of linear thermal expansion respectively. ΔT represents a temperature rise at a point (*x, y, z*) at time *t* with respect to that at $t = 0$ corresponding to stress-free condition.

A typical component of thermal strain from equation (5.11) can be found to be,

$$\varepsilon^{th} = \alpha_e \Delta T = \alpha(T + T_{ref}) \tag{5.15}$$

Where T_{ref} is the reference temperature at $t = 0$. α is a function of temperature and can be written *as*

$$\varepsilon^{th} = \int_{T_{ref}}^{T} \alpha(T)dT \tag{5.16}$$

The effective stress can be given as

$$\sigma_{eff} = \sqrt{\sigma_1{}^2 + \sigma_2{}^2 + \sigma_3{}^2} + 2\nu(\sigma_2\sigma_2 + \sigma_1\sigma_3 + \sigma_2\sigma_2) \tag{5.17}$$

Where σ_1, σ_2, and σ_3 are the three principal stresses. The equivalent stress or VonMises can be computed as,

$$\sigma_{eqv} = \sqrt{\frac{1}{2}[(\sigma_2 \times \sigma_2)^2 + (\sigma_2 \times \sigma_3)^2 + (\sigma_3 \times \sigma_1)^2]} \tag{5.18}$$

The equivalent stress is related to the equivalent strain by this relationship,

$$\sigma' = E\varepsilon' \tag{5.19}$$

For stress analysis, in addition to density ρ, the following thermo-structural material properties depending on temperature are required as listed in table 5.2: thermal expansion coefficient α, elastic modulus *E*, Poisson's ratio *v*, and yield strength σ_y.

Table 5.2 Temperature-dependant mechanical properties of 316L stainless steel (Deng et al. 2010)

Temperature (K)	298	473	673	873	973	1073	1573
Thermal expansion, α (1^0C^{-1} x 10^{-6})	14.3	15.6	16.9	17.7	18.5	19.1	19.5
Elastic modulus, *E* (GPa)	198.5	187	172	157	141	106	10
Poisson's ratio, *v*	0.3	0.3	0.3	0.3	0.3	0.3	0.3
Yield strength, σ_y (MPa)	282	217	161	153	108	50	5

5.4 Results and discussion

5.4.1 Temperature distribution

In SLM, the temperature distribution in the powder bed and consolidated layers changes rapidly with time and space. Fig.5.3 (a) shows the temperature at the beginning of the laser scanning, from which, the very high temperature gradients in the vicinity of the laser spot on the powder bed can be clearly seen due to an applied Gaussian heat source. The temperature of the powder particles is elevated rapidly under the action of absorbed energy, causing a molten pool when the temperature exceeds the melting temperature and heat affected zones in the surrounding loose powder. Note that the energy intensity of the source might also be high enough to cause the material to evaporate (Dong et al. 2009).

The highest predicted temperature corresponding to the molten zone of the powder material is 2600 K for [*P=100 W, V=100 mm/s*] and exceeds the melting temperature of 316L stainless steel (1672 K). However, this maximum temperature at the start of track 1 is reduced at the end of first track scan to 2392 K and so at the end of fifth track to 2225 K as shown in Fig.5.3 (b and c) respectively. The drop of maximum temperature can be attributed to the increased conductivity of the previously solidified regions of the track compared to the low thermal conductivity available initially in the powder bed. The thermal field changes as the laser source moves along the track and the melt pool moves along with the laser source.

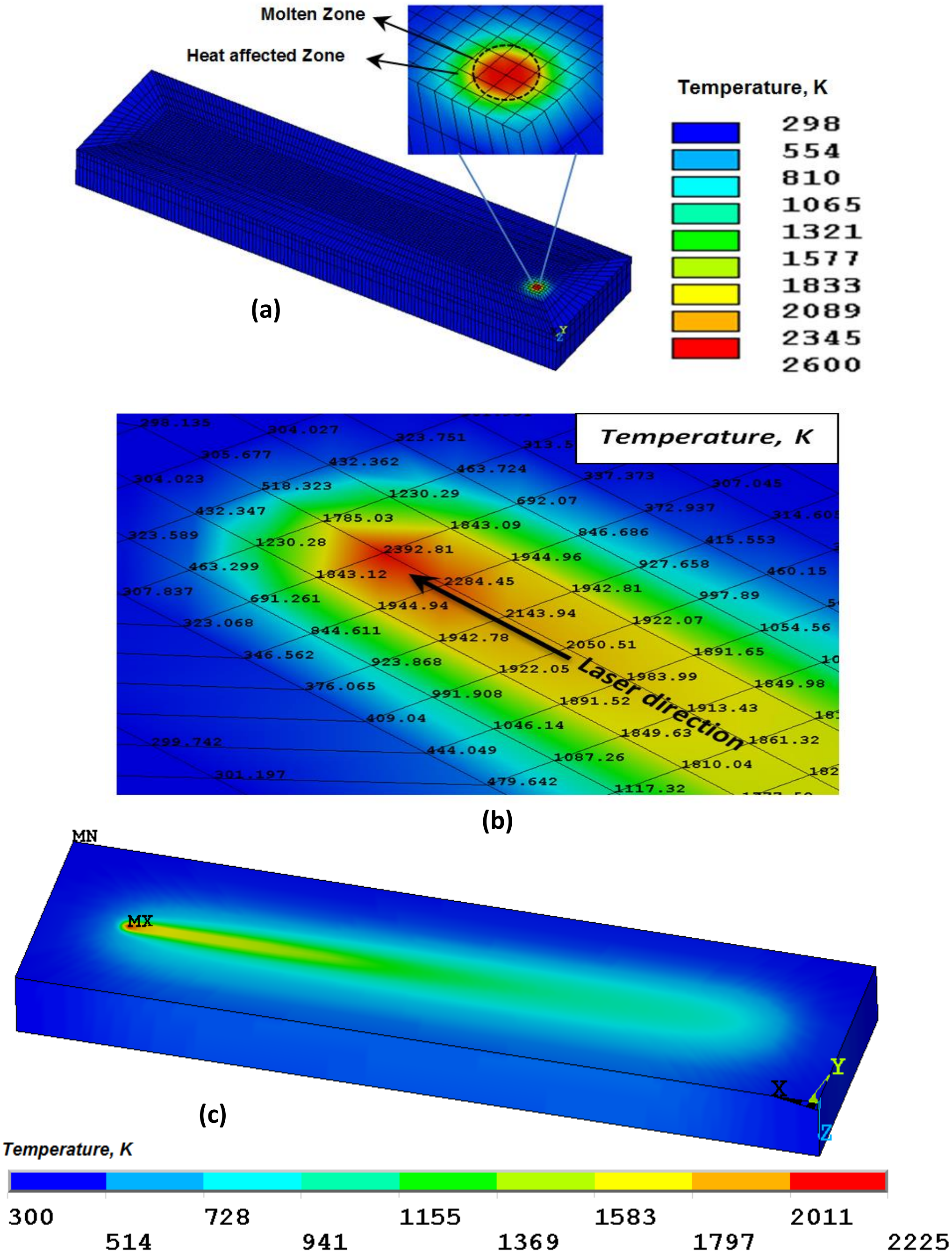

Figure 5.3 Transient temperature distribution during layer melting (a) at the beginning of the first track scan (b) at the end of the first track scan at time =0.091 seconds (c) at the end of the 5th track scan at time = 0.455 seconds

It is further observed that the temperature gradient in the front side of the moving laser beam is much steeper than that in the rear side. The melt pool shape resembles as in comet tail profile (see Fig. 5.3(c)). This trend of skewed temperature distribution towards the rear of the laser was also reported in other previous research on temperature simulations (Roberts et al. 2009; Shen et al. 2005). This can be attributed to the fact that the rapidly cooling molten material has greater conductive properties than the untreated powder in front of the laser.

The temperature distribution in the layer is very much affected by the energy density which is a function of laser power, spot size, scanning speed, hatch spacing and scanning strategy. Additionally, the temperature gradient in the layer is similarly influenced by conductivity of the material underneath the deposited layer being a loose powder bed, previously re-melted layer, support structure or a solid substrate. Fig. 5.4(a and b) shows temporal variation of temperature of single track deposited on powder bed and solid substrate respectively. For the powder bed, the melted layer thickness depends on the energy input from the laser, while for substrate a thin layer of 75 µm is deposited on solid material and then melted with the laser beam. A fast cooling rate can be observed when the track is built on a solid substrate. Because the solid bulk material has higher conductivity compared to powder bed allowing more heat sink through conduction in a shorter period of time and subsequent solidification to room temperature.

Fig. 5.5(a) further shows that the temperature of the scanned first track for powder bed and solid substrate decreases as the distance from the laser beam focus position is increased. The region directly under the laser beam is in the molten state, whereas the remaining portion of the track length experiences a rapid fall in temperature and undergoes solidification. The solidification begins when the temperature drops below the melting temperature of the material and approaches to room temperature. The temperature gradient is higher at the start of solidification and approaches minimum value at the end of solidification. The rapid cooling of tracks built on solid substrate result a more stable molten zone as well as heat affected zone at the vicinity of laser spot. The multiple reflections effect between the powder particles during the laser strike leads to higher optical penetration depths compared to bulk materials.

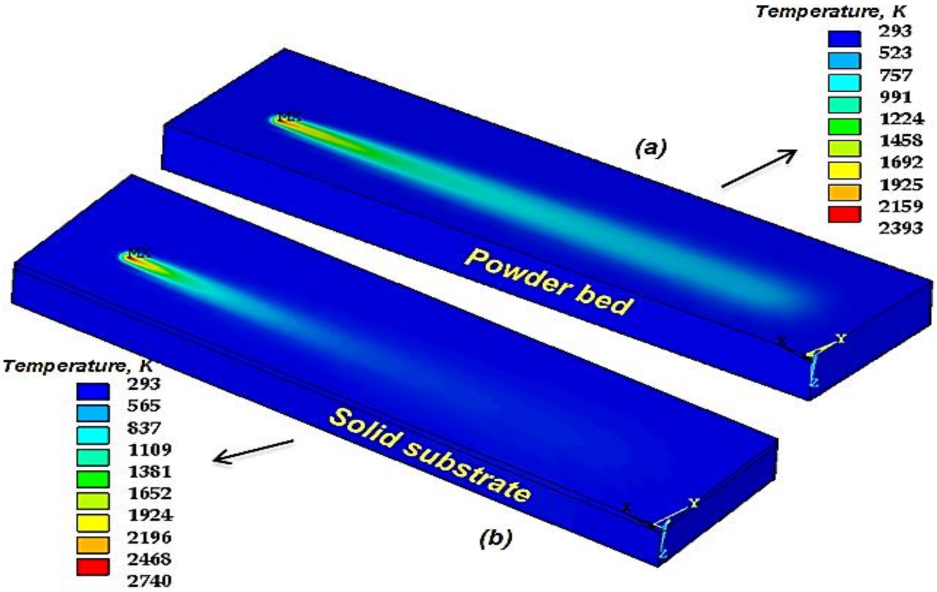

Figure 5.4 Comparison of temperature distribution after the 1st track scan (a) built on a powder bed (b) built on solid substrate

The various heating and cooling cycles taking place in various tracks which form the layer during laser scan are shown in Fig. 5.5 (b) and (c). The peak temperatures represent the start of each track forming the layer and are taken from neighbouring nodes in the Y-axis separated by a hatch spacing of 75 µm between the tracks. For track 1 the recorded temperature are taken from a node located at (X=1.225, Y=1.225, Z=0), track 2 at (X=1.225, Y=1.3, Z=0), tack 3 at (X=1.225, Y=1.375, Z=0), track 4 at (X=1.225, Y=1.45, Z=0), and track 5 at (X=1.225, Y=1.525, Z=0).

Due to overlap between subsequent tracks which depend on the hatch spacing distance, some sections are exposed to multiple scans and melted twice to bond adjacent tracks and form a fully dense layer. The temperature in half portion of the 1st track is raised above its melting temperature while scanning the 2nd track. However, as more tracks are deposited in 3rd and other subsequent tracks, the temperature falls to below the melting temperature of the material. The lower secondary peaks correspond to the laser scanning the same position on successive tracks. This is also exhibited in multi-layer build when upper layers are deposited and suggests that the addition of layers and subsequent scanning are of significance to the temperature field in the model (Roberts et al. 2009). The rate of overlap between track and layers influence the surface roughness, porosity, and mechanical properties of SLM fabricated parts (Guan et al. 2013).

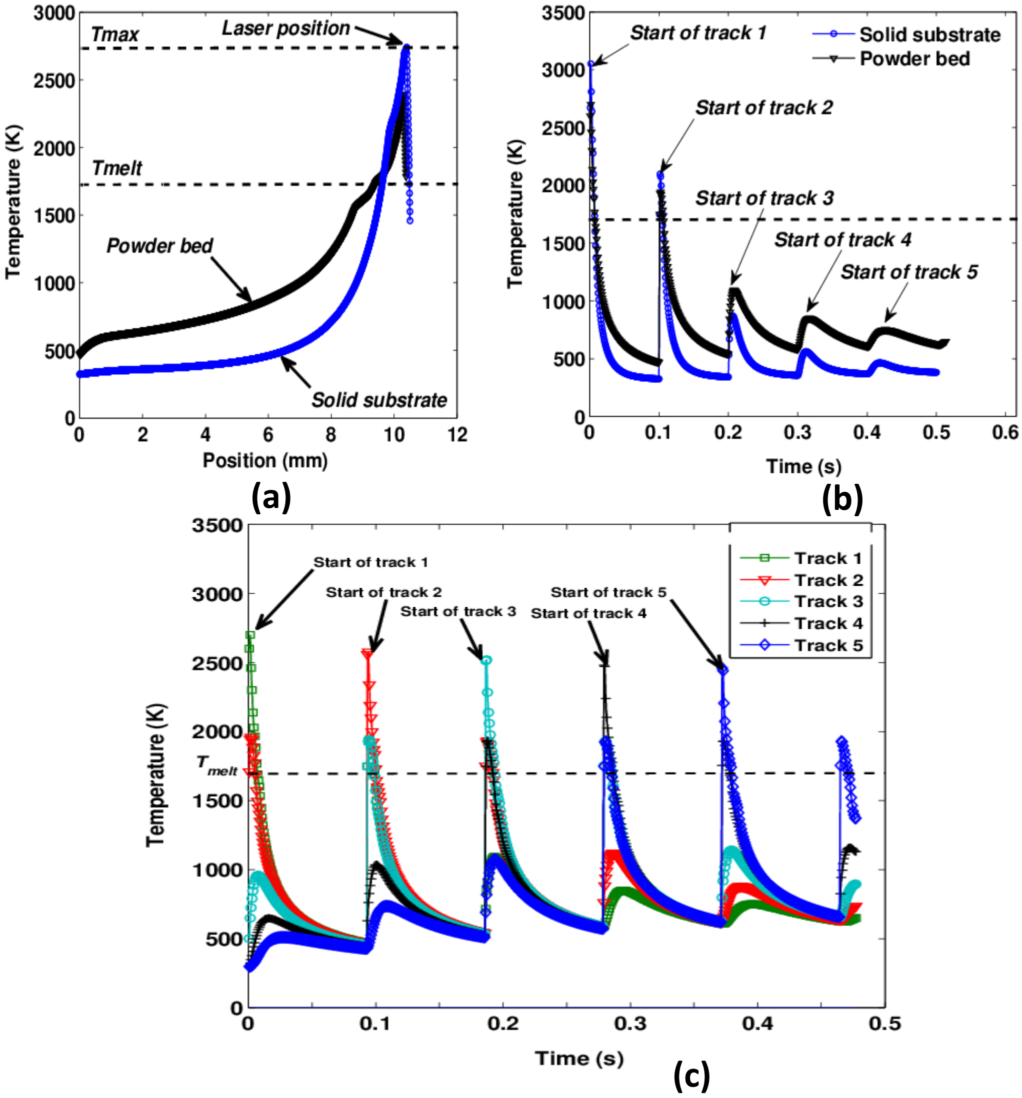

(a)

(b)

(c)

Figure 5.5 (a) Temperature distribution along the path of the 1st track (b) Cyclic melting/heating and cooling of the 1st track (c) Cyclic melting/heating and cooling of 5 subsequent tracks in the layer built on powder bed.

This cyclic melting/heating and cooling continues in all tracks forming the layer. The heating and subsequent cooling to the ambient (chamber) temperature occur within a few tenths of a millisecond of each other, thus suggesting that the irradiated spots are subjected to rapid thermal cycles. These rapid cycles are associated with commensurate thermal stress changes (Dai and Shaw 2002). Long track length of the laser beam highly influences the thermal gradients which occur within the layer, while shorter tracks tend to produce more homogeneous temperature gradients but with increased melting depth. As the vector length increases, the higher delay period between successive irradiation leads to a decrease in the amount of energy stored on the surface.

5.4.2 Melt pool dimensions

Fig 5.6 (a) illustrates the predicted melt pool temperature contours after scanning the 5th track of the layer. The melt pool size measurement was achieved through temperature distribution plots recorded at the instant when the laser had travelled along its path of scanning. The length represents the distance of the molten material along the X-axis and parallel to the scan direction while width is taken as the molten region along the Y-axis and perpendicular the scanning direction of the laser. The melted depth is measured from the powder surface to the molten depth inside the powder bed along the Z-axis. Fig. 5.6 (b and c) shows the width and depth profiles of the melt pool for scanning speeds of 100 mm/s, 200 mm/s, and 300 mm/s with a fixed laser power of 100 W. With liquidus line imposed onto the plots, which represent regions above the melting temperature of 316 L stainless steel; the melt pool dimensions are identified.

The amount of liquid formation depends on the operating temperature of the sintering system, which is controlled by two main parameters, i.e., laser power and scan speed, during a single line scanning (Gu et al. 2009). As shown in Fig 5.6 (d) the length of the melt pool increases with increasing the scanning speed while both width and depth of the melt pool decreases. At higher scanning speeds (200 - 300 mm/s), there is no sufficient time for melted track to cool down and solidify and longer region remain in a molten state. According to Simchi and Pohl (2004) , the applied scan speed has a significant influence on the capillary instability of the liquid track. As a result, pores or regions of non-melted powder forms between layers (Brandl et al. 2012). Previous experimental results reveal that at lower scan speeds of 0.05 m/s a continuous sintered track was formed via the sufficient junction of inter-agglomerate sintering necks, showing no apparent balling effect while with increasing scan speed to 0.07 m/s, the surface of laser sintered track was considerably rough, although the sintered track retained uninterrupted (Gu et al. 2009).

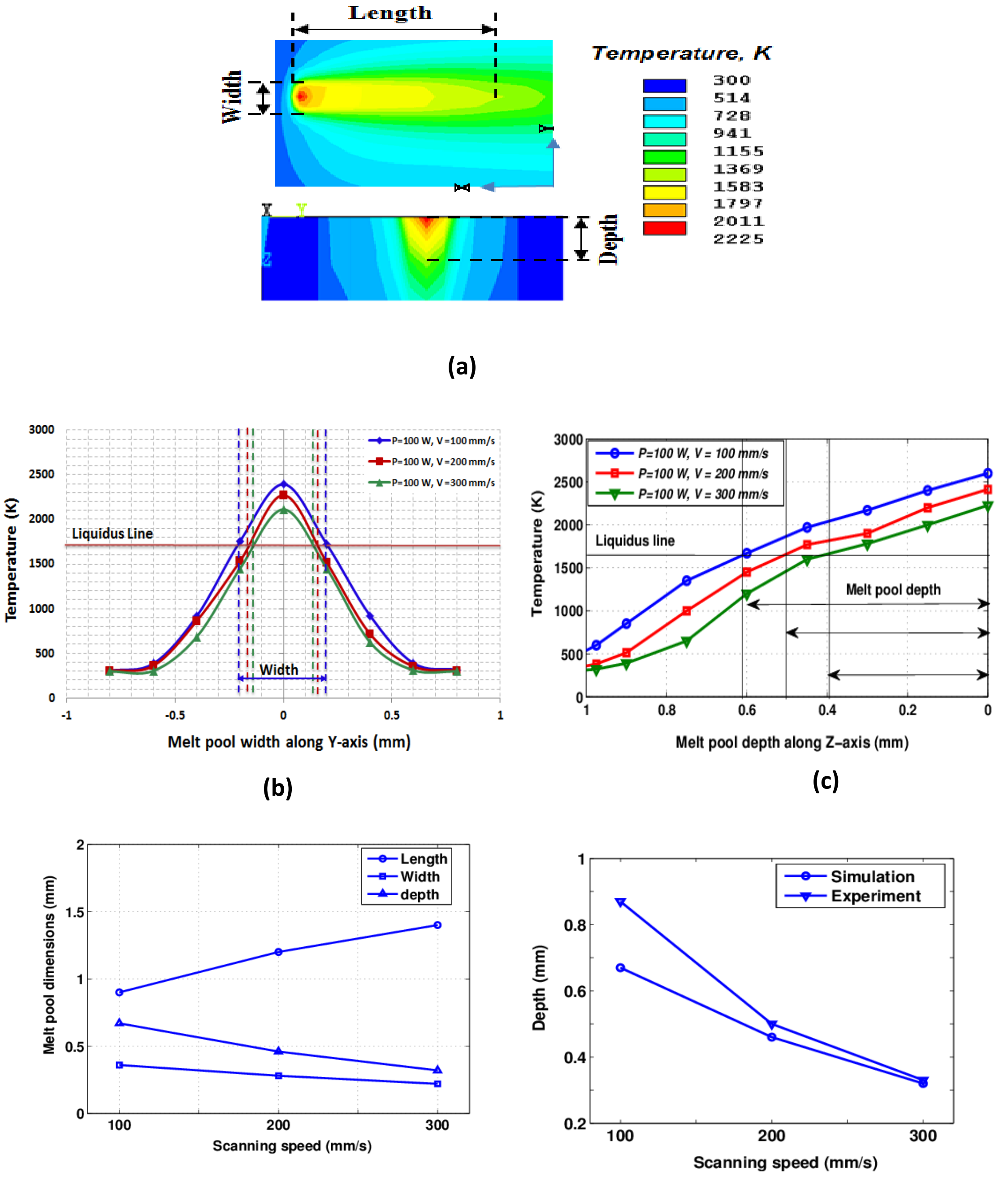

(a)

(b)

(c)

(d)

(e)

Figure 5.6 (a) predicted melt pool temperature contours after scanning the 5th track (b) Melt pool width of various scanning speeds (c) Melt pool depth of various scanning speeds (d) comparison of the predicted melt pool dimensions as function of scanning speed (e) Comparison of the melting depth of simulation and experiment

The predicted length of the melt pool varies from 1.4 mm at 300 mm/s to 0.9 mm at 100 mm/s, whilst the width varies from 0.22 mm to 0.38 mm and depth from 0.4 mm to 0.63 mm respectively. To verify the model, the depth of melting of the simulation is compared to the thickness of the experimentally produced layers using the same processing parameters as displayed in Fig.5.6 (e). There is very close agreement between predicted depth of melting and measured thickness for higher scan speeds (200 mm/s and 300 mm/s), but the variation is more pronounced for 100 mm/s scanning speed. The discrepancy between the theoretical and experimental readings of the melted depth at low scan speed can be contributed due to the longer interaction time of the laser with the powder material which results a higher melting depth increasing both the molten and heat affected zones. This causes partial melting of surrounding powders that is bonded to the melted tracks and increase its thickness and mass. Other melt flow mechanisms driven by the surface tension forces during SLM are not taken into account by the FEA model.

For a given scan speed, the maximum temperature decreases with lowering the laser power, resulting in a smaller amount of liquid formation. The viscosity of the liquid–solid mixture, thus, becomes considerably high, handicapping liquid flow and particle rearrangement (Gu et al. 2009). This in turn decreases the overall rheological performance of the liquid in conjunction with solid particles (Agarwala 1995). On the other hand, a low laser power results in a limited undercooling degree of the melt (Gu et al. 2008; Boccalini et al.2001; Simchi 2004).

5.4.3 Thermal stress analysis

The distributions of residual stresses within single track obtained by FEA model is depicted in Fig. 5.7 (a). It can be seen that there is a strong variation in the level of residual stresses inside the deposited track dependent on the temperature gradients. Peak VonMises stress of (605 MPa) is found at the start of the track and declines towards the molten zone. Von Mises stress reduces when temperature becomes high because of the elastic modulus, which reduces with increase in the temperature. Consequently, VonMises stress attains high values in the region, which is initially heated (i.e. solidified). The VonMises stresses drop after scanning the 2nd track to (551 MPa) and so on 5th track to (492 MPa), because the previous track is re-heated due to track overlap and residual stresses are released as shown in Fig. 5.7(b).

Noticeably peak von-mises stress values were observed on the top surface of part, but this changed after scanning the 3rd track and subsequent tracks where peaks were found in areas at the bottom surface of the scanned layer.

This can be contributed to the higher cooling rates and solidification at the bottom side of the layer through conduction in the powder compared to the upper surface resulting higher residual stresses at the bottom surface. It is expected that the stress in the molten zone is tensile and it will transform to compressive stress as the distance from molten zone increases. According to the equilibrium of force and momentum of the part, the irradiated zone will become surrounded by a zone of compressive stress. Other studies Matsumoto et al., (2002) are on agreement that tensile stresses are developed at vicinity of the laser spot while compressive stresses are more towards the edges.

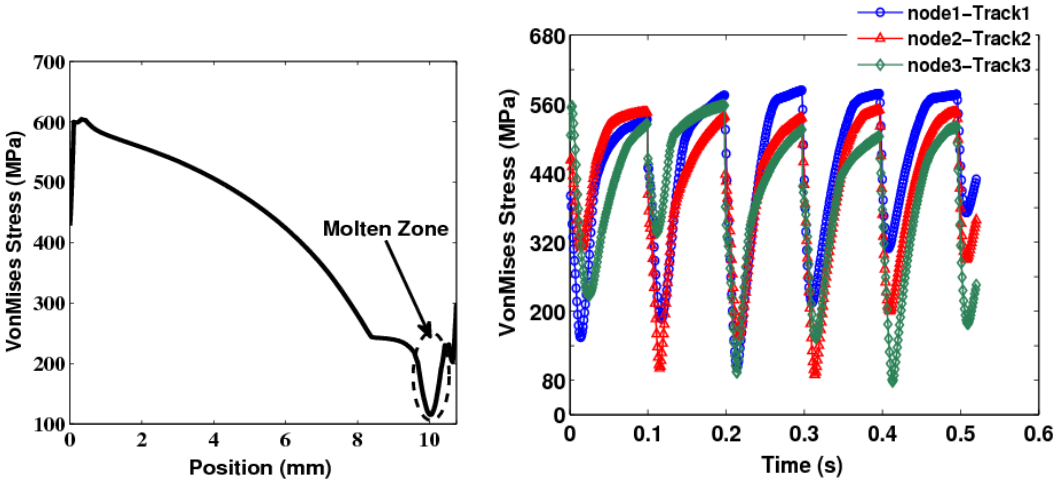

(a) **(b)**

Figure 5.7 (a) VonMises stress profile of the 1st track along X-axis (b) VonMises stress of three different tracks in layer

To further understand the stress variation and history in X, Y, and Z directions, two different nodes (node 1 located at the start of the 1st track, and node 2 located at the start of the 5th track of the layer were investigated (see Fig.5.8). As indicated in Fig. 5.8(a), the X-directional stress of node 1 is cyclic compressive-tensile-compressive stresses; tensile stresses are developed during the laser melting and turned into compressive during cooling cycle (solidification). However, as the heating source moves away, the parts cools down and the node remains compressive throughout. The X-directional stress of node 2 is tensile most of the time and occasionally compressive. Similar trend were also found in Y and Z directional stresses of the nodes as presented in Fig. 5.8 (b) and (c). The highest stress was found in X-component along the direction of laser scan of node 1 and reached (612 MPa), whereas the Y and Z components of the stress reach (172 MPa) and (162 MPa) respectively.

The high stress value in node 1 arises from the fact that it experiences an early heating and cooling cycles and thus causes higher temperature gradients and related thermal stresses. The temperature gradients are higher at the beginning of the layer during laser processing due to the lower temperature of the surrounding powder, and therefore have large effect on the distribution and intensity of residual stresses. The first melted layer shrinks during cooling cycle, but as more layers are deposited, the already solidified layers constrains and prevents further shrinking in the top layer. Since this mechanism occurs for each layer at each step of the SLM process, residual stresses may develop inside the manufactured component. For this reason, SLM parts are stress relieved through heat treated process prior to other finishing operations such as the removal of the part from the solid substrate or supporting structures. Otherwise, the residual stresses will cause part deflection due to stress relaxation. The FEA model did not consider these heat treatment effects.

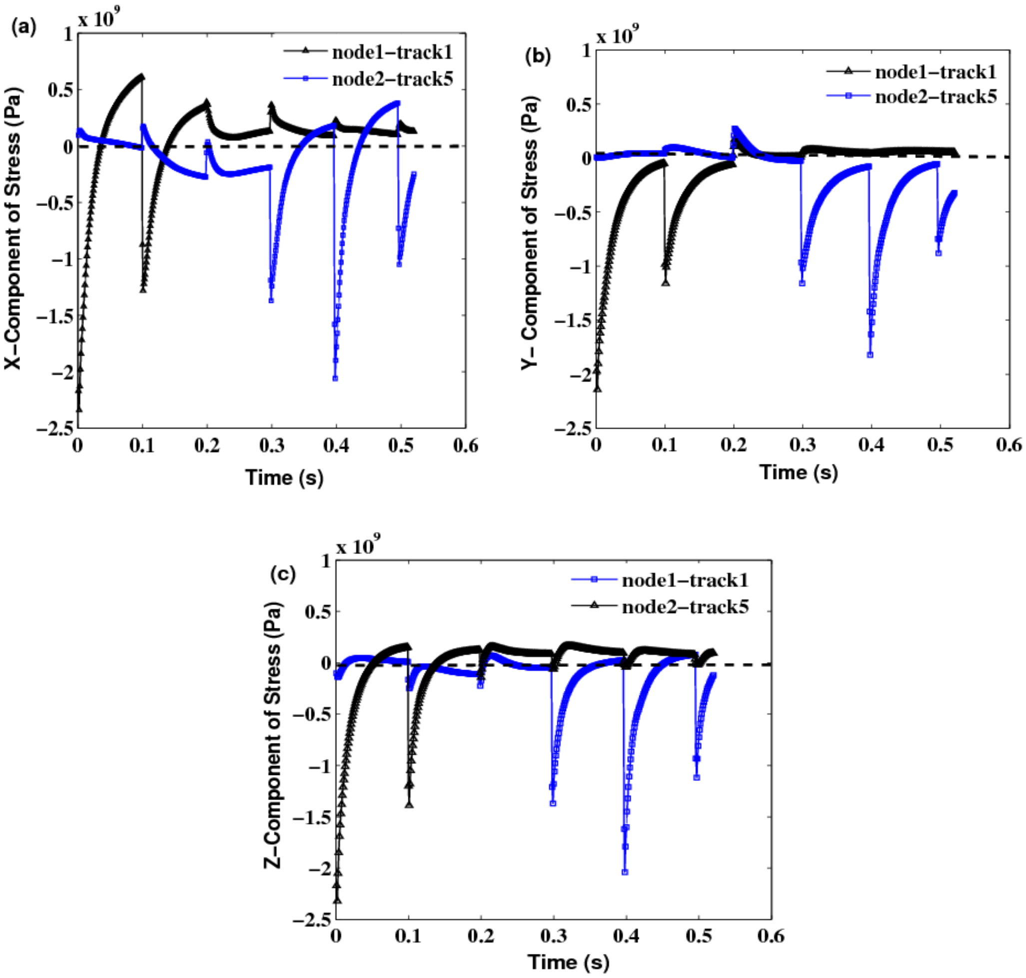

Figure 5.8 Residual stress distributions (a) *X*-component of stress along the scan direction (b) *Y*- component of stress and transversal to the scan direction, (c) *Z*-component of stress through the thickness of the layer

For layers freely built on the powder bed, there is no underlying solid material to constrain the thermal stresses observed in the FEA model. The material expansion (i.e. tensile stresses) during heating cycle and material contractions during cooling (i.e. compressive stresses) cause shrinkages and cracks to the layer. After the laser beam leaves that area, the irradiated zone will cool and tends to shrink. The shrinkage is partially inhibited as a consequence of the plastic deformation developed during heating, yielding a residual tensile stress condition at the irradiated zone. The high tensile stresses generated in the high *x*-direction (along the laser scanning direction) may also lead to transverse cracking of the layer. Cracking can be avoided by preheating or by using shorter scanning tracks which reduce the cooling rate. The mechanism that prevents cracking by preheating increases the ductility of the material and enhances the possibility of stress relief by plastic deformation.

Simulation results reveal the magnitude of the temperature and stress in different locations of the layer and this provides insight on the regions requiring more support structures so that the design aspects of reliable structures can be implemented to withstand residual stress forces and dissipate heat during part building in SLM.

5.5 Conclusion

Three dimensional transient finite element model was developed for predicting the temperature and stress fields within a single metallic layer formed on the bed without support in SLM process. The results generated from simulation model can be summarized in the following points.

- Highest temperature gradient was recorded at the start of first track scan and drops subsequently for all scanning speeds.
- High cooling rates were predicted when the layer is scanned over a solid substrate compared to when layer is scanned on loose powder bed.
- The predicted length of the melt pool increases at higher scan speeds while both width and depth of the melt pool decreases.
- High von mises stresses was predicted in the scanned layer caused by the stepwise increase and decrease in the temperature with each successive overlapping laser tracks which leads to alternating compressive and tensile residual stresses within the layer.

- Cracks usually found in experimental overhang layers not only initiate in areas of compressive stress, but if tensile stress is present which occur if compressive yield stress for the material is exceeded. Such cracks were found in the experimental single layer parts presented in chapter 4.

Part Three:

Design, Manufacturing, and Evaluation of the Mechanical Behaviour of TPMS Cellular Structures

CHAPTER 6

Design and Generation of Triply Periodic Minimal Surface Cellular Structures

---

6.1 Introduction

This chapter describes the design of cellular structure and the procedure of generating cellular structures from a solid CAD model using Simpleware $^+$CAD software. It introduces the various cell topologies of Triply Periodic Minimal Surface (TPMS) cellular structures used in this research. It also explains the characteristics of TPMS cellular structures that make them potential for SLM/DMLS manufacture. It described an efficient method for generating image volumes representing the implicit functions so that both volume and surface meshes can be constructed.

6.2 Triply-Periodic Minimal Surfaces

Minimal surfaces are defined within the language of differential geometry as surfaces of zero mean curvature i.e. the sum of the principal curvatures at each point is zero. This means they are equally convex and concave at all points and their form is therefore saddle–like, or hyperbolic. They are called minimal because given a fixed boundary curve the area of a "minimal surface" which is minimal with respect to other surfaces with the same boundary. Particularly fascinating are minimal surfaces that have a crystalline structure, in the sense of repeating themselves in three dimensions, in other words being triply periodic. Three–periodic minimal surfaces have three lattice vectors, i.e., they are invariant under translation along three independent directions. They are also called triply–periodic minimal surfaces (TPMS).

The first TPMS to be discovered and investigated was reported by Schwarz (1890). He considered a soap-film across a quadrilateral frame, the edges of which are four of the six edges of a regular tetrahedron and realised that such a surface could be smoothly continued by joining the pieces edge to edge, the edges becoming two-fold axes of symmetry of the resulting infinite object. The surface is known as the D surface because its labyrinth graphs are 4-connected 'diamond' networks Schwarz was able to obtain an analytic expression for the D surface, and also for the Primitive P surface, whose labyrinth graphs are networks consisting of the vertices and edges of a primitive cubic lattice. His student Neovius discovered Neoviu's surface C(P), the 'complement' of P, because P and C(P) have the same symmetry group.

The next development in TPMS did not take place until the 1970 when A. H. Schoen (1970) investigated for NASA whether surfaces of this type might be of use as space structures and found more than a dozen new examples. Those surfaces with cubic symmetry are called “Schoen Gyroid - G surface'. Fig. 6.1 shows one cubical unit cell of four TPMS.

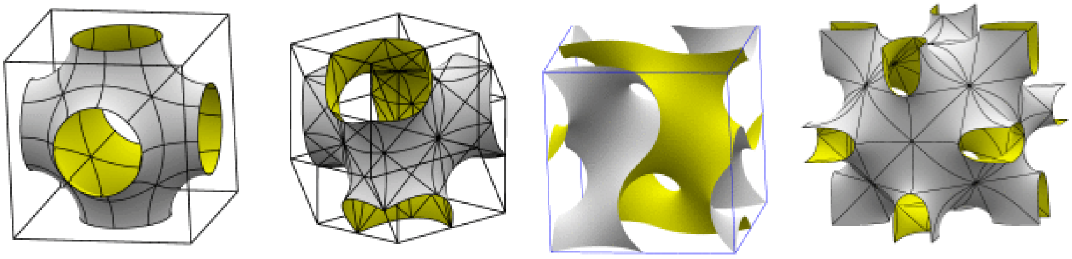

Schwarz Primitive P-Surface   ***Schwarz Diamond D-Surface***   ***Schoen Gyroid G-Surface***   ***Neovius' C(P)-Surface***

Figure 6.1 Triply periodic minimal surfaces [courtesy: susqu.edu]

6.3 The potential of TPMS for SLM/DMLS Manufacture

As a result of the layered build-up, the metal AM allows the manufacturing of components with hollows and undercuts. The designer gets a huge degree of freedom concerning the part geometry without being limited by restrictions of conventional manufacturing methods. SLM and DMLS are particularly well-suited to fabricating computationally generated periodic structures and have allowed for the recent development and manufacturing of more advanced open periodic cellular structure with controlled porosity using metallic powders.

The TPMS which have an infinitely connected triply periodic non-self-intersecting minimal surface with triple junctions and which contains no straight lines on the surface are believed to be suitable for metal AM. These cellular structures such as Schwarz diamond and Schoen gyroid surfaces are continuously curved geometries and self-supporting is deemed to be a suitable and fit for SLM/DMLS manufacture. These periodic cellular structures could be considered a potential for lightweight and support structure applications. For these reasons, the remaining chapters of this thesis will be focusing on the manufacturing, evaluation and the use of these advanced TPMS cellular structures in SLM/DMLS processes.

Triply-periodic minimal surfaces are shown to be a more versatile source of biomorphic scaffold designs than currently reported in the tissue engineering literature. Scaffold architecture with sheet-like morphology based on minimal surfaces is discussed, with significant structural and mechanical advantages over conventional designs. In reconstructive medicine, synthetic porous materials with custom-designed microstructure are used as scaffolds for tissue regeneration, in particular of bone. The designer of such a structure has to overcome several simultaneous challenges, including biocompatibility and biodegradability, constraints imposed by production technology and by the requirement that living cells can adhere to and differentiate on the scaffold interface. The scaffold also needs to provide mechanical and transport properties which enable and promote the regeneration process, properties which depend to a large extent on morphology.

With the advent of rapid prototyping technology however, such as SLM and DMLS, the use of custom-designed complex microstructures for tissue engineering has become a feasible alternative. The informed choice of an optimally adapted scaffold design relies essentially on an in-depth knowledge of structure property relationships. Structures derived from minimal surfaces and other related surfaces were conceived as lightweight construction materials as early as the 1970s and have recently been found to optimize competing properties such as stiffness of the solid framework and transport in the complementary phase. The high-precision fabrication of scaffolds based on the main advantage of minimal surface scaffolds is the open cell structure, deemed to facilitate cell migration and vitalization, while retaining a high degree of structural stiffness. The occurrence of minimal surface geometries in in-vivo biological tissue, such as in beetle shells, weevils, butterfly wing scales and crustacean skeletons, further hints at their usefulness as biomimetic scaffold designs.

A large number of TPMS are known and the most isotropic have cubic symmetry and can be built by periodic repetition of a cubic translational. In this study, several types of bi-continuous triply periodic minimal surfaces (TPMS) is considered, each of which can be realized as two different types of scaffold architectures or topology. Bi-continuous TPMS are smooth infinite surfaces that partition space into two intertwined labyrinthine domains and that are periodic in three distinct lattices. By contrast, minimal surface sheet solids are porous solids obtained by inflating the mathematical minimal surfaces to finite, spatially homogeneous thickness until a solid volume fraction is reached, see Fig. 6.2. The solid domain separates two network-like void domains which are infinite and intertwined, but not interconnected.

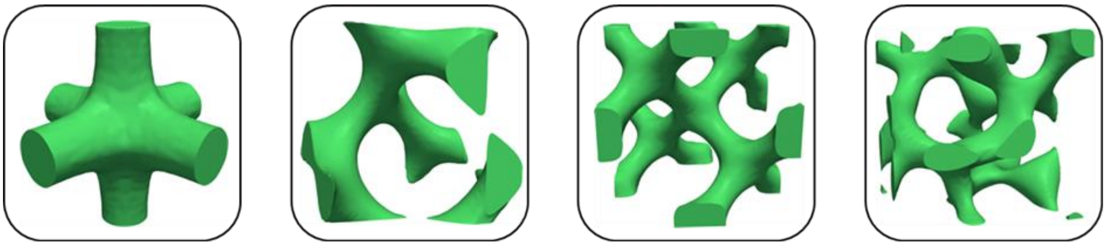

Schwartz primitive Schoen gyroid Schwartz diamond Neovius' surface

Figure 6.2 – TPMS cellular structures with 15% volume fraction

6.4 Computer Modelling of TPMS Cellular Structures

6.4.1 Surface Representations

When dealing with solid 3D objects it is often convenient to only model the object's boundaries using a mathematical representation of the surfaces. The choice of surface representation is particularly important for the computational modelling of 3D objects as each has its own advantages and disadvantages. These include the availability and complexity of operations that can be used to manipulate the surface (e.g. smoothing, Boolean operations) as well as the efficiency of the representation. Each representation also has an impact on how models are visualised and ultimately realised (e.g. via SLM/DMLS). The most common representations can be classified as one of the following forms: explicit, parametric or implicit.

In explicit surface representations points which lie exactly on the surface are explicitly stored. The most common type of explicit surface is a mesh of polygons; typically these are triangles or quadrilaterals although others can be used. These polygons are often stored as an order list of vertex indices – the order being used to define the direction the polygon is facing (i.e. the surface normal). Unlike explicit surfaces, parametric surfaces do not store points on a surface. Instead, points on a parametric surface are expressed as a function of the parametric variables *(u,v)*, which can be generalised to lie on the unit square [0,1] × [0,1]. Non-Uniform Rational B-Spline (NURBS) surfaces are a form of parametric surface commonly used in CAD packages due to their compact representation, smooth surfaces and easy of manipulation. Other forms of parametric surfaces exist, such as Rational Gaussian (RaG) surfaces and Fourier Shape Descriptions.

Implicit surfaces are defined as an iso-surface of some function *f*. In 3D the surface is defined by a set of points $p \in \mathbb{R}^3$ satisfying the equality:

$$f(x, y, z) = 0 \tag{6.1}$$

Where $f\colon \mathbb{R}^{3}\mathbb{R}$

As with parametric forms, implicit surfaces provide a compact representation for potentially complex surfaces. They also offer a number of advantages, notably their flexibility (as will be demonstrated later in this work) and well-defined Boolean operations. However, unlike parametric forms they offer little local shape control and manipulating them can be unintuitive. The implicit formulation of a unit sphere is given below:

$$f(x, y, z) = x^2 + y^2 + z^2 - 1 \tag{6.2}$$

In this instance the implicit form is not only more compact, but potentially more useful as the sign of the function can be used to designate points as either inside or outside the surface. For this purpose the following convention is adopted:

Table 6.1 - Implicit surface in/out convention

Condition	Interpretation
$f(x, y, z) = 0$	On surface
$f(x, y, z) < 0$	Inside
$f(x, y, z) > 0$	Outside

The implicit functions of interest to this work are the set of infinitely periodic surfaces. The most notable of which are those discovered by Schoen (Gyroid) and Schwarz (Diamond). In addition to being infinitely periodic these surfaces are also approximations of minimal surfaces, tha3t is, the surfaces have a mean curvature of zero. Using a combination of trigonometric functions in the form given in Eq. (6.3) a number of periodic surfaces can be generated,

$$\sum_{i=1}^{3} \prod_{j=1}^{n} cos(x_i) + k = 0 \tag{6.3}$$

The simplest triply periodic (or dual periodic in 2D) function in this form is the Schwarz Primitive; $cos(x) + cos(y) + cos(z) + 1 = 0$ (6.4)

6.4.2 Mesh Generation

Accurate and robust mesh generation is an important step towards the fabrication of cellular structures. The work presented in this section looks at methods for generating image volumes representing the implicit functions so that both volume and surface meshes can be constructed. An entirely image-based approach is taken to exploit the advantages of image-based meshing. Methods previously used in relied upon the generation of a floating-point volume which was then iso-surfaced. While this method is straight-forward, simply requiring that the function be sampled at regular intervals, it becomes difficult to generate a volume mesh and integrate with other image data.

To overcome these difficulties we require that the generated volumes' data-type matches that used by +ScanFE from Simpleware Ltd. In the C programming language this is unsigned char, an 8 bit integer. By using this data-type the generated volumes can easily be combined with data from other sources, such as medical imaging devices and meshed with $^{+}$ScanFE. The most straight-forward translation to image-space that can be made from an implicit function is the generation of a binary volume. By evaluating the function, *f*, over a range of values voxels can be determined to be either inside or outside and their value set accordingly.

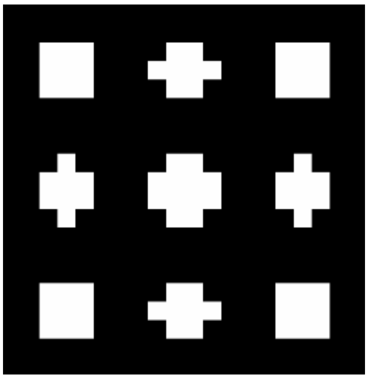

Figure 6.3 Binary slice representing the Schwarz Primitive using 20 × 20 px

Despite being efficient to generate, the binary representation yields a poor reconstruction, as can be seen in Fig. 6.3. The reconstructed surface can be improved by introducing greyscale values into the volume. This can be achieved using a smoothing algorithm such as Gaussian smoothing, however these algorithms can have adverse effects such as shrinking the volume and removing small features. A more appropriate solution is to generate the volume with greyscale values such that they result in the reconstructed surface being placed as close as possible to the 'ideal' surface. The marching cubes algorithm will be used to generate a triangulated surface, as such, the volume can be generated so as to best utilise the greyscale values. As the position of the reconstructed surface is only dependent on the two voxels either side of it, a small region of greyscale values should be placed either side of the ideal surface. These greyscale values should reflect their distance to the surface, mimicking the partial volume effect. Voxels further from the surface may simply be marked as inside or outside. However, unlike many implicit functions used in computer graphics, the functions of interest are not distance functions. That is, their value does not reflect a linear measure of distance from the surface. To overcome this a point is chosen, from the discretising volume, that is close to the ideal surface (i.e. such that $f(x,y,z) \approx 0$). The gradient at this point is then computed, allowing the greyscale values to be set such that their values reflect their distance from the surface. Values inside of the surface may be calculated as follows:

$$V_{inside} = \frac{|f(x,y,z)|}{G_p} \tag{6.5}$$

where Gp is the gradient near the surface.

Figure 6.4 (a) shows an example from a volume generated using this method. The reconstructed surface is shown in Fig. 6.4 (b).

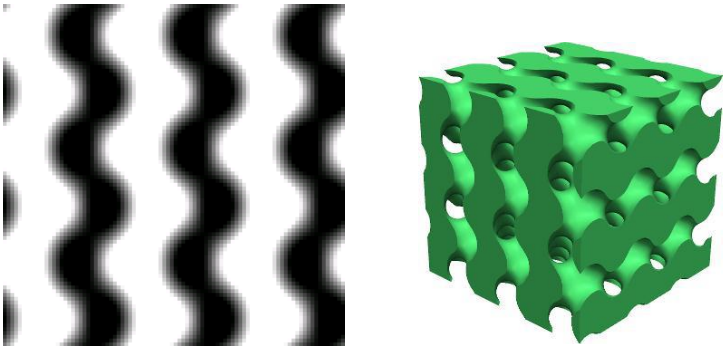

Figure 6.4 (a) Greyscale slice representing the Schoen gyroid (b) Reconstructed surface of the Schoen Gyroid

6.5 Simpleware software

6.5.1 Overview

Simpleware is a spin-off company from the University of Exeter. Simpleware provides the world-leading software solution for the conversion of 3D images into CAD, STL (for AM processes) and Finite Element models. Simpleware offers three software options for processing and meshing 3D image data. The software is based on a core image processing platform, ScanIP, with optional bolt-on modules for mesh generation and CAD integration. The relationship between these products is shown in Fig. 6.5.

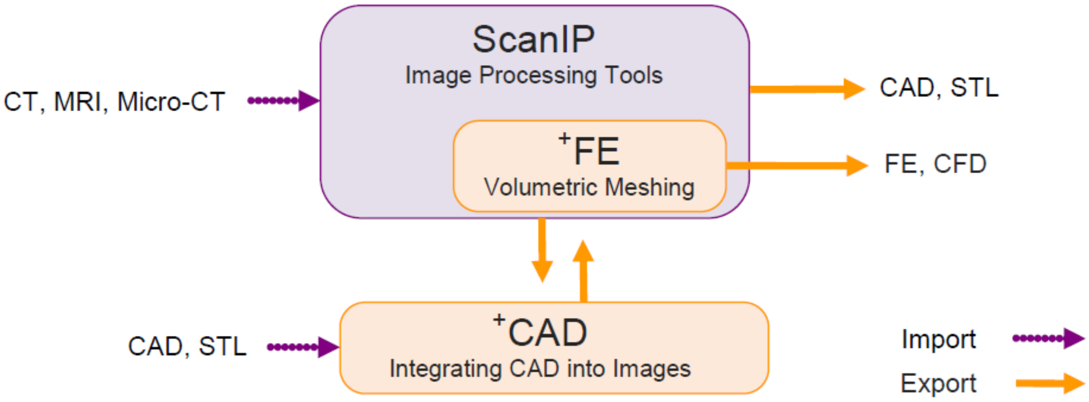

Figure 6.5 Simpleware software products (Simpleware Ltd.)

6.5.2 Generating cellular structure in $^+$CAD

The $^+$CAD Internal structure wizard can be used to create lattice structures inside a STL model. Fig. 6.6 shows the steps involved in creating cellular structure. The solid model can be imported in STL format or designed in the Scan CAD software using the geometry creation feature. Only basic geometries (cube, cylinder, sphere, cone etc.) can be designed in the software. Once a solid geometry is created/imported the preferred cell type, cell size and % volume fraction can be selected.

6.5.2.1 Cell size

Table 6.2 depicts various types of cell sizes available in the Simpleware $^+$CAD software. A unit cell size is referred to the smallest single cell which forms the periodic structure in 3 dimensions. Depending on the cell type, a single unit cell may contain 4 or more struts or beams that meet at a junction node.

6.5.2.2 Volume fraction

The volume fraction defines the relative solid volume that is inside the generated structure. The higher the volume fraction is, the denser the structure will be. The lower the volume fraction is, the more open the structure will be. If the value of volume fraction is very low, it may result in loss of connectivity between adjacent cells in the structure; very high values may result in a closed volume. The volume fraction, Vf can be described as,

$$Vf = \frac{V_{struts}}{V_{solid}} \tag{6.6}$$

where V_{strut} is the volume of the solid struts forming the cellular structure and V_{solid} is the volume of solid.

The porosity is related to volume fraction as,

$$P = 1 - Vf \tag{6.7}$$

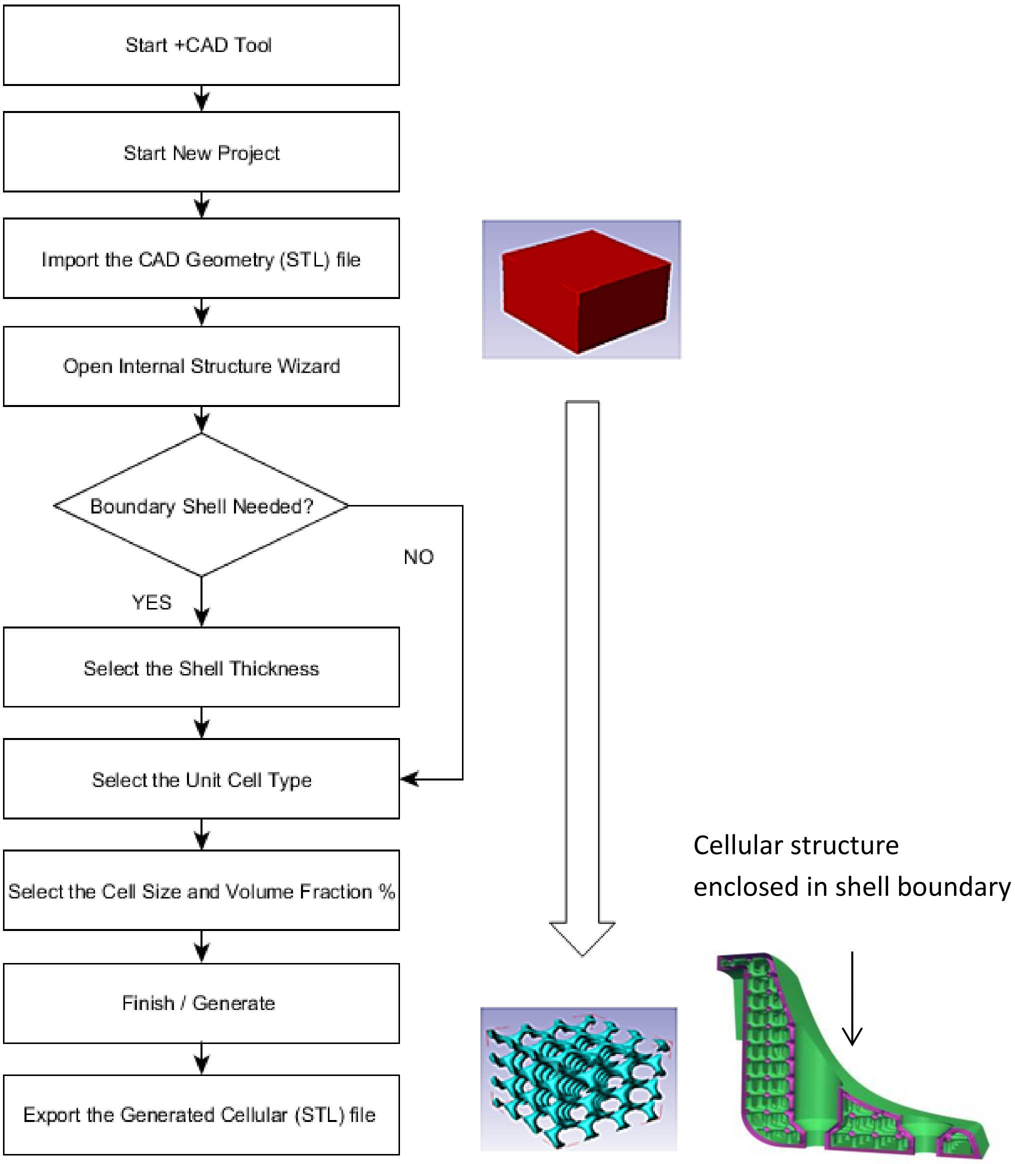

Figure 6.6 Steps involved in generating cellular structure in $^{+}$*CAD*

Table 6.2 - Different cell types in Simpleware $^{+}$CAD software

A single cell	3x3x3 cells	Name of the cell type
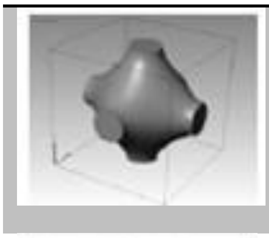	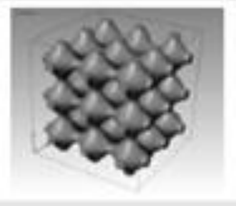	Schwarz Primitive
		Schwarz Diamond
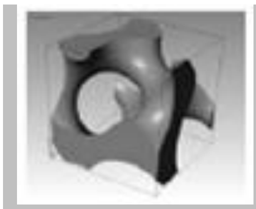		Schoen Gyroid
	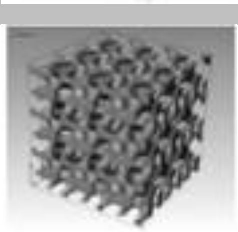	Neovius' Surface
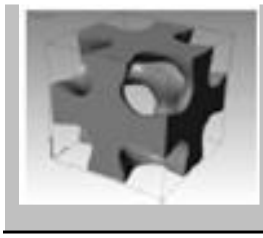	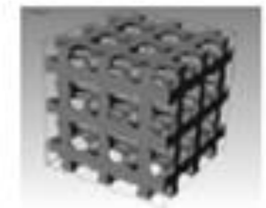	Schwarz 'W'

6.6 Conclusion

This chapter has presented the design and generation tool for advanced cellular structures which will be used in the remaining chapters of this thesis. Introduction was given on the topological design of triply periodic minimal surfaces (TPMS) including Schwarz P, Schwarz Diamond, Neovius', and Schoen Gyroid surfaces. The major difference between TPMS cellular structure and traditional designed cellular structures for metal AM was highlighted. The suitability of TPMS for SLM/DMLS manufacture and their potential for lightweight and support structure applications was highlighted. The need for an efficient method of generating cellular structures and the implementation of these methods in Simpleware software was explained.

It was illustrated how these design tools can provide effective approach to modify or optimise the cellular structures for the uses in the SLM/DMLS process. The steps involved in creating cellular structures from solid STL model using Simpleware $^{+}$CAD software was described.

The TPMS cellular structure presented here and used throughout this research are primarily selected for their good manufacturability in SLM process and not necessarily are optimized for mechanical properties.

The following chapters of the thesis will present a comprehensive evaluation on the manufacturing and mechanical properties of these advanced TPMS cellular structures as well as their use in support structure applications in SLM/DMLS processes using a range of metal powders.

CHAPTER 7

Manufacturability Study of TPMS Cellular Structures in SLM and DMLS Processes

7.1 Introduction

In the introduction and also in chapter 6, it was stressed that one of the potential area in which the largest gain in metal AM can be attained is through the use of lightweight cellular structures which require less build time, material and energy during processing while also offering enhanced functional performance. The development of advanced TPMS cellular structures suitable for metal AM from high performance light alloys is expected to widen the use of these processes for many new applications.

The aim of this chapter is to experimentally investigate and characterise these cellular structures using different metal powders. The purpose of the experiments is to evaluate the manufacturability of various cell types, sizes, orientations, and volume fractions of TPMS cellular structures. The manufacturability is an important factor for the selection of the cell structure. Here the manufacturability refers the easy to manufacture; as some cells are complex with certain areas that might need to be supported. Such supports are always difficult to remove after manufacturing the part. Although metallic AM parts have been produced and used, internal geometries with very fine structures below 1 mm still are a technical challenge. Comprehensive experimental works were conducted in SLM and DMLS (two powder bed fusion processes) on four different cell types using 316L stainless steel, Titanium alloy (Ti-6Al-4V), and Aluminium alloy (AlSi10Mg). Different material and machines were used to know whether these cellular structures can be manufactured reliably at different metal AM machines in a wide range of cell sizes, orientation angles, and volume fractions. The manufactured cellular structures were examined using visual inspections, μ-CT 2D and 3D model reconstruction, SEM morphology analysis, and Optical Microscopy measurements. The mechanical properties of these cellular structures are presented in chapter 8.

7.2 Experimental Procedures

7.2.1 Rationale

Table 7.1 illustrates the experimental framework used for studying the manufacturability of cellular structure. The cellular structure were produced from three metallic powders (316L Stainless Steel, Ti-6Al-4V, and AlSi10Mg) using SLM MCP Realizer and DMLS EOSINT M270/280 machines.

The framework includes experimental studies on four different cell types (Schoen Gyroid, Schwarz Diamond, Schwarz W, Neovius' surface); cell sizes of 2-9mm, cell orientation angles of 0^0 - 180^0 , and volume fractions of 5-20%. The rationale behind the selection of these parameters and ranges in the experimental studies are discussed below,

7.2.1.1 Cell type

The shape of the cell is important parameter for the manufacturability of cellular structures. Fig. 7.1 shows four different cell types used in experiments (details of these cellular structures can be found in chapter 6). Among the other cell type that can be generated in Simpleware software is the Schwarz P which was omitted due to the lower curviness and flat horizontal strut compared to more organic Gyroid, Diamond, Neovius', and was replaced by Schwarz 'W'.

The selected four candidate cell types have differences in their cell topology, which result differences in, strut thickness, strut curviness, and strut connectivity (i.e. the number of struts which share a common node). As a result, the amounts of overhang which result from each particular cell design affect the manufacturability in SLM and DMLS processes. Furthermore, different cell types will have different strength and load bearing capabilities.

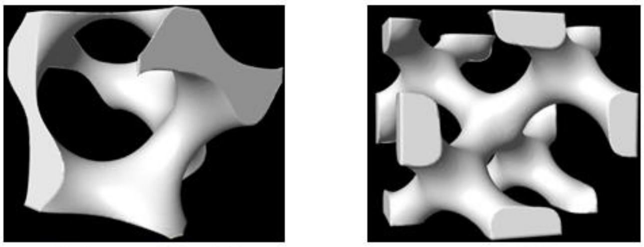

Schoen Gyroid

Schwartz Diamond

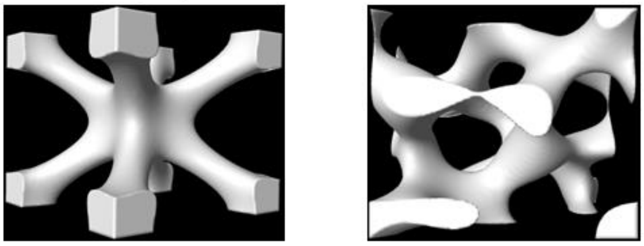

Schwartz W

Neovius Surface

Figure 7.1 CAD models of four TPMS cell types used in the experiments

7.2.1.2 Cell size

The size is another very important parameter which influences the manufacturability. The cell size determines the number of pores per inch, for a given volume fraction, the larger the cell size is, the larger the pore size and vice versa. Depending on cell type, there is a limit on the largest cell size that can be manufactured in SLM and DMLS without using support structure. Because when the size is large, the spherical pore increases and result an upper overhang strut. It is crucial to understand these limitations for different cell types to have a successful and reliable build conditions. The size of the pore and the powder particle size, determines the easy of removing the loose powder which is trapped inside the structure during the build process. Removing loose powder from very small cell size could pose further difficulties and increase post-processing time. In fact, if you efficiently cannot remove the trapped loose powder, then you neither save material nor reduce weight. It is also expected that variation of laser energy densities and cooling rates will exist between cell sizes which could affect the cell strut density. As a consequence, the mechanical properties of the cellular structure will also vary between cell sizes.

7.2.1.3 Cell orientation

The cell orientation angle (i.e. cell rotation) could vary depending on the build orientation of the component in which it is integrated. Example of this is the situation in which the cellular structures are used as a sandwich for lightweight applications. In SLM/DMLS, one of the ways to avoid or minimize support structure is by changing the orientation of the part. Orientation could also be used to reduce the build time by avoiding orientation which result a long vertical Z-height.

Additionally, a cellular structure which is manufacturable in one orientation could fail in another orientation because of the changes in strut overhanging. Each rotation structures a different cell overhang area and strut angle with respect to the horizontal plane causing a distinctive scanning area of laser beam and manufacturing demands. Different materials also present distinctive support structure requirements. For these reason, it is therefore important to determine the relationship between cell orientations to manufacturability in SLM/DMLS processes. This will enable the use of cellular structure in without worrying about their use in various possible build orientations. The effect of cell orientation on mechanical properties is equally vital and will be addressed in the next chapter.

7.2.1.4 Volume fraction

The volume fraction is the solid fraction in the generated volume and determines the thickness of the cell strut. The higher the volume fraction is, the thicker and stronger the strut is which form the cell and vice versa. For a fixed cell size, when the volume fraction is increased, the pore size (i.e. the space between struts) is decreased as the struts are inflated and fill the pore until the volume fraction approaches unity (solid). If the pore is too narrow and small, it may not be possible removed/drained loose powder after the build. For a fixed volume fraction, the thickness of the strut varies for different cell types and sizes due to the difference in cell morphology. Understanding the effect of volume fraction on manufacturability is important for our understanding on the limitations of SLM/DMLS for various cell types, sizes, and materials. Similarly, it is essential to create a relationship between volume fraction and mechanical properties of the manufacturable cellular structures.

Table 7.1 – Experimental framework of manufacturing cellular structures

Experiment No.	Cell type	Cell size	Volume fraction (%)	Cell orientation	Material	Machine
1	Gyroid	2-9	15	Normal	316L Stainless steel	SLM MCP-Realizer
	Diamond	2-9	15	Normal	316L Stainless steel	SLM MCP-Realizer
	Schwartz W	4-6	15	Normal	316L Stainless steel	SLM MCP-Realizer
	Neovius	5-6	15	Normal	316L Stainless steel	SLM MCP-Realizer
2	Gyroid	5	6-15	Normal	316L Stainless steel	SLM MCP-Realizer
3	Gyroid	5	15	20-180 rotation	316L Stainless steel	SLM MCP-Realizer
	Diamond	5	15	20-180 rotation	316L Stainless steel	SLM MCP-Realizer
	Schwartz W	5	15	Worst orientation	316L Stainless steel	SLM MCP-Realizer
	Neovius	5	15	Worst orientation	316L Stainless steel	SLM MCP-Realizer
4	Gyroid	3-7	5-20	Normal	Ti-6Al-4V, AlSi10Mg	DMLS M270/M280
	Diamond	3-7	5-20	Normal	Ti-6Al-4V, AlSi10Mg	DMLS M270/M280
5	Gyroid	5	15	20-180 rotation	Ti-6Al-4V	DMLS M270

316L Stainless steel – Austenitic stainless steel powder supplied by Sandvik Osprey Ltd., UK

Ti-6Al-4V - Titanium alloy Grade 5 powder supplied by LPW Technology Ltd., UK

AlSi10Mg - Aluminium alloy powder supplied by EOS GmbH., Germany

Normal – is the non-orientated cell as normaly generated by simpleware software.

Worst orientation - is the cell orientation angle which result the largest possible overhanging region of the cell strut.

7.2.2 Experiments

The following experiments were conducted to achieve substantial results for various parameters investigated. The numbers of experiments were adequately controlled while maximizing the outcome to achieve the objectives. This is mainly due to AM metal powders being quite expensive and the relatively slow build rate of SLM/DMLS process.

7.2.2.1 Exp.1: The Effect of Cell Type and Size on Manufacturability

This experiment was conducted to investigate the effect of cell type and size on manufacturability. The four cell types shown in Fig.7.1 were used in the experiment. The cell types and sizes were generated for a fixed volume fraction of 15%. The cell size of Gyroid and Diamond cell types was varied from 2 mm to 9 mm, but it was not possible to generate similar cell size range for Schwartz 'W' and Neovius' surface. Because of their cell shape and connectivity which form a fragile cell struts and weakly connected cells at 15% volume fractions additionally, generating cell sizes smaller than 2mm could consume large computational time and computer memory which is difficult to handle by SLM/DMLS machine software.

A solid cubic model with dimensions of 25mm×25mm×15mm was used to represent the test specimen. The steps involved in generating cellular structure using Simpleware software is explained in chapter 6. The selected dimensions provide a sufficient number of adjacent cells suitable for manufacturability and mechanical study. 0The vertical Z-height parallel to the build direction is shortened to reduce the build-time and material consumption.

The experiment was carried out on a SLM MCP-Realizer machine using 316L stainless steel metal powder. The parts were built on thick steel base plate, and then after the part building is completed, it was cut off from the base plate using Wire Electric Discharge Machining (Wire-EDM). The experimental samples then went through a characterization by visual observation, µ-CT, SEM, and optical microscopy.

7.2.2.2 Exp.2: The Effect of Volume-Fraction on Manufacturability

This aim of this experiment was to investigate the effect of volume fraction on manufacturability. The Gyroid cell type with fixed cell size of 5mm and variable volume fractions of 6%, 8%, 10%, 12% and 15% were tested in SLM MCP-Realizer using 316L stainless steel metal powder. The gyroid strut is the most fascinating TPMS shape among the cell types for its continuous curvature. All other experimental conditions are as explained in Exp.1 (refer to section 7.2.2.1).

7.2.2.3 Exp.3: The Effect of Cell-Orientation on Manufacturability

This experiment was performed to investigate the manufacturability of different cell orientations. The as-generated Gyroid and Diamond cell types with fixed volume fraction and cell size of 15% and 5mm, respectively, were rotated in Y-axis from 0^0 reference normal plane to 20^0, 40^0, 60^0, 80^0, 100^0, 120^0, 140^0, 160^0, and 180^0 rotation. The Simpleware software does not permit the automatic cell rotation, and so the cell rotation was created manually. This was done by first generating a cellular structure using a cylindrical part with diameter = 20 mm and height = 15 mm, and then rotating in a fixed axis (Y-axis). After the part was rotated to a specific angle, it was cut into two sections forming a two semi cylinders. One semi cylinder is used for the experimental purpose as depicted in Fig. 7.2 (a). In addition to the 9 cell orientation ranging from 0-180^0 with a step change of 20^0, it was found that there exists a worst orientation for all cell types. Similar procedure was followed for the worst orientation except that instead of semi-cylinder, a cuboid with dimensions of 25mm×25mm×15mm was cut from the cylinder. Fig 7.2 (b) shows the worst orientation of the four cell types. The worst possible orientation is the one with largest overhang area and 40^o–50^0 strut angle with respect to the horizontal base plane. In practice, this orientation should be the most difficult to build in metal AM technologies especially for large cell sizes. The volume fraction and cell size of the Schwartz W and Neovius' surface was also fixed to 15% and 5mm respectively. All other experimental conditions are as explained in Exp.1 (refer to section 7.2.2.1).

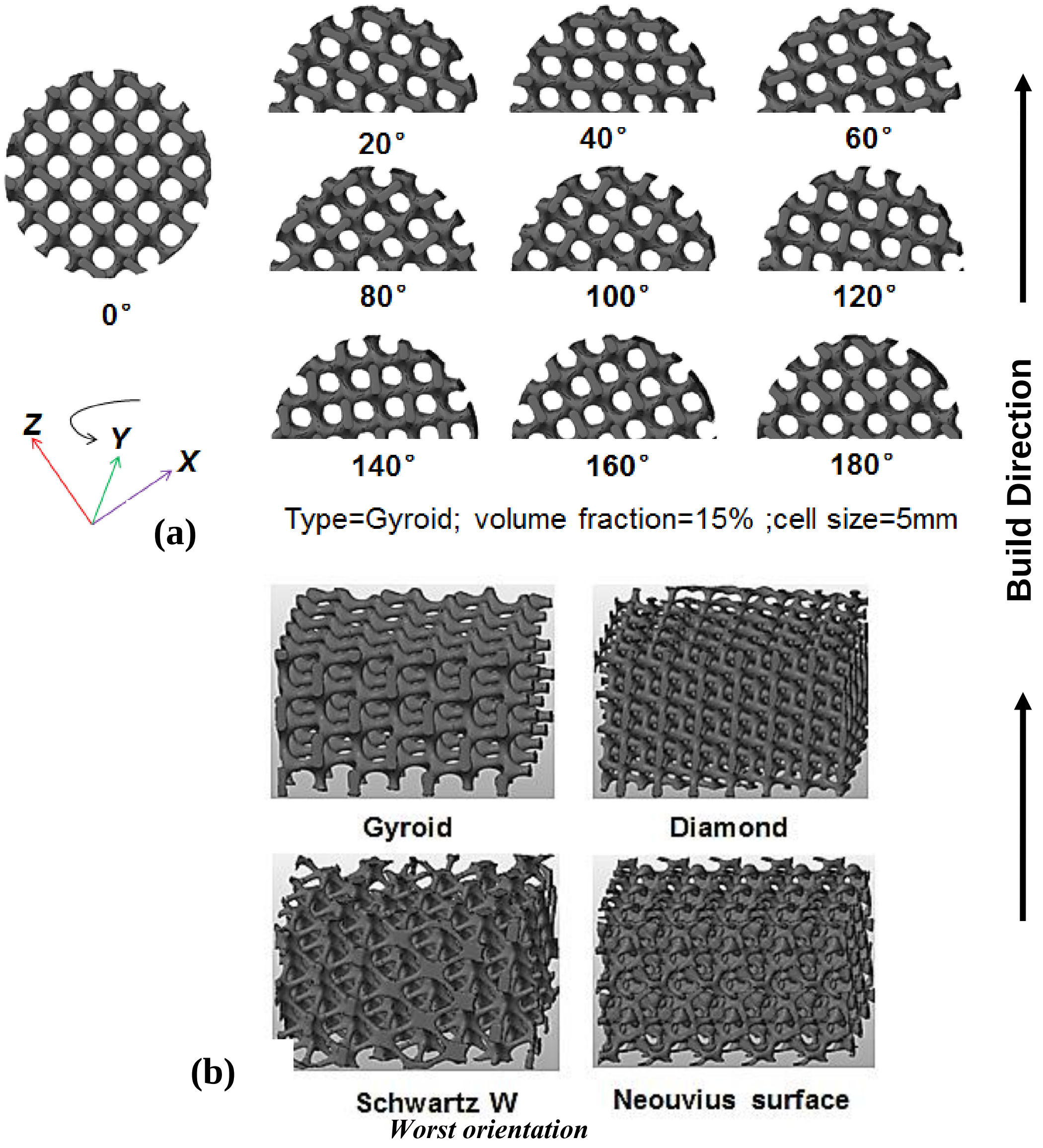

Figure 7.2 (a) Cell orientations of Gyroid structure (Front view) (b) Worst cell orientations of four cell types (Isometric view)

7.2.2.4 Exp.4: Further Tests on the Effect of Cell and Volume Fraction on Manufacturability

Further manufacturing tests on cell size and volume fraction were conducted in DMLS process. The purpose was to test the manufacturability of TPMS cellular structures in different materials and metal AM machine. The manufacturability of cellular structure could be affected by the material being processed, with some materials generating a larger thermal stresses and temperature gradients during the build process. The Ti-6Al-4V and AlSi10Mg are two potential lightweight materials but are considered as one the most difficult materials to process in metal AM due to the high reactivity with oxygen

(Thijs et al. 2010), and has the highest support structures demands in overhang area.

3T RPD Ltd. is one of the leading AM service bureaus in UK and one of the project partners in the SAVING project. Because of this collaboration, they have allowed us to use their DMLS M270 and M280 commercial machines for processing TPMS cellular structures from Ti-6Al-4V and AlSi10Mg metal powders. Unlike the MCP-Realizer which is more a research machine, the DMLS metal machines have highly controlled processing chamber and standardized process parameters for these materials. Further details of processing parameters of these machines can be found in chapter 3 (Materials and Methods). The build chamber is well controlled during the laser processing and very low level <0.13% of oxygen content can be achieved. As commercial environment, 3T RPD has designated different materials to specific machines in order to avoid contaminations in the build and avoid lengthy cleaning pre-processing. DMLS machines also have the options of using hard or soft recoater in the build. The soft recoater (polymer based) is suitable for delicate structures while the hard recoater (metal or ceramic) is expected to provide more dense parts and is the standard used at 3T RPD for functional parts. We used a hard steel recoater for all our experiments in DMLS machines.

Two cell types (Schoen Gyroid and Schwarz Diamond) were investigated in the DMLS machines. The selection was based on the outcome from the previous experiments on 316L stainless steel which demonstrated the suitability of these two cell types which allow building a wider range of cell size and volume fractions. Both cell size and volume fraction were varied from 3-7mm and 5-20% respectively. The range of volume fraction was extended up to a maximum of 20% and a minimum of 5%. Fig. 7.3 depicts Gyroid structure with fixed volume fraction of 5% and cell sizes from 3-7mm. The cellular structures were generated from a cubic specimen with dimensions similar to that in exp.1 *and 2.* The manufactured cellular structures were bead blasted and then heat treated. Details of the heat treatment cycle can be found in chapter 3.

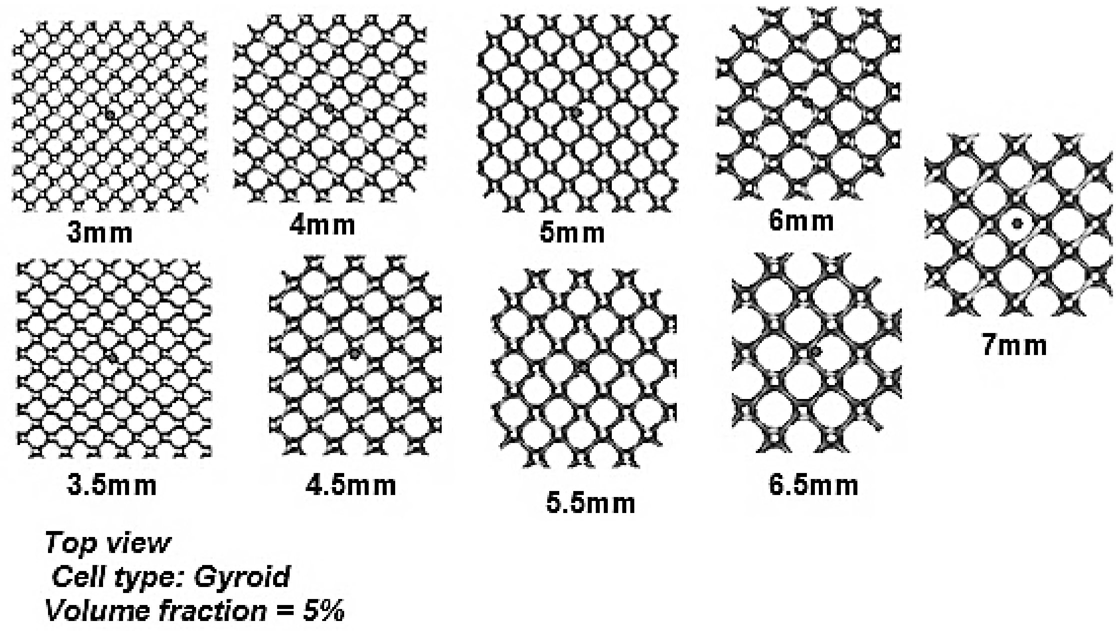

Figure 7.3 Schoen Gyroid structure with variable cell size and fixed volume fraction

7.2.2.5 Exp.5: Further Tests on the Effect of Cell orientation on Manufacturability

The effect of cell orientation was further investigated using Ti-6Al-4V in DMLS M270 machine. The Gyroid cell type with a fixed cell size and volume fraction of 5mm and 15%, respectively, was rotated from reference plane to 20^{0}, 40^{0}, 60^{0}, 80^{0}, 100^{0}, 120^{0}, 140^{0}, 160^{0}, and 180^{0} as shown in Fig. 7.4. The worst orientation of Gyroid was also tested in this experiment. All other experimental conditions are as stated in Exp. 4.

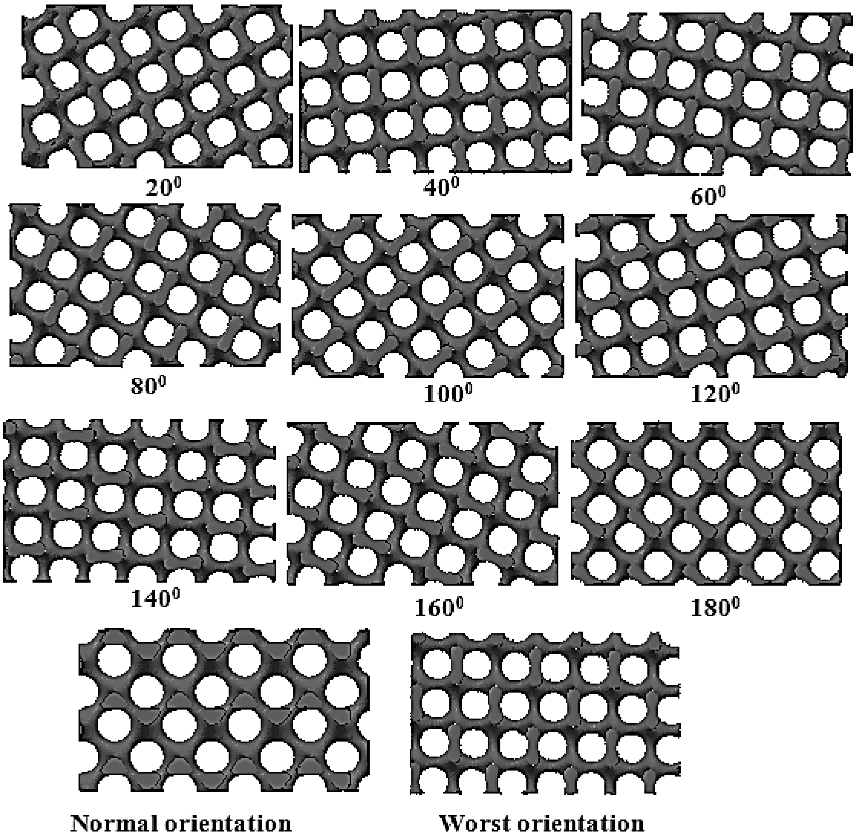

Figure 7.4 Schoen Gyroid with variable cell orientation (Front view)

7.3 Results and discussion

7.3.1 316L stainless steel cellular structures

7.3.1.1 Manufacturability Analysis

Fig. 7.5 shows the four types of TPMS cellular structures manufactured in SLM MCP-Realizer using 316L stainless steel powder. The experiment result reveals that Gyroid and Diamond cell types with cell sizes ranging from 2–8 mm and 15% volume fraction can be successfully manufactured in SLM with no obvious deformations in the cell strut. But for 9 mm cell size, some deformation/sagging were observed specially in Gyroid structure. When sagging occurs during building a large cell, it disrupts the levelness of powder distribution of the next layer. The layer thickness becomes higher in the sagged region and the newly melted layer may not bond well to the previous layer. This however depends on the amount of sagging and the resultant layer thickness.

The sagging/deformation in 9mm cell size were lower in the diamond cell type; however, there was difficulty of removing loose powder for diamond cell sizes smaller than 3mm. The reason is that diamond cell shape and strut interconnectivity is different to that of Gyroid and thus result a higher number of pores per cm and reduced strut thickness. For the same cell size and volume fraction, Gyroid unit cell will have larger struts and pore compared to Diamond, as a result, the overhanging area for large cell sizes > 8mm is reduced in diamond structure which in turn minimize the sagging phenomenon observed in the 9mm Gyroid structure. On the other hand, the reduced pore size in small cell sizes for Diamond structure increases the difficulty of loose powder removal that is trapped in the cellular structure during the build.

The Schwartz W and Neovius Surfaces were also manufactured with cell sizes of 4-6mm and 5-6mm, respectively and fixed volume fraction of 15%. As depicted in Fig.7.5, the Schwartz W unit cell consists of tiny struts 4-5 tiny struts sharing a common node with large head. The laser transition from the cell strut to the large node causes higher energy to be deposited at the node resulting non-uniform melt-pool instabilities at the vicinity of the node. The large temperature and stress gradients could cause the tiny strut to curl during the build. The Neovius structure has a better transition at node-strut intersection and is more close to the diamond cell topology. However, Neovius generates large number of tiny strut even at 6mm cell size. Some of the edges of the Neovius structure were curled and fractured surfaces could be seen on cell struts. The soft rubber recoater used in the SLM MCP-Realizer during the experiments is more forgiving and permits to build fragile geometries. For hard recoater, the fragile struts could easily be broken by the powder recoater system during processing, or the curled edges may block the movement of powder recoater. This could sometimes lead to whole build failure and the machine must be stopped from further processing.

The Neovius surfaces may not be feasible to be used in large components requiring large number of cells, as this could generate large STL files size that is difficult to process and demand high computer processing capacity and memory allocation.

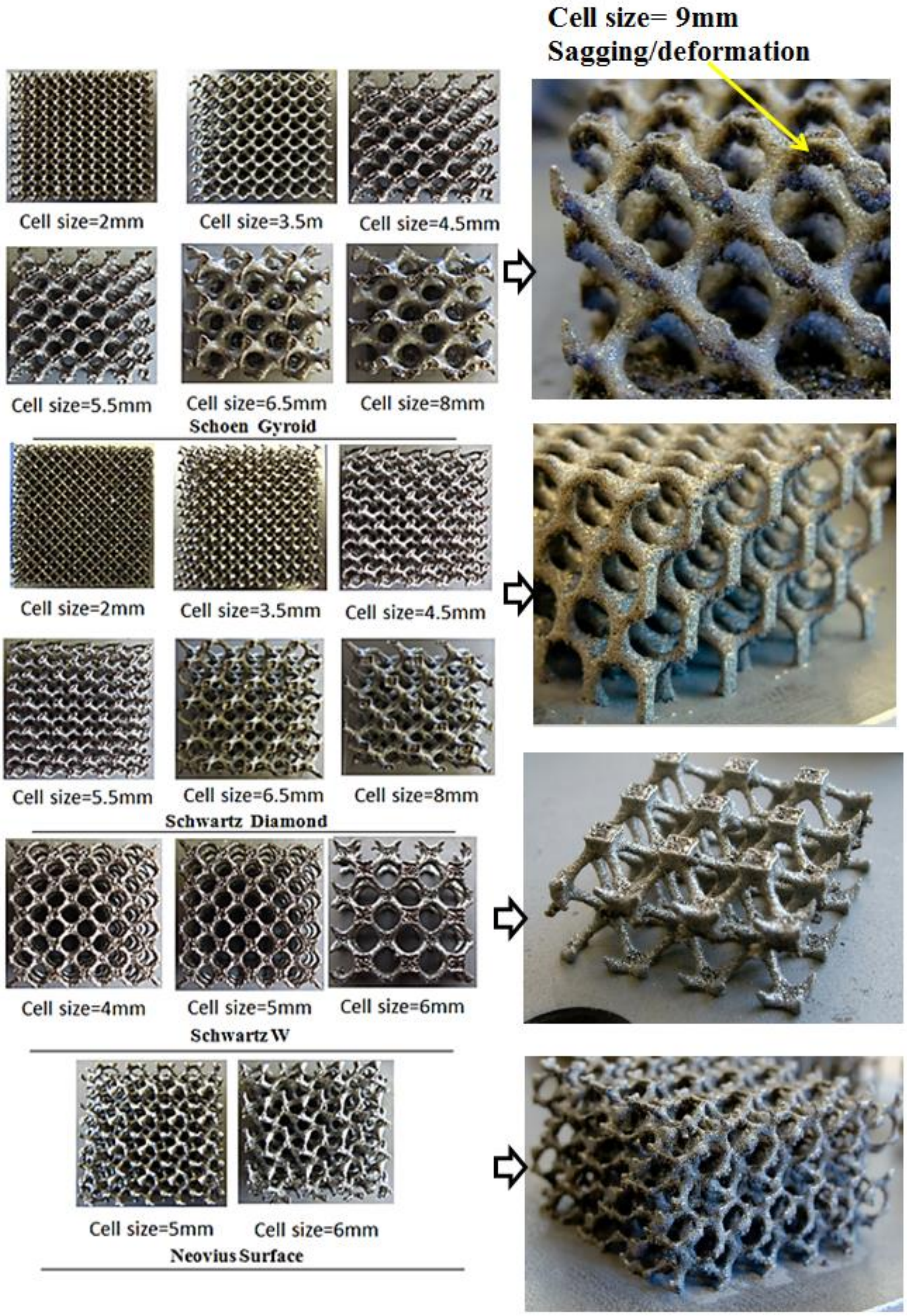

Figure 7.5 Manufactured cellular structures [SLM MCP-Realizer, 316 L stainless steel]

7.3.1.2 μ-CT Analysis

- **Fixed volume fraction and variable cell size**

The 3D reconstruction models captured from the μ-CT of the Gyroid cellular structures with various cell sizes are shown in Fig. 7.6. The analysis of these reconstructions indicates no obvious defects or broken cells within the structures confirming the ability of SLM to manufacture the Gyroid cellular structure, and over the whole range of cell sizes tested. This is with the exception of minor sagging observed in 9mm Gyroid cell size. However, this result is based on fixed volume fraction of 15%, and therefore, any increase on volume fraction would attain larger and non-deformed cell sizes.

In this work, the smallest cell size that was tested in SLM process is 2mm as shown in Fig. 7.6 (a). There trapped loose powder was completely removed after the build. Without the file size constraints, the minimum unit cell size of Gyroid cellular structures that can be manufactured by SLM mainly depends on particle sizes of metal powders and the laser focus diameter of the SLM machine. When the volume fraction is set constant and the cell size is increased, the number of cells in the volume decreases and the struts become thicker. However, as the struts become longer, the length of overhanging horizontal region in the structures increases and deformation during the manufacturing process is more likely to occur. As shown in Fig.7.6 (f), the μ-CT of Gyroid cellular structure with cell size of 8mm shows no sign of external defects or sagging in the structure.

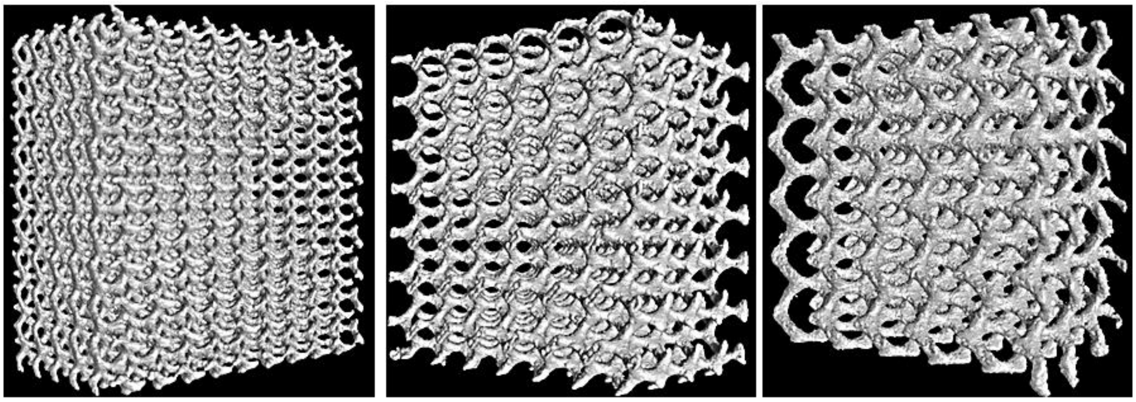

(a) Cell size=2 mm (b) Cell size=3.5 mm (c) Cell size=4.5 mm

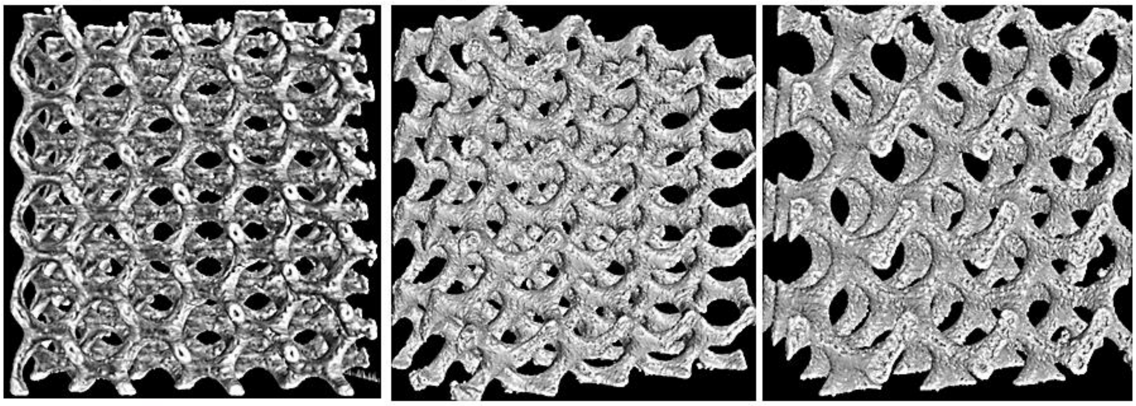

(d) Cell size=5.5 mm (e) Cell size=6.5 mm (f) Cell size=8 mm

Figure 7.6 μ-CT 3D reconstruction models of the Schoen Gyroid cellular structure with fixed volume fraction of 15% and varying unit cell sizes [SLM MCP-Realizer, 316 L stainless steel].

To examine if there are pores present in the solid struts of the cellular structure, μ-CT 2D cross-sectional images was taken from the manufactured Gyroid cellular structure as shown in Fig. 7.7. The cross-sectional images in Fig. 7.7(a) reveal the presence of micro-pores inside the strut of the manufactured Gyroid structure with cell size of 2mm. The micro-pores appear as small black dots in the white strut image. The number of micro-pores increase as the cell size is increased (see Fig. 7.7 (b-f). The maximum amount of pores was found in largest cell size scanned which is 8mm as shown in Fig. 7.7(f). The increasing density for smaller cell sizes may be attributed to their shorter scan vector length during the laser processing. The cross-sectional area of the strut to be scanned by the laser is smaller in small cell sizes enabling higher energy concentration compared to large cell sizes. In short scan vectors, the adjacent laser tracks are scanned more rapidly one after the other, leaving little cool down time in between them, and thus resulting in higher temperatures of the scanned area. Consequently, better wetting conditions are present to form denser struts of the cellular structures with smaller cell sizes. It is noted that better density of the struts could be achieved for the larger unit cell lattice structures by optimizing the processing parameters of the SLM process. This may include optimized laser scanning strategy for small and bigger cell size.

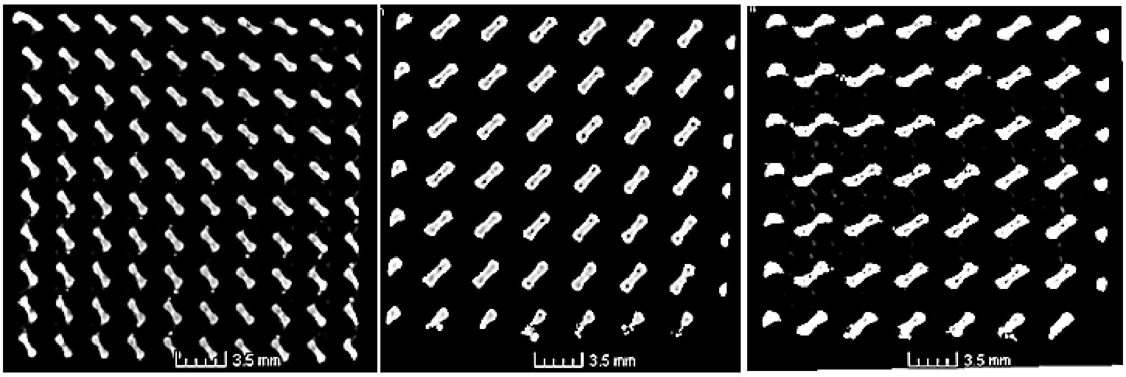

(a) Cell size=2 mm (b) Cell size=3.5 (c) Cell size=4.5

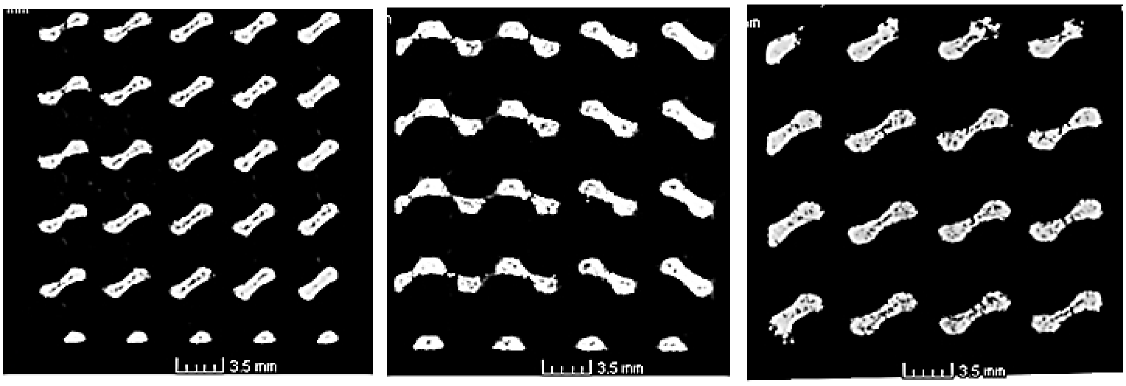

(d) Cell size=5.5 (e) Cell size=6.5 (f) Cell size=8 mm

Figure 7.7 2D cross sectional μ-CT images of the Gyroid cellular structures with fixed volume fraction of 15% and various unit cell sizes [SLM MCP-Realizer, 316 L stainless steel].

To assess the geometrical accuracy of the SLM MCP-Realizer, the manufactured Gyroid structure was compared to its original CAD model. The graphical data obtained by μ-CT scanning was superimposed on the CAD data, enabling both visual and quantifiable comparisons. Fig. 7.8 shows merged μ-CT 3D reconstruction model and the 3D CAD model of the Gyroid structure. Fig. 7.8 (a) shows Gyroid structure with cell size of 2mm and 15% volume fraction. It can be seen that over the whole porous structure the designed and built architectures nearly coincide within with a standard deviation of 0.137mm, indicating a very high accuracy of the technique. Similarly it can be seen in Fig.

7.8 (b) that Gyroid structure with 5.5mm cell size and 15% volume fraction is generally well reproduced in comparison to the original design CAD model with standard deviation of 0.154mm.

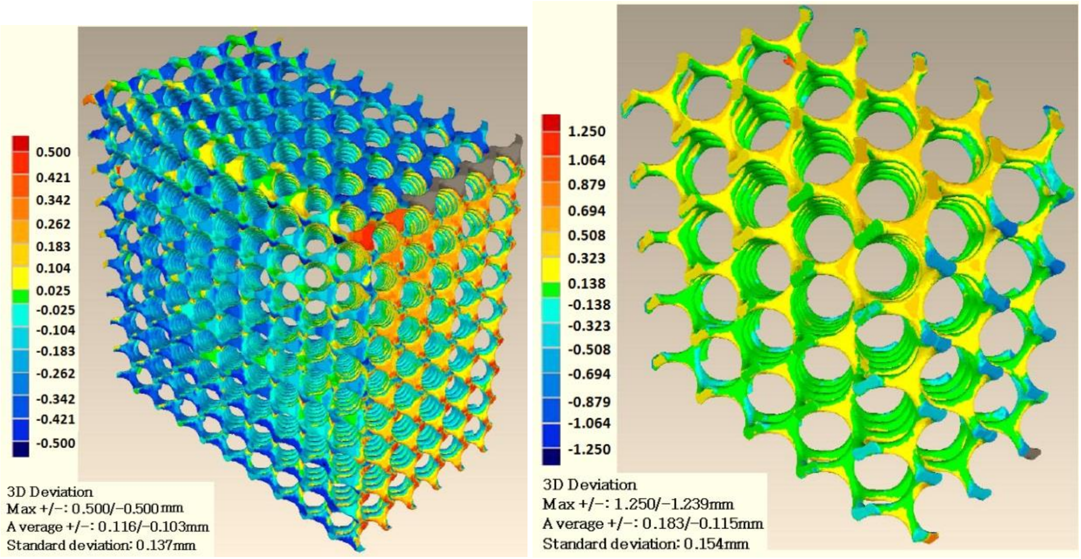

(a) (b)

Figure 7.8 Comparisons of the µ-CT 3D reconstructed surface and 3D CAD model of the Schoen gyroid cellular structure with fixed volume fraction of 15% (a) cell size=2mm (b) cell size = 5.5mm [SLM MCP-Realizer, 316 L stainless steel].

- **Fixed cell size and variable volume fraction**

The µ-CT 3D reconstruction models of the SLM-manufactured cellular structures with fixed cell size of 5 mm and volume fractions of 6%, 8%, 10%, 12%, and 15% are shown in Fig. 7.9. The µ-CT 3D reconstructions show well-defined struts and no apparent defects or broken cells throughout the structures network, indicating the ability of SLM to fabricate Gyroid cellular structures with a wide range of volume fractions as low as 6%.

By analyzing the µ-CT reconstruction models, the bounding volume of the cellular structure and volume of solid struts can be determined to give the experimental volume fraction. The designed and experimental volume fractions are listed and compared in Table 2. The experimental volume fraction calculated from µ-CT data are 6.51%, 8.75%, 10.66% and 13.12% which correspond to the designed volume fraction of 6, 8, 10 and 12% respectively. This shows a slight increase in experimental volume fractions in comparison with the corresponding designed values. The discrepancy between the theoretical and experimental volume fractions can be attributed to the non-uniform little increase of the experimental strut size of the cellular structures.

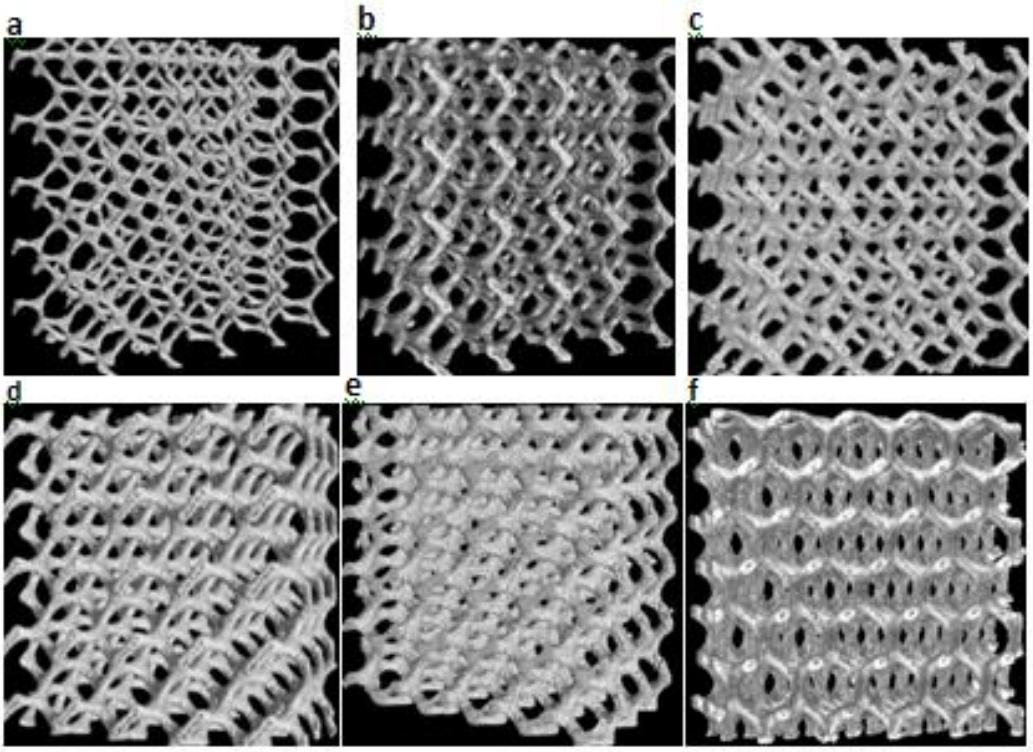

Figure 7.9 μ-CT 3D reconstruction models of the Gyroid cellular structures with fixed cell size of 5mm and different volume fractions: (a) 6%, (b) 8%, (c) 10%, (d) 12%, (e) 15% and (f) 15% (worst orientation) [SLM MCP-Realizer, 316 L stainless steel]

Table 7.2 Comparison between the designed volume fraction and experimental calculated volume fraction

Volume of the lattice structure/ mm^3	CT-tested volume of the solid struts / mm^3	Experimental volume fraction /%	Designed volume fraction /%	Increase /%
9537.192	620.871	6.51	6	8.5
9670.542	846.172	8.75	8	9.4
9548.220	1017.840	10.66	10	6.6
9530.880	1250.451	13.12	12	9.3

7.3.1.3 SEM analysis

- **Fixed volume fraction and variable cell size**

The SEM micrograph taken from the strut of the Gyroid structure made by the SLM process is shown in Fig. 7.10. Fig. 7.10(a) represents the Gyroid structure with cell size of 2mm and volume fraction of 15%. As can be seen, the cross-section of the fractured cell strut is circular in shape which is in agreement with the strut shape of the generated CAD model. A higher magnification of the strut cross-section in Fig. 7.10(b) reveal a near fully dense melted surface, but with some micro cracks in the range of 1 μm width and 20 μm in length. It is supposed that this type of cracks could exist in the part due to the high residual stresses formed during SLM process. Furthermore, Fig. 7.10(c) shows partially bonded tiny powder particles on the surfaces of the struts of the cellular structure.

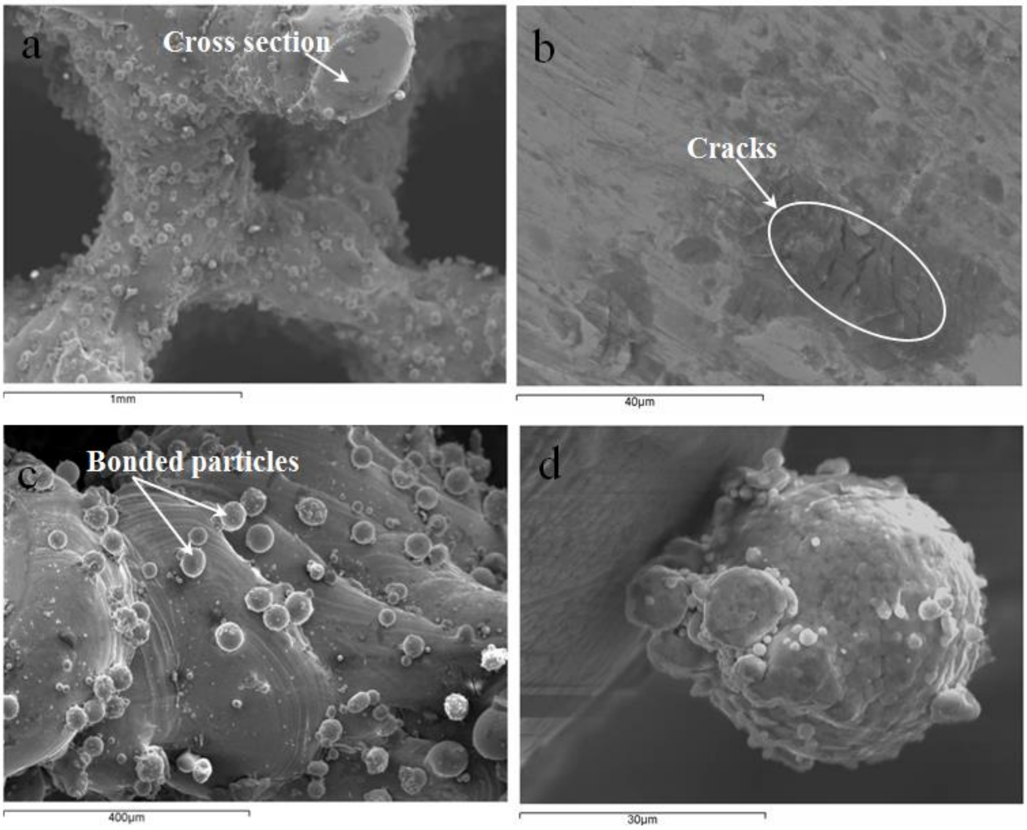

Figure 7.10 SEM micrographs of (a) the struts of the Gyroid cellular structure with cell size of 2 mm and the volume fraction of 15%, (b) A magnified cross section of a strut (c) Tiny particles bonded to the surfaces of the struts and (d) Magnified single tiny particle on the surface of the strut [SLM MCP-Realizer, 316 L stainless steel].

Similar phenomenon has been observed in previous literature works of Santorinaios et al. (2006) and McKown et al. (2008) on 316L stainless steel structures manufactured in SLM. It was also reported in the work of Pattanayak et al. (2011) of titanium porous structures. However, the reason for this phenomenon has not been explained comprehensively. The author believes that bonded particles are formed as a result of large melt pool instabilities and heat affected zone created during laser scan of the strut. The high laser energy introduced in the alternating scanning strategy is repeatedly concentrated in small region of the strut to create the larger melt pool. The large melt-pool instabilities lead to large heat affected zone and partial melting of surrounding powder. Additionally, the surface tension and balling phenomenon of the melt pool which is the result of short laser exposure time allows the absorption of some surrounding loose powders. As a result, the partially melted particles remain attached to the strut after solidification. The ‘balling’ which gives rise to beads being formed mainly on laser melted surfaces perpendicular to the building direction.

A higher magnification of the bonded particle is further illustrated in Fig. 7.10(d). The bonded particle has a nearly spherical shape with an approximate size of 35µm and rough in surface. This particle morphology is similar to the one found in raw 316L steel metal powders. The size of the bonded particle varies in the strut and is a function of the powder particle sizes and distribution. This further supports the argument that these bonded particles are caused by partially melting of the surrounding raw stainless steel particles. These bonded particles increase the surface roughness of struts of the cellular structure. To improve the surface quality of the manufactured struts of the cellular structure, the metal powders with smaller particle size should be used, and the post processing operation of sand or bead blasting can be carefully carried out to systematically remove the bonded particles while avoiding the destruction of the thin struts. Pattanayak et al. (2011) used heat treatment at 1300 ^{o}C in an argon gas atmosphere to make partially melted titanium particles fully fuse and bond in the strut core, thus smoothing the surface. This is particularly necessary in Titanium structures used for medical applications.

- **Fixed cell size and variable volume fraction**

Fig. 7.11 shows the SEM images of the SLM-manufactured Gyroid cellular structures with volume fractions of 6%, 8%, 10% and 12%. All these structures have the same unit cell size of 5mm. It can be seen from the SEM images that the SLM-manufactured cellular structures show circular struts and spherical pores, which is in agreement with the CAD model, and no interlayer delamination indicating metallurgical bonding between the layers during the manufacturing process. It is also observed that the cellular structures exhibit very rough surfaces with curvatures and corrugations. The roughness of strut is further contributed by stepping-effect resulting from the curviness of the struts of TPMS cellular structures. A higher SEM micrograph magnification of the strut in

Fig. 7.12(a) demonstrates a staircase-shaped profile and some partially melted metal particles bonded on the surfaces of the cellular structure.

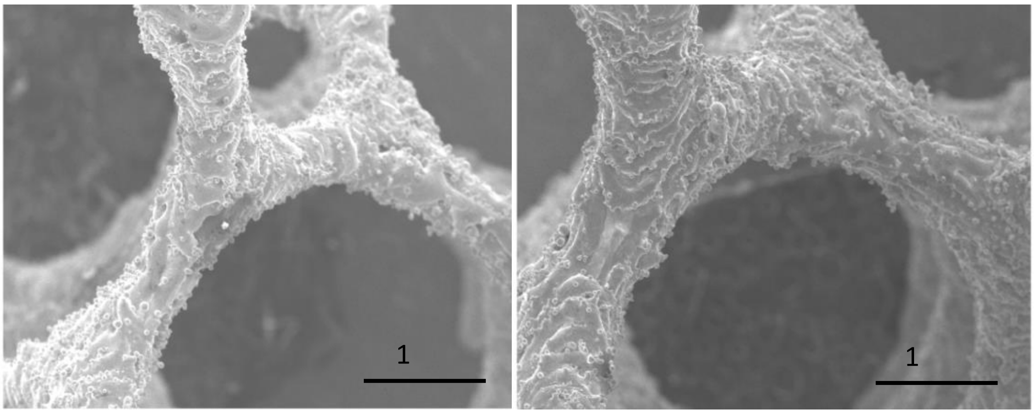

(a) Volume fraction= 6 % **(b) Volume fraction= 8 %**

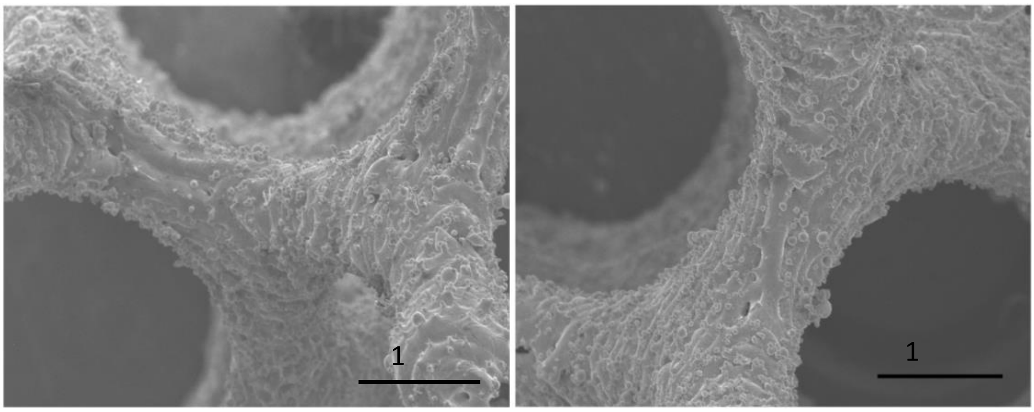

(c) Volume fraction= 10 % **(d) Volume fraction= 12 %**

Figure 7.11 SEM images of the Gyroid cellular structures with different volume fractions and fixed cell size of 5mm [SLM MCP-Realizer, 316 L stainless steel]

The rough strut surfaces of the SLM-manufactured structures can mainly be attributed to following reasons:

(1) Stair-stepping effect: As illustrated in Fig. 7.12(b), CAD model of the part is decomposed into many right-angular polyhedron layers which are then built one by one and combined together to form 3D physical part in the SLM process. For any curved surfaces or inclined plane, the effect of laminar build is noticed as stair steps, which are referred to as stair-stepping effect, leading to the staircase-shaped profile. The stair stepping effect has a great influence on the surface roughness of SLM parts, and can be diminished by decreasing the layer thickness, but this increases the time required to complete the fabrication.

(2) Circular struts are partially built on the loose powder: To ensure firm combination of adjacent layers, laser melting depth, which is the depth of laser

melting and permeation into the powder, is slightly higher than the layer thickness to form overlaps between layers. However, the circular struts with varying inclined angles are partially built on the loose powder, and thus some metal particles below each layer will be totally or partially melted and then bonded on the bottom of the layer.

(3) Thermal diffusion: Thermal diffusion occurs between loose powder and solid material due to temperature gradients, causing the loose powder particles to stick to the strut surface.

(4) Partially melted raw metal particles on the boundary of each layer: A new layer of metal particles is scanned by the contour laser track, followed by the hatching laser track. Some stainless steel particles on the boundary are partially melted by the outer contour laser track, and thus bonded to the boundary of each new formed layer.

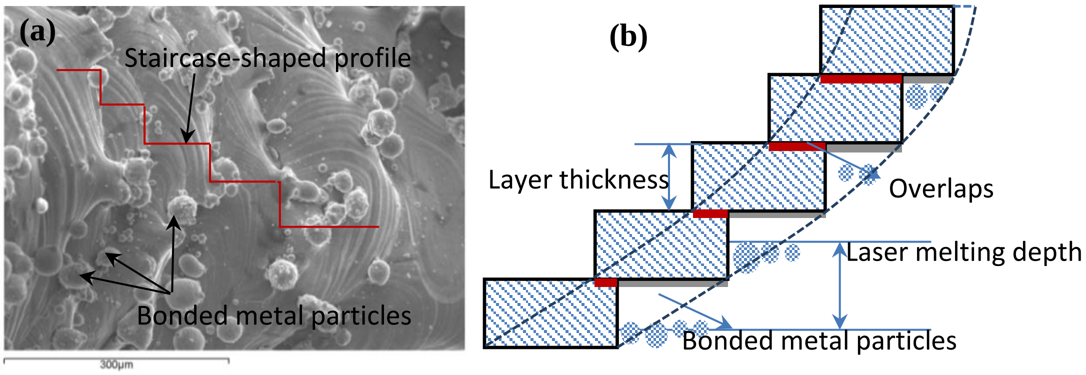

Figure 7.12 (a) High magnification SEM micrograph of the strut and (b) schematic illustration of the SLM manufacturing process of the circular strut [SLM MCP-Realizer, 316 L stainless steel].

It important to remember that all 316L stainless steel cellular structures manufactured in SLM-MCP Realizer and presented here neither go through air sand/bead blasting nor been heat-treated which is usually performed in commercial metal parts. It is expected that these partially bonded particles could be eliminated systematically by these post-processes and smoother cellular struts could be achieved.

7.3.1.4 Optical Microscopy

- **Fixed cell size**

Fig. 7.13 shows the optical microscopy images of the SLM-manufactured Gyroid cellular structures with fixed cell size of 5mm and different volume fractions of 6%, 8%, 10% and 12%. The strut sizes of the SLM-manufactured cellular structures were measured from the optical microscope images as indicated in Fig. 7.13(d). The designed strut sizes were measured from the CAD models of the cellular structures. The experimental and designed strut sizes as a function of the volume fraction were plotted and compared in Fig. 7.14. It is found that the measured dimensions of experimental strut sizes are higher than the designed CAD values. As expected, this is in agreement with the μ-CT and SEM analysis showing an increase in strut size (i.e. average strut thickness).

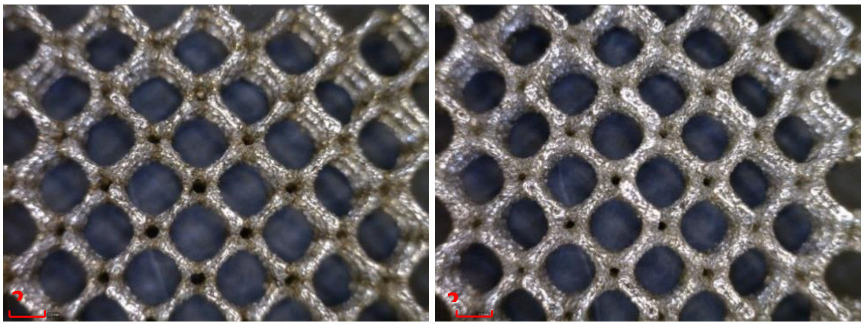

(a) Volume fraction= 6 % (b) Volume fraction= 8 %

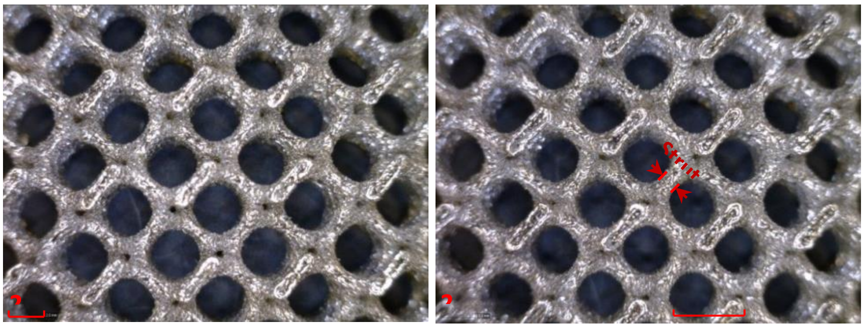

(c) Volume fraction= 10 % (d) Volume fraction= 12 %

Figure 7.13 Optical microscope images of the Gyroid cellular structures with different volume fractions and fixed cell size of 5mm [SLM MCP-Realizer, 316 L stainless steel].

Parthasarathy et al. (2010) reported that an increase of 140 μm was found in strut size of the electron beam melted porous Ti-6Al-4V structures, and thus a decreased pore size by 210 μm. Van Bael et al. (2011) evaluated the SLM-manufactured Ti-6Al-4V porous structures though micro-CT image analysis and noticed the increase in strut size with 112 μm compared to the original designed value, and in accordance the structure volume and surface area increased significantly.

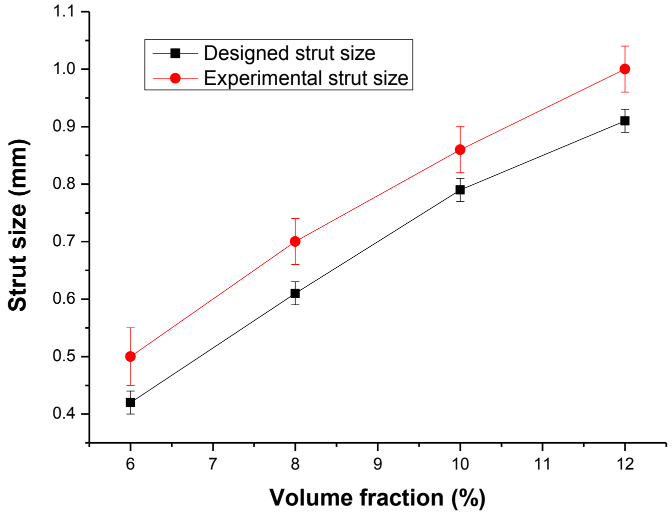

Figure 7.14 Strut sizes measured from optical as a function of volume fraction [SLM MCP-Realizer, 316 L stainless steel].

- **Worst orientation**

All tested orientations of Gyroid and Diamond starting from 20^0 to180^0 including the worst orientation has been successfully manufactured in SLM. The worst orientation of Schwartz and Neovius' surface has also been manufactured without difficulty. Fig. 7.15 depicts the worst orientation of Gyroid cellular structure with 15% volume fraction and 5mm cell size showing no obvious deformation. The optical microscope images in Fig. 7.15(b-d) display top, bottom and lateral views of the structure. The exhibited Inset images represent the corresponding CAD models. It can be seen from these optical micrographs that there are no defects or broken cells in the worst orientation. This further supports the use of Gyroid structure in all possible orientations. This characteristic of TPMS cellular structure makes them interesting for SLM use.

The manufacturability of most lattice structures proposed and investigated in majority of the previous research work and having straight beam-like struts and polyhedral pores are limited by the cell orientation. If their cell orientation from the horizontal plane is less than a certain angle, say as the rule of thumb by 45^0, the cell wall will quickly deform and lead to build failure. Cansizoglu et al. (2008) observed that structures whose struts were oriented at an angle of less than 20^o with respect to the build plane had little or no overlap between the successive melted layers resulting very week structures.

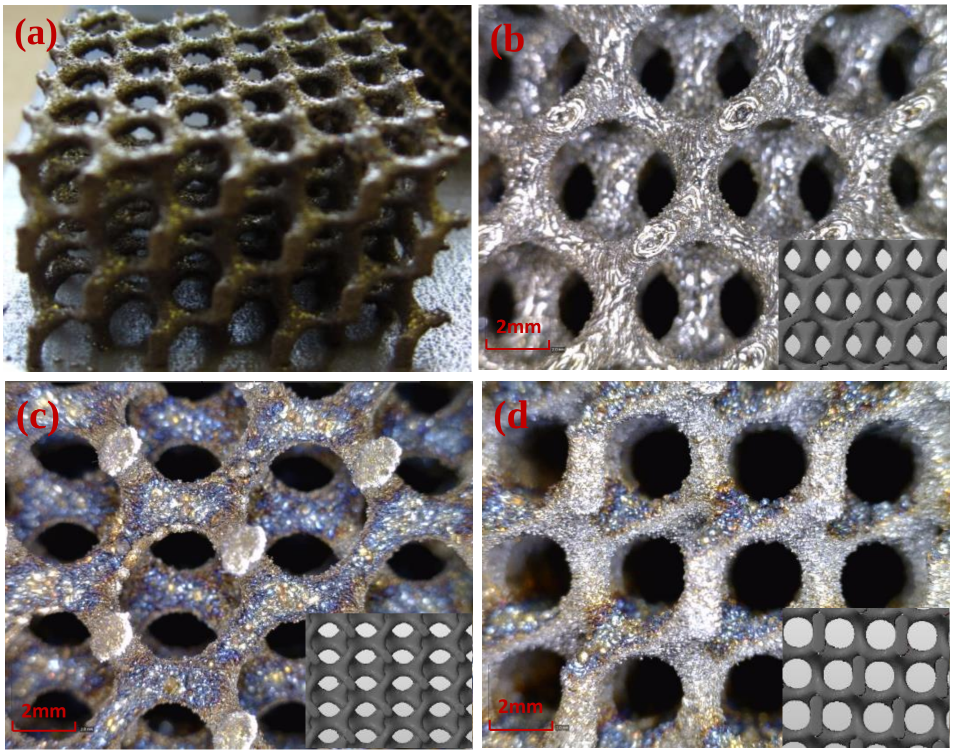

Figure 7.15 (a) optical microscope images of gyroid cellular structure worst orientation (volume fraction=15% and cell size=5mm) (b) top (c) bottom and (d) side view. Insets in (b- d) exhibit the corresponding CAD model of the worst orientation respectively [SLM MCP-Realizer, 316 L stainless steel].

7.3.2 AlSi10Mg cellular structures

7.3.2.1 μ-CT Analysis

The Gyroid and Diamond cellular structures with the volume fractions of 5%, 7.5%, 10%, 12.5% and 15%, and unit cell sizes of 3mm, 3.5mm, 4mm, 4.5mm, 5mm, 5.5mm, 6mm, 6.5mm and 7mm were produced in DMLS M280 machine using AlSi10Mg metal powder. Fig. 7.16 shows the manufactured Diamond structures with different cell sizes. The μ-CT cross-sectional images and 3D reconstruction models established from the Diamond cellular structure are shown in Figs. (7.17 - 7.18). In general, the analysis of these reconstructions indicate no defects or broken cells within the cellular structures, demonstrating the ability of DMLS machine to manufacture lightweight AlSi10Mg cellular structures with a wide range of the volume fraction and cell size. This is with the exception of cells of the Diamond structure with low volume fraction of 5%

which shows some broken struts inside the for cell sizes ≤ 6.5mm. At 7mm cell size, no broken cells where found for 5% volume fraction. This indicate lower limit of volume fraction and cell size of AlSi10Mg Diamond cellular structures. Gyroid cellular structure has a favourable manufacturability capability for AlSi10Mg when low volume fractions and small cell sizes are combined.

The 2D cross-sectional images from the μ-CT display a very dense solid strut of AlSi10Mg with no sign of feasible porosities.

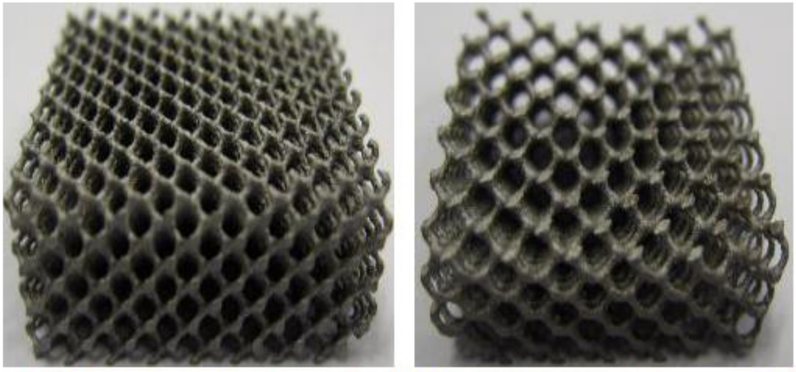

(a) Unit cell size=3mm, volume fraction=10% (b) Unit cell size=4mm, volume fraction=10%

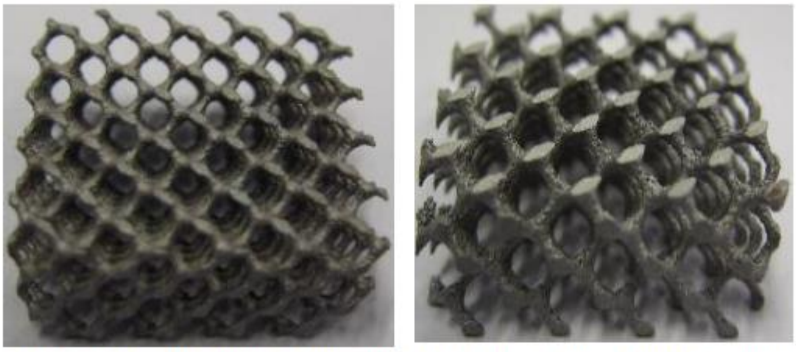

(c) Unit cell size=5mm, volume fraction=10% (d) Unit cell size=6mm, volume fraction=10%

Figure 7.16 DMLS-Manufactured AlSi10Mg Schwartz Diamond cellular structures

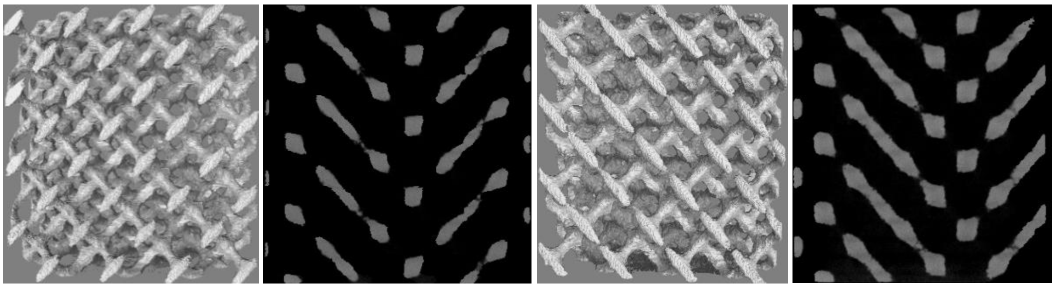

Volume fraction=15%; Cell size=5.5mm Volume fraction=15%; Cell size=6mm

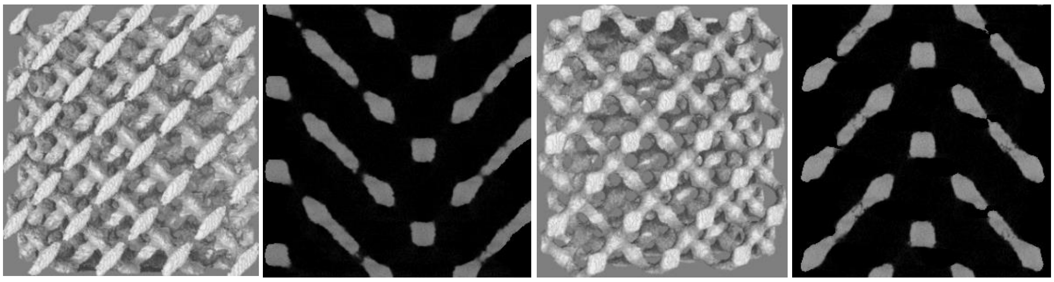

Volume fraction=15%; Cell size=6.5mm Volume fraction=15%; Cell size=7mm

Figure 7.17 μ-CT reconstruction models and cross section images of diamond cellular structures at different unit cell sizes [DMLS M280, AlSi10Mg]

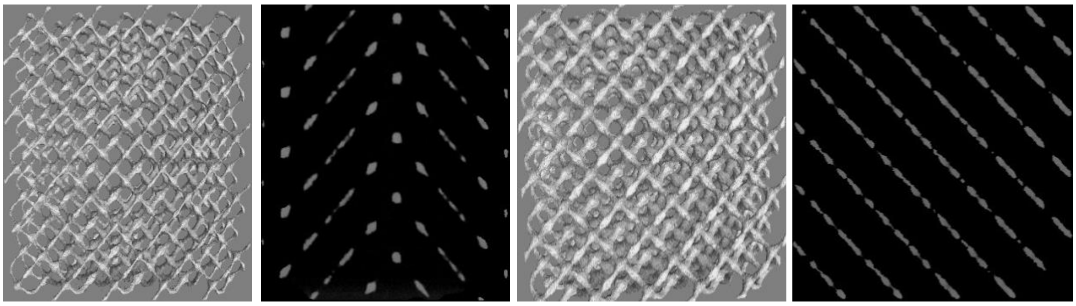

Volume fraction=5%; Cell size=5mm Volume fraction=10%; Cell size=5mm

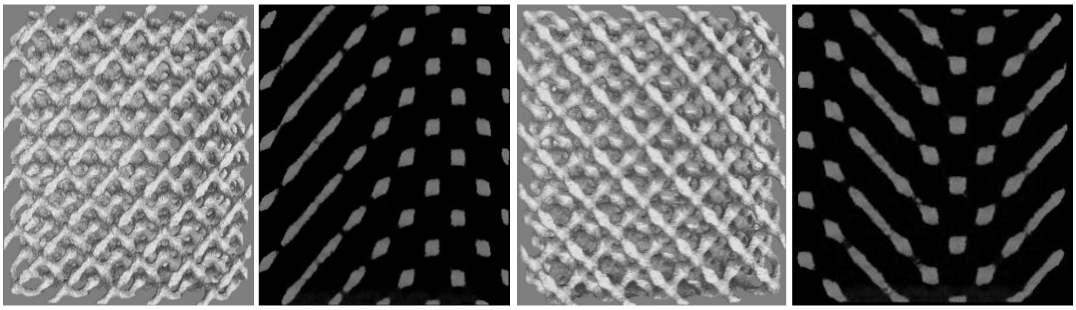

Volume fraction=12.5%; Cell size=5mm Volume fraction=15%; Cell size=5mm

Figure 7.18 μ-CT reconstruction models and cross section images of diamond cellular structures at different volume fractions [DMLS M280, AlSi10Mg].

7.3.2.2 SEM analysis

The SEM images taken from DMLS-manufactured Diamond struts are shown in Fig. 7.19. This image is based on cellular structure specimen that was not heat treated or bead blasted. This was done deliberately to compare with other bead-blasted and heat-treated parts. Bonded particles can be seen on the surfaces of the struts which are lesser but similar in shape to those observed in the 316L stainless steel cellular structure manufactured in SLM-MCP Realizer. Since the natures of the two processes are similar, it is believed that the mechanisms which form the bonded particles are also the same as discussed previously (Refer to section 7.3.2.1). A hull and core strategy is used in DMLS which is similar to the SLM outer-boundary and inner-hatch scanning strategy. On heated the outer boundary, some AlSi10Mg particles are partially melted by the contour laser scan. As a result, partially melted particles are bonded on the surfaces of the cell strut.

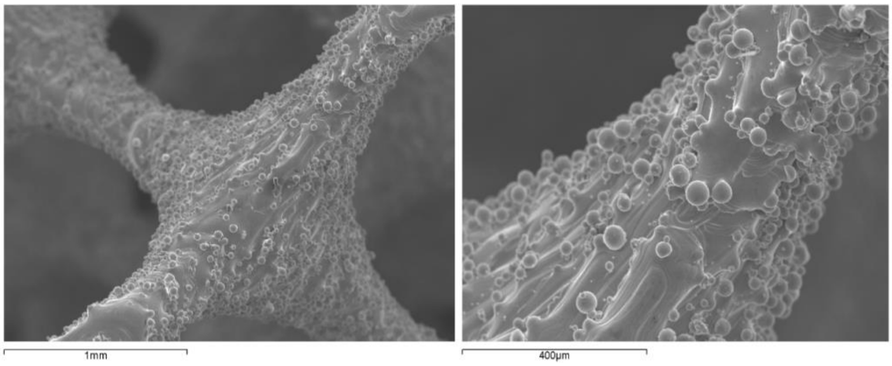

Figure 7.19 SEM images of the struts of Diamond cellular structures before the heat treatment (Volume fraction=15%; unit cell size=3.5mm) [DMLS M280, AlSi10Mg]

To improve the surface quality of the struts, a post-processing heat treatment and bead-blasting process was performed on cellular structures. Fig. 7.20 shows the captured SEM images of the heat-treated struts of the DMLS-manufactured cellular structures. It can be seen that nearly all the bonded particles on the strut have been eliminated and smoother surfaces is formed after the post-processing. This is because the bead-blasting operation removes any loosely sticking particles on surface, and heat treatment makes partially melted AlSi10Mg powder particles fuse and bond to the core of the strut. The manufactured Diamond structure having a volume fraction of 7.5% and cell size of 3mm has a thin strut size of 280 ±10µm. This demonstrates the DMLS ability to build fine and delicate cellular structures and offer lightweight structures from AlSi10Mg. More importantly, DMLS can make more accurate structures to achieve controllable and repeatable properties.

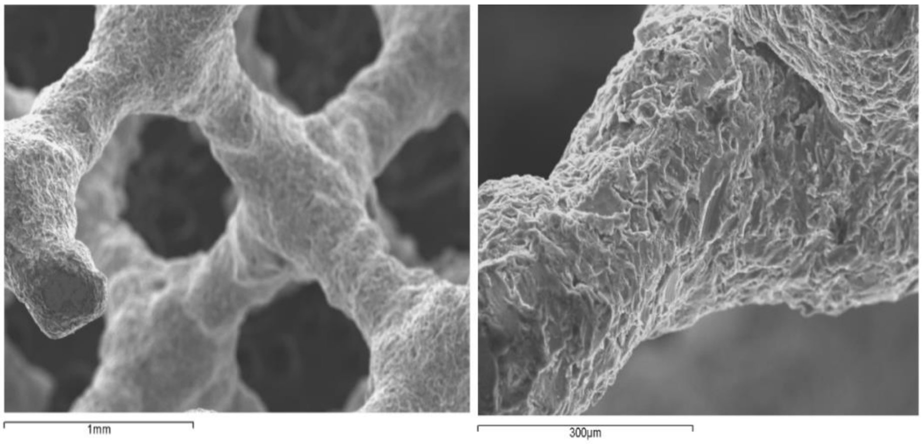

Figure 7.20 SEM images of the struts of Diamond cellular structures after it has been bead-blasted and heat treated (Volume fraction=7.5%; unit cell size=3mm) [DMLS M280, AlSi10Mg]

7.3.2.3 Optical Microscopy

Fig. 7.21 shows the optical microscope images captured from the DMLS-manufactured AlSi10Mg Diamond structures having a fixed volume fraction of 10% and cell sizes ranging from 3.5-6.5mm. The measured dimensions of the cellular structures are compared with the nominal CAD dimension as depicted in Figs.(7.22 and 7.23)

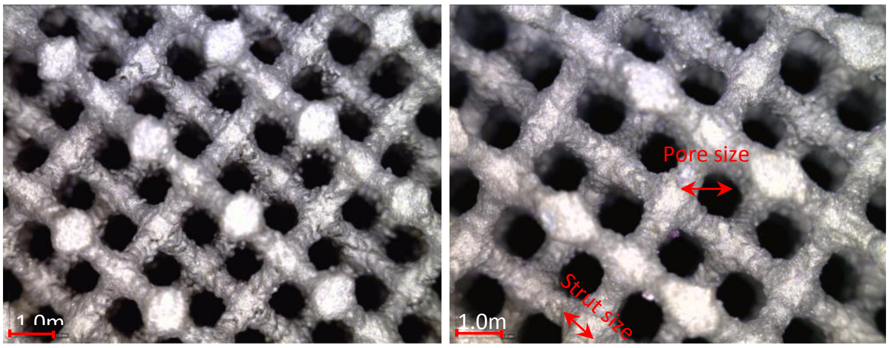

(a) Cell size=3.5mm; volume fraction=10%

(b) Cell size=4.5mm; volume fraction=10%

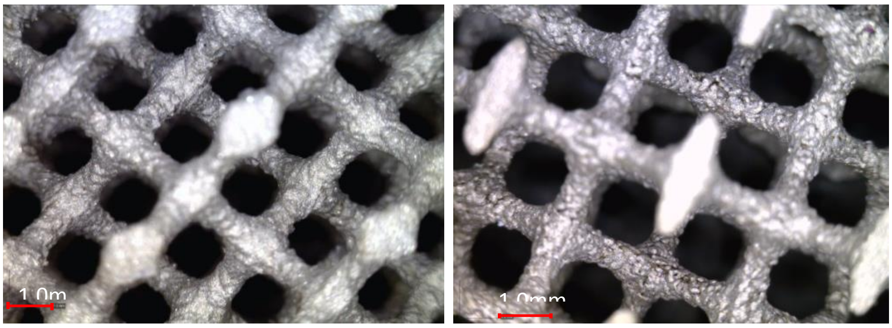

(c) Cell size=5.5mm; volume fraction=10%

(d) Cell size=6.5mm; volume fraction=10%

Figure 7.21 Optical microscope images of the DMLS-manufactured cellular structures with volume fraction = 10% and different cell sizes [DMLS M280, AlSi10Mg]

Fig. 7.22 reveals that the experimental strut sizes are higher than the CAD values while experimental pore sizes are lower compared with the CAD pore sizes. The increase in the strut size and decrease in the pore size compared with the CAD values can be attributed to the bonded and partially melted metal particles on the strut surfaces. The bead blasting helps remove the particles which are not strongly bonded to the strut surface, while the heat treatment makes the remains of the bonded particles to fuse and bond to the strut, leading to an increase of strut sizes and decrease in the pore size. The strut and pore sizes both increase with increasing the cell size for a fixed volume fraction. The opposite is true when the cell size is decreased. As shown in Fig. 7.23, the strut size increases and the pore size decreases when increasing the volume fraction at a fixed cell size

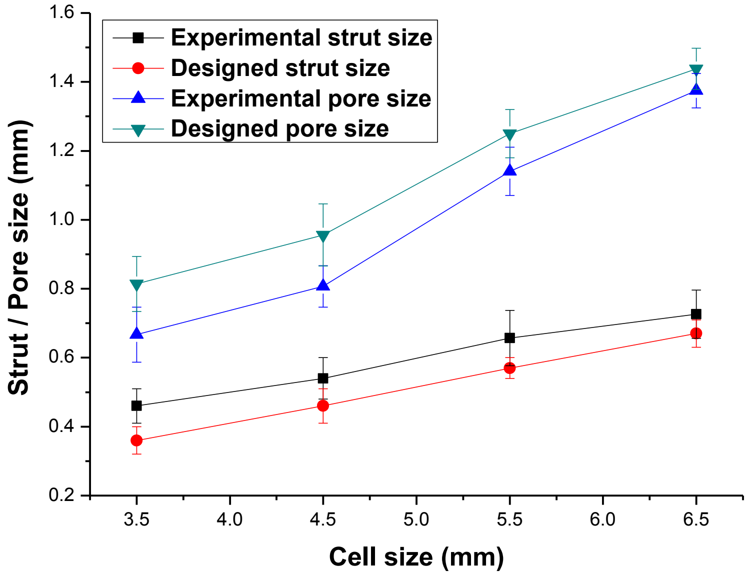

Figure 7.22 Strut and pore sizes measured from optical microscope image (experimental) and CAD models (designed) in function of the unit cell size. The volume fraction is set as a constant of 10% [DMLS M280, AlSi10Mg].

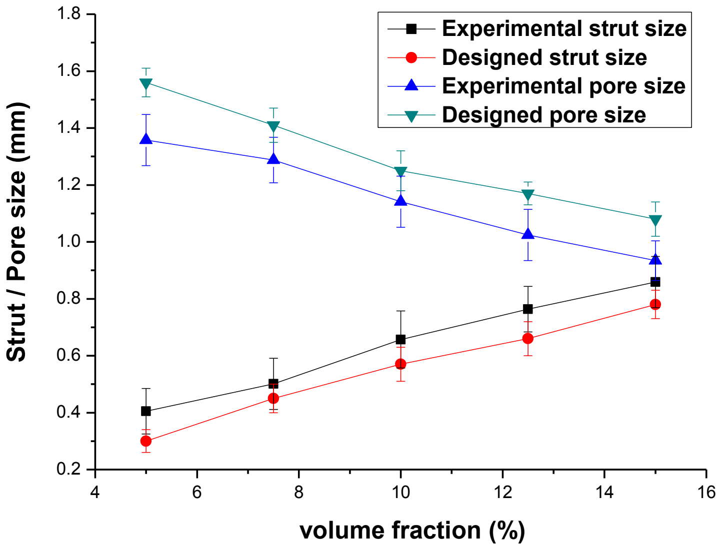

Figure 7.23 Strut and pore sizes measured from optical microscope image (experimental) and CAD models (designed) in function of the volume fraction. The unit cell size is set as a constant of 5.5 mm [DMLS M280, AlSi10Mg].

7.3.3 Ti-6Al-4V Cellular Structures

7.3.3.1 Manufacturability study

Figs. (7.24-25) show the DMLS-processed Gyroid and Diamond cellular structures with various cell sizes and volume fractions. For both cell types, all tested cell sizes (3-7mm) and volume fractions (5-20%) were successfully manufactured in DMLS-M270 machine using Ti-6Al-4V metal powder. Of all the standard materials used in DMLS, the Ti-6Al-4V as used in this study is considered as one of the most difficult material to process in SLM and DMLS due to its high reactivity with oxygen. There is high mechanical stresses involved in the build process and thus has the highest demands of support structure. Fig. 7.26 shows the DMLS-manufactured Gyroid cellular structure with different cell orientations from 20^0 to 180^0. These cellular structures were built with a fixed cell size of 5mm and volume fraction of 15%. As indicated in the figure, all tested cell orientation was built without failure. The self-supporting characteristic of the cell type and topology enable to build all possible cell orientation.

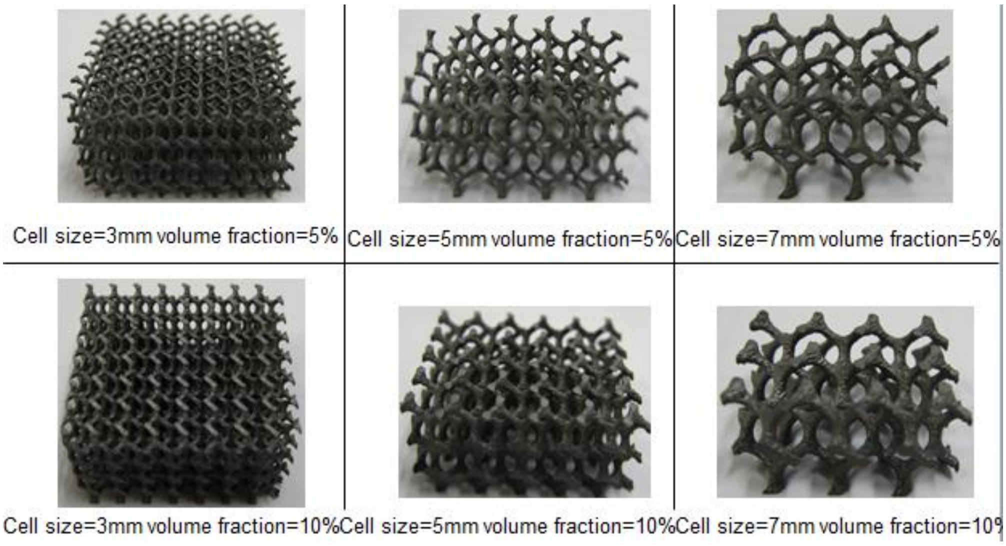

Cell size=3mm volume fraction=5%
Cell size=5mm volume fraction=5%
Cell size=7mm volume fraction=5%
Cell size=3mm volume fraction=10%
Cell size=5mm volume fraction=10%
Cell size=7mm volume fraction=10

Figure 7.24 Manufactured Gyroid cellular structures with various cell sizes and volume fractions [DMLS M270, Ti-6Al-4V]

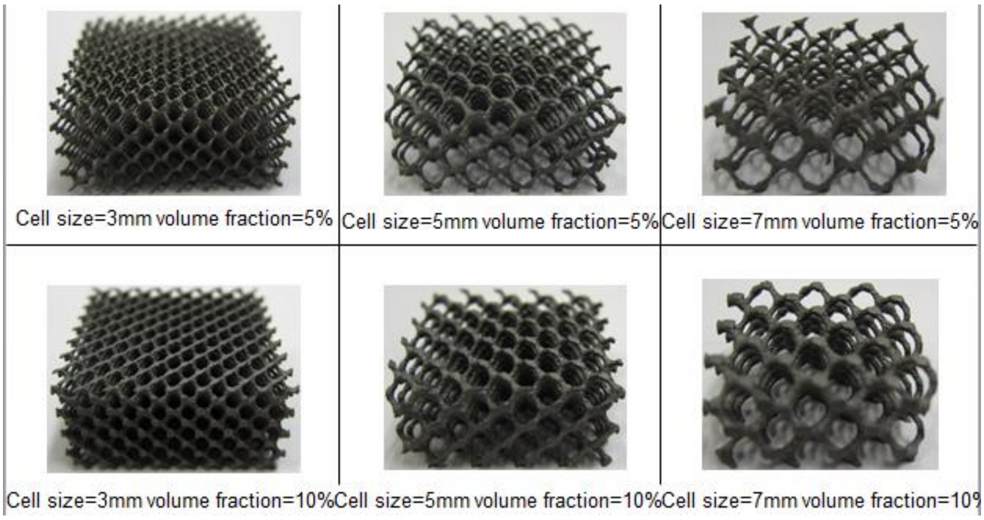

Cell size=3mm volume fraction=5%
Cell size=5mm volume fraction=5%
Cell size=7mm volume fraction=5%
Cell size=3mm volume fraction=10%
Cell size=5mm volume fraction=10%
Cell size=7mm volume fraction=10

Figure 7.25 Manufactured Diamond cellular structures with various cell sizes and volume fractions [DMLS M270, Ti-6Al-4V]

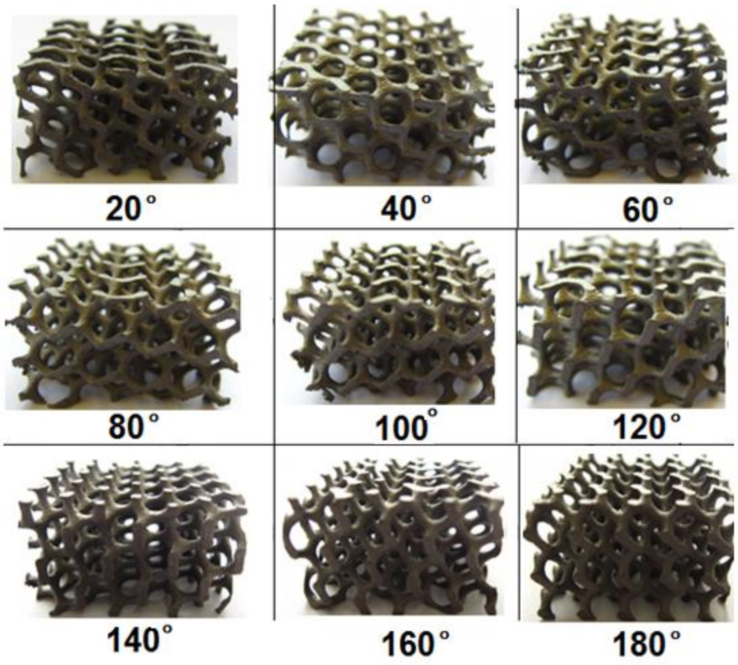

Figure 7.26 Manufactured Gyroid cellular structures with cell size = 5mm, volume fraction=15%, and various cell orientations (20^0-180^0) [DMLS M270, Ti-6Al-4V]

7.3.3.2 μ-CT Analysis

Fig. 7.27 shows the μ-CT 3D reconstruction models of Gyroid structure and reveals that no defects or broken cells are present within the structures, indicating the good manufacturability of these cellular structures in DMLS process. Fig. 7.28 further shows the 3D construction models of cellular structures with different cell orientations which also show no feasible broken struts in lattice network. The cross-sectional images in Fig. 7.29 show fully dense and no apparent pores in the cellular struts. The Titanium structure show favourable manufacturability at low volume fraction and cell sizes for both Gyroid and Diamond structure.

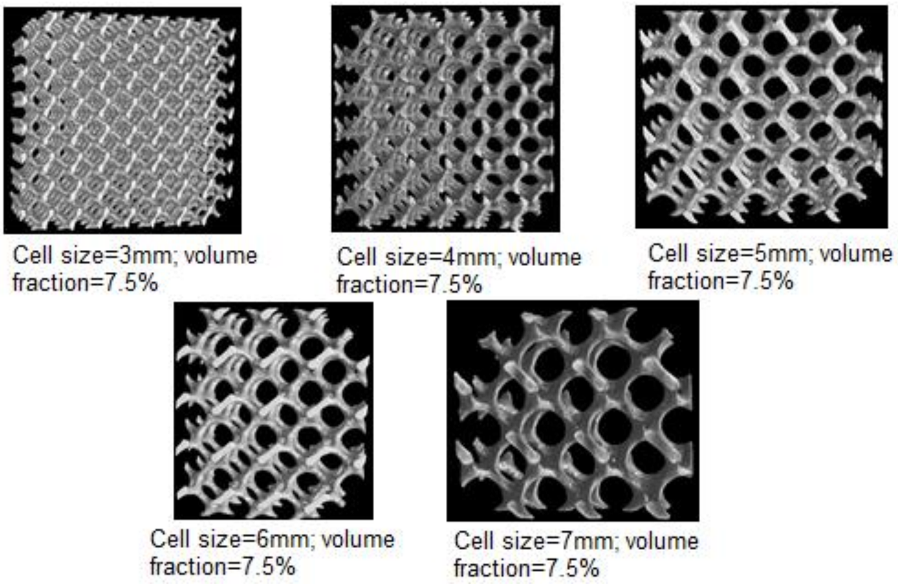

Cell size=3mm; volume fraction=7.5%

Cell size=4mm; volume fraction=7.5%

Cell size=5mm; volume fraction=7.5%

Cell size=6mm; volume fraction=7.5%

Cell size=7mm; volume fraction=7.5%

Figure 7.27 CT reconstruction 3D models of Gyroid cellular structure with varying cell size [DMLS M270, Ti-6Al-4V]

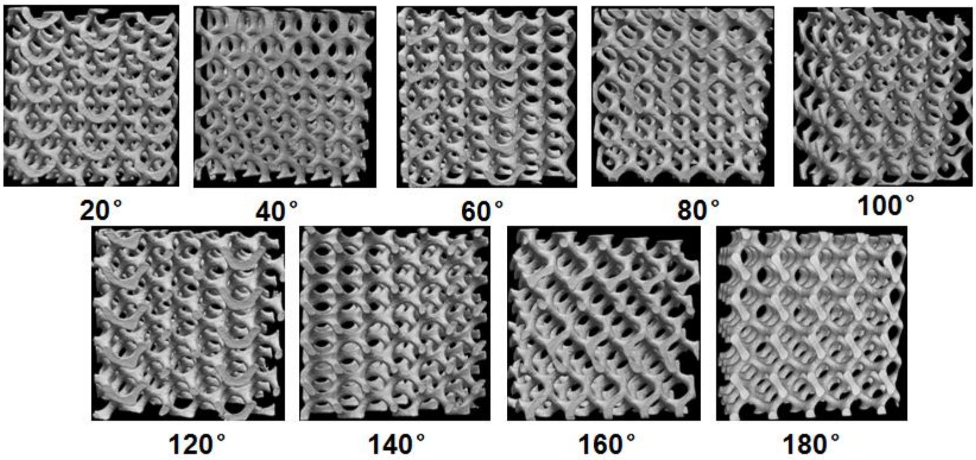

Figure 7.28 CT reconstruction 3D models of Gyroid cellular structure with varying cell orientation [DMLS M270, Ti-6Al-4V]

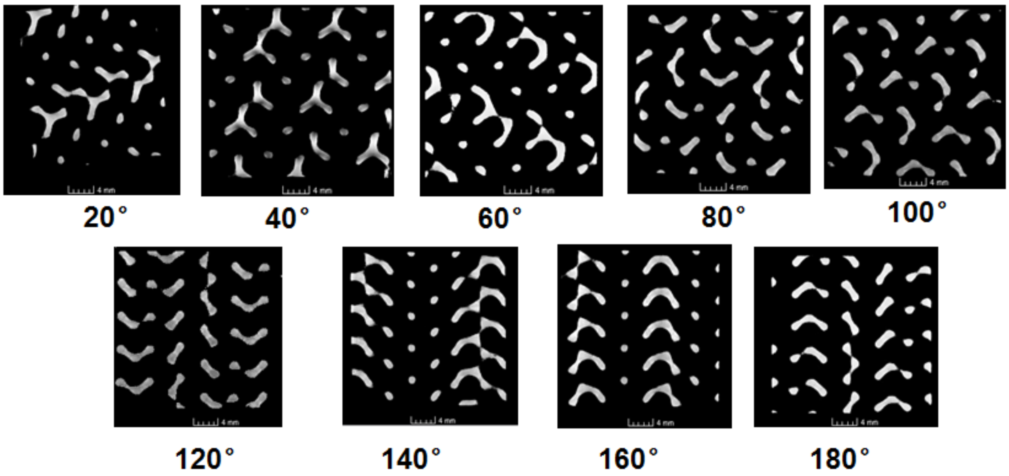

Figure 7.29 µ-CT cross-sectional images of the struts of Gyroid cellular structures at various cell orientations [DMLS M270, Ti-6Al-4V]

Fig. 7.30 shows merged µ-CT 3D reconstruction model and the 3D CAD model of the Gyroid structure. This was done to compare the dimensional accuracy of the manufactured cellular structures with the nominal CAD model. Fig. 7.30 (a) shows Gyroid structure with 4mm cell size and 7.5% volume fraction. The gradient shows that the designed and built architectures nearly coincide within at a standard deviation of 0.1196mm, indicating a very high accuracy of the technique. Similarly it can be seen in Fig. 7.30 (b) that Gyroid structure with 7mm cell size and 7.5% volume fraction is very well reproduced in comparison to the original design CAD model with standard deviation of 0.2103mm. This variation can be attributed to a non-uniformity of the bonded powder particles observed in the experimental samples.

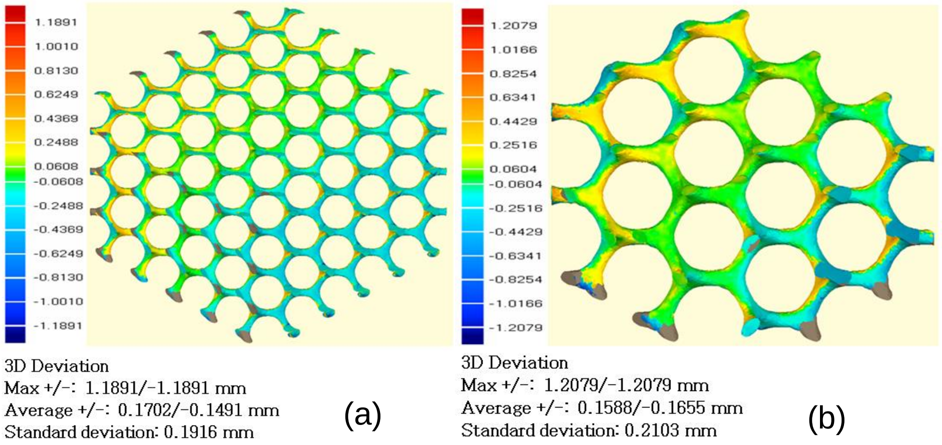

Figure 7.30 Comparisons of the µ-CT 3D reconstructed surface and 3D CAD model of the Schoen Gyroid cellular structure with fixed volume fraction of 7.5% (a) cell size=4mm (b) cell size = 7mm [DMLS M270, Ti-6Al-4V].

7.3.3.3 SEM analysis

The SEM micrograph of Gyroid structure with 3mm cell size and 8% volume fraction shows powder particle covering all over the cell strut as shown in Fig. 7.31(a). Partially melted bonded-particles can be seen on the surface of the manufactured strut when the normal post-processing of bead-blasting and heat treatment is not performed. The fractured rough surface of the strut is an indication of brittle fracture. Fig. 7.31(b) shows the SEM images of a rough fractured surface features similar to shear yielding and crack pinning, indicating that more energy was required to form the deformation strain of titanium samples.

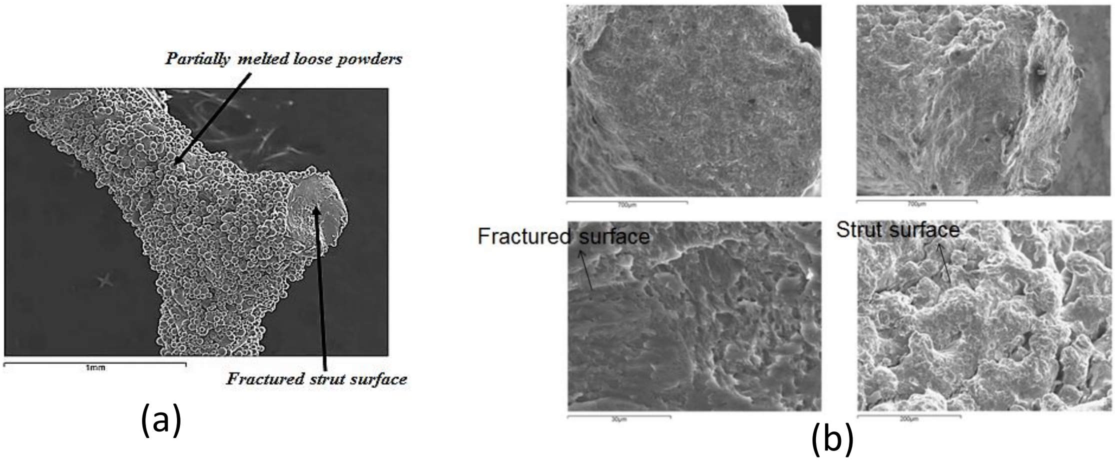

Figure 7.31(a) SEM micrographs of cellular strut without post-processing, (b) Strut and fractured surfaces of Gyroid with post-processing [cell size =3mm, volume fraction =8% - DMLS M270, Ti-6Al-4V].

7.4 Conclusion

This chapter has presented a comprehensive manufacturability study of advanced TPMS cellular structures using SLM and DMLS processes. The cellular structures were produced from three most commonly used metal AM powders being 316L stainless steel, Titanium alloy (Ti-6Al-4V), and Aluminium alloy (AlSi10Mg). Cell sizes ranging from 2-9mm, orientation angles from 20^0 to180^0, and volume fractions from 5-20% were investigated. The manufactured cellular structures were characterized by visual observations, µ-CT (porosity and defects, by 2D and 3D reconstruction models), SEM (size, morphology), and Optical Microscopy (size). The following conclusions can be made from these investigations,

- Gyroid and Diamond cellular structures made from 316L stainless steel with cell sizes ranging from 2–9 mm and volume fractions from 6-15% were manufactured in SLM. Samples show good manufacturability except for 9 mm cell size which exhibit some deformed horizontal struts perpendicular to the build direction. The deformation in the form of sagging was observed specially in Gyroid cell structure. However, by increase on volume fraction above 15% would attain un-sagged larger cell sizes >9mm. There was no problem of removing the loose powder from the 2mm cell sizes which is trapped inside the cellular structures.
- The AlSi10Mg Diamond structures manufactured in DMLS with low volume fraction of 5% and with cell sizes ≤ 6.5mm reveal some broken struts inside

the cellular structure. However, as the cell size was increased to 7mm, no broken cells were found in the structure. This indicates the lower limit of volume fraction and cell size for AlSi10Mg Diamond cellular structures. Gyroid cellular structure has better manufacturability compared to Diamond for AlSi10Mg when low volume fractions less than 6% are combined with small cell sizes less than 7mm.

- The Ti-6Al-4V Gyroid and Diamond cellular structures were produced in DMLS. Cell size as small as 3mm and volume fraction as low as 5% have shown good manufacturability characteristics.
- All tested cell orientation including the worst orientation (i.e. cell orientation that forms the maximum unsupported overhanging of the strut) was manufactured in both SLM and DMLS processes.
- The Schwartz W and Neovius surface also prove to be manufacturable at large cell sizes and volume fractions. The large node of Schwartz W is associated with more material to be melted by the laser beam which could cause unstable melt pool and temperature-stress gradients. Some of the edges of the Neovius structure were curled and fractured surfaces could be seen on manufactured cell struts.
- The 2D cross-sectional images of the µ-CT for AlSi10Mg and Ti-6Al-4V display very dense solid struts in all cell sizes and volume fractions with no sign of feasible porosity. However, tiny micro-porosities were obtained in 316L stainless steel structures in particular for large cell sizes. Better wetting conditions and proper bonding between layers exist in small cell sizes that permit denser struts of the cellular structures. Unlike DMLS M270, which use optimized parameters for different materials, the parameter for SLM MCP Realizer were not optimal and it was difficult to control the oxygen content in build chamber. The layer thickness used in stainless steel structures was also higher. These factors are believed to contribute to the low densities found in stainless steel parts.
- The 3D reconstruction models captured from the µ-CT indicates no obvious defects or missing/broken cells within the structure, confirming the ability of SLM to manufacture the Gyroid and Diamond cellular structures, and over the whole range of cell sizes tested. The µ-CT was particularly helpful in providing more details on small cell sizes where defects of the interior cells could not be detected by visual observation only. The comparison of the 3D

reconstructed data and original CAD models generally shows good dimensional accuracy of SLM/DMLS manufactured cellular structures.

- The SEM micrograph of the manufactured cellular structure of cell struts shows bonded powder particles caused by partially melted surrounding loose powders. The attached loose powders are the result of stair-stepping effect and outer contour scanning of the laser beam. This increases the surface roughness of the cell struts forming the structure. Much improvement of the strut surface roughness was obtained for cellular structures processed in DMLS that were bead-blasted and heat treated.
- Optical microcopy measurements shows small increase in strut sizes in all experimental parts, irrespective of, the cell type, size, volume fraction, material, and the process involved. Increases thickness of strut and shrinking pore size is the result of the bonded powder particles. This is also from increased melt-pool due to the high laser energy concentrated in small cell strut cross-sections.
- These organic cellular structures with controlled cell sizes and densities which are very difficult or impossible to be manufactured by means from light metallic alloys such Ti-6Al-4V and AlSi10Mg are now proved to be manufacturable in SLM and DMLS processes. The good manufacturability of Gyroid and Diamond cell types in SLM/DMLS can be attributed to the curved struts and spherical pore forming the unit cell. The inclination angle of the circular strut continuously varies along the spherical pore, which makes layers grow up gradually with slight changes in area and position between two subsequent layers during the SLM/DMLS process. In this way, the next layer is well supported by previously solidified layer. That means that these TPMS cellular structures have a self-supported unique characteristic in a wider range of cell sizes, volume fractions, and cell orientation which makes them suitable for SLM and DMLS processes.
- Possible improvements on the manufacturability, density, and dimensional accuracy of the cellular structures could be achieved by using specialized processing parameters and scanning strategy suitable for these structures. The current methods used in the experiments were designed for large cross-sectional geometries and generates large melt-pool in tiny cross-sectional of cell struts. By optimization of the laser power, speed, and scanning pattern, the energy input in these structures could be reduced. This will result more

accurate and denser structures. Well controlled powder particle distribution is also needed, and a proper post-processing steps such as sand/air/bead blasting and heat treatment of structures to improve the surface quality.

- This verification should allow the use of advanced TPMS cellular structures in wider applications. For example, Titanium alloy which is currently processed in metal AM for aerospace components for its high strength to weight ratio can be made from these functional lightweight structures while also reducing the processing cost and energy consumption. Cellular structure made from Ti-6Al-4V is also getting a considerable interest in for implants in medical industry for its biocompatibility. T. Traini et al (2008) reported that the direct metal laser sintering technique can efficiently build porous titanium dental implants. He highlighted that DMLS proved to be an efficient means of construction of dental implants with functionally graded material. This is particularly important as Titanium alloy is one of the most difficult materials to process in conventional manufacturing techniques.
- Besides its lightweight, AlSi10Mg has a good thermal property suitable in heat transfer applications such heat exchangers, while stainless steel can be used in applications where moderate strength is needed such as structural sandwiches. Matthew Wong et al (2007) fabricated the heat sink devices from Aluminium 6061 via SLM which evidently proved to be more feasible and efficient. Cellular structures made from these materials can also play important role in promoting the use of metal AM in much larger sale.

Chapter 8 Evaluation of the Mechanical Behaviour of TPMS Cellular Structures

8.1 Introduction

Metallic cellular structures are used in many structural applications due to their lightweight and high energy absorption capability. If such materials are to be used efficiently, a detailed understanding of their mechanical behaviour is very important. In the design development, it is of highest importance to choose the proper shape, size, orientation, and volume fraction of cellular structures to fulfil specific functional requirements. This is based on studying the stress-strain behaviour of different cell shapes, sizes, and volume fractions that can be extracted from experimental test curves or predicted by means of mathematical models. The compressive properties, such as the elastic modulus and plastic collapse stress of the cellular materials are important parameters for the mechanical design of components.

It could be very onerous to experimentally characterise and identify the mechanical behaviour of different shapes of cellular structures with wide range of cell sizes, volume fractions, and cell orientations. A unified mathematical model which can predict the properties of a large set of cell sizes and volume fractions for a given material and identified with less experimental testing could be very helpful to direct the selection of cellular structures for specific application. A number of micromechanical models have been developed over the years to describe the mechanical behaviour of cellular solids; however, the model developed by Gibson and Ashby (1997) is the most commonly used and appears to predict their behaviour with reasonable accuracy.

This chapter investigates the compressive properties of TPMS cellular structures (Schoen Gyroid and Schwartz Diamond) manufactured in SLM MCP-Realizer and DMLS M270/280 machines. Chapter 7 provides detailed explanations on the manufacturability of these cellular structures. These structures were manufactured from 316L stainless steel, AlSi10Mg, and Ti-6Al-4V metallic powders. Rigorous mechanical testing was performed to enhance the understanding of the behaviour of these cellular structures under uniaxial compression testing. The effect of cell size, volume fraction, and cell orientation on compressive elastic modulus and yield strength were examined. The experimental results were compared with the analytical model developed by Gibson and Ashby. This was done to determine and improve the accuracy of the model for future predictions using experimental data.

8.2 Gibson-Ashby (GA) Model

For design purposes, a unified prediction model of a larger set of cellular structures and materials with less experimental testing could be very beneficial. A unique model for cellular solids made of the same constitutive material and for a wide range of cell size and volume fractions could be used to direct the choice of the optimal cellular structure density for defined impact energy absorption. The approach in these various analyses is usually to identify a unit cell and assume a deformation mode leading to failure. The Gibson and Ashby model is based on a cubic unit cell (see Fig. 8.1) where the deformation is controlled by the bending of the individual struts within the unit cell. This feature of the GA model is useful when few experimental data on the density effect are available which can be used to improve the model accuracy. The cell shapes in Gyroid and Diamond cellular structure are, of course, more complex than that shown in Fig. 8.1. But if they deform and fail by the same mechanisms, their properties can be understood using dimensional arguments which omit all constants arising from the specific cell geometry.

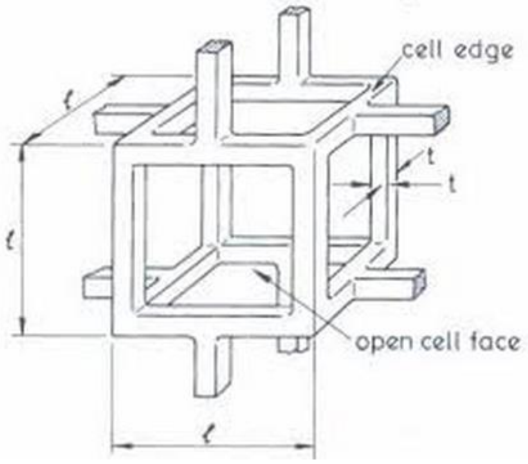

Figure 8.1 A cubic model for an open-cell foam showing the edge length, l, and edge thickness, t (Gibson and Ashby, 1997).

GA model uses a simple dimensional approach to describe the mechanical behaviour in terms of the strut dimensions which are also related to the relative density. Because many applications of cellular structures result in compressive loading, Gibson and Ashby formulate expressions for the mechanical properties of cellular foams or honeycomb structures based on the compressive behaviour. The relative density (This is equivalent to the volume fraction) of the cell, ${\rho^*}/{\rho_s}$, and the second moment of area of cell strut, I, can be related to the dimensions t and *l* by,

$$\rho^*/\rho_s \propto (t/l)^2 \tag{8.1}$$

$$I \propto t^4 \tag{8.2}$$

where *t* is the thickness of a strut of square cross section and *l* is the length. The strut length is directly proportional to the cell size and therefore l is sometimes used to represent the cell size. ρ^* and ρ_s are densities of the cellular structure and bulk material respectively.

The elastic modulus is calculated from the linear elastic deflection of a strut of length, *l,* loaded at its midpoint by a load F. Standard beam theory (Timoshenko and Goodier, 1970), gives the deflection as,

$$\delta \propto Fl^3/E_S I \tag{8.3}$$

where E_S is the elastic modulus for the material of the cell strut. The force F, is related to compressive stress by,

$$F \propto \sigma . l^2 \tag{8.4}$$

while the global strain is proportional to the displacement as,

$$\varepsilon \propto \delta/l \tag{8.5}$$

These relationships are then combined using Hooke’s law of elasticity to determine expression for the elastic modulus,

$$E^* = \frac{\sigma}{\varepsilon} = \frac{F}{l^2} \cdot \frac{l}{\delta} \tag{8.6}$$

or,

$$E^* = \frac{C_1 E_S I}{l^4} \tag{8.7}$$

In general form,

$$E^*/E_s = C_1(\rho^*/\rho_s)^2 \tag{8.8}$$

The plastic-collapse strength of the cellular structure can be determined as,

$$\sigma_{pl}^{*}/\sigma_{ys} = C_2({\rho^{*}}/{\rho_s})^{3/2} \tag{8.9}$$

where E_s and E^* are the elastic modulus of a bulk solid material and cellular structure respectively; σ_{ys} and $\sigma_{pl}{}^{*}$ are the yield strength of a bulk solid material and plastic yield strength of cellular structure respectively, and $C_{,1,2}$ are constants of proportionality which is characteristic of the cell geometry. Data by Gibson and Ashby show that showed that $C_1 \approx 1, and\ C_2 \approx 0.3.$ The density exponents give reasonable agreement for many types of cellular foams. Equations (8.8) and (8.9) suggest that compressive properties mainly depend on relative density of the structure.

8.3 Uniaxial compression test

Static uniaxial compression tests have been performed on two types of TPMS cellular structure with different cell sizes, volume fractions (relative density), and cell orientations. The Schoen Gyroid and Schwartz Diamond cellular structures were selected for the uniaxial compression test. These cellular structures have a relative density ranging from 5 to 15%, cell size from 2 to 8mm, and an orientation from 20 to 180 degree. The experimental procedures used to manufacture these cellular structures have been presented in chapter 7. These TPMS cellular structures were made from 316L stainless, AlSi10Mg, and Ti-6Al-4V metal powders. The test pieces were provided in a cubic shape (dimensions: 25mm x 25mm x 15mm) as shown in Fig. 8.2. A cube is selected for the geometric shape of specimens to prevent buckling during the compression process. The cube dimensions were kept the same for all samples tested. Both the top and bottom of these compression samples are sandwiched between 15mm thick facing smooth plates made from hardened steel. This allows proper alignment between a test sample and the upper/lower platforms of testing frame. The facing plates are treated as rigid bodies.

Compression tests were performed directly from the as-received specimens at ambient temperature. The load vs. displacement was monitored by a computer with a data acquisition system that controlled test under either constant loading speed or constant strain rate conditions. Further details on the testing procedure and equipment are described in chapter 3.

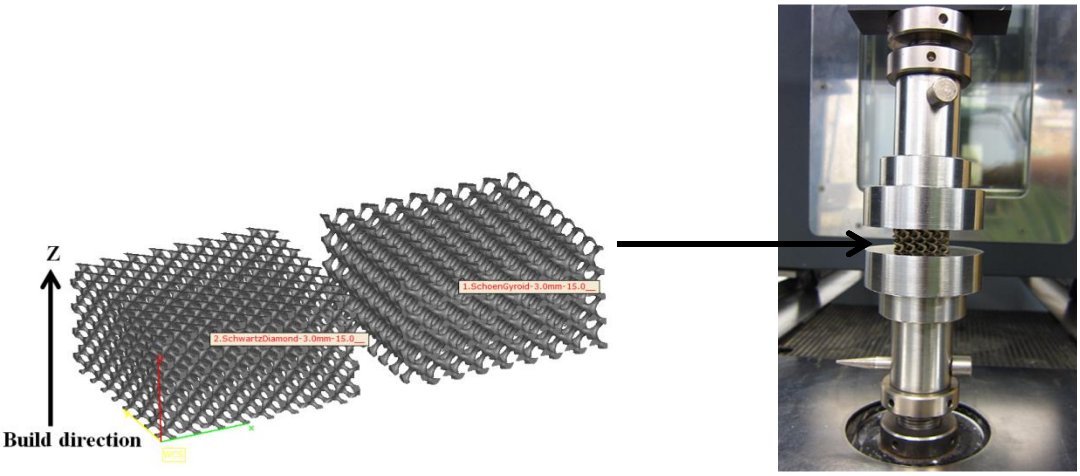

Figure 8.2 Gyroid and Diamond compression test samples

8.4 Results and Discussion

8.4.1 316L Stainless steel cellular structures

8.4.1.1 Effect of cell size on compressive behaviour

The compressive stress-strain curves obtained from Gyroid cellular structure with cell size ranging from 2 to 8mm are shown in Fig. 8.3(a). At the very beginning of loading, the curves have an initial portion which is non-linear and concave upwards. This is attributed to small amount of distortion of the struts when they are cut off from the base plate, or unevenness of the upper surface of the cellular structure. After that, the stress-strain curves exhibit a linear elastic region, followed by stress plateau, caused by plastic yielding and bending of cell struts. Further straining cause the collapse of the cell struts and densification (i.e. a sharp rise in stress) of the overall structure.

When the cells have almost completely collapsed opposing cell walls touch and further strain compresses the solid itself, giving the final region of rapidly increasing stress. The densification strain slightly varies for different cell size and occurs above 0.4 of compressive strain. At about 0.6 of compressive strain, the collapse of struts in the cellular structure is complete and the voids that were initially present in the material no longer exist. With densification complete, the stress drastically increases as the cellular structures take on the properties of the bulk solid material.

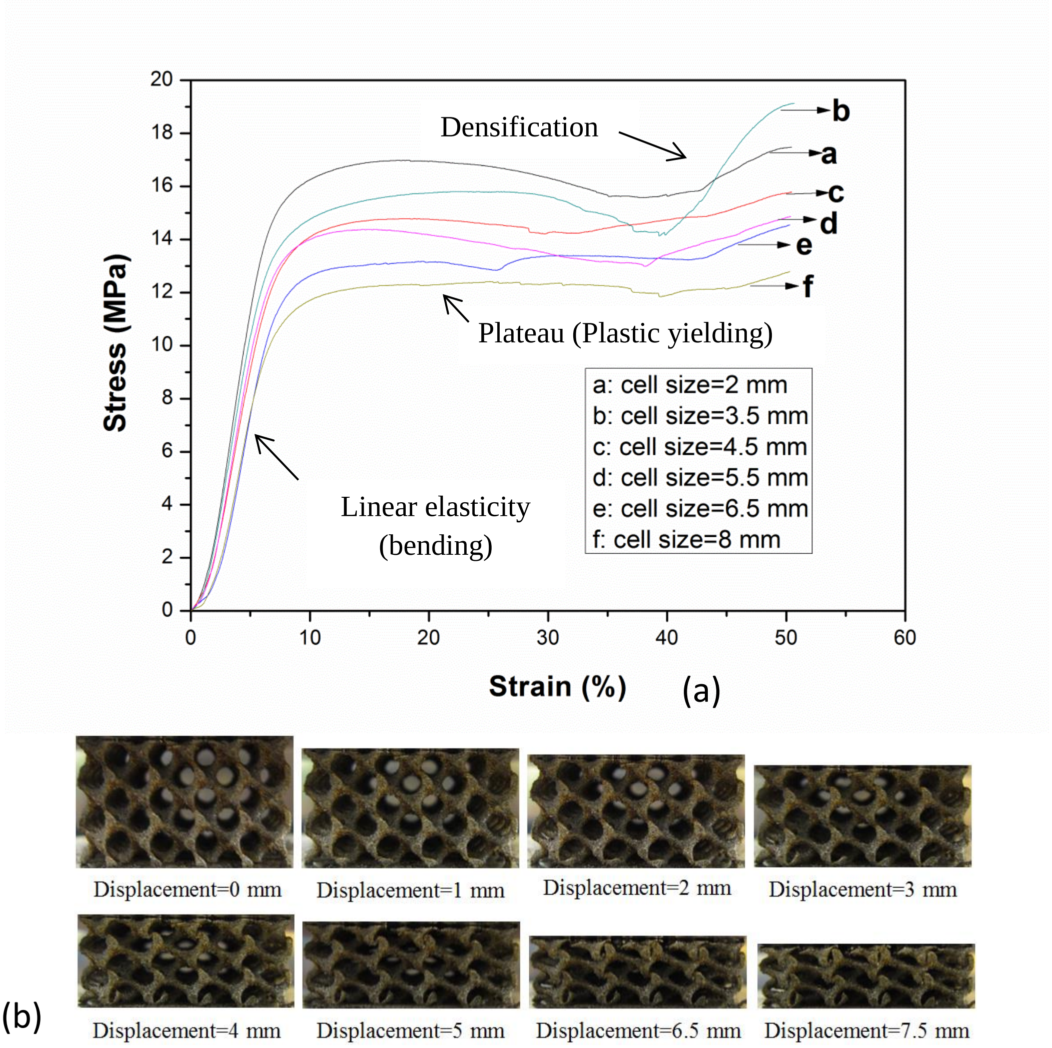

Figure 8.3 (a) Stress-strain curve of various cell sizes (b) Displacement steps of the test sample during compression test [cell size=5.5mm, volume fraction = 15% , stainless steel, SLM – MCP Realizer]

The images in Fig. 8.3(b) shows an increasing displacements compression crush behaviour of Gyroid cellular structures with constant volume fraction of 15% (i.e. relative density =0.15) and cell size of 5.5mm. Both the stress-strain curves in Fig. 8.3(a) and the snapshots in Fig. 8.2(b) show no signs of visible local brittle failure, and the cellular lattice structures show a steady, smooth progression of deformation throughout the testing process. Table 8.1 summarises the results of the yield strength and Elastic modulus of the Gyroid cellular structures. The data reveal that cell size influences both the elastic modulus and yield strength for a fixed relative density and that the influence is more significant for the plastic-yield strength. The yield strength varies from 12.98 MPa for cell size of 2mm to 12.41 MPa for cell size of 8mm. This represents an increase of 36% of yield strength and 27% of elastic modulus for cell size with 2mm in comparison to 8mm.

Table 8.1 Yield strength and Elastic modulus obtained from the compression tests of Gyroid cellular structures with constant volume fraction (i.e. relative density) of 15% and the variable unit cell sizes.

Unit cell size (mm)	Plastic yield strength, ${\sigma_{pl}}^*$ (MPa)	Elastic modulus, E^* (MPa)
2.0	16.98	305.72
3.5	15.80	281.72
4.5	14.78	251.71
5.5	14.37	251.14
6.5	13.17	243.94
8.0	12.41	241.36

The Gibson-Ashby model presented in equations (8.8 and 8.9) assumes that compressive properties are mainly dependant on relative density of the foam material. They argue that most mechanical and thermal properties depend only weakly on cell size and that cell shape matters more. There are a number of studies on the properties of metal foams under static and dynamic loading (Andrews et al. 1999; Li et al., 2003; Onck et al., 2001; Zhou et al. 2004), however, little has been reported on the effects of cell size on the mechanical properties. Many of these studies support that cell size has negligible effect on compressive properties. Nieh et a1 (2000) studied the compressive properties of open-cell 6101 aluminium foams with different relative densities and morphologies and found that cell size has a negligible effect (<0.5MPa) on the strength of foams, at a fixed density, whereas the cell shape affects the strength of foams. Chen (2003) studied the effect of cellular microstructure on the mechanical properties of open-cell aluminium foams produced by infiltrating process and found that cell size has a negligible effect on the compressive properties (modulus and strength).

On the other hand, there are other studies which strongly agree that cell size has significant effect on compressive properties. Wang et al. (2001)] studied the effect of cell size on the quasi-static compression and tension properties (strength and elastic modulus) on aluminium foam made by infiltrating process, and found that both the strength and elastic modulus were influenced by the cell size. Cao et al (2006) found that the elastic modulus and compressive strengths of the studied aluminium foam are not only dependent on the relative density but also dependent on the cell size of the foam under both quasi-static loading and dynamic loading. The contradictory results obtained till now about the effect of cell size on the elastic modulus and yield strength may be caused by the different method by which foams are made or the different morphology of foam structures.

The high elastic modulus and yield strength values obtained in small cell sizes could be attributed to the higher strut density of the strut solid. This was confirmed in chapter 7 by the μ-CT images of the 2D slices of small cell sizes which have shown higher number of micro pores (porosity) in big cell sizes. This manufacturing phenomenon is influenced by the higher energy of the laser beam which is concentrated in small cross-sectional area for small cell struts leading to a fully dense solid strut. Furthermore, in big cell sizes, the larger overhanging of the struts could cause some geometric imperfections/sagging during SLM/DMLS process which could lead to reduced stiffness and plastic yielding stress. However, the findings from this study did not address the effect of geometric imperfections on compressive properties of cellular structures. Full assessment on the effect of geometric imperfections (i.e. deformed cell walls, missing cells, porosity, and inclusion) on mechanical properties of TPMS cellular structure requires a separate experimental design and measurements. Such work is recommended for future works in chapter 11.

8.4.1.2 Effect of cell orientation on compressive behavior

Fig. 8.4 shows the relationship between the elastic modulus and cell orientation. The result is based on Gyroid cellular structure sample with 5mm cell size and 15% volume fraction. It can be seen that elastic modulus drastically varies at different orientations. As the graph indicate, the highest modulus lies somewhere between 40 and 60 degree of cell rotation. The compressive stress-strain curve of the worst manufacturable cell orientations with 5mm cell size and 15% volume fraction is shown in Fig. 8.5. The trend of the curve is consistent with the trends found in Fig.8.3 (a) and follows the general trends (linear elastic-plateau of plastic yielding-densification) seen in metal foams. The graph also shows that the worst orientation of Gyroid cellular structure has higher yield strength than normal cell with no orientation. The

Elastic modulus of the worst orientation is found to be 302.57 MPa, which is 20.37% higher than that of the normal orientation of similar cell size and volume fraction. Similarly, the yield strength of the worst orientation is 14.41 MPa and is 7.78% higher than that of the normal orientation. This indicates that the modulus difference is more significant than strength.

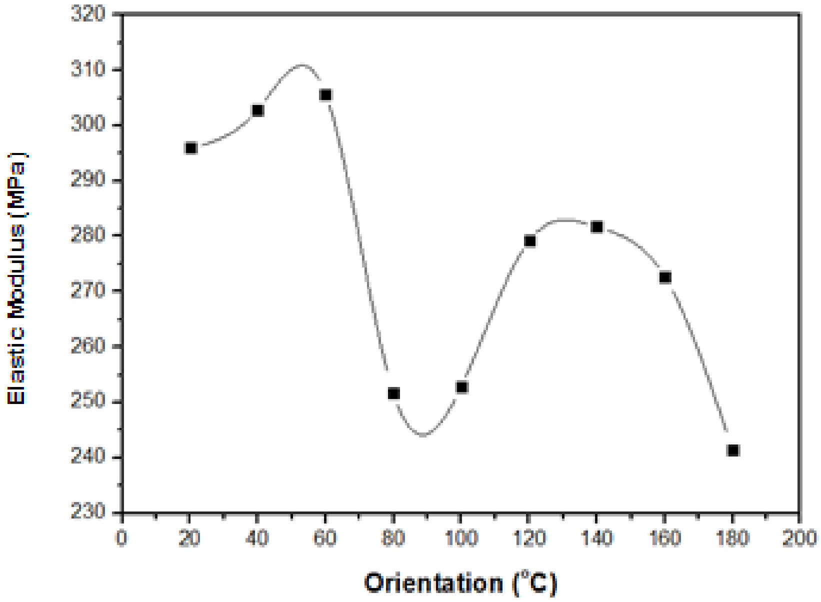

Figure 8.4 Effect of cell orientation on elastic modulus [stainless steel, SLM – MCP Realizer]

The increased stiffness and strength for the worst orientation can be attributed to the presence of the vertical struts in the cellular structure that are parallel to the loading direction. Similar conclusions were made for other cell shapes made from stainless steel in SLM (McKown et al., 2008), which found that the lattices with vertical struts greater than 45^{o} angle offer a significantly higher modulus despite the having the same porosity and possessing conditions. Cansizoglu et al. (2008) reported that lattices whose struts were oriented at an angle of less than 20o had little or no overlap between the successive melted layers resulting in weak structures. In this sense, a good overlap between subsequent layers provides a better bonding between subsequent layers and improved density of the cellular strut.

The cell orientation is mainly determined by the build orientation of the component in which the cellular structure is integrated. Since cell orientation influences the compressive properties, they can be deliberately rotated to match the strength requirements of the component. This is particularly beneficial as all Gyroid orientations have been proved to be manufacturable in SLM/DMLS process. These finding has provided importance information for the proper selection of cell orientation for different strength demands.

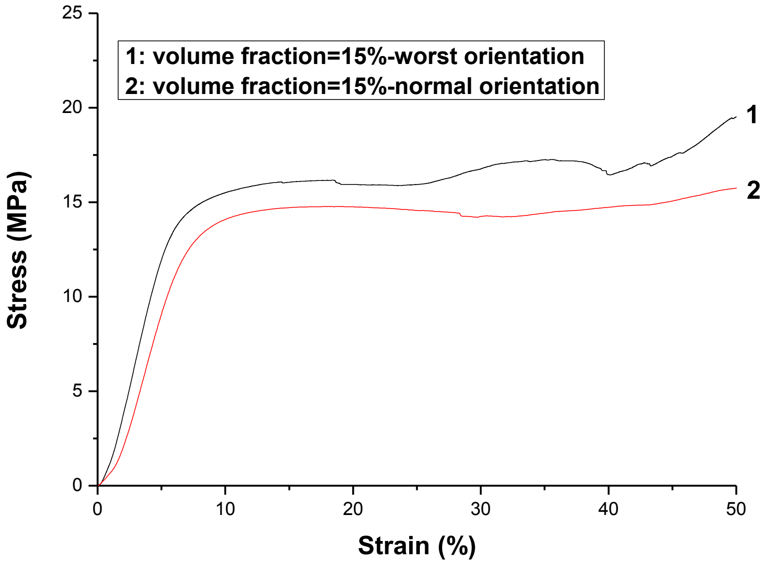

Figure 8.5 Stress-strain curves obtained from the compression tests on the gyroid cellular lattice structures at the normal or worst orientations. [Volume fraction is 15% and unit cell size is 5mm [stainless steel, SLM – MCP Realizer]

8.4.1.3 Experimental result vs. Modified Gibson-Ashby model

The elastic modulus and yield strength of bulk solid 316L stainless steel material is needed for calculating the compressive properties of cellular structure using Gibson-Ashby model. These values are considered to be 170 MPa and 193 GPa for yield strength and elastic modulus, respectively. In this work the parameters have been identified on the basis of the experimental curves so that the identified values can be compared to the theoretical ones. The original Gibson-Ashby model has been modified in order to test the possibility to improve its fitting capability. For this aim the structure of the Gibson parameters-density laws have been maintained but its parameters have been identified through the experimental data. The constants, C1 and C2, were estimated from experiments to be 0.06184 and 1.29165, respectively. Two equations were established to predict the approximate compressive properties of the Gyroid cellular structures. The result is based on constant cell size of 5 mm and relative densities ranging from 0.06 to 0.15. These relative densities are equivalent to solid volume fraction % from 6% to 15%. The calculated and experimental elastic modulus and yield strength are plotted against relative density (see Fig. 8.6 (a and b).

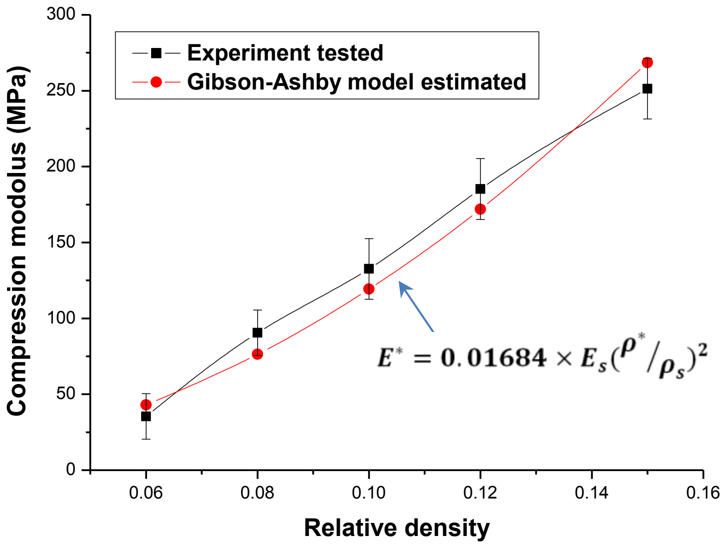

(a)

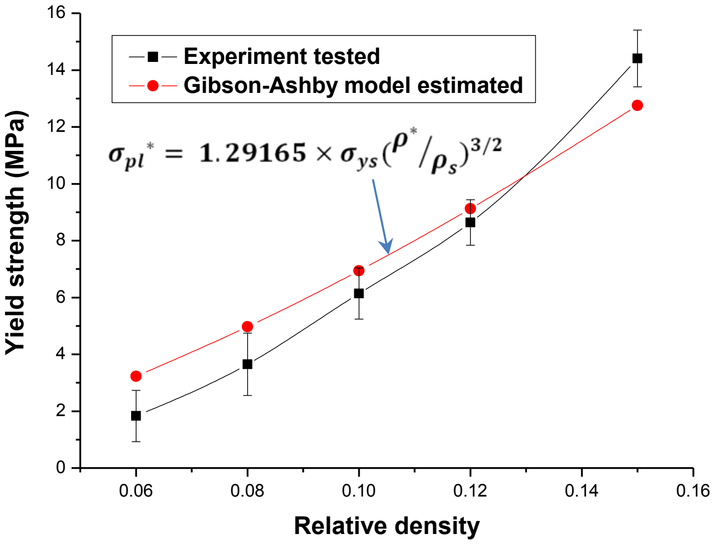

(a)

Figure 8.6 Experimental results of the Gyroid cellular structure compared to the modified Gibson-Ashby model with the identified parameters (a) compressive modulus and (b) compressive strength as a function of relative density [stainless steel, SLM – MCP Realizer]

The results reveal that both modulus and yield strength increase with relative density, which is consistent with expectations for porous materials in Gibson-Ashby model. The two curve trends show that model slightly over-predict the elastic modulus and under-predict the yield strength in most part of the graph. The differences are more pronounced in the yield strength compared to elastic modulus. However, both variations are reasonably within or little offset from the experimental error range. The maximum error between the modified Gibson-Ashby model and experimental result is 16 MPa for elastic modulus and 1.6 MPa for yield strength. To further modify and improve the accuracy of Gibson-Ashby model, it is essential to identify the model parameters from best fit curve using experimental data of tested samples.

8.4.2 AlSi10Mg cellular structures

8.4.2.1 Effect of cell size and volume fraction on compressive behaviour

Fig 8.7 shows typical stress-strain curves obtained from compression tests of AlSi10Mg Gyroid cellular structures with constant cell size of 4 mm and volume fractions ranging from 5 to 15%. The stress-strain behaviour of AlSi10Mg is different to the one we have seen with stainless steel cellular structures in Fig. 8.3. The stainless steel curves have shown elastic-plastic behaviour followed by cellular densification when cells collapse and touch each other. In contrast, the AlSi10Mg follow elastic-brittle behaviour, suggesting the brittle collapse mode, i.e. brittle fracture of the cell walls.

The cell edges collapse as soon the yield stress is reached without or little plastic straining and consequently the stress drops. The stress rises again when new face of fresh cells is loaded. The oscillations of the stress-strain curves of the AlSi10Mg cellular structures possess can be interpreted as repeating of collapse and squeezing of the cell walls. This process continuous until the point in which further straining compresses the solid itself, giving the final region of rapidly increasing stress.

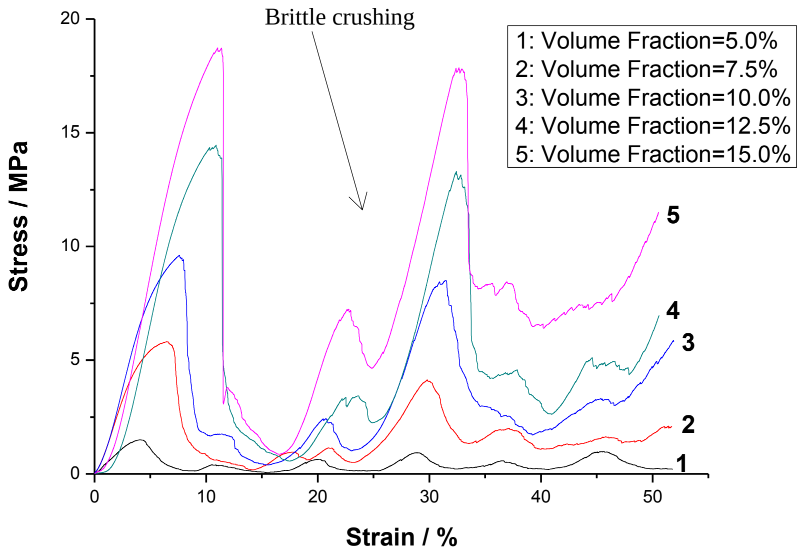

Figure 8.7 Stress-strain curves of Gyroid cellular structures with constant cell size of 4 mm and volume fractions ranging from 5 to 15% [AlSi10Mg, DMLS M280]

The elastic-brittle failure mode is common in brittle foams where a crack nucleates at a weak cell or pre-existing flaw and propagates catastrophically, giving fast brittle fracture. A cell wall will fail when the moment acting on it exceeds (Gibson and Ashby, 1997).

$$M_f = \frac{1}{6}\sigma_{fs}t^3 \tag{810}$$

where, σ_{fs} is the modulus of rupture of the cell-wall material.

Force acting with a component normal to the cell wall length l, exerts a moment which is proportional to *Fl*. The stress on the cellular structure is proportional to F/l^2. Combining these results give the brittle collapse stress $\sigma^*{}_{cr}$ as,

$$\sigma^*{}_{cr} \propto \frac{M_f}{l^3} \tag{8.11}$$

From which using $\frac{\rho^*}{\rho_s} = (t/l^2)$

$$\frac{\sigma^*{}_{cr}}{\sigma_{fs}} = C_3\left(\frac{\rho^*}{\rho_s}\right)^{3/2} \tag{8.12}$$

$C_3 \approx \frac{2}{3}$ of that for plastic − collapse strength $C_2 \rightarrow C_3 \approx 0.2.$

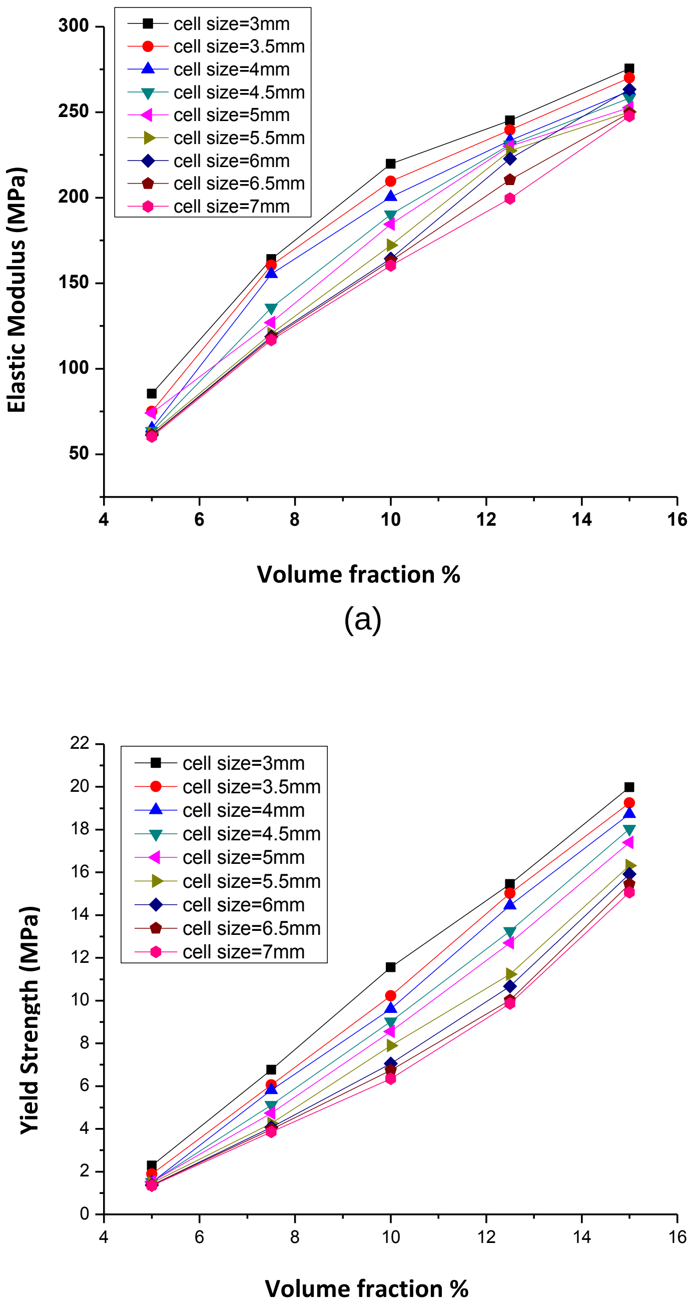

(a)

(b)

Figure 8.8 Experimental test results (a) compressive elastic modulus and (b) compressive yield strength [Schwartz Diamond, Cell size=3-7mm, Volume fraction=5-15%, AlSi10Mg – DMLS M280].

For brittle open-cell cellular structures of the same relative density, the crushing strength decreases with increasing cell size. The variations of elastic modulus and yield strength are depicted in Fig 8.8 (a) and (b), respectively. As expected both elastic modulus and yield strength increase with an increase in volume fraction percentage (i.e. relative density %) which is consistent with the previous findings of 316L stainless steel. The figure also exhibits some variations in the elastic modulus and yield strength for different cell sizes having the same volume fraction %. Both the compressive modulus and yield strength increase with decrease of the cell size. This is in agreement of our previous findings of 316L stainless steel. The differences between 2mm and 8 mm cell size are 25 MPa and 5 MPa for elastic modulus and yield strength, respectively. However, this variation is significantly low compared to the stainless steel results, in particular, the yield strength. The differences in yield strength for different cell sizes are much lower in low volume fractions.

Tables 8.2 and 8.3 list the Yield strength and Elastic modulus of AlSi10Mg Gyroid cellular structure. In comparison, the Diamond structure slightly shows increased elastic modulus compared to Gyroid cellular structures. The % increase in elastic modulus for 3mm cell size and 20% volume fraction is about 39%. The Diamond strength is also little bit higher and ranges from 6-15%. These can be contributed to the difference in the cell shape and strut orientation in relation to the applied compressive applied.

Table 8.2 Compressive Yield strength of Gyroid cellular structures [AlSi10Mg, DMLS M280]

Cell size / mm	**Volume fraction / %**					
	5	7.5	10	12.5	15	20
3	3.29	6.53	10.56	14.34	19.56	30.54
3.5	3.01	6.23	10.12	14.02	19.12	29.82
4	2.60	6.02	9.00	13.71	18.52	29.05
4.5	2.31	5.75	8.56	11.98	18.11	26.31
5	2.01	5.46	7.76	10.83	17.02	25.35
5.5	1.92	5.01	7.64	10.72	16.53	26.33
6	1.88	4.56	7.40	11.05	15.54	25.44
6.5	1.80	4.05	7.42	10.32	15.00	24.15
7	1.78	3.89	7.45	9.73	14.89	23.93

Table 8.3 Compressive Elastic modulus of Gyroid cellular structures
[AlSi10Mg, DMLS M280]

Cell size / mm	**Volume fraction / %**					
	5	7.5	10	12.5	15	20
3	87.37	167.56	198.39	227.67	252.36	1105.6
3.5	79.56	160.02	190.23	220.89	245.36	1023.5
4	67.59	150.26	187.34	218.16	239.54	943.76
4.5	66.53	139.56	182.14	215.78	236.12	942.35
5	65.39	127.56	179.31	213.40	233.24	1301.8
5.5	63.47	120.48	175.84	212.98	231.41	932.6
6	61.85	115.56	171.24	212.49	229.56	922.16
6.5	60.98	114.25	170.03	208.84	228.98	856.23
7	60.61	113.23	177.89	204.59	228.78	734.86

8.4.2.2 Experimental result vs. Modified Gibson-Ashby model

To compare experimental results with Gibson-Ashby model, the bulk material yield strength and elastic modulus of AlSi10Mg alloy was taken to be 240 MPa and 72 GPa, respectively. The constants C1 and C2 were found to be 0.189 and 1.183, respectively. Comparisons of the modified Gibson-Ashby model and experimental compressive modulus and strength are shown in Fig 8.9(a and b). The yield strength curves are well aligned, indicating good agreement with experimental values with a maximum error of ±3 MPa; however, the error in elastic modulus is more pronounced and reaches between 40±5 MPa for low relative densities.

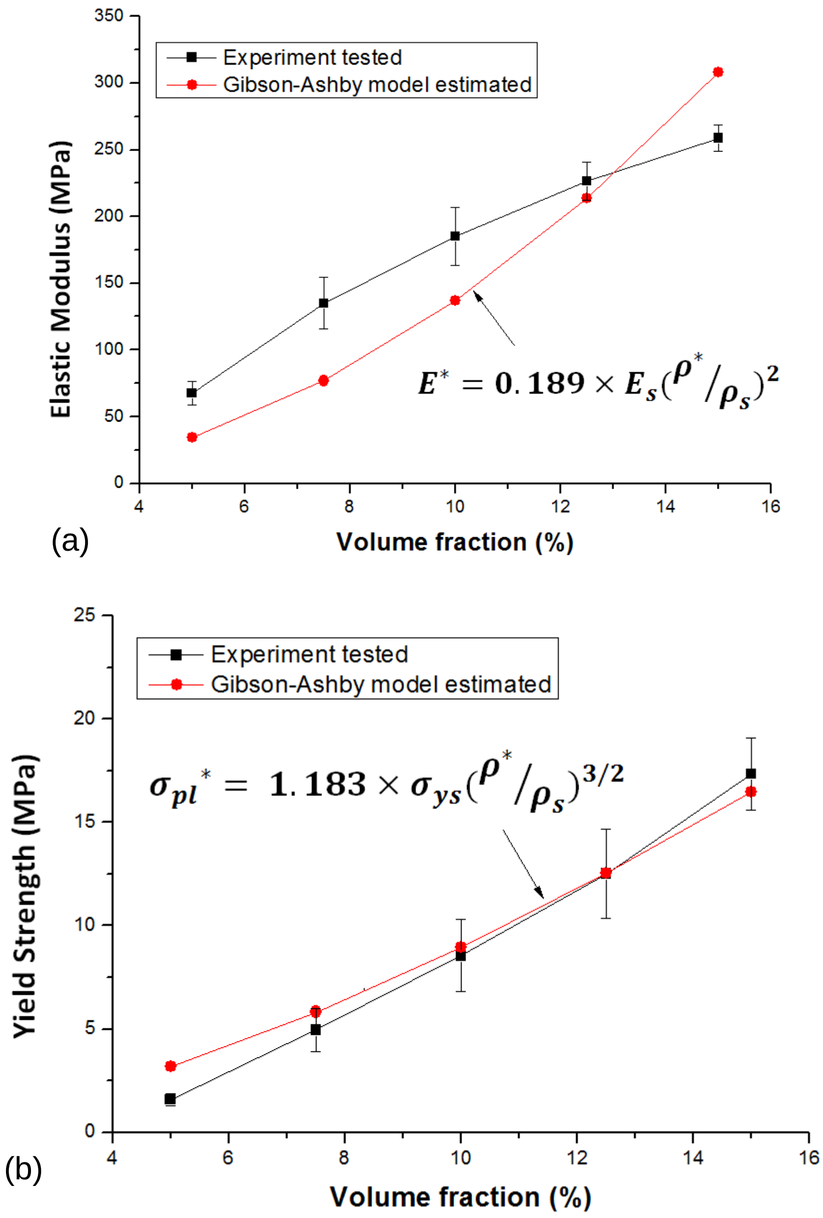

Figure 8.9 Comparison of experimental results and the modified Gibson-Ashby model as a function of volume fraction (a) Compressive elastic modulus and (b) compressive yield strength [AlSi10Mg, DMLS M280]

8.4.3 Ti-6Al-4V cellular structures

8.4.3.1 Effect of cell size and volume fraction on compressive behaviour

Fig. 8.10 illustrates the stress-strain curves of Titanium alloy (Ti-6Al-4V) cellular structure subjected to monotonic compression loading. As the curve show, the material is characterized by a linear elasticity region followed by sudden, brittle crushing of cellular structures. The material loses significant strength almost immediately after the yield. This behaviour is governed by brittle fracture of individual struts or ligaments of cellular network with very small region of plastic deformation. Properties of the cell struts such as cross-section area, thickness or length and surface conditions can greatly affect the behaviour and initiation of brittle crack. Cracks could be formed due to internal or external structural defects and propagate across the cross-section of strut. As the collapse progresses, the cell walls touch, resulting a rapid increase of stress due to densification. This is again followed by a sudden collapse of subsequent broken cellular structures. This process continues until the collapse of cellular structures is complete (i.e. > 60% strain), and voids that were initially presents in cellular network are filled with the broken pieces of the material. Further compression at this point causes a drastic increase in stiffness as cellular structure takes the elastic properties of bulk material. Both Gyroid and Diamond cellular structures demonstrate similar stress-strain behaviour as shown in Fig.8.10 (b).

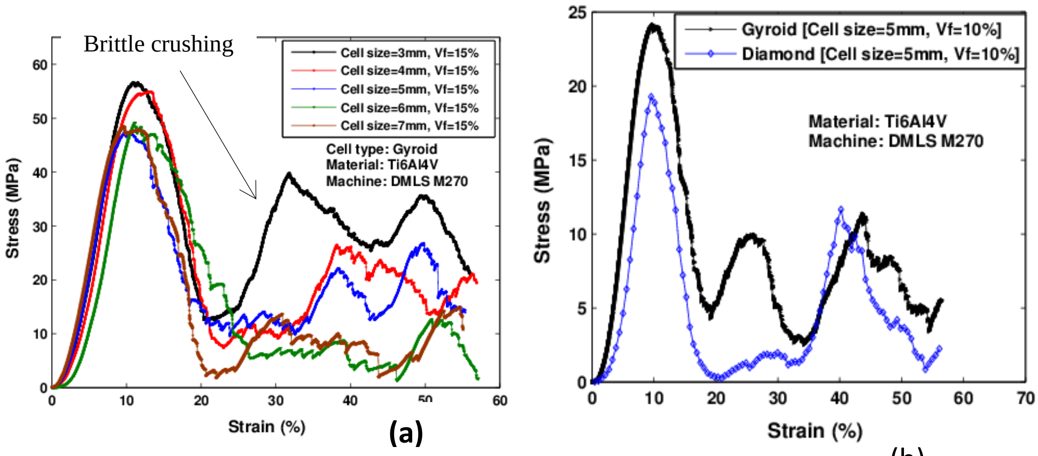

(a)

(b)

Figure 8.10 Stress-strain curves of the TPMS cellular structures (a) Gyroid structure with variable cell sizes and volume fractions (b) Gyroid and Diamond structures with cell size of 4 mm and volume fraction of 10%.

Fig. 8.11 (a-c) further illustrates the effect of both cell size and volume fraction on compressive properties of gyroid and diamond cellular structures. It shows that higher volume fractions provide higher elastic modulus and yield strength across the cell sizes and types. The elastic modulus of gyroid with 5mm cell size increases 8 times and the yield strength increases 13 times when the volume fraction is increased from 5% to 20%. Similar behaviour can also be observed for Diamond type cellular structure. The Gyroid structure relatively provide approximately 10 % and 40 % increase in elastic modulus and yield strength compared to diamond structure for 5mm cell size and 5% volume fraction. However, the difference is reduced to 0.4% and 19% as the volume fraction is increased to 20%.

Smaller cell sizes show slight increase in compressive elastic modulus and yield strength compared to bigger cell when volume fraction is fixed. This is with the exception of 5mm cell size which result a lowest value due to manufacturing external defects (broken cells) present in the sample before the compression test was applied on the structure. In practice, any imperfection in the cellular structure (such as non-uniformities in relative density or initially bent wall) induces bending of the cell walls, reducing the compressive elastic modulus and yield strength.

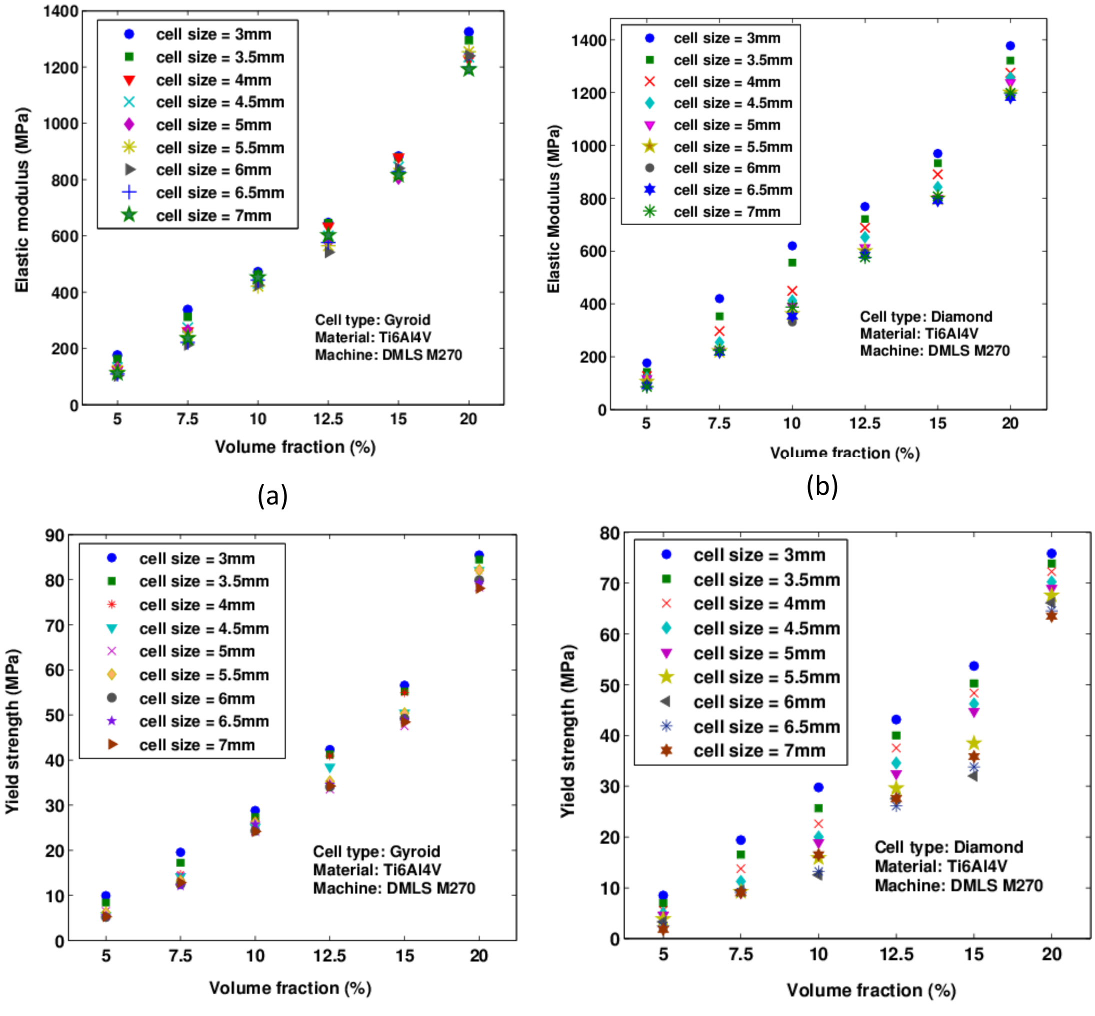

(a)

(b)

(c)

(d)

Figure 8.11 Effect of cell size and volume fraction on compressive properties (a) Gyroid elastic modulus (b) Diamond elastic modulus (c) Gyroid yield strength (d) Diamond yield strength

The microstructure of the Ti alloy processed by SLM will be different from those obtained with conventional manufacturing methods. This will also affect the mechanical properties of the components. Chang et al. (2011) also found that the fracture surfaces of Ti-6Al-4V tensile samples manufactured in SLM demonstrate a mixture of ductile and brittle fracture. Luca Fachini (2009), Ola. LA Harryson et al (2008) investigated the mechanical properties and microstructure of a Ti6Al4V alloy and pure titanium produced by electron beam melting.

8.4.3.2 Experimental result Vs. Modified Gibson-Ashby model

Fig. 8.12 shows the comparison of the experimental and GA model prediction of elastic modulus and compressive yield strength of Ti64 manufactured in DMLS process. Two type of cell structure (Gyroid and diamond) with varying cell size and volume fractions are compared relatively. Figs .8.10 (a-d) displays the data fitting graphs used from the experimental test data to obtain the constants C_1 and C_2 to develop and correct the GA prediction model for Ti64. The Figs. 8.12(e-h) indicate the experimental and GA curves and shows compressive elastic modulus and yield strength as a function of relative density (i.e. volume fraction) of the gyroid and diamond cellular structures. Good agreement between the GA prediction and experimental models can be seen in the figures indicating the high dependence of these properties on relative density.

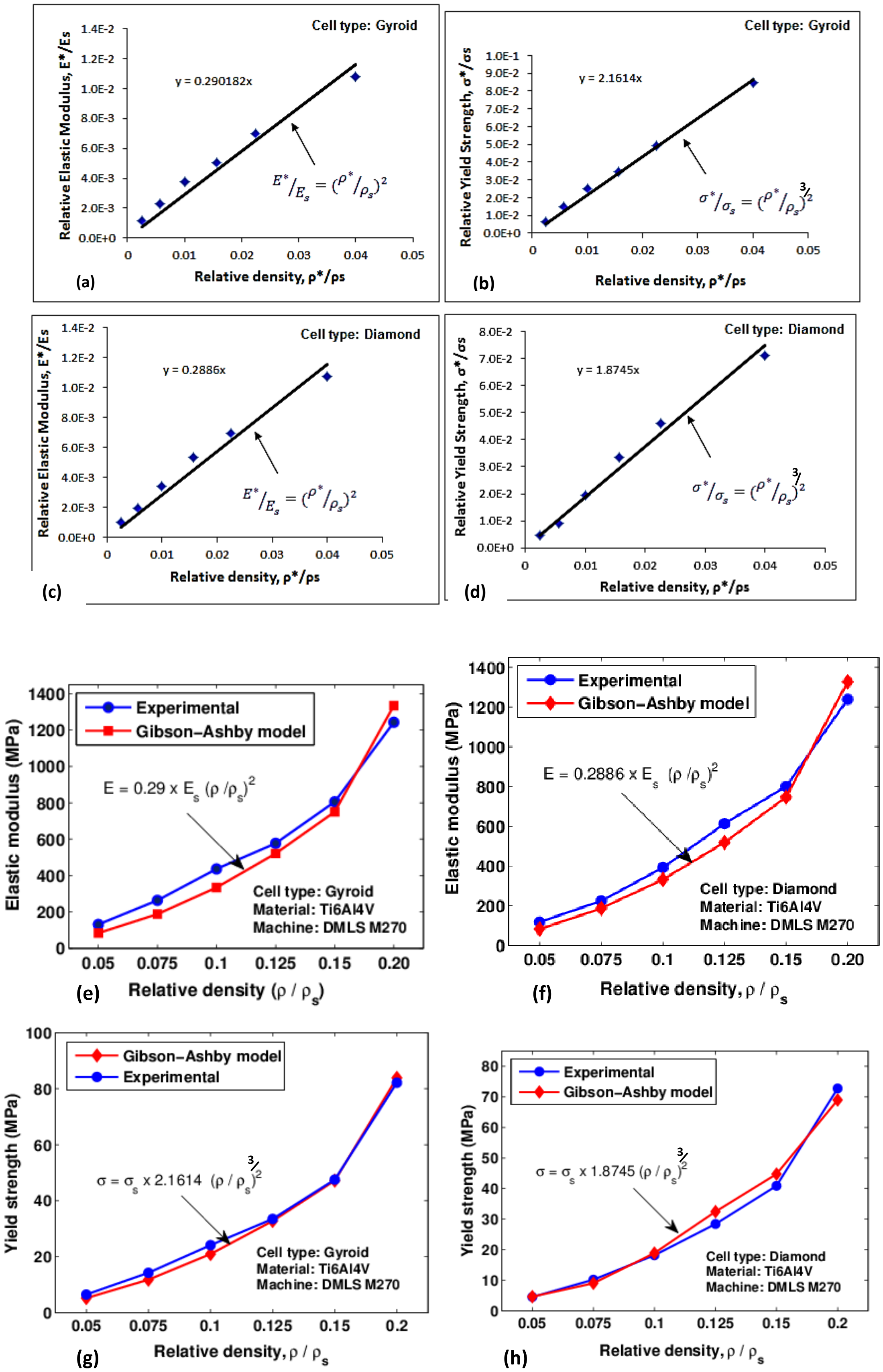

Figure 8.12 (a-c) Fitting graphs used from the experimental test data to obtain the constants C_1 and C_2 (e-h) indicate the experimental and GA curves and shows compressive elastic modulus and yield strength as a function of relative density (i.e. volume fraction) of the gyroid and diamond cellular structures.

8.5 Conclusion

In this chapter, rigorous mechanical testing was performed to enhance the understanding of the mechanical behaviour of TPMS cellular structures (Gyroid and Diamond) under uniaxial compression testing. Since mechanical properties of cellular structure depend on those of the solid cell-wall material of which the structure is made, as well as, the manufacturing method, specimens were manufactured from three commonly used metallic materials in metal AM machines. These are, 316L stainless steel processed in SLM-MCP Realizer, Aluminium alloy AlSi10Mg manufactured in DMLS M280, and Titanium alloy Ti-6Al-4V processed in DMLS M270). The objective was also to expand the scope of material data on both manufacturability and mechanical properties of these cellular structures. The effect of cell size, volume fraction, and cell orientation on compressive elastic modulus and yield strength were examined. The analytical model of Gibson-Ashby used for predicting the properties of cellular solids was modified by tuning the characteristic constants identified from experimental curves and compared with real experimental results. The main findings from this study can be summarized as follows,

- The compressive stress-strain curves of 316L stainless steel cellular structures exhibit elastic- plastic behaviour followed by a region of densification. The cellular structure has a plastic yield point, the cells connecting the structure collapse plastically when loaded beyond the linear-elastic regime. Plastic collapse of 316L stainless steel, gives a long horizontal plateau to the stress-strain curve, though the strain is no longer recoverable. Both lattices (Gyroid and Diamond) exhibited similar characteristics under compression loading.
- Linear elasticity is limited to small strains, typically 5% or less. The large plastic strains found in 316L stainless steel cellular structures cause the cell walls to crush together, and make the stress-strain curves rise steeply to a limiting strain ϵ_D which is mainly a function of relative density of the cellular structure as described by Gibson and Ashby (1997),

$$\epsilon_D = 1 - 1.4\left(\frac{\rho^*}{\rho_s}\right)$$

- The densification strain slightly varies for different cell sizes of stainless steel cellular structure and occurs between 0.4 and 0.6 of compressive strain.
- The compressive stress-strain curves found in AlSi10Mg and Ti-6Al-4V cellular structures were different to that stainless steel cellular structures and follow

elastic-brittle behaviour followed by a region of densification. There is no plateau region resulting from plastic yielding indicating a brittle collapse mode, i.e. brittle fracture of the cell walls. This densification begins at the point in which further straining compresses the solid itself, giving the final region of rapidly increasing stress.

- For all the three tested materials, both compressive elastic modulus and yield strength increase with the increase of solid volume fraction of the strut (i.e. relative density). For example, the elastic modulus and yield strength of Gyroid structure both drop by approximately 69.3 and 77.7% for 316L stainless steel, 47.9 and 69.75% for AlSi10Mg, 68.75 and 72% for Ti-6Al-4V, respectively, when volume fraction is reduced from 15 to 7.5%, at constant cell size of 5.5mm. The large % increase of compressive properties for all material is also close to each other with the exception of elastic modulus of AlSi10Mg, indicating the high dependence of compressive properties on solid volume fraction of the cellular structure.
- In material comparison, the compressive elastic modulus and yield strength of Gyroid cellular structure with 5.5 mm cell size and 15% solid volume fraction (equivalent to 0.15 relative density) is about, 251 MPa and 14 MPa for 316L stainless steel, 231 MPa and 16 MPa for AlSi10Mg, and 810 MPa and 50 MPa for Ti-6Al-4V, respectively. Cellular structures made from Ti-6Al-4V are 3-4 superior to that of 36L stainless steel and AlSi10Mg of similar cell size and volume fraction, making them attractive material for lightweight and load bearing applications.
- The experimental results reveal that cell size has relatively a minor influence compared to volume fraction for both elastic modulus and yield strength of cellular structure, when the volume fraction is kept constant. The % increase in modulus and yield strength when the cell size is decreased from 5.5mm to 3.5mm with a fixed volume fraction of 15% is about, 12 and 10% for 316L stainless steel, 6 and 15.6% for AlSi10Mg, 8.6 and 12% for Ti-6Al-4V, respectively. The microstructure of the metal powders processed by SLM/DMLS will be different from those obtained with conventional manufacturing methods. As was observed in µ-CT images in chapter 7, SLM/DMLS produces denser small cells compared to large cell size due to the differences in their energy density input and melt-pool characteristics.

- The pores formed are mainly due to the lack of bonding between layers. This could be the reason for the higher compressive properties found in small cell sizes. For brittle open-cell cellular structures of the same relative density, the crushing strength decreases with increasing cell size due to the presence of micro-porosities in large cell sizes which could initiate fast fracture.
- The cell orientation has a significant effect on the compressive properties of cellular structures. It was found that the highest modulus 316L stainless steel Gyroid structure lies between 40 and 60 degree of cell rotation. The Elastic modulus of the worst cell orientation in manufacturing (i.e. nearly vertical cell struts which are parallel to the loading direction) is found to be 20.37% higher than that of the normal un-rotated cell orientation of similar cell size and volume fraction. Similarly, the yield strength was found to increase only by 7.78%. Due to anisotropy of SLM/DMLS, there are always two sets of data points for the same structure depending on the loading direction (i.e. horizontal X-Y or vertical Z).
- The curves generated by comparing the modified Gibson-Ashby model and experimental results show that the model slightly over-predicts the elastic modulus and under-predict the yield strength for 316L stainless steel Gyroid structures. Generally, the model results found in other materials are also within or little offset from the experimental error range indicating it is potential as a predictive model. The model could be used in the initial design for screening the compressive properties of different cell sizes, orientations, and volume fractions.
- In comparison, the Diamond structure slightly shows increased elastic modulus compared to Gyroid for both Ti-6Al-4V and AlSi10Mg cellular structures. The % increase in elastic modulus for 3mm cell size and 20% volume fraction is about 4% for Ti-6Al-4V and 39% for AlSi10Mg. The Gyroid give slightly better yield strength between 5-20% for Ti-6Al-4V compared to Diamond structure, while in AlSi10Mg, the Diamond strength is little bit higher and ranges from 6-15%. These can be contributed to the difference in the cell shape and connectivity between Gyroid and Diamond.
- In practice, any imperfections in the cellular structure (such as non-uniformities in relative density or initially bent cell walls) induce bending of the cell walls, reducing the compressive properties. However, this was out of the scope of this study and will be recommended as future work.

- This study has contributed to our understanding of the compressive properties of TPMS cellular structures manufactured in SLM/DMLS. It helps the designer who is using these cellular structures to confidently select the cell size, orientation, and volume fraction knowing their compressive properties. Data presented include cellular structure with remarkably very low solid volume fractions of up to 5%. This is particularly attractive for low load bearing and ultra-lightweight components. The data covers three commonly used metallic materials in metal AM.
- The Titanium alloy porous structure is difficult to machine, or produce from the liquid state due to high melting point, high reactive activity at high temperature above 1000 ºC and contamination susceptibility. The production of Titanium alloys via SLM/DMLS route is attractive due to the ability to produce lightweight cellular structures. Since Titanium is denser and more expensive than aluminium, the use of cellular structure is expected to reduce material costs and improve fuel efficiency (by reducing weight). Using Ti cellular structure will also increase the impact resistance of airplanes. The bio-compatibility, lightweight, and load bearing capable of Ti-6Al-4V cellular structures makes them attractive in medical implants for human bone substitute. The organic TPMS cellular structures resemble those found inside of a bone in terms of its structural configuration. Not only does this make it less stiff than conventional massive implants. It also promotes ingrowth into surrounding bones.
- The aluminium cellular structures are potential in heat exchanger application due to their superior thermal properties and lightweight. Cellular structure could be used for heat transfer enhancement and fluid mixing to maximum the thermodynamic efficiency of heat exchanger systems.

Part Four:

Developing Low Volume Cellular Support Structures for Metal Additive Manufacturing

CHAPTER 9

Advanced Cellular Support Structures for Metal Additive Manufacturing

---

9.1 Introduction

Additive manufacturing (AM) of complex metallic parts typically require the building of sacrificial support structures to hold the overhanging regions during part building. These structures which are built simultaneously with the part, anchors the overhanging geometry to the base plate and prevent distortion/curling resulting from thermal stresses. It was found in chapter 5 (Finite element simulations of single overhang layers) that these thermal gradients and stresses are the result of cyclic rapid melting and solidification of the powder material. Support structures are necessary, but add constraints to the geometries that the processes can make. The design and selection of support structure can influence the manufacturability of complex metal parts, material and energy utilization, manufacturing time and cost.

This study takes a new step on the design and manufacturing more efficient support method through the novel application of cellular lattice structures with very low volume fraction. The chapter presents the development of an advanced support structure method using periodic cellular structures. Lightweight TPMS cellular structures are used as support in order to minimize the material and build time of sacrificial support structures. Experimental studies on two types of cellular structures (Gyroid and Diamond) were conducted in DMLS M270 machine using Ti-6Al-4V metal powder. The following sections will address the development of the cellular support structures foe metal AM.

9.2 Support Structures in Metal AM Processes

The SLM/DMLS processes use high energy laser beam to melt the powder material layer upon layer for making fully dense and high precision metallic parts. The geometric complexity, which they offer, coupled with freedom of tool-less manufacturing is compelling; however in practice, complete geometrical freedom is desired but not possible in complex overhanging geometries. Mumtaz et al. (2011), described one of the limitation of SLM is the use of sacrificial structures which are removed after the build must be used to support and hold overhanging features during laser processing. This severely restricts the geometries that the processes can make, adds significant time and cost to production.

Mercelis and Kruth (2006) reported that rapid heating of materials is followed by a rapid solidification inducing high thermal variations resulting residual stresses that can introduce part warpage, cracks or undesired effects to the part. According to Pohl et al. (2001), this could even sometimes lead to whole build failure due to de-lamination of the part from base plate. Re-melting the first layer is a practice used to prevent delamination of the first layer from base plate. Yasa (2011) obtained that post-scanning (i.e. re-melting the layer) the layer with the same laser beam spot size have little effect on reducing thermal stresses. Shiomi et al. (2004) proposed that post heat treatment through temperature cycles in a furnace is an effective way of relieving residual stresses trapped inside the part. However, stresses can induce cracks during the processing before the part is complete. Kruth et al. (2012) established that by using short scanning vectors and increasing the process temperature by preheating the base plate up to 180 ◦C reduces the curling effect.

In SLM, since the first layer forms the foundation for the subsequent layers, it is important to make it without deformation to avoid part dimensional loss or process failure. For overhanging features where there is no underlying solid layer to support, major deformation is usually expected. Thomas and Bibb (2008) investigated the SLM process and found that it is limited in its ability to build overhanging structures with angles less than 40–45◦ from horizontal without building fixed support structures. The removal of support structure from the part/base plate is a tedious job; in particular, large amount of supports for delicate parts would increase the difficulties and time of support removal, causing small pieces of the part to break off. Furthermore, the commonly used conventional support method which consists of straight rectangular solid walls or blocks as in Fig. 9.1 is unsuitable for recovering the raw loose powder which are trapped inside the support structures during the build. Especially when the support is removed by EDM-wire cutting, the part along with the support is submerged in water that washes away all trapped raw powders. Since SLM is a layer wise process with relatively low build rate, it is important that this non-productive time is reduced.

Supports are necessary evil in SLM process and good design practice will minimize them, as they use a lot of material and energy, but they are also used to fulfil the following vital functions:

- To raise the part off the platform for easy removal.
- To anchor the overhanging and floating sections introduced during the buil to the platform (Jhabvala et al., 2012).
- To strengthen thin-and-tall part during the build. This prevents
- the toppling and destruction of the part by the forces of the powder wiper.
- To prevent part curling or distortion resulting from thermal stresses by dissipating heat away from newly melted surface and ensure regular thermal conditions in the consolidation zone (Vandenbroucke and Kruth, 2007).
-

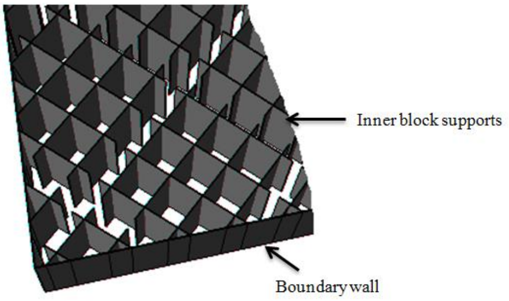

Figure 9.1 Straight solid walls or block support

The geometrical design of support structures could influence the manufacturability of the support and the part as well as the removal and surface roughness left in the part. Papadakis et al. (2012) found that both building platform temperature and support structure effect structural part behavior. Too much support will increase material usage, build time, and removal, while weak support structures might not be sufficient to withstand the residual stresses and the forces from powder wiper system and prevent layer deformation. Proper selection of support structure design is crucial for the metal AM processes and its final products.

In light of this, the present study takes a new step on the design and manufacturing a more efficient support through the novel application of cellular lattice with very low volume fractions to be used as an external support structures for SLM parts. To prove this new concept, a comprehensive experimental study was performed in a DMLS machine using commercial titanium alloy Ti6Al4V powder. The effect of type, % of volume fraction and unit cell size of lattice structure on the support performance in terms of manufacturability, building time, weight of support, and resulting part deformation was investigated and analyzed.

9.3 Design and manufacturing of the cellular support structure

In recent years, there has been increasing interest in manufacturing lattice structures in SLM process. While at the beginning of the decade this mainly involved regular rectangular forms used at heat exchangers or filter elements, it is now possible create far more complex structures consisting of open-pored cellular lattice structures Rehme and Emmelmann (2006). The works by Seepersad et al. (2004) and Wang et al. (2006) has focused in designing the mesoscopic topology of cellular materials in order to effectively support and improve multiple design objectives. The most fundamental requirement of any lattice structure design is that it must be self-supporting. This is particularly the case with lattice structures having large unit cell size greater than 5 mm. This is where previous lattice structures with straight beamlike struts and a polyhedral core failed to manufacture in large cell size ranges. The large overhang strut resulting from these designs caused a serious deformation or sagging to occur. Additionally, the design of lattice structure should permit the easy removal of the loose powder trapped inside of these structures after the build is completed. This is a necessary step before the part is heat treated or wire-cut by EDM.

These advanced cellular structures which are shown in Fig. 9.2 (Schoen Gyroid and Schwartz Diamond) are used for generating support structures. Unlike previous designs, these lattice structures have circular and smooth struts with a spherical core. The inclination angle of the circular and smooth struts of the unit cell continuously varies along the spherical core, which makes layers grow up gradually with slight changes in area and position between two adjacent layers. This inter-connected network of open structure is well suited for loose powder removal. The lattice can be made very thin by using very low fractions below 10%. It also has a proven structural strength, which can act as a permanent fixed support for complex internal geometries with overhanging sections. These characteristics are well suited for support structure in metallic AM process for saving material and energy, while reducing build time and cost. To the best of author’s knowledge, the design and manufacturing of lattices as an external support structure is a new and novel approach in metal AM processes and offers new possibilities in building support structure for complex metallic parts.

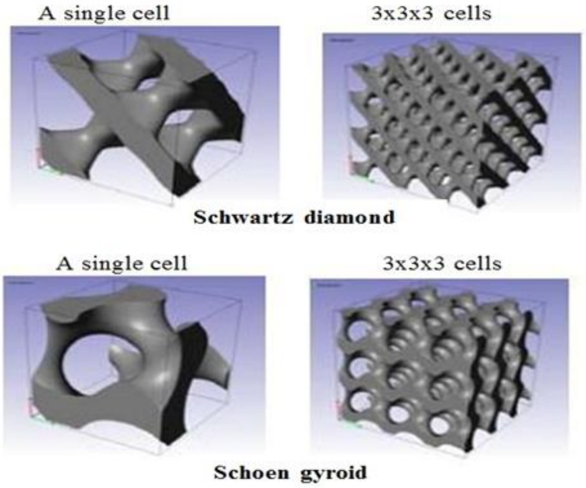

Figure 9.2 CAD model of gyroid and diamond lattice structures

9.4 Experimental Procedure

9.4.1 Design process

Fig. 9.3 shows the cantilever part used for testing the lattice support structure. The large overhang of the cantilever was chosen for studying the effectiveness of the lattice support structure and to collect sufficient data on cantilever deformation. Schoen Gyroid and Schwartz diamond lattice types with cell sizes ranging from 3 mm to 5 mm and volume fractions from 8 to 15% have been generated to support the overhang of the cantilever part. The cantilever part with the lattice support is then exported as a single STL (standard tessellation language) file format to the SLM machine for manufacturing.

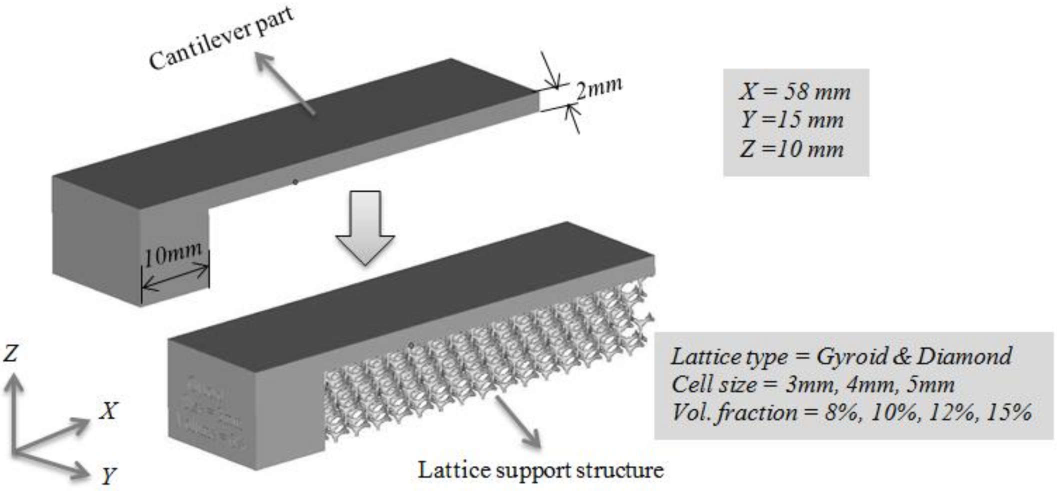

Figure 9.3 CAD Geometry of the cantilever part supported with lattice structures

9.4.2 Manufacturing process

The experiments were performed in DMLS EOSINT M270 machine. The processing parameters used are described in chapter3. The processed material was titanium alloy powder Ti6Al4V. The particle size of the powder and the laser spot size are both very important factors, which determine the smallest cell size structure manufacturable in DMLS. With this powder distribution, the laser beam spot size is roughly equivalent to 3–6 particles of the powder. The layer thickness was kept to 30 µm, and then following the build, the loose powder was drained. The only post-processing was wire-cutting off the cellular support from the platform and the cantilever part (done in two stages, with a white-light scan for measurement between the two cuts and then wire-cutting by EDM).

9.4.3 Characterisation and Analysis

The manufacturability of the lattice support structure was evaluated through visual inspection to judge the success and failure of part building. The data of the build time of each part was retrieved from the EOSINT M 270 machine software PSW Version: 3.4 after the build were completed. The actual weight of the lattice support was taken using simple weight scale. Hitachi S-3200N equipment for scanning electron microscope (SEM) was used to check the defects on the surface of lattice struts and if there are remains of attached loose powder. The deflection of the cantilever parts after wire-cutting of the support was measured using Roland’s 3D scanning machine which uses scanning probe to touch the cantilever upper surface. The digitised data of the cantilever surface is then processed using MATLAB software for visualization.

9.5 Results and Discussion

9.5.1. Manufacturability of cellular support structures

Fig. 9.4 shows the processed parts still attached to the building plate after the manufacturing process was completed. Prior to wire-cutting the support, the unprocessed powder trapped inside the lattice support was removed for later use. Most of the trapped loose powder can be removed by tilting up the base plate in which lattice has been built on without spending much effort. This is a good characteristic of the open cellular lattice support design in which otherwise more material could have been wasted if a thin wall block support method is used. For the support using 8% volume fraction, this could mean 92% of loose powders embedded within lattice support could be recycled and reused. However, it is worth noting that it is difficult to ensure that all powder particles are removed in the process unless specialized cleaning process are employed for medical applications.

Majority of the tested cellular support structures were manufactured successfully; however, there were a number of parts, which also failed during the build. Table 9.1 depicts the manufacturability at different cell size and volume fractions of the tested cellular support structures. The manufacturing failure can be contributed to the geometrical constrains of SLM process. The manufacturability of the lowest % of volume fraction depends on the type of lattice structure and the unit cell size involved.

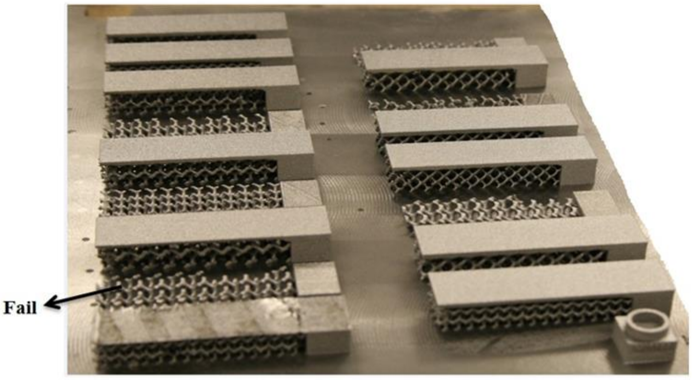

Figure 9.4. Manufactured cantilever parts still attached on the base plate (DMLS - EOSINT M270)

The manufacturing failure can result from the large distance between the adjacent point contacts to the supported surface so that there is too much overhang cantilever area that is unsupported. The gap of the contacting points for gyroid with 5 mm cell size and 8% volume fraction is 3.8 mm as shown in Fig. 6(b). This represents a large overhang area, which could not be manufactured without support structure. Majority of the failures occurred due to this second type while building the first overhang layer of the cantilever part. The underneath lattice support structures did not prevent the newly melted layers from distortion in the form of curling and the process must be stopped from further building of that part. Very low volume fractions are desired in lattice support for saving material and reducing built time and energy, but there are limits to their manufacturability influenced by laser spot size, size of powder particles, and strength requirements during the build.

The design of gyroid structure permits better manufacturability at lower volume fraction due to its struts, which are thicker and more open compared to closely packed thinner struts of diamond structures. It could be possible that even lower volume fractions can be achieved with gyroid type subject to further research. For use as a support structure, it is vital that consistent, reliable lattices are proposed, as the operator selecting them, needs confidence that they are not going to cause any failures within the manufacturing process.

Table 9.1- Manufacturability of cellular support structures

Type	Cell size (mm)	Volume fraction (%)	Build condition
Diamond	4	10	×
Diamond	4	12	✓
Diamond	4	15	✓
Diamond	5	10	×
Diamond	5	12	✓
Diamond	5	15	✓
Gyroid	3	8	✓
Gyroid	3	12	✓
Gyroid	3	15	✓
Gyroid	4	8	✓
Gyroid	4	10	×
Gyroid	4	12	✓
Gyroid	4	15	✓
Gyroid	5	8	×
Gyroid	5	10	×
Gyroid	5	12	✓
Gyroid	5	15	✓

✓- sucessfully build × - build failure

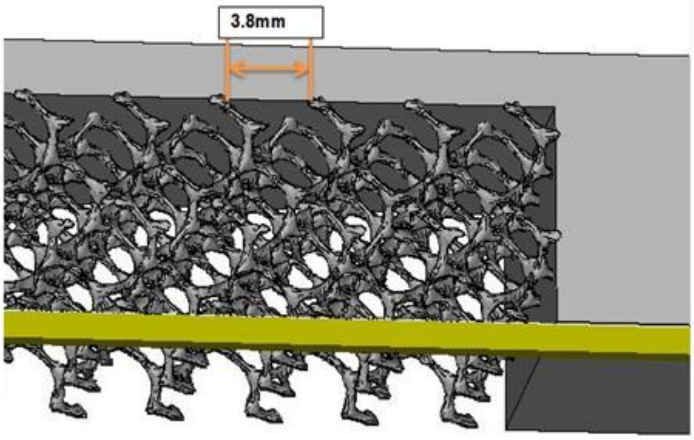

Figure 9.5 Large gaps between lattice support points at the cantilever bottom surface

9.5.2. Scanning time and weight of cellular support structures

Table 2 gives the laser scanning time and measured weight of the cellular support structures. The type of cellular structure, the volume fraction, and the cell size all influence the laser scanning time of the lattice support structure. Gyroid structure builds faster when compared with diamond having similar cell size and volume fraction. For example, the scanning time of gyroid with 4 mm cell size and 8% volume fraction is 28 min and 40 s while diamond finished at 32 min and 36 s. The volume fraction being the prominent factor influencing the scanning time, it is important to keep it very low provided it can be manufactured. High % of volume fraction means more closed lattice structure and hence more material to be melted by the laser. In all the parts built, the gyroid structure with 4 mm cell size and 8% volume fraction resulted the lowest scanning time of 23 min and 11 s as displayed in Fig. 9.6.

The unit cell size of the lattice structure also influences the scanning time of both types of the cellular support structure. To understand why smaller cell sizes take longer time to build compared to bigger cells when the volume fractions is unchanged, it is important to understand the laser scanning strategy. This is also called the scanning pattern of the laser beam and is a very important factor when it comes to scanning lattice support structures. As shown in Fig. 9.7(a), the laser beam first scans the contour (outer boundary) of the lattice structure; this is followed by the inner hatch scanning as in Fig. 9.7(b). With this scanning strategy, even though hatching time does not change when the volume fraction is fixed, the contour scanning time is increased when smaller cell size is used. This is because smaller cell size means more struts per unit volume, which results in many contours to be scanned by the laser as shown in Fig. 9.7(c–d).

The ideal lattice structure that is fast to build is to have a combination of very low volume fraction and big cell size of Gyroid structure. However, in terms of manufacturability, bigger cell sizes increase the gap between support points and may cause a part failure due to thermal deformations of the unsupported regions. Hence, the ideal choice for lattice support will be to use the cell size that give allowable minimum gap having the minimum volume fraction that can be consistently manufactured. At this time, optimal scanning strategies for these lattices have not been investigated. When used for support purposes the lattices are only sacrificial parts built to enable the final component to be produced. As such, it is likely that much quicker strategies for their manufacture could be developed in a possible future project.

The weight of lattice support structure is mainly proportional to the % of volume fraction used, the higher the percentage the more material used for the support. For example, there is 1.44 g of support material used in gyroid lattice structure with cell size of 4 mm and volume fraction of 8% compared to 2.6 grams of material for 15% volume fraction. This difference could be significant for big parts requiring large amount of support. For the two types of lattice support structure, Gyroid weight less compared to diamond for similar volume fraction and cell size. The apparent difference in weight between the Gyroid and diamond structures can be explained by the difference in their unit cell design. Diamond structure forms more crowded and thinner struts of lattice network compared to Gyroid structure.

In addition, the size of the cell also influences the weight of lattice support structure. This is apparent in Fig. 9.8, where smaller cell sizes weighted more than the bigger cell sizes when the volume fraction is unchanged. This is because smaller cell sizes have thinner struts, and thus high laser energy is concentrated in a smaller region, which leads to large melt pool increasing both the density of the structure and chance of partial melting of the surrounding loose powder. SEM analysis undertaken in chapter 7, has confirmed that wetting occurs to the surrounding loose powder particles which are then attached to the struts of the lattice structures after re-solidification.

The loosely attached powder particles do not contribute to mechanical properties, increase component weight, and, being only lightly attached, can be removed subsequent to the build in normal handling. As such they are normally removed after the build is completed by post-processing procedures, such as sand, bead or compressed air blasting but this was not done in this study.

Overall, gyroid structure provides more material saving, has better manufacturability in low volume fractions, and is faster to build compared to diamond structures. These characteristics make it more favourable to be used as a lattice support structure for metallic parts.

Table 9.2- Laser scanning time and weight of lattice support structures

Type	Cell size (mm)	Volume fraction (%)	Scanning time (hr)	Weight (grams)
Diamond	4	12	00:32:36	2.35
Diamond	4	15	00:33:43	3.32
Diamond	5	12	00:29:06	2.15
Diamond	5	15	00:30:30	3.05
Gyroid	3	8	00:26:51	1.51
Gyroid	3	12	00:33:39	2.32
Gyroid	3	15	00:35:03	3.20
Gyroid	4	8	00:23:11	1.44
Gyroid	4	12	00:28:40	1.94
Gyroid	4	15	00:30:07	2.60
Gyroid	5	12	00:26:21	1.89
Gyroid	5	15	00:28:55	2.54

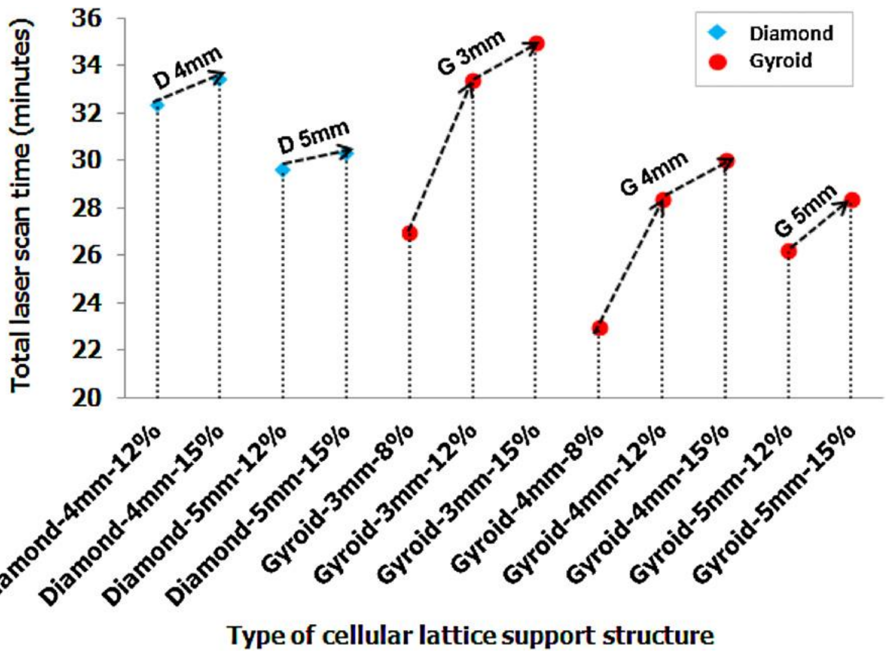

Figure 9.6 Comparison of the laser scanning time of cellular support structures

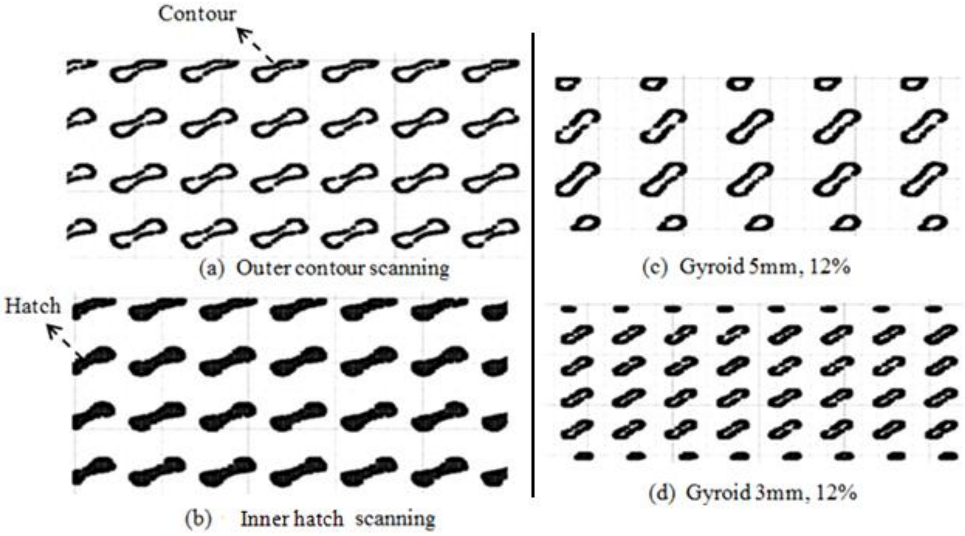

(a) Outer contour scanning

(b) Inner hatch scanning

(c) Gyroid 5mm, 12%

(d) Gyroid 3mm, 12%

Figure 9.7 2D slice view of single layer of lattice support structure

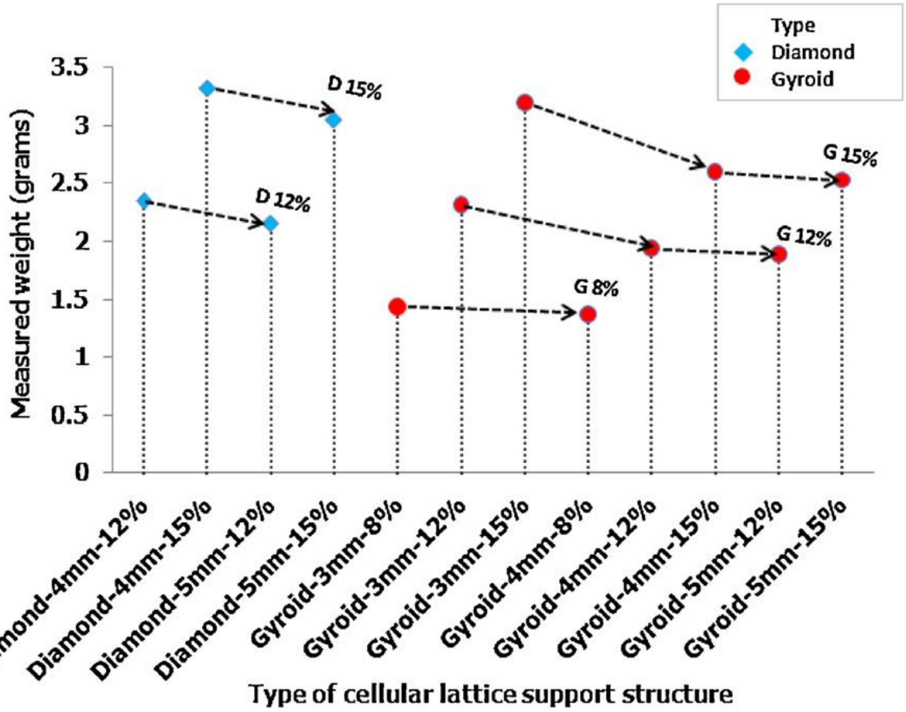

Figure 9.8 Comparison of the measured weights of lattice support structures

In addition, the unit cell size of the lattice support structure as though not direct but influences the weight of lattice support structure. This is apparent in Fig. 9.8, where smaller cell sizes weighted more than the bigger cell sizes when the volume fraction is unchanged. This is because smaller cell sizes have thinner struts, and thus high laser energy is concentrated in a smaller region which leads to large melt pool increasing both the density of the structure and chance of partial melting of the surrounding loose powder. SEM study also confirms that wetting occurs to the surrounding loose powder particles which are then attached to the struts of the lattice structures after re-solidification. The attached powder particles remain on the structure after the build is completed, especially if the structure has not gone through post-processing procedures such as, sand or bead blasting which was the case in this study.

In this respect, Gyroid structure is the best cell type that provides more material saving, has better manufacturability in low volume fractions, and is faster to build compared to diamond structures. These characteristics make it more favorable to be used as a cellular support structure for metallic parts.

9.5.3 Deformation analysis

In normal practice, all parts go through stress-relieving heat treatment process prior to support structure removal, whereby all residual stresses are released from the part. As shown in Fig. 9.9(a and b), the trapped stresses are released through longitudinal deflection as expected and have similar shape and little variation in amount (2.5–4 mm) over all the gyroid and diamond lattice support structures. This uplifting or deflection is an indication of the amount of residual stresses, which was present in the part. This is in good agreement with other research findings by Shiomi et al. (2004) that residual stresses if not properly released through heat treatment processes causes the part to deflect after it is removed from base plat/platform and the supporting structure. In this study, a component design (the cantilever) was deliberately chosen with a geometry which would induce a significant stress due to its geometry, with a right-angle corner and flat layer of solid part manufactured.

Since one of the primary functions of the support structure is to dissipate heat away from the newly melted layers of the part, less heat is dissipated through the support when less solid material is available underneath the newly melted layer. Smaller cell sizes with higher volume fraction are the best candidates for this purpose, because they have higher contacting surfaces with the part enabling more heat transfer through conduction. Zaeh and Branner (2010) stated that the number of support and location depend on the geometry of the part and the building orientation. Other simulation work by Papadakis et al. (2012) also demonstrated that wide meshed supports (i.e., support having bigger gap) involve greater deformation of cantilever wings because of powder inclusion and reduced heat conductivity. Additionally, the other process parameters such as laser scanning energy, layer thickness and scanning strategy are all influential factors in the development of residual stress and the resultant deformation in SLM parts (Kruth et al., 2012).

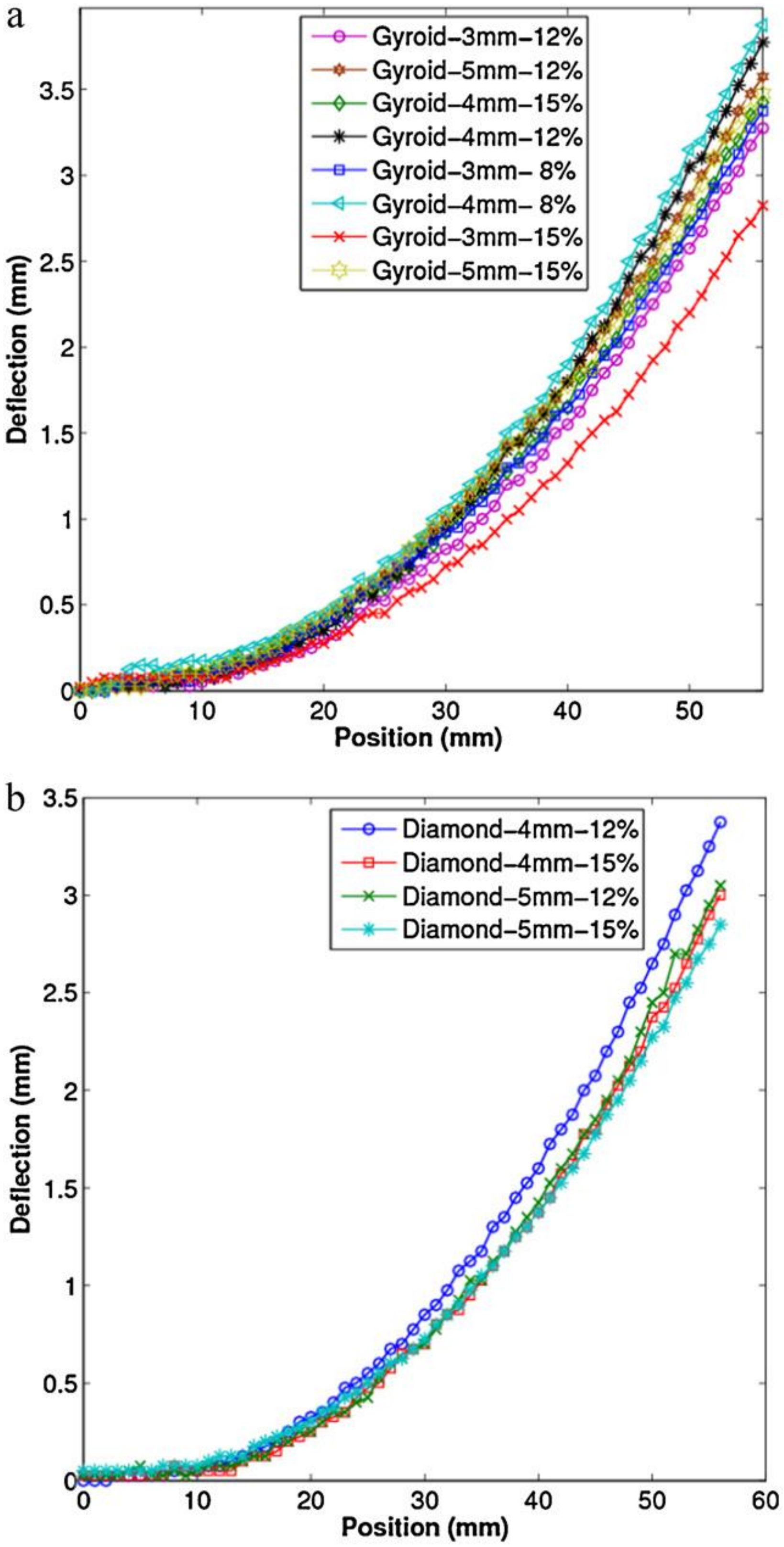

Figure 9.9 Deflection in the cantilever part after wire-cutting (a) supported with Gyroid cellular structures and (b) supported with Diamond cellular structure.

9.6 Conclusion

This chapter proposes a new and advanced cellular lattice support structures for SLM/DMLS processes. Two types of lattice structure (Diamond and Gyroid) have been investigated for their suitability as support structures in reducing material and built-time while fulfilling the structural demands required from a metallic support structure. The experimental results have revealed that a potential material saving can be achieved when lattice support structure with lower volume fractions is used. For example, it was possible to manufacture Gyroid lattice structures with 8% of relative volume, which means more than 90% of loose powders, can be removed and reused. The unprocessed material retrieval is a major benefit beyond the material saving achieved in low volume support structure. Low volume fraction also allows minimum build time and required energy for SLM parts.

The lattice support structures show good manufacturability characteristics; however, some of the parts failed during the build. For big cell sizes, the distance between the adjacent contact points to the supported surface is too large; therefore, there is too much material that is unsupported and the part is distorted by the thermal stresses. The volume fraction is the prominent factor influencing the scanning time, it is therefore important to keep it very low provided it can be manufactured. Small cell sizes take longer time to build compared to bigger cells when the volume fractions is unchanged, because of the more time needed in scanning the outer contours of increased cell struts.

It should be noted that many factors have to be considered during the design and manufacturing of more efficient lattice support structures. A compromise has to be reached between the best combination of cell size and volume fraction that is manufacturable, fast to build, easy to remove and has good thermal and mechanical properties to constrain deformation while ensuring reliable build for the part. In addition, different parts and their geometries might set up different requirements and preferences for the design of lattice support structures.

The gyroid cell type has better manufacturability in low volume fractions, and is faster to build compared to diamond type. These characteristics make it more favorable to be used as a cellular support structure for metallic parts. Therefore, it is recommended to use gyroid cell type with low volume fraction of up to 8% and cell sizes equal or less than 3mm. The data and findings presented in this study could provide valuable information and guidance for the selection and design of lattice support structures. In addition, it has built a foundation for future research and development to design graded lattice support structures to meet different requirements simultaneously.

CHAPTER 10

Developing Functionally Graded Cellular Support Structures for Metal Additive Manufacturing

10.1 Introduction

This chapter aims to further develop the work in chapter 9 on uniform cellular support structures by designing a novel and low-density functionally graded cellular support structure for metal AM parts. The results of chapter 9 have shown that some of the cantilever parts supported with large cell sizes did not build, because of the large gap between adjacent support points. It was also found that small cell sizes are the suitable for dissipating heat, because they have higher contacting surfaces with the part enabling more heat transfer through conduction. In this work, graded cellular support was developed to meet the functional and support requirements of both internal and external overhanging geometries.

10.2 Graded Cellular Support Structures

Functionally graded cellular structures are those where a property is deliberately varied within the structure (Ajdari et al. 2011). These cellular structures can be engineered to meet specific requirements such as a superior mechanical, thermal, and acoustic behaviour. Fig 10.1 shows the CAD models of graded Schoen gyroid cellular structure used for the generation of the support structures. Gyroid structure was selected as it provides more material saving, has better manufacturability in low volume fractions, and is faster to build compared to diamond structures. In this work, a form of functionally graded structures was studied. This involves varying the local volume fraction and cell size of the cellular structure with position. This has been done in two different ways, both in a smoothly varied way, and also in the form of step-graded structures, with abrupt transitions between different regions.

The gyroid cellular structure was graded to meet functional requirements of both internal and external support structure in metal AM. Fig 10.1(a) shows the generated gyroid structure with a uniform volume fraction of 8 % throughout the part while Fig 10.1(b and c) shows smoothly graded structures with volume fraction exponentially increased from 8% at the bottom to 50% or 100 % towards the vertical top surface of the part. Fig 10.1(d) shows step-graded cellular structure with a thin solid layer separating the big and small cell sizes. Fig 10.1(e) shows internal graded cellular structure with increasing density towards the surface of the cube. To generate graded cellular structure the volume fraction % and the distance to vary the volume fraction over should be selected as depicted in the exponential variation curve in Fig. 10.1 (f). The transition function was implemented in the ScanIP tool of Simpleware software.

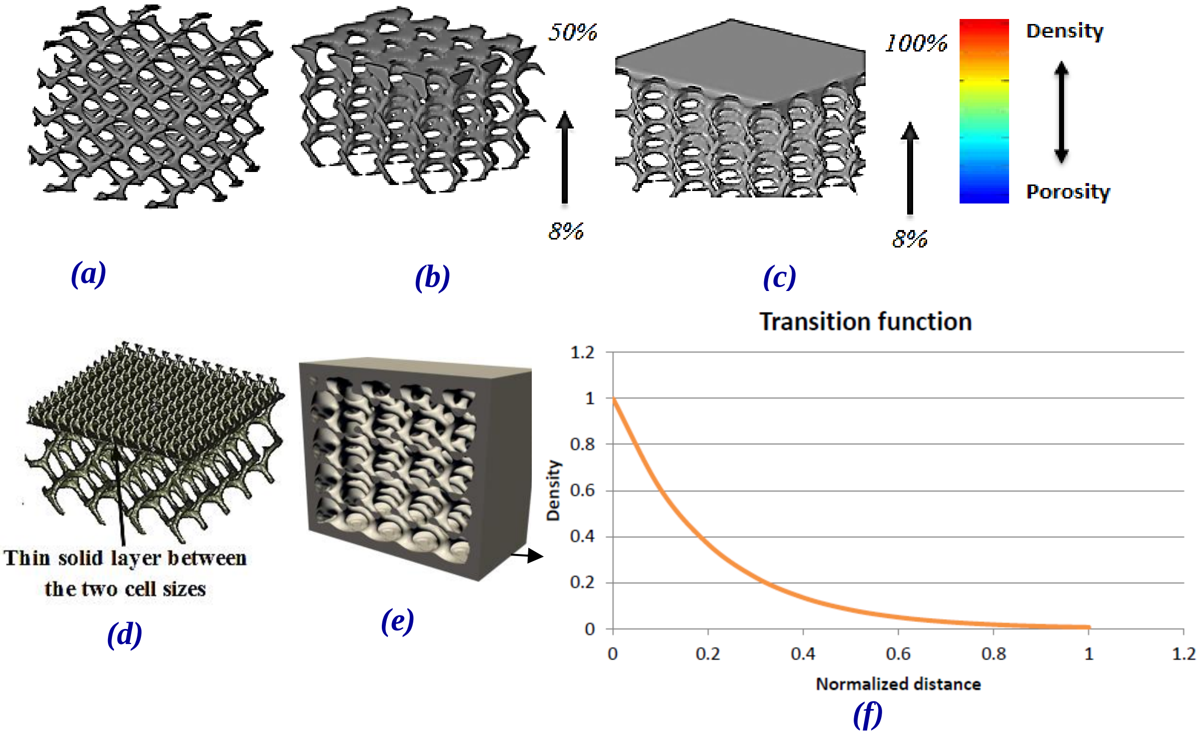

Figure 10.1 CAD models of the Schoen gyroid cellular structure (a) ungraded uniform structure (b) Graded structure 8% - 50% (c) Graded structure 8% -100% (d) Step graded with solid layer separating the two cell sizes (e) Internal graded cellular structure with increasing density towards the surface (f) Exponential transition function for the smoothly graded cellular structures

10.3 Experimental Procedure

10.3.1 Design process

Fig. 10.2 (a-d) shows cantilever parts with dimensions 58mm x 15mm x 10mm and overhang thickness of 2mm, supported by the graded Schoen gyroid cellular structure shown in Fig. 10.1. The large overhanging of the cantilever cannot be manufactured in the DMLS process without support and so was chosen for studying the effectiveness of the cellular support in this role and to collect data on cantilever deformation. In Fig. 10.2 (a) a vertical step grading of gyroid cellular support structure was used that has a big cell sizes *(3-5mm)*with lower volume fractions *(6-7%)* at the bottom section and a small cell sizes *(0.8-1mm)*with higher volume fractions*(10-15%)* in contact with the cantilever part. The transition from big cell size to small cell size is achieved by placing a thin solid layer between the two cell sizes. The small cell size at the interface enables many contact points on the cantilever overhang bottom surface and smaller gaps between the supporting points of lattice struts, thus improving both the manufacturability of the cantilever and the subsequent removal of cellular support structure after the build is complete. A bigger cell size is used in the lower 80% of the support to speed up the building process and enable easy removal of loose (unmelted) powder trapped in the structure during the build.

In Fig. 10.2 (b), a horizontal side-graded cellular support structure was used that has a small cell size *(2mm)* with higher volume fraction *(8-12%)* around the edges and a big cell size *(4-5mm)* with lower volume fraction *(6-7%)* in the middle portion of the support. The cell structures are strengthened around the edges due to an expected higher stress from the manufacturing process, which can result a curling effect on cantilever edges. In Fig. 10.2 (c), a vertical smoothly graded cellular support was generated using an exponential densification function which takes into account the volume fraction % and the distance to vary the volume fraction over. The volume fraction of the lower part of the support is varied gradually from 6% to full density of 100%. Small cell-size structures *(0.5-1.5mm)* with 15% volume fraction are then placed at the interface in contact with supported cantilever surface. Fig 10.2 (d) shows a perforated thin boundary wall or shell (*thickness=0.5mm*) used along with cellular support structure to improve the support stiffness, dimensional accuracy on cantilever edges, and withstand thermal distortions. Fig 10.2 (e) shows curved convex geometry supported by cellular support structure with *0.5-1mm*cell size and 15% volume fraction. Fig 10.2 (f) shows permanent internal cellular structures *(cell size 3-4mm, volume fractions 8-60%)* with boundary shell thickness of 2 mm for lightweight applications.

The test geometries with the internal and external cellular support structure were exported as a single STL (standard tessellation language) file into the

DMLS process software which then converts to machine specific slice file format ready to pass to the DMLS machine for manufacturing.

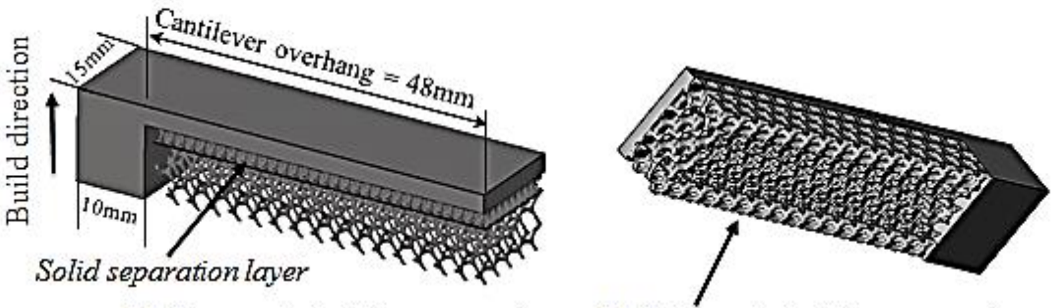

(a) Step graded cellular support (b) Side graded cellular support

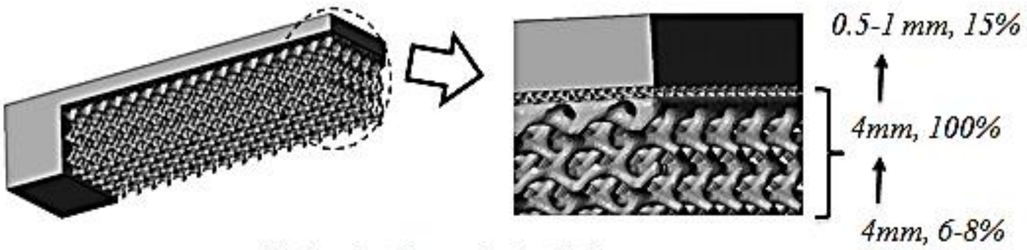

(c) Gradually graded cellular support

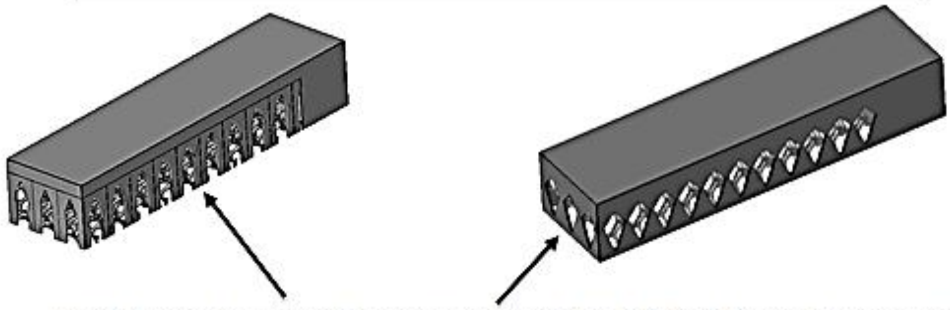

(d) Cellular support with perforated boundary shell/wall at cantilever edges

(e) Cellular support structure for curved surface

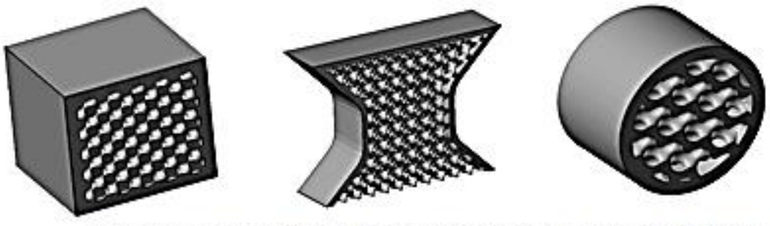

(f) Permanent internal cellular structures for lightweight components

Figure 10.2 CAD representations of external and internal cellular structures for support structure and lightweight applications

10.3.2 Manufacturing Process

The experiments were conducted at 3T RPD Ltd. UK using DMLS EOSINT M270 machine manufactured by EOS GmbH, Munich, Germany. The oxygen content in the chamber was kept below <0.13% and a fixed layer thickness of 30 µm is used for both the part and the cellular support structure. The material used was titanium alloy powder (Ti6Al4V) supplied by LPW Technology Ltd., UK. For further details on process parameters, refer to chapter 3 (materials and methods).

10.3.3 Characterisation and Analysis

The manufacturability of the graded cellular support was evaluated through visual inspection to judge the success and failure of part building. A sample of the powder was studied in scanning electron microscope (SEM - Hitachi S-3200N) to investigate the shape and morphology of the particles. No stress relieving heat treatment (part of the standard full manufacturing sequence for this process) was performed to allow investigation of the residual stresses in the manufactured cantilever parts.

Wire-Electric Discharge Machine (EDM) was used to separate the cellular support from the cantilever part. The resulting deflection in the cantilever overhang was measured using a Roland MDX-20. This is a 3D scanner for scanning 3D objects and creating 3D cloud data by using a moving needle probe to touch the surface of the object and record data points. “Dr. PICZA” scanning software installed on this machine was used for dynamic graphic display, curve smoothing, and adjusting the height of the scanned surface. The scanned data was exported as a point cloud data (ASCII) and processed in MATLAB software for visualization. Digital optical scan (Dino-Lite) was used for measuring the strut size of the cellular structure and for measuring the dimensional accuracy of the manufactured cantilever part.

10.4 Results and Discussion

10.4.1 Manufacturability analysis

As depicted in Fig. 10.3(a and b), different geometries with external and internal cellular structures and varying cell size and volume fractions were manufactured in the DMLS machine. This includes cell sizes varying from 0.5

mm to 5 mm and volume fractions varying from 6 % to 60 %. In addition to the regular structures, some graded cellular structures with varying densities were also successfully manufactured. However, some parts failed to manufacture during processing as depicted in Fig 10.3 (b). The following sections discuss in detail the manufacturability of the test samples for both internal and external cellular support structures.

10.4.1.1 Manufacturability of cellular support structure

The manufacturability of cellular structure depends on the cellular topology (i.e. cell shape, cell size, and % of volume fraction). Cell shape refers to the connectivity among unit cells in a structure and defines whether the structure is self-supporting during the build. The most fundamental requirement of any cellular structure shape is that it must be self-supporting. The gyroid used in this study is a triply periodic minimal surface structure that has no planes of symmetry and no embedded straight lines. Unlike some previous designs, these structures have circular and smooth struts with a spherical core. The inclination angle of the circular and smooth struts of the unit cell continuously varies around the spherical core which enables the layers to grow up gradually during the DMLS build with minimum changes in area and position between two subsequent layers. This characteristic shape of the gyroid structure also make possible to build large cell sizes with large spherical core. This was not the case with previous cellular designs with straight beam-like struts and a polyhedral core failed to manufacture in large cell size ranges greater than 5mm. The large overhang strut resulting from these designs caused a serious deformation or sagging to occur.

Establishing relationships between cell topology and manufacturability is crucial in the design of a suitable cellular support structure for metal AM processes. Fig. 10.3 (c) shows the relationship between cell size, % volume fraction, and strut size (i.e. the beam diameter) of the gyroid structure. The strut size shown here is based on measurements taken from the CAD geometry. From this correlation, it can be noted that for 1 mm cell size and 50% volume fraction the strut size is approximately 0.832mm. Which means by either increasing the volume fractions or the cell size we can increase the strut size of the cellular structure.

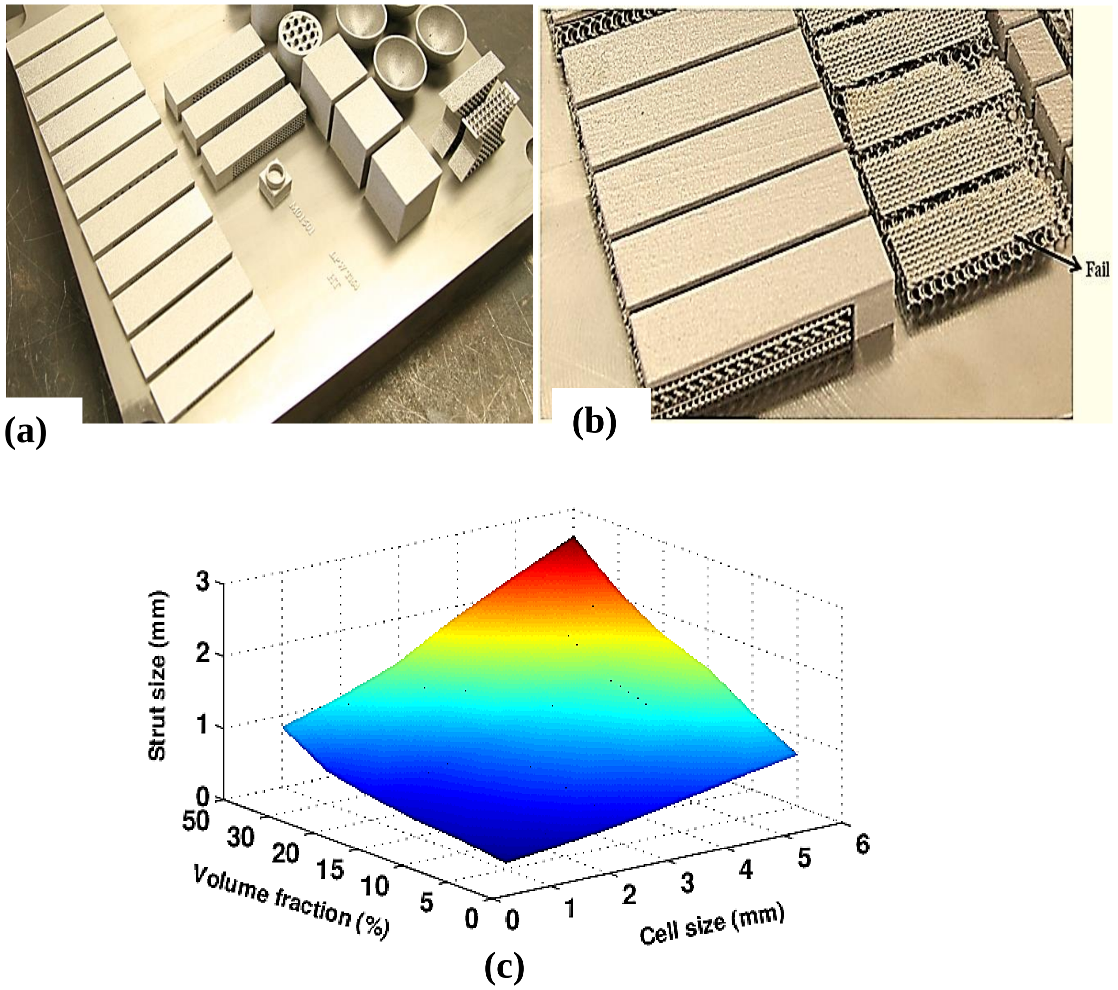

Figure 10.3 (a) and (b) External and internal cellular support structures manufactured in DMLS machine (c) relationship between cell size, % volume fraction, and strut size [DMLS M270, Ti-6Al-4V]

Low volume fractions are desirable for external support structure in minimizing build time and material, while higher volume fractions are suitable for permanent internal structures where a combination of light-weight and high strength is needed. In our experimental study, external cellular support with 3mm cell sizes and 6% volume fraction was built without failure. This combination yields a strut size of approximately 0.3mm which is the safe manufacturing region for this cell size. The 6% volume fraction was intentionally used in the lower section of the cellular support to speed up the scanning time and maximise material saving. This has resulted a significant saving in both material and energy consumption. For the smaller cell sizes used at the support and part interface, it was possible to build a minimum strut size of 0.127mm for 0.5mm cell size and 15% volume fraction. This strut size could not be achieved in bigger cell sizes due to a lack of cell connectivity and will probably cause manufacturing failure. The height and overhang resulting from 0.5mm-1mm cell sizes is very small and unlikely to cause a manufacturing failure during the build.

The DMLS process allows a choice of powder recoater blade including steel, ceramic and a soft brush; however one recoater must be used for the full build, including both support structures and the supported part. The soft brush coater is used for building delicate and fragile structures but cannot achieve full powder density due to the lower compaction applied to powder layer , and so is of little use for building functional parts. Although all our tests were performed on hard steel recoater, it could be possible to build cellular structures with smaller strut sizes by using the brush recoater. As the build height increases, the density of surrounding powder also offers some structural stability to withstand recoater forces during the build. Recoating is one area where different brands of machine differ. The broadly similar SLM process uses a silicone elastomer recoater as the default choice.

10.4.1.2 Manufacturability of supported surface

The geometric shape, size, and orientation of the part alter the amount and type of support needed, as downward facing regions of part need to be fixed to the platform under the build area. This is also affected by the material being manufactured, with some materials requiring a higher amount of support than others, due to larger mechanical stresses building up during the build process. Of the standard materials used in DMLS, the Ti64 as used in this study is considered the most difficult material to build due to the high reactivity (Thijs et al. 2010), and has the highest demands on its support structures. The first overhanging layer which is supported is crucial for a successful build as it lays the foundation for subsequent upper layers of the part. Thermal distortions in particular are a problem to the manufacturing technique, as if they obstruct the blade spreading powder for the next layer can cause a machine crash, stopping the machine and leaving all partially-built items incomplete.

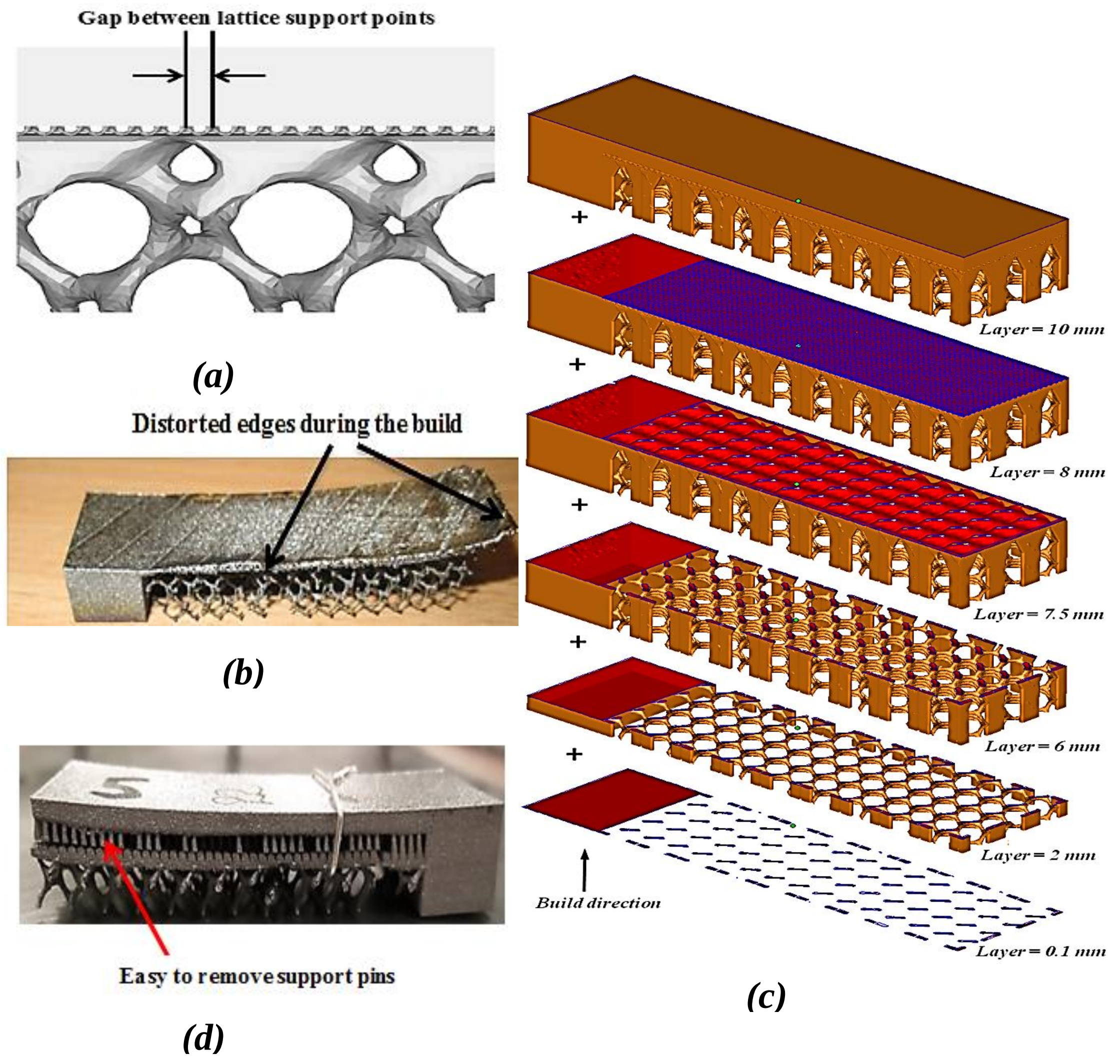

Figure 10.4 (a) Stages of building the cantilever part and graded cellular support simultaneously layer-upon-layer (b) Distorted cantilever edges during the build (c) Gap between adjacent supports points of graded cellular structure (d) Support pins used to facilitate the removal of the support.

The effectiveness of the support is determined by the structural strength of the cellular structures and the gap between adjacent support points in contact with the part. The smaller the gap the more effective the support is in controlling the thermal distortions in overhang regions. As shown in Fig 10.3 (b) some cantilever parts with step graded cellular support have failed to build. There was a large unsupported region measuring > 2mm horizontally in the transition between lower bigger cells (cell size=3-4mm, volume fraction=6%) and upper smaller cells (cell size=0.5-1mm volume fraction=15%). The gap here refers to the size of the pore between the struts of the cellular structure as shown in Fig.

10.4 (a). Similarly, Fig. 10.4 (b) shows a cantilever part which is supported with uniform cellular structure (cell size of 4mm and volume fraction of 6%), which failed due to de-lamination of the overhang layer from support. Although the side graded cellular support improved the support stiffness, it has the same shortcomings related to large support gap and adds further complications to support removal. The smallest support gap tested was 0.5mm, used with the gradually graded cellular support. This size results a support gap of 0.5mm which is very suitable for DMLS manufacture. Fig. 10.4 (c) shows the stages in building the cantilever part and the gradually graded cellular support with shell simultaneously layer-upon-layer. The use of graded lattice structures has the advantage of low volume fraction supports in the bulk of the structure, while also reducing the support gap. This has improved the manufacturability of the part making them ideal for material saving and meeting different geometric support requirements.

Graded support with bigger support gaps of up to 1.5mm was also successfully built. Given this, it is recommended that small support gaps between contact points should be maintained. For reliable and safe builds, it is recommended that unsupported area should not exceed 1.5 mm in any direction for horizontal flat geometries. Large quantities of support structure also increase the surface roughness of the supported regions. To facilitate a manual removal of cellular support, support pins having a breakable neck were used in some of the step graded cellular support structure as shown in Fig. 10.4 (d). Wire-erosion techniques such as Electric Discharge Machining (EDM) are commonly used to cut large support structures provided that there is a path for the tool to access the cutting area.

10.4.1.3 Graded cellular support for curved geometries

For a complex, curved part there will often be features which have a lowest point in space above the build platform. Fig. 10.5 (a) shows the building stages of convex geometry with the lowest point shown by the red spot. It is important that this feature is well supported (ideally with multiple support points in contact with the feature) otherwise they will be brushed away by the recoater action during powder deposition. As shown in Fig. 10.5 (b), a small cell size (0.5mm) was used in the experiment to make sure that the lowest point of the curve is properly supported. Careful positioning of the lattice (i.e. moving the structure in

X,Y or Z by fractions of a unit cell) in relation to this location can also be considered to ensure good connectivity at this critical point in the manufacture. Adaptive graded cellular support can be effectively used for curved geometries which require higher support height and as part complexity increases to meet the different support requirement for different regions.

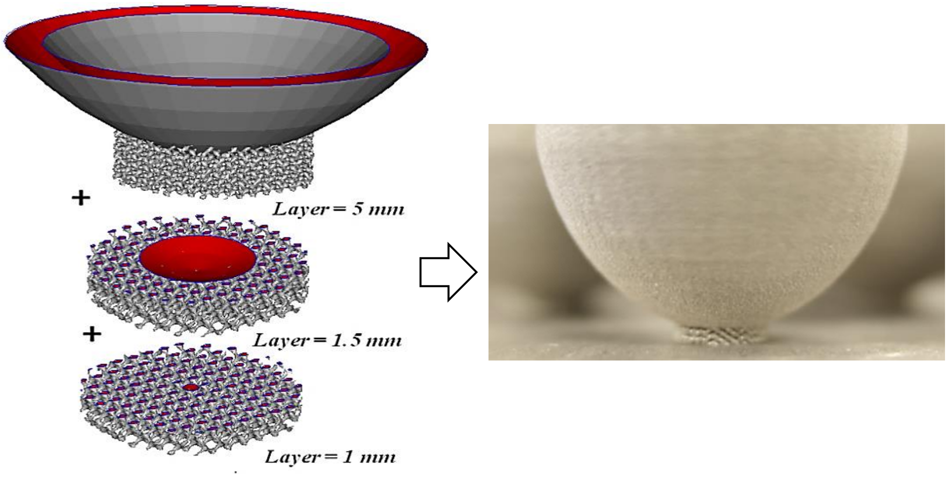

Figure 10.5 (a) CAD model showing the cellular support stages for curved geometry (b) DMLS manufactured part using small cell sizes.

10.4.1.4 Permanent internal lattice structures for lightweight applications

As was shown in Fig. 10.3 (a), cylindrical and cubic parts with internal cellular structures surrounded by a boundary shell of 2mm were manufactured in DMLS. The structural requirement of internal lattice structure is different to external cellular support structures. Internal lattice structures remain in the final component and are used as lightweight permanent structures and must provide sufficient strength and structural rigidity to meet part loading conditions. Compare this to the external lattice support structures previously discussed, which are temporary and just used to enable the manufacturing of complex overhang geometries during the build. Similar to external support, the internal structures must be manufacturable in the process and similarly they also act as support on the downward facing surfaces within cavities. Internal cellular structures with high volume fractions or graded ones allow small distances between support points and thus improve manufacturability of the most difficult case, the horizontal flat surface. Cylinder and concave geometries if self-supporting may not require support unless the internal radius is large causing an overhang upper section.

Since internal structures are built within a shell surrounding the structure, it is important that the removal of loose powder is facilitated by introducing one or a number of small holes in the shell. These allow loose powder to be drained after part building is completed. Cell sizes above 2 mm have relatively bigger spaces in the lattice network and thus allow simpler removal of loose powder compared to small cell sizes. If the cell sizes are too small and especially if the shape of the cavity is complex it can be very difficult to remove all the loose powder. Functionally graded internal lattice structures can be used in many applications in which the strength and stiffness required varies with position within the component.

10.4.2 Dimensional accuracy of the cantilever part

The primary function of support is not only to enable the manufacture of complex geometries but also to ensure accurate dimensions of the supported surface. Fig. 10.6 (a) shows the dimensional inaccuracy in one of the manufactured cantilever overhangs that was supported with uniform cellular support structure. The dimensions of the overhang edges are reduced from the original CAD design size due to distortions during laser processing. This edge effect phenomenon is more prominent in cantilever parts in which cellular support with a large cell sizes are in contact with the supported surface. As a result, sections of the edge boundary are not properly supported and when exposed to the laser energy shrink freely causing dimensional changes in the final part as illustrated in Fig. 10.6 (b). The red colour gradient shows that maximum dimensional loss occurred at the overhang edges and gradually decreases towards the middle region (shown in blue colour) of the supported cantilever surface.

To compare the dimensional accuracy of the various cellular support methods, the edges of the overhang was measured and the percentage of dimensional error E was calculated.

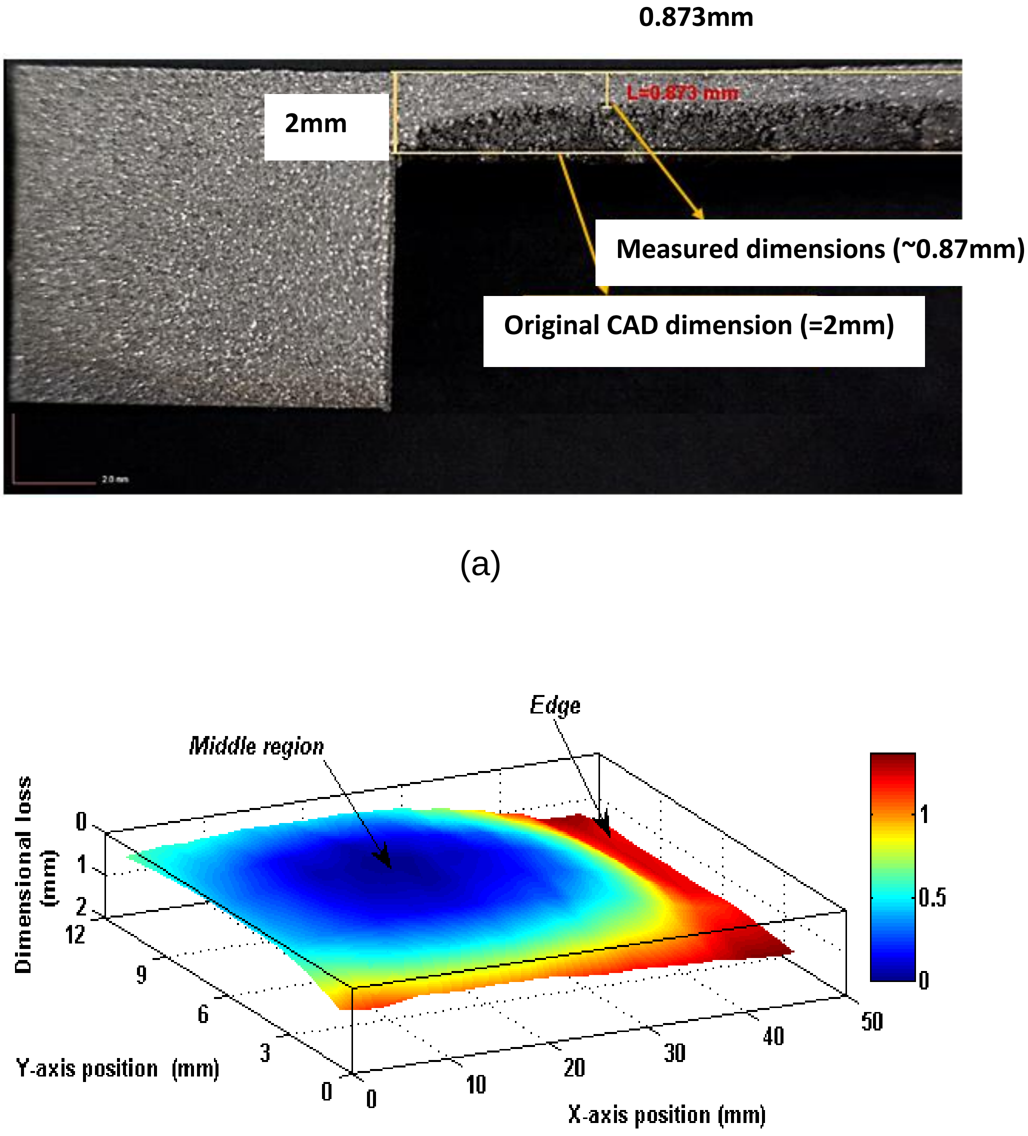

(a)

(b)

Figure 10.6 (a) Optical scan micrograph showing the dimensional loss in cantilever edges supported with uniform cellular structures manufactured in DMLS (b) Dimensional loss profile of the supported surface of cantilever overhang after 3D scanning.

Table 10.1 lists the calculated % error of the cantilever part for various cellular support methods. The result in Fig. 10.7 shows a maximum dimensional error of 4.05 % for step graded cellular support. The use of step graded cellular support with shell has improved the dimensional error from 4.05% to 2.35%.A further refinement to this approach is to also add breakable interface pins at the interface of the support and the part.

Manufacturing difficulties associated with step graded method such as defects within cellular support structure could be translated to the part building increasing the dimensional error in the cantilever. No significant advantage is achieved in terms of dimensional error by the use of side graded method except that it adds structural stiffness to the support provided by used of high volume fraction around cantilever edges. Additional challenges such as difficulties of manual support removal for fragile geometries may be faced by the use of this method. However, this method could be suitable for use in large geometries where high residual stresses are formed in which the support structure is to be removed by machining methods.

Cantilever part supported with uniform cellular support has a dimensional error of 3.09%; however, with the use of boundary shell surrounding the cellular structure the dimensional error is reduced to 1.56%. Similar to side graded cellular support, this method is not practical for fragile thin geometries where the support removal is likely to add further distortions and part damage to the part. Uniform cellular support is also limited to certain flat geometries and not applicable to some curved surfaces. The gradually graded cellular support provided the best solution among all support methods in minimizing the dimensional error and is suitable for many geometric shapes. This support method with shell has the minimum dimensional error of 1.07% among all cellular support methods tested. The highest error of 1.48% was recorded when this support method is used without the boundary shell. The smaller separation between adjacent support points provided by the smaller cell sizes used at the interface are suitable for thermal management and constraining the edge distortions. They are at the same time individually easy to break and can be removed manually with the help of hand tools such as pliers. This also makes this method suitable for thin, fragile and curved geometries that require lowest point support in multiple locations. The addition of thin boundary shell with the cellular support has significantly improved the dimensional accuracy and provided additional stiffness to all support methods.

Table 10.1-Dimensional error of the cantilever overhang edges

Measured location (mm)	A_O (mm)	Dimensional error, E (%)							
		1	2	3	4	5	6	7	8
Thickness:									
X = 12 , Y = 0	2	1.00	0.50	3.94	4.27	6.36	4.37	1.02	1.51
X = 29 , Y = 0	2	5.50	3.70	5.61	10.81	12.20	0.56	10.50	4.50
X = 58 , Y = 0	2	2.50	6.15	6.56	1.03	4.66	9.41	0.00	4.37
X = 12 , Y = 15	2	1.50	0.49	1.47	10.14	4.30	7.73	16.20	12.50
X = 29 , Y = 15	2	1.00	1.01	1.00	6.93	0.53	3.74	9.44	9.64
X = 58 , Y = 15	2	6.00	3.72	1.54	4.04	2.63	4.86	4.64	3.24
X = 58 , Y = 7.5	2	10.50	10.06	0.76	6.30	1.61	8.20	4.17	1.14
Width, w	15	1.67	0.52	0.07	0.07	0.20	0.26	0.26	0.59
Length, l	58	0.16	0.02	0.10	0.02	0.16	0.07	0.02	0.05
Average, E (%)		2.35	1.42	1.07	1.48	1.56	3.09	4.05	3.79

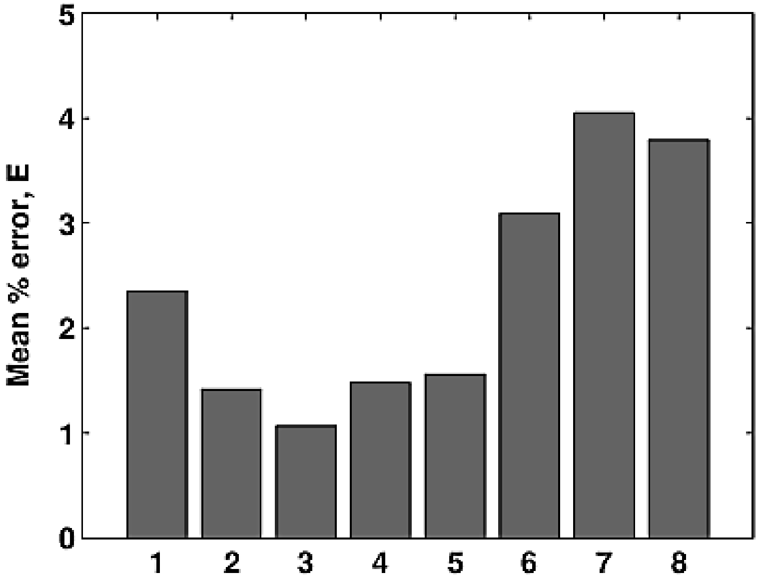

Cellular support method:

1. Step graded cellular support with shell (3mm-pins, 6%)
2. Gradually graded cellular support (4-0.6mm, 8-100-15%)
3. Gradually graded cellular support with shell (4-0.5mm, 8-100-15%)
4. Gradually graded cellular support (4-0.7mm, 8-60-15%)
5. Uniform cellular support with shell (3mm, 6%)
6. Uniform cellular support with shell (3.5mm, 6%)
7. Step graded cellular support (3mm-pins, 6%)
8. Side graded cellular support (4-2mm, 6-10%)

Figure 10.7 Average dimensional error of the measured cantilever part

10.4.3 Deflection method for estimating the residual stress

AM processes accumulate residual stresses during material build-up. Residual stresses can be defined as the stresses that remain within a material or body after manufacture and material processing in the absence of external forces or thermal gradients (Rossini et al. 2012). The expansion or contraction associated with a newly melted layer in metal AM processes is constrained by the preceding layers of part and/or support structure which generates significant residual stress in most metallic materials. The engineering properties of materials, notably fatigue life, distortion, dimensional stability, layer delamination, corrosion resistance, and brittle fracture can be considerably influenced by residual stresses (Totten et al. 2002). To avoid this, usual manufacturing of metal parts by AM processes would always include a stress-relieving heat treatment cycle before removal of all supports from the component.

Over the years, different methods have been developed to measure residual stress for different types of components in order to obtain reliable assessment (Lu, 1996). In this study, we used a splitting method (Walton 2002; Baldwin 1949), to estimate residual stress present in the part by removing some of the constraints and observing the distortion obtained as stresses relax. This is a destructive method that relies on the measurement of deflection due to the release of residual stress upon removal of support from the cantilever part.

To develop a mathematical model for interpreting deflection measurements after slitting or separating the cantilever part from the lattice support, a simple beam theory is used (Gordon, 1968):

$$\frac{M}{I} = \frac{\sigma}{C} = \frac{E}{R} \tag{10.1}$$

Where *M* is the bending moment to which the beam is subjected. Bending moment *M* is equal to load multiplied by distance (N. m). *I* is the moment of inertia of the section of the beam, usually in (m^4). *R* is the radius of curvature of the beam when it bends under load in (m). *E* is the Young's modulus (Pa). C is the distance from neutral mid-point axis (m). σ is the stress in the material in (Pa).

For a rectangular beam at the surface where the stress is greatest:

$$I = \frac{bt^3}{12} \tag{10.2}$$

Where *b* and *t* are the width and thickness of the part cross section, respectively.

The distribution of residual stress in the deflected cantilever in Fig. 10.8 is unlikely to be exactly linear due to cyclic variation corresponding to differences in heating and cooling rates in different parts of the component. However, to enable analysis, this approximation is made and the beam stress is assumed to vary linearly through the section. The bending moment created by the residual stress may be expressed as:

$$M = \frac{EI}{R} \tag{10.3}$$

Given that:

$$C = \frac{t}{2}$$

Therefore,

$$\sigma = \frac{Et}{2R} \tag{10.4}$$

R may be expressed in terms of the deflection, *d*, and the length of the curved surface, *L*, by:

$$R = \frac{L^2}{2d} \tag{10.5}$$

Therefore,

$$\sigma = \frac{Etd}{L^2} \tag{10.6}$$

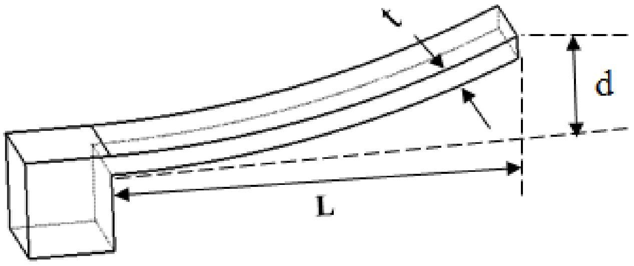

Figure 10.8 Determination of residual stresses by deflection method

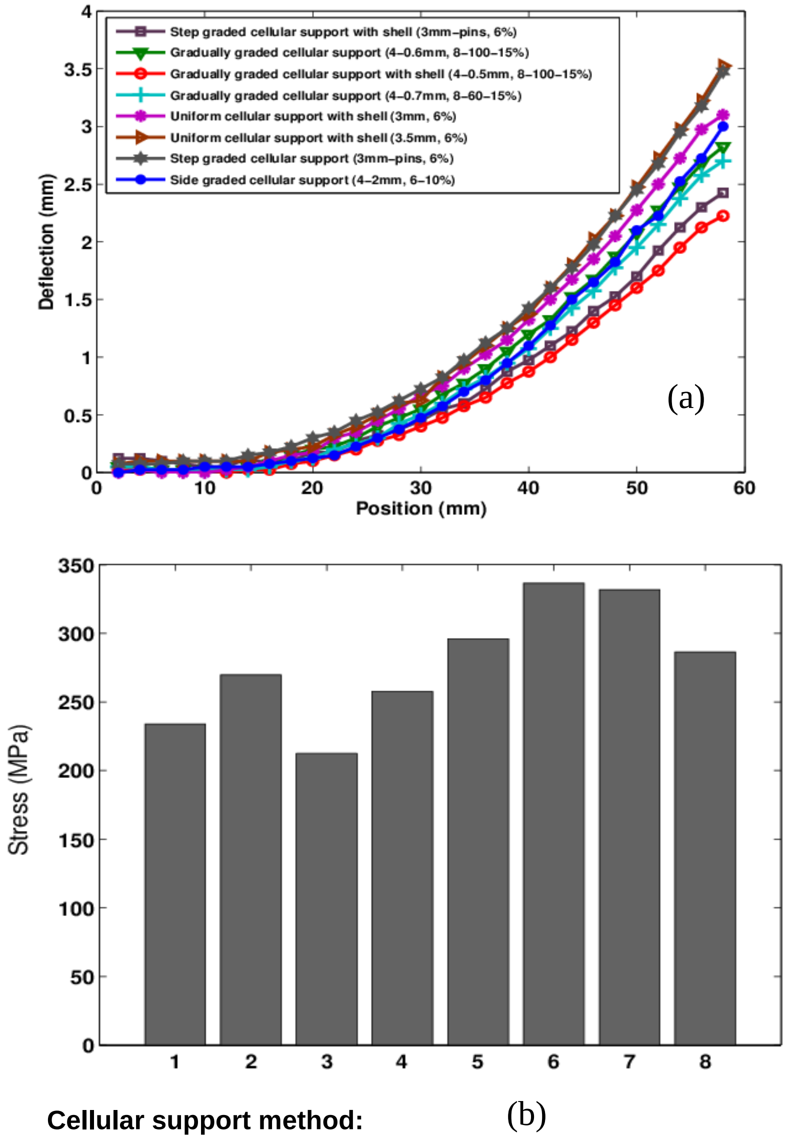

Cellular support method:

1. Step graded cellular support with shell (3mm-pins, 6%)
2. Gradually graded cellular support (4-0.6mm, 8-100-15%)
3. Gradually graded cellular support with shell (4-0.5mm, 8-100-15%)
4. Gradually graded cellular support (4-0.7mm, 8-60-15%)
5. Uniform cellular support with shell (3mm, 6%)
6. Uniform cellular support with shell (3.5mm, 6%)
7. Step graded cellular support (3mm-pins, 6%)
8. Side graded cellular support (4-2mm, 6-10%)

Figure 10.9(a) - Measured deflection of the cantilever parts (b) Calculated residual stress for various cellular support structure methods.

Fig. 10.9 (a) displays the deflection profiles of the cantilever parts along the overhang. They all follow the same profile with little variation in amount of maximum deflection between different types of cellular support. Gradually graded cellular support with small cell size at the interface and boundary shell provided the minimum deflection among all support types. Fig 10.9(b) illustrates the calculated longitudinal residual stresses from various cellular support structure methods used for the cantilever overhang. The depth and intensity of the residual stresses is proportional to the lift height. The maximum calculated longitudinal stress is (336.59 MPa) for cellular structure with shell and the lowest is (212.46 MPa) for exponentially graded lattice support structures with small cell sizes in contact with the part. The more rigid the design of lattice structure, the higher the resulting residual stress. Lattice structures having higher volume fractions are more rigid compared to lower volume fractions. Rigidity of the structure is also influenced by the interface structures which are in contact with the cantilever.

The levels of residual tensile stress may become high for large geometries which are built horizontally requiring large areas of support material. Catastrophic fracture can occur due to cracking when the tensile stress level exceeds the cohesive strength of the material, and may sometimes lead to stopping the manufacturing process and preventing the part being completed. As such, premature failure due to residual surface tensile stress in the manufactured product is to be avoided at all costs. Stress-induced deformations can be avoided by passing the component through stress-relieving heat treatment process prior to support structure removal, whereby most residual stresses (depending on exact cycle chosen) are released from the part, although to get to this stage the manufacturing process needs to complete the component first.

10.5 Conclusion

In this study, a novel graded cellular support structure was developed for metal additive manufacturing. Experimental tests were conducted using a DMLS machine on different geometries, manufactured using commercially available Titanium alloy (Ti-6Al-4V). The manufacturability, dimensional accuracy, and resultant residual stresses of manufactured parts were investigated to compare the effectiveness of various graded cellular support structure methods. It was found that the manufacturability of cellular structure is influenced by the cellular topology (i.e. cell shape, cell size, and % of volume fraction). External cellular support with 3mm cell sizes and 6% volume fraction was built without failure. The 6% volume fraction was intentionally used in the lower section of the cellular support to speed up the scanning time and provide 94 % material saving. The minimum strut size that was built is

0.127mm for 0.5mm cell size and 15% volume fraction.

Some cantilever parts supported with step graded cellular support have failed to build. There was large unsupported region > 2mm in the transition between lower bigger cells and upper smaller cells separated by thin solid layer. The smallest support gap tested was 0.5mm, used in the gradually graded cellular support. This size results a support gap of 0.5mm which is very suitable for DMLS manufacture. Given this, it is recommended that small support gaps between contact points should be maintained. The gradually graded cellular support provided a minimum dimensional error of 1.07 % for the cantilever part among all support methods tested. A maximum error of 4.05 % was calculated for step graded support. The maximum calculated longitudinal stress is (336.59 MPa) for uniform cellular support with shell and the lowest is (212.46 MPa) for gradually graded cellular support.

Overall, the use of gradually graded cellular support structures has improved the manufacturability of both the cellular structure and the supported part. The potential material saving combined with multi-functionalities they offer, makes them suitable for internal lightweight and external support structure applications of metal additive manufacturing. These graded cellular structures are applicable to various metallic materials and machines used in AM industry, in particular, the powder bed fusion processes. The enhanced manufacturability due to the gradient density combined with the lightweight functionalities will promote the design of more advanced and complex components that were difficult before.

CHAPTER 11

Conclusions and Future Recommendations

This study has investigated the manufacturability and mechanical behaviour of advanced lightweight cellular structures in metal AM processes. The cellular structures used in the research are based on Triply Periodic Minimal Surface (TPMS) cell topologies. Comprehensive experimental tests were conducted at different cell topologies using commercially available 316L stainless steel, Titanium alloy (Ti-6Al-4V), and Aluminium alloy (AlSi10Mg) metal powders. The experiments were performed in SLM MCP Realizer and the DMLS EOSINT M270/M280, two of the most commonly used metal AM systems. The finite element method was used to simulate the temperature and stress fields of unsupported overhang layers built in SLM process.

It was found that the manufacturability of cellular structure is influenced by the cellular topology (i.e. cell shape, cell size, and % of volume fraction). Gyroid and Diamond structure prove to be suitable for SLM/MDLS processes. The minimum strut size that was built was 0.127mm for Gyroid with 0.5mm cell size and 15% volume fraction. These organic cellular structures with controlled cell sizes and densities which are very difficult or impossible to be manufactured by means from light metallic alloys such Ti-6Al-4V and AlSi10Mg are now proved to be manufacturable in SLM and DMLS processes. The good manufacturability of Gyroid and Diamond cell types in SLM/DMLS can be attributed to the curved struts and spherical pore forming the unit cell. The inclination angle of the circular strut continuously varies along the spherical pore, which makes layers grow up gradually with slight changes in area and position between two subsequent layers during the SLM/DMLS process. In this way, the next layer is well supported by previously solidified layer. That means that these TPMS cellular structures have a self-supported unique characteristic in a wider range of cell sizes, volume fractions, and cell orientation which makes them suitable for SLM and DMLS processes

For all the three tested materials, both compressive elastic modulus and yield strength increase with the increase of solid volume fraction of the strut (i.e.

relative density). The experimental results reveal that cell size has relatively a minor influence compared to volume fraction for both elastic modulus and yield strength of cellular structure, when the volume fraction is kept constant. The cell orientation has a significant effect on the compressive properties of cellular structures. It was found that the highest modulus 316L stainless steel Gyroid structure lies between 40 and 60 degree of cell rotation. The Elastic modulus of the worst cell orientation in manufacturing (i.e. nearly vertical cell struts which are parallel to the loading direction) is found to be 20.37% higher than that of the normal un-rotated cell orientation of similar cell size and volume fraction. the compressive elastic modulus and yield strength of Gyroid cellular structure with 5.5 mm cell size and 15% solid volume fraction (equivalent to 0.15 relative density) is about, 251 MPa and 14 MPa for 316L stainless steel, 231 MPa and 16 MPa for AlSi10Mg, and 810 MPa and 50 MPa for Ti-6Al-4V, respectively. Cellular structures made from Ti-6Al-4V are 3-4 superior to that of 36L stainless steel and AlSi10Mg of similar cell size and volume fraction, making them attractive material for lightweight and load bearing applications.

The uniform cellular support structures show good manufacturability characteristics; however, some of the parts failed during the build. For big cell sizes, the distance between the adjacent support points to the supported surface is too large; therefore, there is too much material that is unsupported and the part was distorted by the thermal stresses. The use of graded cellular support structures has improved the manufacturability of the supported part. The potential material saving combined with multi-functionalities they offer, makes them suitable for internal lightweight and external support structure applications of metal AM. The experimental results have revealed that a potential material saving can be achieved when lattice support structure with lower volume fractions is used. For example, it was possible to manufacture gyroid lattice structures with 8% of relative volume, which means 92% of loose powders can be easily removed and recycled. Low volume fraction also allows minimum build time and required energy for SLM parts. The theoretical energy consumptions model in Appendix A indicate that build time is the most significant factor to consider when reducing the energy consumption of AM parts.

The results of single layer simulation show that the highest temperature gradient is found at the start of first track scan of the layer and drops subsequently for all scanning speeds. The predicted length of the melt pool increases at higher scan speeds while both width and depth of the melt pool decreases. High von mises stresses was predicted in the scanned layer caused by the stepwise increase and decrease in the temperature with each successive overlapping laser tracks which leads to alternating compressive and tensile residual stresses within the layer. High cooling rates were predicted when the layer is scanned over a solid substrate compared to when layer is scanned on loose powder bed.

From these results, the following potential areas will be considered potential for further future research,

- In practice, any imperfections in the cellular structure (such as non-uniformities in relative density or initially bent cell walls) induce bending of the cell walls, reducing the compressive properties. However, this was out of the scope of this study and will is recommended future work.
- The effect of powder particle size and distribution on the manufacturability of cellular structures will be investigated in the future works.
- Optimal scanning strategies for these cellular structures have not been investigated. When used for support purposes the lattices are only sacrificial parts built to enable the final component to be produced. As such, it is likely that much quicker strategies for their manufacture could be developed in a possible future project.
- The cellular support structure studies presented here did not consider the effect of cellular support on the surface roughness of the supported regions as well as the manual removal of the external cellular support. These are important for the design of more efficient support structure method for delicate geometries.
- The heat transfer characteristics and extended mechanical properties of these cellular structures will be analysed in the future using finite element simulation method.
- Further improvement and validation is needed for the analytical energy consumption model presented in Appendix A, so that energy consumption of different competing options can be compared during the design process.

The research has contributed to new knowledge in,

- The understanding of the temperature and stress fields in overhang geometries during SLM processing.
- The manufacturability of low-density TPMS cellular structures with varying cell size, orientation and volume fractions from various metallic powders using SLM and DMLS processes. The manufacturability study has presented the limitations of SLM/DMLS in building cellular structures in terms of cell shape, volume fraction, cell size, orientation, and powder material.
- The mechanical behaviour of TPMS cellular structures. The evaluation of the mechanical properties of these cellular structures on different materials aims to illustrate the effect of different cell types, sizes, and volume fractions, and orientation on compressive properties. The data on the mechanical properties will aid the designer on the selection and use of the right cell type, size, and volume fraction to suit the functional demands of particular application.
- The design and manufacturing of support structures through the novel applications of low-density uniform and graded cellular support structures for metal AM parts. The new support structure method addresses the saving of energy (via reduced built-time), and material saving of the internal or external cellular support structures which could waste very expensive raw metal materials and built-time in complex parts that require large support. The aim of the cellular support is to tackle the process limitation in building complex and hollow internal geometries that will otherwise require non-removable support structures by replacing them with multifunctional permanent cellular support.

Design recommendations of cellular lattice structures:

- Any lattice structure used for support structure applications should be designed in such a way that, the volume fraction generated is as minimum as possible, and provided that both support structure an loose powder material can be removed after the build. Grading the cellular structure is the best option in achieving multiple goals such as reduced build-time, reduced support volume, maximum heat dissipation, easy removal of powder and support. However, proper grading tools should be used for generating the graded support, in particular, the transition from low volume fraction to higher volume fractions and vice versa.

- The main determining factors for manufacturability are the cell shape, volume fraction and cell siz. The material itself has a particular influence in small cell sizes with low volume fractions. Cell sizes smaller than 1mm should be avoided as it will be difficult to remove the loose powder trapped in the cell structures. Similarly, depending on the cell type, very low volume fractions below 6% (e.g. for Gyroid) should be avoided as it will result a very fragile cell ligaments/struts that will fail during the build. The cell type should be self-supporting, and as such, the cell horizontal overhang that is perpendicular to the build direction should be minimized to below 1mm.
- It is recommended to use proper cleaning and air/bead blasting post-processing to remove any loose powders attached to the cell legaments/struts. This will significantly improve the dimensional accuracy of the cellular structures. However, proper care should be practiced when cleaning very low volume fractions that are too fragile as some of the struts may break during post-processing. It is equally important to perform proper cleaning operation before any stress-relievign heat treatment is conducted on the cellular lattice structure. This minimizes the risk of bonding loose powders to the cell struts.
- Cell struts that are parallel to the loading direction provide highest compressive properties but are difficult to be manufactured in large cell sizes due to the resulting overhang in the horizontal strut forming the cell. An optimisation could be achieved between manufacturability and best orientation to achieve certain mechanical properties.

References

Abe, F., Santos, E. C., Kitamura, Y., Osakada, K., & Shiomi, M. (2003). Influence of forming conditions on the titanium model in rapid prototyping with the selective laser melting process. *Proceedings of the Institution of Mechanical Engineers, Part C: Journal of Mechanical Engineering Science*,*217*(1), 119-126.

Agarwala M, Bourell D, Beaman J, Marcus H, Barlow J. (1995). Direct selective laser sintering of metals. Rapid Prototyp J;1:26–36.

Ajdari, A., Nayeb-Hashemi, H., & Vaziri, A. (2011). Dynamic crushing and energy absorption of regular, irregular and functionally graded cellular structures. *International Journal of Solids and Structures*, *48*(3), 506-516.

Allen S. and Dutta D. (1994) "On the computation of part orientation using support structures in layered manufacturing", Report No. UM-MEAN-94-15, July, 1994.

Amato, K. N., Gaytan, S. M., Murr, L. E., Martinez, E., Shindo, P. W., Hernandez, J.,. & Medina, F. (2012). Microstructures and mechanical behavior of Inconel 718 fabricated by selective laser melting. *Acta Materialia*,*60*(5), 2229-2239.

Anderson, R.L., and Fahlman, E.G. (1924). A Method for Measuring Internal Stress in Brass Tubes, *J. Inst. Met.,* Vol 32, p 367–383.

Andrews, E., Sanders, W., & Gibson, L. J. (1999). Compressive and tensile behaviour of aluminum foams. Materials Science and Engineering: A, 270(2), 113-124.

Asberg B., Blanco G., Bose P., Garcia-Lopez J., Overmars M., Toussaint G., Wilfong G. and Zhu B. (1997) “Feasibility of design in stereolithography”, Algorithmica, Vol. 19, pp. 61–83.

Ashby, M. F. (2000). *Metal foams: a design guide*. Butterworth-Heinemann.
sintering of metals. Rapid Prototyp J 1995;1:26–36.

Baldwin WM. (1949). Residual stresses in metals. Philadelphia: Proc. American Society for Testing and Materials;. p. 49.

Beaman, K.L. Wood, H. Marcus (eds.) (2005). Solid Freeform Fabrication Proceedings, The University of Texas, Austin Texas, , pp.231-241

Bertol, L.S., Júnior, W. K., da Silva, F.P., Aumund-Kopp, C.. (2010). Medical design: Direct metal laser sintering of Ti–6Al–4V. Materials & Design, , 31(8): 3982-3988.

Boccalini M, Goldenstein H. (2001). Solidification of high speed steels. Int Mater Rev;46:92–115.

Boresi AP, Schmidt RJ, Sidebottom OM. (1993). Advanced mechanics of materials. 5th ed. New York: John Wiley;

Brandl E, Heckenberger U, Holzinger V, Buchbinder D. (2012) Additive manufactured AlSi10Mg samples using Selective Laser Melting (SLM): microstructure, high cycle fatigue, and fracture behavior. Mater Des;34:159–69.

Brandl, E., Heckenberger, U., Holzinger, V., & Buchbinder, D. (2012). Additive manufactured AlSi10Mg samples using Selective Laser Melting (SLM): Microstructure, high cycle fatigue, and fracture behavior. *Materials & Design*,*34*, 159-169.

Brooks, W., Sutcliffe, C., Cantwell, W., Fox, P., Todd, J., & Mines, R. (2005). Rapid design and manufacture of ultralight cellular materials. In Proceedings of the Solid Freeform Fabrication Symposium. Austin, TX.

Cansizoglu, O., Harrysson, O., Cormier, D., West, H., & Mahale, T. (2008). Properties of Ti–6Al–4V non-stochastic lattice structures fabricated via electron beam melting. Materials Science and Engineering: A, 492(1), 468-474.

Cao, X. Q., Wang, Z. H., Ma, H. W., Zhao, L. M., & Yang, G. T. (2006). Effects of cell size on compressive properties of aluminum foam. Transactions of Nonferrous Metals Society of China, 16(2), 351-356.

Carslaw H, Jaeger J. (1959).Conduction of heat in solids, 2nd ed. vol. 1.

Chen Chu, Greg Graf, and David W. Rosen, (2008) “Design for additive manufacturing of cellular structures”, computer-aided design and applications, 5(5), 686-696.

Chen He-fa. (2003) Effect of cellular microstructure on the mechanical properties of open-cell aluminum foams[J]. Hot Working Technology, (3): I-2.

Childs, T. H. C., Hauser, C., & Badrossamay, M. (2005). Selective laser sintering (melting) of stainless and tool steel powders: experiments and modelling. Proceedings of the Institution of Mechanical Engineers, Part B: Journal of Engineering Manufacture, 219(4), 339-357.

Chiras, S., Mumm, D.R., Evans, A.G., Wicks, N., Hutchinson, J.W., Dharmasena, K.P., Wadley, H.N.G., and Fichter, S., (2002), The structural performance of nearoptimized truss core panels, *Int'l J. Solids and Structures*, 39, p.4093.

Dai K, Shaw L. (2002). Distortion minimization of laser-processed components through control of laser scanning patterns. Rapid Prototyp J;8(5):270–6.

Deng D, Kiyoshima S. (2010). Numerical simulation of residual stresses induced by laser beam welding in a SUS316 stainless steel pipe with considering initial residual stress influences. Nucl Eng Des;240:688–96.

Deshpande V.S., Fleck N.A., (2001). Collapse of truss core sandwich beams in 3-point bending, *Int. J. Solids & Structures*, , 38, p.6275.

Deshpande V.S., Fleck N.A., Ashby M.F., (2001). Effective properties of the octet-truss lattice material, *J. Mechanics & Physics of Solids*, , 49, p.1747.

Dong L, Makradi A, Ahzi S, Remond Y. (2009). Three-dimensional transient finite element analysis of the selective laser sintering process. J Mater Process Technol.;29:700–6.

Earl, J.M., Manners C. R., Kerekes, T. A., Marygold, P. H., Thayer, J. S. (1999). "Rapid prototyping system and method with support region data processing" US Patent 5,943,235 Assignee: 3D Systems, Inc., Calif.

Evans A.G., Multifunctionality of cellular metal systems, *Prog. Materials Sci.*, 1999, 43, p.171.

Facchini, L., Magalini, E., Robotti, P., & Molinari, A. (2009). Microstructure and mechanical properties of Ti-6Al-4V produced by electron beam melting of pre-alloyed powders. Rapid Prototyping Journal, 15(3), 171-178.

Gibson, L.J., Ashby, M.F., (1997).*Cellular Solids, Structure and Properties*, 2nd Edition, Cambridge, Cambridge University Press

Gordon, J.E. (1968). *The New Science of Strong Materials,* Penguin Books, , p 258–261

Gu D, Shen Y. (2009) Balling phenomena in direct laser sintering of stainless steel powder: metallurgical mechanisms and control methods. Mater Des.;30(8):2903–10.

Gu DD, Shen YF, Xiao J. (2008). Influence of processing parameters on particulate dispersion in direct laser sintered WC–Cop/Cu MMCs. Int J Refract Met Hard Mater;26:411–22.

Gu, D., & Shen, Y. (2009). Balling phenomena in direct laser sintering of stainless steel powder: metallurgical mechanisms and control methods.*Materials & Design*, *30*(8), 2903-2910.

Guan K, Wang Z, Gao M, Li X, Zeng X. (2013). Effects of processing parameters on tensile properties of selective laser melted 304 stainless steel. Mater Des ;50:581–6.

Hague, R., Mansour, S., & Saleh, N. (2003). Design opportunities with rapid manufacturing. *Assembly automation*, *23*(4), 346-356.

Harrysson, O. L., Cansizoglu, O., Marcellin-Little, D. J., Cormier, D. R., & West II, H. A. (2008). Direct metal fabrication of titanium implants with tailored materials and mechanical properties using electron beam melting technology. Materials Science and Engineering: C, 28(3), 366-373.

Heinl, P., Müller, L., Körner, C., Singer, R. F., & Müller, F. A. (2008). Cellular Ti–6Al 4V structures with interconnected macro porosity for bone implants fabricated by selective electron beam melting. *Acta biomaterialia*, *4*(5), 1536-1544.

Hopkinson, N., Hague, R., & Dickens, P. (Eds.). (2006). *Rapid manufacturing: an industrial revolution for the digital age*. John Wiley & Sons.

Huang, X. M., Ye, C. S., Wu, S. Y., Guo, K. B. and Mo, J. H. (2009) “Sloping wall structure support generation for fused deposition modeling”, Int. J. Adv. Manuf. Technol. Vol: 42, pp:1074–1081.

Hur, J. and Lee K. (1998) “The development of a CAD environment to determine the preferred build-up direction for layered manufacturing”, The International Journal of Advanced Manufacturing Technology, Volume 14, Number 4, pp. 247- 254.

Hyun S., Karlsson, A.M., Torquato, S., Evans, A.G., Simulated properties of Kagomé and tetragonal truss core panels, *Int. J. Solids & Structures*, 2003, **40**, 25, p.6989.

Ibraheem Ameer K, Derby Brian, et al. (2003). Thermal and residual stress modelling of the selective laser sintering process. Mater Res Soc;758:47–52.

Jhabvala, J., Boillat, E., Glardon, R., (2012). An innovative method to build support structures with a pulsed laser in the selective laser melting process. International Journal of Advanced Manufacturing Technology 59, 137–142.

Kim B., Christensen R.M., (2000). Basic two-dimensional core types for sandwich structures, *Int’l J. Mechanical Sciences*, , 42, p. 657.

Kirschman, C. F., Jara–Almonte, C.C., Bagchi, A., Dooley. R.L. and Ogale, A.A. (1991). “Computer Aided Design of Support Structures for Stereolithographic Components” Proceedings of the 1991 ASME Computers In Engineering Conference, Santa Clara, pp 443–448,

Kruth, J. P., Froyen, L., Van Vaerenbergh, J., Mercelis, P., Rombouts, M., & Lauwers, B. (2004). Selective laser melting of iron-based powder. *Journal of Materials Processing Technology*, *149*(1), 616-622.

Kumar C, Larry J, Larry R (1995) Support generation for fused deposition modeling, Solid Freeform Fabrication Symposium, University of Texas, Austin, pp: 229–241 (3D Systems, Inc., 1989).

Laura Castillo. (2005). Study about the rapid manufacturing of complex parts of stainless steel and titanium. TNO I report with the collaboration of (AIMME) Instituto Technologico Metalmacanico

LI J R, CHEN H F, YU J L, HAN F S. (2003). Effect of dual-size cell mix on the stiffness and strength of open-cell aluminum foams J. Mater Sci & Eng, , A362: 240-248.

Li, R., Shi, Y., Liu, J., Xie, Z., & Wang, Z. (2010). Selective laser melting W–10 wt.% Cu composite powders. *The International Journal of Advanced Manufacturing Technology*, *48*(5-8), 597-605.

Lu J. Handbook of Measurement of Residual stresses, vol. 1. SEM, Bethel (1996). ISBN: 978-0132557382. p. 319–22.

Ma, L., & Bin, H. (2007). Temperature and stress analysis and simulation in fractal scanning-based laser sintering. The International Journal of Advanced Manufacturing Technology, 34(9-10), 898-903.

Majhi, J., Janardan R., Smid, M. and Gupta, P. (1999), "On some geometric optimization problems in layered manufacturing", Computational Geometry, Vol. 12, pp. 219–239.

Mansour, S., & Hague, R. (2003). Impact of rapid manufacturing on design for manufacture for injection moulding. *Proceedings of the Institution of Mechanical Engineers, Part B: Journal of Engineering Manufacture*, *217*(4), 453-461.

Markaki, A. E., & Clyne, T. W. (2001). The effect of cell wall microstructure on the deformation and fracture of aluminium-based foams. Acta Materialia, 49(9), 1677-1686.

Matsumoto, M., Shiomi, M., Osakada, K., & Abe, F. (2002). Finite element analysis of single layer forming on metallic powder bed in rapid prototyping by selective laser processing. *International Journal of Machine Tools and Manufacture*, *42*(1), 61-67.

McKown, S., Shen, Y., Brookes, W. K., Sutcliffe, C. J., Cantwell, W. J., Langdon, G. S., & Theobald, M. D. (2008). The quasi-static and blast loading response of lattice structures. International Journal of Impact Engineering, 35(8), 795-810.

Mercelis, P., & Kruth, J. P. (2006). Residual stresses in selective laser sintering and selective laser melting. *Rapid Prototyping Journal*, *12*(5), 254-265.

Mercelis, P., & Kruth, J. P. (2006). Residual stresses in selective laser sintering and selective laser melting. Rapid Prototyping Journal, 12(5), 254-265.

Mills, K. C. (Ed.). (2002). Recommended values of thermophysical properties for selected commercial alloys. Woodhead Publishing.

Mognol, P., Lepicart, D., & Perry, N. (2006). Rapid prototyping: energy and environment in the spotlight. Rapid Prototyping Journal, 12(1), 26-34.

Morgan, R., Sutcliffe, C. J., & O'Neill, W. (2001). Experimental investigation of nanosecond pulsed Nd: YAG laser re-melted pre-placed powder beds. *Rapid Prototyping Journal*, *7*(3), 159-172.

Mullen, L., Stamp, R. C., Brooks, W. K., Jones, E., & Sutcliffe, C. J. (2009). Selective Laser Melting: A regular unit cell approach for the manufacture of porous, titanium, bone in-growth constructs, suitable for orthopedic applications. Journal of Biomedical Materials Research Part B: Applied Biomaterials, 89(2), 325-334.

Mumtaz, K., Vora, P., Hopkinson, N., 2011. A method to eliminate anchors/supports from directly laser melted metal powder bed processes. In: Proceedings of the 22nd International Solid Freeform Fabrication Symposium, Austin, USA.
Nickel A, Barnett D, Prinz F. (2001). Thermal stresses and deposition patterns in layered manufacturing. Mater Sci Eng;A317(1):59–64.

Nieh, T. G., Higashi, K., & Wadsworth, J. (2000). Effect of cell morphology on the compressive properties of open-cell aluminum foams. Materials Science and Engineering: A, 283(1), 105-110.

Onck P R, Andrews E W, Gibson L J. (2001). Size effects in ductile cellular solids(Part I): modeling[J]. International Journal of Mechanical Sciences, ,43: 681-699.

Oud-Heverlee, G. E. and Herenthout, K. R. (2010). "Method and apparatus for automatic support generation for an object made by means of a rapid prototype production method" US Patent 2010/0228369 A1. Assignee: Materialise NV, Belgium.

Patil RB, Yadava V. Finite element analysis of temperature distribution in single metallic powder layer during metal laser sintering. Int J Mach Tools Manuf 2007;47(7–8):1069–80.

Pattanayak, D. K., Fukuda, A., Matsushita, T., Takemoto, M., Fujibayashi, S.,Sasaki, K., & Kokubo, T. (2011). Bioactive Ti metal analogous to human cancellous bone: fabrication by selective laser melting and chemical treatments. Acta biomaterialia, 7(3), 1398-1406.

Pohl, H., Simchi, A., Issa, M., & Dias, H. C. (2001). Thermal stresses in direct metal laser sintering. In *Proceedings of the Solid Freeform Fabrication Symposium* (pp. 366-372).

Pullin, J., & Offen, A. (2008). 'Back to the Drawing Board - Addressing the design issues of RM'. *Time Compression Technologies Rapid Manufacturing Conference 2008*, Rapid News Publications Plc, Coventry, West Midlands.

Putte, B. S., Bornem, J. P., Huldenberg, W. V. (1997) "Method for supporting an object made by means of stereolithography or another rapid prototype production method" US Patent 5,595,703. Assignee: Materialise, Belgium.

Ramirez D.A., Murr, L.E. et al. (2011). "Open-cellular copper structures fabricated by additive manufacturing using electron beam melting." Materials Science and Engineering: A 528(16-17): 5379-5386.

Rännar, L. E., Glad, A., & Gustafson, C. G. (2007). Efficient cooling with tool inserts manufactured by electron beam melting. *Rapid Prototyping Journal*,*13*(3), 128-135.

Roberts, I. A., Wang, C. J., Esterlein, R., Stanford, M., & Mynors, D. J. (2009). A three-dimensional finite element analysis of the temperature field during laser melting of metal powders in additive layer manufacturing. International Journal of Machine Tools and Manufacture, 49(12), 916-923.

Rombouts, M., Kruth, J. P., Froyen, L., & Mercelis, P. (2006). Fundamentals of selective laser melting of alloyed steel powders. *CIRP Annals-Manufacturing Technology*, *55*(1), 187-192.

Rosen, D. W. (2007). Computer-aided design for additive manufacturing of cellular structures. *Computer-Aided Design & Applications*, *4*(5), 585-594.

Rossini, N. S., Dassisti, M., Benyounis, K. Y., & Olabi, A. G. (2012). Methods of measuring residual stresses in components. *Materials & Design*, *35*, 572-588.

Santorinaios M., Brooks W.,. Sutcliffe C.J, Mines, R.A. (2006) Crush behaviour of open cellular lattice structures manufactured using selective laser melting, High Performance Structures and Materials Iii 85481-490.

Schoen, A.H., (1970). Infinite Periodic Minimal Surfaces Without Self-Intersection. National Aeronautics and Space Administration (NASA) Tech, Washington, DC (Note no. D-5541).

Schwarz, H.A., (1890). Gesammelte Mathematische Abhandlungen. Springer, Berlin (Reprinted by Chelsea Publishing Company, 1972).

Shen X-F et al. (2005) ;Finite element simulation of thermal distribution in direct metal laser multi-track sintering. J Sichuan Univ (Eng Sci Ed) 37(1):47–51.

Shuai C, Feng P, et al. (2012). Simulation of dynamic temperature field during selective laser sintering of ceramic powder. Mathe Computer Modell Dynam Syst. 1(11).

Simchi A, Asgharzadeh H. (2004). Densification and microstructural evaluation during laser sintering of M2 high speed steel powder. Mater Sci Technol ;20:1462–8.

Simchi A, Pohl H (2004). Direct laser sintering of iron–graphite powder mixture. Mater Sci Eng A;383:191–200.

Simchi, A. (2006). Direct laser sintering of metal powders: mechanism, kinetics and microstructural features. Materials Science and Engineering: A, 428(1), 148-158.

Spierings, A. B., Levy, G., Labhart, L., & Wegener, K. (2011). Production of functional parts using SLM–Opportunities and limitations. Virtual and Rapid Manufacturing: Advanced Research in Virtual and Rapid Prototyping, 785-790.

Spierings, A.B. & Levy, G. (2009). Comparison of density of stainless steel 316L parts produced with selective laser melting using different powder grades. In Proceedings of the Annual International Solid Freeform Fabrication Symposium, ed. D. L. Bourell, 342-353. Austin, Texas.

Thijs, L., Verhaeghe, F., Craeghs, T., Humbeeck, J. V., & Kruth, J. P. (2010). A study of the microstructural evolution during selective laser melting of Ti–6Al–4V. Acta Materialia, 58(9), 3303-3312.

Thomas, D. (2010). The development of design rules for selective laser melting (Doctoral dissertation, University of Wales).

Thummler F, Oberacker R. An introduction to powder metallurgy. Cambridge (London): The University Press; 1993.

Timoshenko, S. P., & Goodier, J. N. (2011). Theory of elasticity. International Journal of Bulk Solids Storage in Silos, 1(4), 567-567.

Totten, G. E., Howes, M. A., & Inoue, T. (2002). Handbook of residual stress and deformation of steel. vol. 1. SEM, Bethel 2005, ISBN: 978- 0871707291; p. 417.

Traini, T., Mangano, C., Sammons, R. L., Mangano, F., Macchi, A., & Piattelli, A. (2008). Direct laser metal sintering as a new approach to fabrication of an isoelastic functionally graded material for manufacture of porous titanium dental implants. Dental materials, 24(11), 1525-1533.

Walton HW. Deflection methods to estimate residual stress (2002). Handbook of residual stress and deformation of steel. ASM International; ISBN: 0-87170-729-2; p. 89–98.

Wang J., Evans A.G., Dharmasena, K.H., Wadley, N.G., (2003). On the performance of truss panels with Kagomé cores, Int. J. Solids & Structures, 40, 25, p.6981.

Wicks, N., Hutchinson, J.W. (2001). Optimal truss plates, Int. J. Solids & Structures, , 38, p.5165.

Wohlers, T. (2013). Wohlers Report.

Wong, M., Tsopanos, S., Sutcliffe, C. J., & Owen, I. (2007). Selective laser melting of heat transfer devices. Rapid Prototyping Journal, 13(5), 291-297.

Wu, W., Yang, Y., & Huang, Y. (2007). Direct manufacturing of Cu-based alloy parts by selective laser melting. Chinese Optics Letters, 5(1), 37-40.

Yang, C. C., & Nakae, H. (2000). Foaming characteristics control during production of aluminum alloy foam. *Journal of Alloys and Compounds*, *313*(1), 188-191.

Yasa, E., Deckers, J., Kruth, J. P., Rombouts, M., & Luyten, J. (2010). Charpy impact testing of metallic selective laser melting parts. *Virtual and physical prototyping*, *5*(2), 89-98.

Yilbas BS, Arif AFM. (2001) Material response to thermal loading due to short pulse laser heating. Int J Heat Mass Transfer;44:3787–98.

Yin J, Zhu H, et al. (2012). Simulation of temperature distribution in single metallic powder layer for laser micro-sintering. Comput Mater Sci;53(1):333–9.

Zaeh M, Branner G. (2010) Investigations on residual stresses and deformations in selective laser melting. Prod Eng;4(1):35–45.

Zhang DQ, Cai QZ, et al. (2010) Select laser melting of W–Ni–Fe powders: simulation and experimental study. Int J Adv Manuf Technol;51(5–8):649–58.

Zhang, L. C., Klemm, D., Eckert, J., Hao, Y. L., & Sercombe, T. B. (2011). Manufacture by selective laser melting and mechanical behavior of a biomedical Ti 24Nb–4Zr–8Sn alloy. Scripta Materialia, 65(1), 21-24.

Zhou J, Shrotfuya P, Soboyelo W 0. (2004). Mechanism and mechanics of compressive deformation in open-cell A1 foams [J1. Mechanics of Materials, ,36: 78 1-797.

Website links:

http://www.xpress3d.com]
http://www.additive3d.com/bpm.html
http://www.jharper.demon.co.uk/rptc01.htm
http://www.eos.com
http://www.3trpd.co.uk
http://www.astm.org/COMMITTEE/F42.htm
http://www.susqu.edu/brakke/aux/evolver/examples/periodic/periodic.html
http://www.hieta.co.uk
http://www.ilt.fraunhofer.de

http://www.sandvik.com/en/search/?q=additive+manufacturing

http://www.lpwtechnology.com/

http://www.exeter.ac.uk/

http://www.economist.com/node/21552892

APPENDIX A

Analytical Model for Estimating the Energy Consumption in SLM/DMLS Process

A.1 Energy equation

The energy absorbed by the part is calculated from the laser power laser scanning velocity (v), layer thickness (t), and hatch spacing (h) between two adjacent scan vectors.

$$E = \frac{P}{vht} \tag{A.1}$$

Energy required for melting or energy required for phase change is,

$$E_{melt} = m\rho[C_p(T_m - T_o) + L_h] \tag{A.2}$$

Where Cp– average specific heat [J/g.K] from ambient bed temperature T_0 to metal melting temperature T_m , and L_h [J/g] is latent heat of fusion, – density of the material [g/mm3].

Total energy consumption can be estimated as power consumed and time taken during the building of the part.

$$E_{Total} = P_s T_s + P T_i \tag{A.3}$$

Where Ps – Setup Power required by the motor for powder deposition [W], Ts - Setup time for powder deposition [s], and its constant for all layers, Pl– Laser power [W], Ti – Laser interaction time [s].

Setup time Ts can be estimated as,

$$T_s = t_d + t_z \tag{A.4}$$

Where, t_d time for powder deposition, t_z time for work bed to move down in z direction so that new layer of powder can be deposited

$$T_i = \frac{d}{v} \quad = \frac{\sum_i^N d_i}{v} \tag{A.5}$$

Where, d – Scanning distance with in a layer [mm] , *v* – Laser scanning velocity [mm/s], N - is the number of layers

The distance travelled by the laser can divided into,

$$d = C_l + H_l \qquad \text{(A.6)}$$

Where C_l is the contour length and H_l is the hatch length. The length of the contours is calculated as the sum of all vectors defining the slice borders. The hatching length, on the other hand, is calculated either by dividing the hatching area with the hatching space h or as the sum of all hatching vectors, depending on whether a contour or a vector file, respectively, is involved.

$$T_i = \frac{\sum_i^N (C_{li} + H_{li})}{v} \qquad \text{(A.7)}$$

Sometimes, it is very convenient to be able to estimate the build-time before the slicing phase. In such cases the STL file must be used as a source for the required geometry information. Assuming that a constant layer thickness t¸ is employed during fabrication,

Total contour length,

$$C_l = \sum_{i=1}^N C_{li} = \frac{A_s}{t} \qquad \text{(A.8)}$$

Total hatching length,

$$H_l = \sum_{i=1}^N H_{li} = \frac{V_p}{ht} \qquad \text{(A.9)}$$

Total energy consumption is therefore,

$$E_T = P_s\left[(t_d + t_z).\frac{y}{t}\right] + P\left[\frac{\sum_{i=1}^N C_{li} + H_{li}}{v}\right] \qquad \text{(A.10)}$$

Where V_p is the volume of the part, and A_s is the area sum of all triangles of the tessellated model of the part projected on a vertical (normal to the machines platform) plane. y is the vertical height of the part parallel to the build direction.

A.2 Comparison of the Energy Consumption of Different Parts

By using the equation (A.10), the total energy consumptions of cylindrical parts of the same geometrical dimensions, but with different densities (solid, hollow, and cellular structure) were calculated. The model predicts that the energy consumption of the cylindrical part filled with internal cellular structures is 65 % less than the solid part. The minimum energy is achieved when the cylinder is made hollow and this is most logical and first step in reducing both material and energy consumption. However, in most case there are manufacturing constraints for internal hollow parts and the use of support structure becomes necessary. Furthermore, hollow parts may not be able to sustain loads applied on them and thus weaken the performance of the part. In light of this, cellular structure are thought to be the best candidate for making lightweight parts and their superiority in enabling the manufacturability of complex parts while fulfilling functional needs.

Table A.1 Comparison of energy consumption of different parts

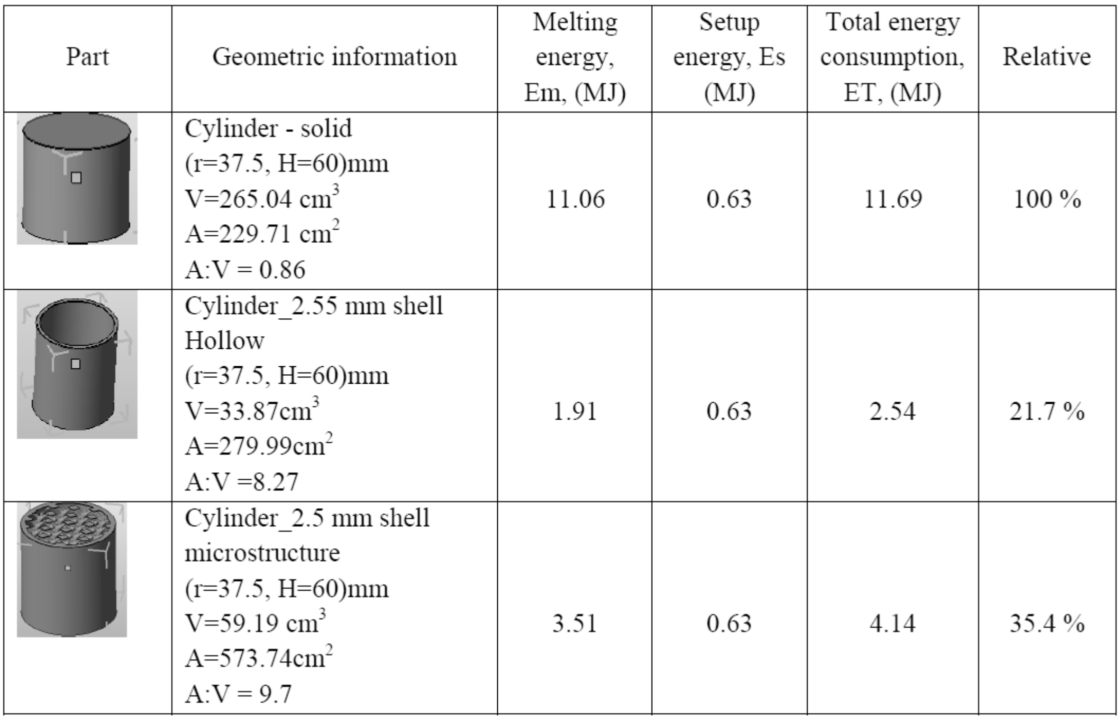

Part	Geometric information	Melting energy, Em, (MJ)	Setup energy, Es (MJ)	Total energy consumption, ET, (MJ)	Relative
	Cylinder - solid (r=37.5, H=60)mm V=265.04 cm^3 A=229.71 cm^2 A:V = 0.86	11.06	0.63	11.69	100 %
	Cylinder_2.55 mm shell Hollow (r=37.5, H=60)mm V=33.87cm^3 A=279.99cm^2 A:V =8.27	1.91	0.63	2.54	21.7 %
	Cylinder_2.5 mm shell microstructure (r=37.5, H=60)mm V=59.19 cm^3 A=573.74cm^2 A:V = 9.7	3.51	0.63	4.14	35.4 %

Fig. A.1 shows the energy consumption of large X-Y cross-sectional Disc shaped part and vertically tall cylindrical part. The objective was to weight the percentage contribution of E_m (energy for melting) and E_s (energy for powder deposition and machine setup) on overall total energy consumption. It is evident that the contribution of E_s is estimated to be 16.5% for 200mm toll part and is negligible for the large X-Y cross-sectional part. The height is the determinant factor the setup energy while the volume and surface area is the determinant factor of the melting energy. Indicating that the orientation of the part should be taken into account in or reduce the energy usage. The downside to short and large X-Y cross-sectional part would be, the high thermal stresses that it generates which may cause thermal distortions to the part or delamination from the base plate.

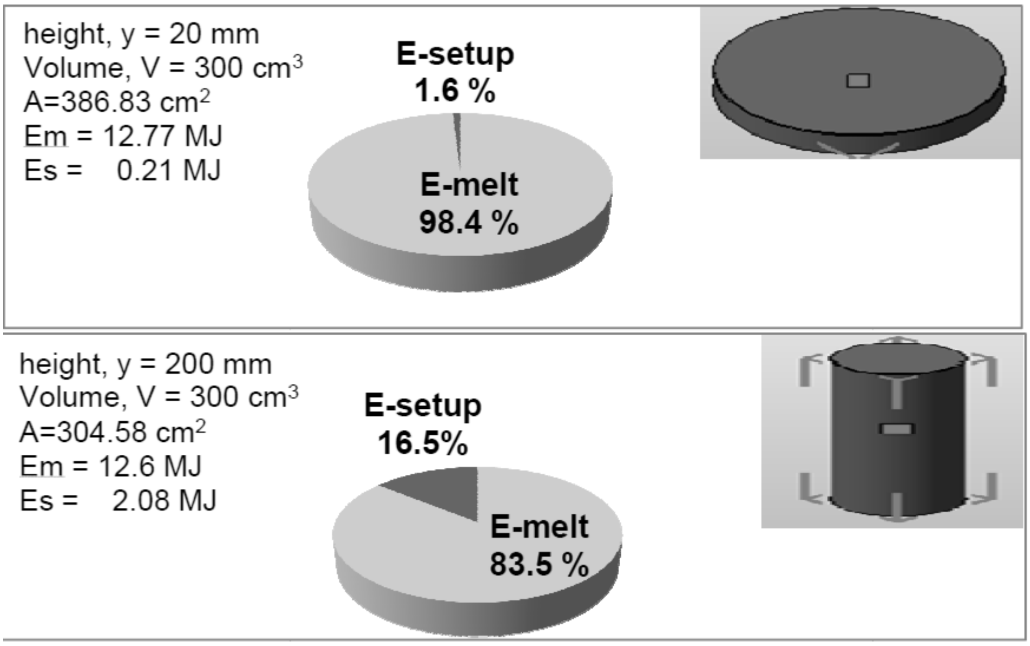

Figure A.1 Comparison of the energy consumption of tall cylinder and large Disc shaped parts

The calculation is based on a single part in the build chamber. When many parts are nested together in the same build, the E_m will increase as more materials are melted, but E_s will remain roughly the same (i.e. the powder deposition time is constant). Nesting parts together in the build will help minimize the energy consumption and time requiring for setting up the machine. Also by using thicker layers decreases the number of layers need in the build, but may compromise the bonding between layers and as result the density required from the part.